THE IMPACTS OF SHORT-LIVED OZONE PRECURSORS ON CLIMATE AND AIR QUALITY

Meridith McGee Fry

A dissertation submitted to the faculty of the University of North Carolina at Chapel Hill in partial fulfillment of the requirements for the degree of Doctor of Philosophy in the Department of Environmental Sciences and Engineering.

Chapel Hill
2013

Approved by:

Dr. J. Jason West

Dr. William Vizuete

Dr. Jason Surratt

Dr. Adel Hanna

Dr. Vaishali Naik

Abstract

MERIDITH MCGEE FRY: The Impacts of Short-Lived Ozone Precursors on Climate and Air Quality
(Under the direction of Dr. J. Jason West)

Human emissions of short-lived ozone precursors not only degrade air quality and health, but indirectly affect climate via chemical effects on ozone, methane, and aerosols. Some have advocated for short-lived air pollutants in near-term climate mitigation strategies, in addition to national air quality programs, but their radiative forcing (RF) impacts are uncertain and vary based on emission location.

In this work, global chemical transport modeling is combined with radiative transfer modeling to study the impacts of regional ozone precursor emissions (NO_x, CO, and NMVOCs) on climate, via changes in ozone, methane, and sulfate, and on regional and global air quality. The first study evaluates NO_x, CO, and NMVOC emission reductions from four regions across an ensemble of models, finding that NMVOC and CO reductions from all four regions cool climate (negative RF) by decreasing ozone and methane, while improving air quality. NO_x and NMVOC global warming potentials (GWPs), a measure of the relative radiative effects of individual climate forcers, vary strongly among regions, while CO GWPs show less variability. The second and third studies investigate further the RF and air quality impacts of CO and NMVOC emission reductions from 10 world regions. The greatest benefits to RF and air quality (per unit emissions) are achieved by CO reductions from the tropics, due to more active

photochemistry and convection. CO GWPs are fairly independent of the reduction region (GWP_{20}: 3.71 to 4.37; GWP_{100}: 1.26 to 1.44), while NMVOC GWPs are more variable (GWP_{20}: -1.13 to 18.9; GWP_{100}: 0.079 to 6.05). Accounting for additional forcings from CO and NMVOC emissions would likely change RF and GWP estimates. Regionally-specific GWPs for NO_x and NMVOCs and a globally-uniform GWP for CO may allow these gases to be included in a multi-gas emissions trading framework, and enable comprehensive strategies for meeting climate and air quality goals simultaneously.

Future research could investigate full climate responses using coupled chemistry-climate models, and perform regional analyses of specific emission control measures to maximize climate and air quality benefits.

Acknowledgements

I am extremely grateful to my advisor, Jason West, for his guidance, support, and dedication to my growth as a researcher. To my committee members, thank you for providing valuable insight and suggestions toward improving this work. I especially thank Vaishali Naik and Dan Schwarzkopf for your endless support with the standalone RTM. I am grateful to the NOAA Geophysical Fluid Dynamics Laboratory and UNC Research Computing for providing the necessary computational resources.

I would like to thank Bill Collins for contributing his expertise in climate metrics, and for the opportunity to collaborate on another project. I thank the Task Force on Hemispheric Transport of Air Pollution modelers, who graciously shared their data for my first study. I am also grateful to Louisa Emmons for her support with MOZART-4.

I would like to acknowledge my funding from Jason West, the U.S. EPA Science to Achieve Results Graduate Fellowship Program, and the U.S. EPA Office of Air Quality Planning and Standards. I also thank the U.S. EPA for supporting me as a summer fellow, and especially Dale Evarts, Carey Jang, and Pat Dolwick.

To my family and friends, thank you for your continuous support. To my parents and sister, thank you for always believing in me, and my husband, Lars, for taking a chance by moving to NC and for your infinite understanding and encouragement.

Disclaimer

This dissertation was developed under STAR Fellowship Assistance Agreement no. FP917184 awarded by the U.S. Environmental Protection Agency (EPA). It has not been formally reviewed by EPA. The views expressed in this dissertation are solely those of Meridith McGee Fry, and EPA does not endorse any products or commercial services mentioned in this dissertation.

Table of Contents

List of Tables

List of Figures

List of Abbreviations

AF	Africa
AM2	NOAA GFDL Atmospheric Model Component of CM2
AM3	NOAA GFDL Atmospheric Model Component of CM3
AU	Australia and New Zealand
ΔB	Change in burden
BC	Black carbon
C	Carbon
CASTNET	Clean Air Status and Trends Network
CH_4	Methane
CM3	NOAA GFDL Coupled Physical Model
CMDL	Climate Monitoring and Diagnostics Laboratory
CMIP5	Coupled Model Intercomparison Project Phase 5
CO	Carbon monoxide
CO_2	Carbon dioxide
CTM	Chemical transport model
CV	Coefficient of variation
DMS	Dimethylsulfide
DU	Dobson unit
ΔE	Change in emissions
EA	East Asia
EMEP	European Monitoring and Evaluation Programme
EPA	Environmental Protection Agency
EU	Europe

F	CH_4 feedback factor
FSU	Former Soviet Union
GEOS-5	Goddard Earth Observing System Model, version 5
GFDL	Geophysical Fluid Dynamics Laboratory
Gg	Gigagram
GWP	Global warming potential
GWP_{20}	Global warming potential at 20-year time horizon
GWP_{100}	Global warming potential at 100-year time horizon
HNO_3	Nitric acid
HO_2	Hydroperoxy radical
H_2O_2	Hydrogen peroxide
hPa	Hectopascal
IIASA GAINS	International Institute for Applied Systems Analysis Greenhouse Gas and Air Pollution Interactions and Synergies
IMPROVE	Interagency Monitoring of Protected Visual Environments
IN	India
IPCC	Intergovernmental Panel on Climate Change
ΔL	Change in loss
LM2	NOAA GFDL Land Model Component of CM2
mb	Millibar
ME	Middle East and Northern Africa
MEGAN	Model of Emissions of Gases and Aerosols from Nature
MOZART-2	Model of Ozone and Related Chemical Tracers, version 2
MOZART-4	Model of Ozone and Related Chemical Tracers, version 4
$\mu g\ m^{-2}$	Micrograms per square meter

$\mu g\ m^{-3}$	Micrograms per cubic meter
$\mu mol\ m^{-2}$	Micromoles per square meter
$mW\ m^{-2}$	Milliwatts per square meter
N	Nitrogen
$^{\circ}N$	Degrees North
NA	North America
$ng\ m^{-2}$	Nanograms per square meter
$ng\ m^{-3}$	Nanograms per cubic meter
NH	Northern hemisphere
NH_3	Ammonia
NH_4NO_3	Ammonium nitrate
NMVOC	Non-methane volatile organic compound
NOAA	National Oceanic and Atmospheric Administration
NO_2	Nitrogen dioxide
NO_3	Nitrate
NO_x	Nitrogen oxides
N_2O	Nitrous oxide
O_3	Ozone
ObjECTS GCAM	Object-oriented Energy, Climate, and Technology Systems Global Change Assessment Model
OC	Organic carbon
OH	Hydroxyl radical
ΔP	Change in production
PAN	Peroxyacetyl nitrate
$PM_{2.5}$	Particulate matter, 2.5 micrometers or less in diameter

POET	Precursors of Ozone and their Effects in the Troposphere
ppbv	Parts per billion by volume
pptv	Parts per trillion by volume
RCP	Representative Concentration Pathways
RCP8.5	Representative Concentration Pathway 8.5
RETRO	REanalysis of the TROpospheric chemical composition over the past 40 years
RF	Radiative climate forcing
RO_2	Peroxyl radical
RTM	Radiative transfer model
$^{\circ}S$	Degrees South
SA	South Asia; South America
SD	Standard deviation
SE	Southeast Asia
SH	Southern hemisphere
SOA	Secondary organic aerosol
SO_2	Sulfur dioxide
SO_4^{2-}	Sulfate aerosol
SR	Source-Receptor
STAR	Science to Achieve Results
TF HTAP	Task Force on Hemispheric Transport of Air Pollution
Tg	Teragram
τ_{OH}	CH_4 lifetime against loss by tropospheric OH
τ_{total}	Total CH_4 lifetime
UNEP	United Nations Environment Programme

US	United States of America
UT	Upper troposphere, 500 hPa to the tropopause
VOC	Volatile organic compound
W m^{-2}	Watts per square meter
WMO	World Meteorological Organization
ΔX	Change in export

Chapter 1. Introduction

Air pollution and global climate change are two leading environmental challenges facing the world today. These interrelated problems are driven by common emission sources and chemical feedbacks, and can span both near and far-reaching spatial and temporal scales (Unger et al., 2012). Many air pollutants influence climate, while climate change itself can worsen air quality (Fiore et al., 2012). In this dissertation, we focus on ozone (O_3) precursors (methane [CH_4], nitrogen oxides [NO_x], carbon monoxide [CO], and non-methane volatile organic compounds [NMVOCs]) as an opportunity to address air pollution and global climate change together. We study the influence of O_3 precursor emissions on several important short-lived air pollutants: O_3 and aerosols, and climate forcers: CH_4, O_3, and aerosols (Pham et al., 1995; Unger et al., 2006; Shindell et al., 2009; Leibensperger et al., 2011).

Human-induced global climate change traditionally has been related to the increasing abundance of long-lived greenhouse gases (e.g. carbon dioxide [CO_2]) in our atmosphere, whose impacts can take decades to centuries to be realized. Short-lived climate forcers, on the other hand, have gained recent interest as an opportunity to slow the rate of near-term climate warming and to expedite the mitigation of climate impacts over the next few decades, while simultaneously improving air quality. Current air quality legislation, however, does not consider the impacts of these short-lived species on climate, and international climate agreements have excluded them from the basket of relevant species for emissions trading (Unger et al., 2012), given the dependence of their

climate impacts on emission location and chemical interactions with co-emitted species (Fiore et al., 2012). This dissertation aims to inform future policies and further the understanding of the climate and air quality effects of short-lived climate forcers.

Tropospheric O_3, a secondary air pollutant and short-lived climate forcer, forms through the nonlinear photochemical oxidation of O_3 precursors: CH_4, CO, or NMVOCs by the hydroxyl radical (OH) in the presence of NO_x. Given that the mean tropospheric lifetimes of O_3 (~22 days) (Stevenson et al., 2006), CH_4 (9 to 10 years), and NO_x, CO, and NMVOCs (days to months) often exceed intercontinental transport times (5 to 10 days) (Fiore et al., 2009), O_3 precursor emissions can affect surface and tropospheric O_3 concentrations over intercontinental scales (Akimoto, 2003; TF HTAP, 2010). O_3 concentrations also can respond more gradually over the long term due to changes in CH_4, a longer-lived O_3 precursor.

By altering the availability of atmospheric oxidants, O_3 precursors affect other short-lived climate forcers including secondary aerosols and tropospheric CH_4. SO_4^{2-} aerosols form through the oxidation of sulfur dioxide (SO_2) by OH in the gas phase or by H_2O_2 or O_3 in the aqueous phase. Because O_3 itself is a source of OH (and thus, hydrogen peroxide [H_2O_2]), tropospheric O_3 and sulfate aerosol (SO_4^{2-}) chemistry are closely coupled in the troposphere (Unger et al., 2006, 2008). Similarly by changing oxidant levels, O_3 precursor emissions influence the abundance of nitrate (NO_3^-) and secondary organic aerosols (SOA) (Bauer et al., 2007; Hoyle et al., 2009). SO_4^{2-}, NO_3^-, and SOA are all important components of fine particulate matter ($PM_{2.5}$), a key air pollutant that also impacts climate.

Tropospheric CH_4 and O_3 are also closely linked by precursor-driven changes in oxidants. NO_x emissions tend to increase OH and hence, decrease CH_4 lifetime, while CO, NMVOC, and CH_4 emissions have the opposite effect, decreasing OH and increasing CH_4 lifetime (Prather et al., 1995; Wild et al., 2001; Fiore et al., 2002; Naik et al., 2005; Unger et al., 2008). Through their influence on CH_4, O_3 precursors (including CH_4 emissions themselves) also impact tropospheric O_3 on the longer timescale of the CH_4 lifetime (Berntsen et al., 2005; West et al., 2007).

Radiative climate forcing (RF) is one measure used to assess the influence of climate forcers (i.e. greenhouse gases and aerosols) and their precursors on the Earth's energy balance and thus, the relative warming or cooling of climate. RF is the change in net radiation fluxes (net shortwave minus net longwave radiation) at the tropopause after allowing stratospheric temperatures to readjust to radiative equilibrium, where a positive RF implies climate warming and a negative RF indicates climate cooling. Since preindustrial times, changes in tropospheric O_3 and CH_4 have contributed abundance-based positive RFs of 0.35 [-0.1, +0.3] W m^{-2} and 0.48 ± 0.05 W m^{-2}, approximately 21% and 31% of the RF due to CO_2. In addition, tropospheric SO_4^{2-}, a component of $PM_{2.5}$ that scatters solar energy, has provided a negative RF of -0.40 ± 0.2 W m^{-2} (direct effect only) (Forster et al., 2007). O_3 precursors contribute importantly to these RFs, with emissions-based estimates of 0.99 ± 0.14 W m^{-2} (CH_4), 0.25 ± 0.04 W m^{-2} (CO + VOCs), and -0.29 ± 0.09 W m^{-2} (NO_x) (Shindell et al., 2009).

1.1 Policy relevance

In the U.S., the National Ambient Air Quality Standards set forth by the Clean Air Act establish both primary (protective of public health) and secondary (protective of

public welfare) standards for six criteria air pollutants including CO, NO_2, O_3, and $PM_{2.5}$. These standards, however, do not take climate impacts into consideration, focusing mainly on individual air pollutant attainment in a particular area over annual time periods. The Gothenburg Protocol, adopted by the United Nations Economic Commission for Europe and amended in 2012, is one of the first multi-national agreements that moves toward addressing transboundary air pollution by setting emission reduction commitments (including for NO_x, VOCs, sulfur, and ammonia) for EU member states to meet by 2020 and beyond. Existing air pollution legislation, however, will likely be inadequate to address rising O_3 and $PM_{2.5}$ levels worldwide, which will continue to harm human health and the environment, despite the downward trend of O_3 levels in the U.S. and Europe. Developing nations, in particular, may lack the experience needed to implement future air pollution control policies (Dentener et al., 2006). As a result, more stringent emissions control measures will be needed to ensure a sustainable atmospheric environment in the future.

As part of the United Nations Framework Convention on Climate Change, the Kyoto Protocol, an international agreement focused on climate change mitigation, sets long-lived greenhouse gas reduction targets for its Parties to achieve within a multi-year commitment period. The Kyoto Protocol allows Parties to design and implement comprehensive and cost-effective policies, where emissions constraints can be met by substituting between different long-lived greenhouse gases (Forster et al., 2007). Global warming potential (GWP), the climate metric adopted in the Kyoto Protocol, provides the framework for comparing the RF impacts of different greenhouse gases over time; thus allowing for their inclusion in emissions trading and multi-gas abatement strategies.

Over the past decade, several studies have suggested that short-lived climate forcers and their precursors be included in climate agreements like the Kyoto Protocol (Fuglestvedt et al., 1999; Rypdal et al., 2005, 2009; Naik et al., 2005; Unger et al., 2008; Fry et al., 2012), as a way to address climate change in the coming decades and to complement longer term CO_2 mitigation efforts (Jackson et al., 2009; Shindell et al., 2012; Unger et al., 2012). Reducing certain short-lived climate forcers also provides important benefits to human health and the environment, as O_3 and $PM_{2.5}$ exposure have been linked to adverse respiratory and cardiovascular health effects, premature mortality, and ecosystem damages. However, short-lived species including O_3 precursors (apart from CH_4) impact RF non-uniformly and can contribute to both climate warming and cooling, making it difficult to identify different regions' contributions to global climate change. As a result, geographically-varying GWPs may be needed (Fuglestvedt et al., 1999; Wild et al., 2001; Berntsen et al., 2005; Naik et al., 2005; West et al., 2007; Derwent et al., 2008), in contrast to long-lived greenhouse gases (e.g. CO_2) whose more uniform RF impacts allow for globally-uniform GWPs. There is a need to more fully understand the effects of O_3 precursors on the distributions of O_3, SO_4^{2-}, and other secondary species, and the corresponding variability in RF and GWP estimates (Berntsen et al., 2005). Future mitigation efforts will likely need to consider air quality and global climate change together, as many air pollutants and climate forcers originate from the same precursors and emission sources (Unger et al, 2012).

1.2 Motivation and objectives

Several past studies have used global chemical transport and radiative transfer modeling to evaluate the air quality and RF impacts of regional and global NO_x emission

reductions (Fuglestvedt et al., 1999; Wild et al., 2001; Berntsen et al., 2005; Naik et al., 2005; West et al., 2007; Derwent et al., 2008), finding that O_3 concentrations and RF depend considerably on the location or sector of NO_x emissions, with greater sensitivity to emissions from the tropics. One global model's results show that NO_x emission reductions from 9 world regions produce overall positive global net RFs (Naik et al., 2005), while West et al. (2007) found that global reductions in CH_4, CO, and NMVOCs result in negative net RFs. Naik et al. (2005) also analyzed reductions in NO_x, CO, and NMVOC emissions together from 3 regions, and Berntsen et al. (2005) evaluated CO emissions changes from 2 regions.

This dissertation examines the air quality, tropospheric burden, and RF impacts of individual O_3 precursor emission reductions through three separate studies (Table 1.1). The first study aims to evaluate O_3 precursor emissions from 4 regions across an ensemble of 11 global chemical transport models (CTM) that participated in the Task Force on Hemispheric Transport of Air Pollution multimodel intercomparison of Source-Receptor sensitivity (Chapter 2). This study improves upon previous methods by providing the spread in tropospheric burden and RF estimates across multiple CTMs as an indicator of model uncertainty, and by differentiating the contributions of O_3, CH_4, and SO_4^{2-} to global net RF and GWP using a radiative transfer model (RTM). The RF and GWP estimates for each precursor are compared among the 4 regions and to previous studies, improving our understanding of the sensitivity to different regions' emissions.

The second and third studies, which build upon the first study, are mainly motivated by the absence of studies investigating CO and NMVOC emission reductions from many world regions, where previous studies examine four regions or less (Prather et

al., 1996; Wild et al., 2001; Fiore et al., 2002; Naik et al., 2005). More detailed analyses of the air quality and RF impacts of CO (Chapter 3) and NMVOC (Chapter 4) emission reductions from 10 regions and globally, and how their magnitudes vary across regions, are presented using a global CTM and RTM. These two follow-on studies provide the basis for assessing the potential climate impact of different emission control measures, where our estimated GWPs of CO and NMVOCs can be combined with those of co-emitted species. Stakeholders considering reductions in non-CO_2 climate forcers, such as the G8 nations and the Arctic Council, may be especially interested in using these results to calculate the net climate impact of regionally-implemented emission controls (Shindell et al., 2012). More broadly, our results may inform future policies and actions aimed to address air quality and climate change jointly at the regional to international level (Rypdal et al., 2005, 2009; Jackson et al., 2009; Shindell et al., 2012). Chapter 5 concludes the dissertation by reviewing the key scientific findings, uncertainties, future research needs, and policy implications across the three studies.

1.3 Table

Table 1.1. Summary of three dissertation studies.

Study	O_3 precursors studied	Number of regions	Method of calculating air quality impacts	Method of calculating climate impacts
1. Chapter 2	CH_4, NO_x, NMVOCs, CO	4	Ensemble of 11 CTMs	Standalone RTM
2. Chapter 3	CO	10, global	Single CTM	Standalone RTM
3. Chapter 4	NMVOCs	10, global	Single CTM	Standalone RTM

Chapter 2. The influence of ozone precursor emissions from four world regions on tropospheric composition and radiative climate forcing[1]

2.1 Introduction

Tropospheric ozone (O_3), methane (CH_4), and aerosols make important contributions to the global mean radiative forcing (RF) of climate (Forster et al., 2007; Ramaswamy et al., 2001). Here we aim to quantify the net RF of these species due to regional changes in O_3 precursor emissions, across an ensemble of global chemical transport models (CTMs). We define net RF as the net (incoming minus outgoing) change in irradiance (solar and infrared) at the tropopause between a base and perturbed state (in Watts per square meter [W m^{-2}]) after allowing stratospheric temperatures to readjust (Forster et al., 2007). The contribution of changes in tropospheric O_3 to the global mean RF since preindustrial times is an estimated 0.35 ±0.15 Wm^{-2}, which is approximately 21% of the RF due to changes in carbon dioxide (CO_2) (Forster et al., 2007). Changes in CH_4 have contributed approximately 0.48 Wm^{-2}, while those in sulfate aerosols (SO_4^{2-}) have contributed approximately -0.4 ±0.2 Wm^{-2} (direct effect only) (Forster et al., 2007).

Changes in O_3 precursor emissions (nitrogen oxides [NO_x], non-methane volatile organic compounds [NMVOC], carbon monoxide [CO], and CH_4) affect the abundance

[1] Fry, M. M., V. Naik, J. J. West, M. D. Schwarzkopf, A. M. Fiore, W. J. Collins, F. J. Dentener, D. T. Shindell, C. Atherton, D. Bergmann, B. N. Duncan, P. Hess, I. A. MacKenzie, E. Marmer, M. G. Schultz, S. Szopa, O. Wild, and G. Zeng (2012), Journal of Geophysical Research, 117, D07306, doi:10.1029/2011JD017134

of gaseous species (O_3 and CH_4), and aerosols via changes in the availability of atmospheric oxidants (hydroxyl radical [OH], hydrogen peroxide [H_2O_2], O_3) (Pham et al., 1995; Unger et al., 2006; Shindell et al., 2009; Leibensperger et al., 2011). These perturbations in turn influence the RF due to O_3 and CH_4 and inorganic aerosol-phase species (Ming et al., 2005; Unger et al., 2006; Naik et al., 2007; Shindell et al., 2009). O_3 precursors also affect organic aerosols, including the formation of secondary organic aerosols (SOA) (Carlton et al., 2010), but the resulting RF remains to be quantified. O_3 decreases plant growth and hence reduces the removal of CO_2 from the atmosphere (Felzer et al., 2007; Sitch et al., 2007; Collins et al., 2010), while NO_x emissions influence nitrogen deposition and the subsequent uptake of CO_2 in terrestrial and oceanic ecosystems (Holland and Lamarque, 1997; Duce et al., 2008). Because of these influences, actions to control O_3 precursor emissions affect both air quality and global climate (Fiore et al., 2002; Dentener et al., 2005; West et al., 2007).

Past studies have shown that both regional and global reductions in NO_x surface emissions produce an overall positive RF from global CH_4 increases via decreases in OH, which outweigh the negative forcing from tropospheric O_3 decreases. The magnitude of forcing, however, depends on the location or sector of emission reduction (Fuglestvedt et al., 1999; Wild et al., 2001; Berntsen et al., 2005; Naik et al., 2005; West et al., 2007; Derwent et al., 2008). In contrast, CO, NMVOC, and CH_4 reductions contribute an overall negative RF by decreasing tropospheric O_3 and increasing OH, leading to global CH_4 decreases (Prather et al., 1996; Wild et al., 2001; Fiore et al., 2002; Naik et al., 2005). Global anthropogenic CH_4 emission reductions were shown to produce the most

negative RF of the O_3 precursors, mainly due to direct reductions in CH_4 forcing (Fiore et al., 2002; Shindell et al., 2005; West et al., 2007).

Because of the short atmospheric lifetimes of O_3, aerosols, and their precursors (apart from CH_4), studies of regional O_3 precursor reductions show that air quality and RF effects depend strongly on the geographical location of emissions (Fuglestvedt et al., 1999; Berntsen et al., 2005; Naik et al., 2005). The dependence on location, however, has made it difficult to include O_3 precursors in emissions trading schemes or international climate agreements (Rypdal et al., 2005), and to evaluate the co-benefits of actions to reduce O_3 for slowing global climate change. Studies have shown substantial dependence of O_3 concentrations and RF on the region of NO_x emissions (Fuglestvedt et al., 1999; Berntsen et al., 2005; Naik et al., 2005; Derwent et al., 2008; Fuglestvedt et al., 2010), where O_3 and RF are more sensitive to NO_x reductions from tropical regions, yet positive global annual average net RFs result from NO_x reductions in each of nine world regions (Naik et al., 2005). While NMVOCs typically have atmospheric lifetimes comparable to NO_x, CO has a longer atmospheric lifetime of 1-3 months (Seinfeld and Pandis, 2006), suggesting that the influence of CO on O_3 and OH may be less dependent on reduction region (Berntsen et al., 2005; Rypdal et al., 2005). Apart from Naik et al. (2005) who also examined combined reductions in NO_x, CO, and NMVOCs from three regions, and Berntsen et al. (2005) who evaluated CO changes from two regions, less attention has been placed on regional CO and NMVOC emissions and their effects on tropospheric O_3, CH_4, and SO_4^{2-} and global and regional net RF. In response to nonuniform forcings, some regional climate responses are also sensitive to the location and distribution of O_3, aerosols, and RF (Shindell and Faluvegi, 2009).

Here we investigate the effects of a 20% reduction in global CH_4 abundance and 20% reductions in anthropogenic emissions of NO_x, NMVOC, and CO, individually and combined, from four world regions on tropospheric O_3, CH_4, and SO_4^{2-} concentrations and on the resulting distribution and magnitude of global net RF for all precursor-region pairs. We use results from an ensemble of global CTMs that participated in the Task Force on Hemispheric Transport of Air Pollution (TF HTAP) multimodel intercomparison study of Source-Receptor (SR) sensitivity (Fiore et al., 2009), which allows for an assessment of uncertainty as the spread across CTMs. We examine the regional dependency of RF and global warming potential (GWP) to individual precursors by comparing estimates across the four regions of reduction.

2.2 Methodology

We use the results from an ensemble of 11 global CTMs (TF HTAP, 2010) to evaluate changes in the tropospheric distributions of O_3, CH_4, and SO_4^{2-} for each reduction scenario. The net RF is calculated from the simulated changes in O_3, CH_4, and SO_4^{2-} using the standalone radiative transfer model (RTM) developed by the National Oceanographic and Atmospheric Administration (NOAA) Geophysical Fluid Dynamics Laboratory (GFDL) (Schwarzkopf and Ramaswamy, 1999; GFDL GAMDT, 2004). We estimate the RF due to SO_4^{2-}, as SO_4^{2-} responds to oxidant changes, considering only its direct effects on radiation (Naik et al., 2007); few CTMs reported other aerosol species for all reduction scenarios. Although we account for variability across the CTM ensemble in the O_3, SO_4^{2-}, and CH_4 estimates, we likely underestimate the uncertainty in net RF by using only a single RTM.

2.2.1 HTAP CTM simulations

The SR simulations performed by each CTM are outlined in Table 2.1. We analyze O_3 and CH_4 results from 11 CTMs and SO_4^{2-} results from four CTMs (Table 2.2). Each CTM utilized its own emissions inventory and prescribed meteorological fields for the year 2001 (Fiore et al., 2009). Anthropogenic emissions of NO_x, NMVOCs, CO, and all precursors combined were reduced by 20% in each of four world regions: East Asia (EA), Europe and Northern Africa (EU), North America (NA), and South Asia (SA). For CH_4, the present-day abundance (1760 parts per billion by volume [ppbv]) was imposed in all simulations except for the CH_4 control simulation (SR2), where global CH_4 abundance was decreased by 20% to 1408 ppbv. All simulations were performed for a full year (2001), after an initial spin-up of at least six months (Fiore et al., 2009).

The multimodel mean ±1 standard deviation changes in the anthropogenic emissions of NO_x, NMVOCs, and CO, across 11 CTMs, are presented in Table 2.3. There is considerable variability in the emission reduction magnitudes across CTMs. Coefficients of variation (CVs) (standard deviation / mean) are lowest for NO_x emissions from EU, NA, and SA, while there is more variability in NMVOC and CO emissions from the four regions, consistent with the comparison of current global emission inventories by Granier et al. (2011).

Previous publications based on the HTAP SR experiments have emphasized the effects of long-range transport on surface O_3, and other components, and comparisons with observations (Sanderson et al., 2008; Shindell et al., 2008; Fiore et al., 2009; Jonson et al., 2010; Reidmiller et al., 2009). Fiore et al. (2009) found that the HTAP ensemble mean surface O_3 concentrations compared well with observations over EU for the year

2001, but overestimated measurements by more than 10 ppb during the summer and fall over the eastern United States and Japan. Jonson et al. (2010) compared simulated vertical O_3 profiles with observed ozonesonde profiles, finding that the spread in CTM results (and their over and underestimation of O_3 soundings) increases in the spring and summer with more active chemistry. In the winter and spring, seasonal averages for most CTMs were within 20% of sonde measurements in the upper and middle troposphere. Simulated SO_4^{2-} concentrations at the surface for the base simulation (SR1) also have been compared to observations (M. Schulz, personal communication, 2011, preliminary results available at http://aerocom.met.no/cgi-bin/aerocom/surfobs_annualrs.pl), where the results show that the CTMs are generally realistic.

Short-lived O_3 precursors affect tropospheric O_3 within hours to weeks after their emission; however, they also affect OH, which influences the lifetime of CH_4 and in turn, O_3 in the long term (Prather et al., 1996; Wild et al., 2001; Berntsen et al., 2005; Naik et al., 2005). Global CH_4 changes were calculated by Fiore et al. (2009), based on the CH_4 loss by tropospheric OH diagnostic reported for each CTM and SR3 through SR6, relative to the fixed CH_4 abundance of 1760 ppbv. Long-term O_3 responses are then calculated in each grid cell, following West et al. (2007, 2009b), by scaling the change in O_3 from the CH_4 control simulation (SR2 minus SR1) to the calculated global CH_4 change for each SR simulation and CTM. We then add the long-term O_3 responses to the simulated short-term O_3 responses to give O_3 concentrations at steady state.

Since the HTAP CTMs were typically not designed to model stratospheric chemistry, we use the same three-dimensional monthly mean O_3 concentrations in the stratosphere and merge these with calculated steady-state (short-term + long-term)

tropospheric O_3 concentrations for each simulation and CTM. Stratospheric O_3 is taken for the year 2001 from the AC&C/SPARC O_3 database prepared for CMIP5 (Available: http://pcmdi-cmip.llnl.gov/cmip5/forcing.html). Søvde et al. (2011) found that around 15% of the RF from O_3 precursors is due to O_3 changes in the lower stratosphere, using a single model with both standard and updated chemistry. Since we ignore lower stratospheric O_3 changes, our RF estimates may underestimate the full effect of O_3 precursors. After each CTM's O_3 and SO_4^{2-} results are interpolated to a common resolution (longitude x latitude x level) as required by the RTM (72 x 37 x 33 for O_3; 96 x 80 x 14 for SO_4^{2-}), the HTAP ensemble mean ±1 standard deviation O_3 and SO_4^{2-} distributions are calculated in each grid cell and month in three dimensions, in addition to the ensemble mean ±1 standard deviation global CH_4 abundances (derived from the CH_4 loss by tropospheric OH diagnostics). Global O_3, CH_4, and SO_4^{2-} changes are calculated for each CTM as perturbation (SR2 to SR6) minus base (SR1) values.

2.2.2 GFDL radiative transfer model

We employ the GFDL RTM to estimate the net RF at steady state due to the changes in atmospheric gases (O_3 and CH_4) alone and due to combined changes in O_3, CH_4, and SO_4^{2-} aerosols. The GFDL RTM is a module of the GFDL coupled atmospheric-ocean model (AM2) and simulates solar and infrared radiative transfer (GFDL GAMDT, 2004; Naik et al., 2005, 2007). It has been used in studies of long-lived greenhouse gases (Schwarzkopf and Ramaswamy, 1999) and short-lived forcing agents such as O_3 and aerosols (Naik et al, 2005, 2007; West et al., 2007; Fiore et al., 2008; Saikawa et al., 2009). Here the RTM is employed as for Naik et al. (2007) and Saikawa et al. (2009), at 144 x 90 x 24 levels, except for the following changes. We

update well-mixed greenhouse gas concentrations based on observations for the year 2001 included as part of the historical period (1750-2005) of the CMIP5 Representative Concentration Pathways (RCP) database (Meinshausen et al., 2011) (Available: http://www.iiasa.ac.at/web-apps/tnt/RcpDb/dsd?Action=htmlpage&page=download). We also update the solar data used by the RTM to the CMIP5 solar forcing data (Available: http://www.geo.fu-berlin.de/en/met/ag/strat/forschung/SOLARIS/Input_data/CMIP5_solar_irradiance.html). The RTM simulations do not include the indirect effects of aerosols on clouds or the internal mixing of aerosols. RF contributions from changes in nitrate aerosols, changes in stratospheric O_3 and water vapor, changes to the carbon cycle via O_3 and nitrogen deposition, and changes to CO_2 from CH_4, CO, and NMVOC oxidation are also omitted in the RTM simulations.

The multimodel monthly mean ±1 standard deviation O_3, CH_4, and SO_4^{2-} concentrations are used as input in the RTM simulations, along with meteorological fields from GFDL's atmosphere model (AM2) and land model (LM2), sampled one day per month at midmonth for the year 2001 to represent monthly mean conditions (Naik et al., 2005). Substantial variability in the SO_4^{2-} estimates across only four CTMs precluded evaluating the mean -1 standard deviation for SO_4^{2-} (e.g., several grid cells had standard deviations exceeding the mean). We simulate the monthly mean net radiation fluxes for the base and perturbed cases and calculate the net RF as the difference between the perturbed and base net fluxes (net shortwave minus net longwave) at the tropopause, after allowing stratospheric temperatures to readjust to radiative equilibrium (Naik et al., 2007; Saikawa et al., 2009).

2.3 Tropospheric composition changes

2.3.1 Tropospheric ozone changes

Figure 2.1 shows the changes in global annually averaged steady-state tropospheric O_3 burden and its variability across 11 HTAP CTMs. Full troposphere and upper troposphere (UT) O_3 burdens are distinguished because O_3 in the UT has a higher RF efficiency on a per molecule basis (Lacis et al., 1990; Wang et al., 1993; Forster and Shine, 1997). For each CTM's regridded O_3 distributions that have been blended with CMIP5 stratospheric O_3 values (section 2.1), the UT is defined from 500 hPa to the tropopause, where the tropopause is identified at the 150 ppbv O_3 level.

The largest changes in full troposphere and UT O_3 burden are found for the 20% CH_4 reduction, followed by the 20% combined precursor reductions from NA and EA, respectively. However, there is considerable diversity among the 11 CTMs' estimates of full troposphere and UT O_3 burden changes. In these 17 SR simulations relative to the base case, the change in UT O_3 burden per change in full troposphere O_3 burden (UT O_3 / full troposphere O_3) is largest for reductions in global CH_4 (0.36 to 0.47) and regional CO emissions (0.19 to 0.53), and smallest for regional NMVOC reductions (0.16 to 0.42) across the 11 CTMs, reflecting the longer lifetimes of CO and CH_4 in comparison to NMVOCs and NO_x. UT O_3 / full troposphere O_3 is also largest for individual O_3 precursor (NO_x, NMVOC, and CO) reductions from SA in comparison to the other regions.

To evaluate regional sensitivities, we consider how changes in full troposphere and UT O_3 burdens per unit change in emissions vary by region for each precursor (Figure 2.2). The CTMs mostly agree that the SA NO_x reduction produces the greatest

change in full troposphere and UT O_3 burden per change in emissions out of the four regions, which can be attributed to more rapid vertical mixing, stronger photochemistry, and greater sensitivity of O_3 to precursor emissions from the tropics and southern hemisphere (SH) (Kunhikrishnan et al., 2004; West et al., 2009a). We find less variability across the four regions in reducing full troposphere and UT O_3 burden per change in NMVOC and CO emissions (Figure 2.2), but six CTMs show that SA NMVOC and CO reductions produce the largest reductions in UT O_3 burden per change in emissions.

For each regional reduction, the greatest changes in steady-state tropospheric total column O_3 occur over the reduction region, in each individual CTM and across the HTAP ensemble (Figure 2.3). For NO_x reductions from each region, slight increases in O_3 burden occur in the SH, in contrast to overall decreases in the northern hemisphere (NH), due to long-term O_3 increases via CH_4 that are globally-distributed (according to the pattern of O_3 response to CH_4) (West et al., 2007, 2009b) (see section 3.2). As SA is further south than the other regions, the largest O_3 decreases occur near the tropics and do not extend as far north. The slightly higher increases in O_3 in the SH from the NA NO_x reduction correspond to this region producing greater increases in global CH_4 (Figure 2.4). For NMVOC and CO reductions from the four regions, we find decreases in total column O_3 in both the SH and NH, as sustained decreases in these precursors cause both short- and long-term global O_3 decreases. NMVOC reductions also reduce global annual average peroxy acetyl nitrate (PAN) burdens from the four regions by 1.4 ±0.6% (SR4EA), 2.0 ±0.8% (SR4EU), 1.5 ±0.5% (SR4NA), and 0.5 ±0.2% (SR4SA), relative to the base, through which NMVOCs can influence the nitrogen cycle and therefore long-

range O_3. Across the 11 CTMs, we find that tropospheric PAN decreases are correlated to the changes in NMVOC emissions for the EA, EU, and NA reductions.

2.3.2 Tropospheric methane changes

Although global CH_4 was held constant by each CTM in all perturbations, we analyze the changes in global tropospheric CH_4 calculated off-line for each perturbation. NO_x reductions from all four regions increase global CH_4 abundance via decreases in OH, while NMVOC and CO reductions from all four regions decrease global CH_4 (Figure 2.4). These changes in CH_4 drive the long-term O_3 changes discussed in the previous section. For particular precursors, reductions from certain regions, e.g. CO reductions from EA, are slightly more effective at decreasing global CH_4 than other regions. However, there is noticeable variability among the CTMs' changes in global CH_4 (Figure 2.4), which is partly explained by variance in CTM emissions for CO, but not for NO_x and NMVOCs.

For several CTMs, some emissions perturbations had minimal impact on global OH, resulting in calculated steady-state CH_4 changes of zero. In addition, the CVs of CH_4 change are lowest in magnitude for NO_x reductions (0.22 to 0.39) and highest for NMVOC reductions (-0.40 to -1.12), perhaps reflecting differing NMVOC speciation and chemical schemes among the CTMs (Collins et al. 2002).

We compare the change in global CH_4 from the combined precursor reductions to the sum of global CH_4 changes from NO_x, NMVOC, and CO reductions to assess the additivity of individual precursor reductions on global CH_4. Based on the HTAP multimodel mean results, global CH_4 changes from SA and NA combined precursor reductions are approximately 59% and 75%, respectively, of the sum of CH_4 changes

from individual precursor reductions, while global CH_4 changes from EA and EU combined precursor reductions are slightly negative in contrast to small positive global CH_4 changes from the sum. The three (of 11) CTMs that did not include reductions in SO_2 and aerosols in the SR6 experiments (Fiore et al., 2009) show global CH_4 changes from the combined precursor reductions close to the sum of CH_4 changes from individual NO_x, NMVOC, and CO reductions. This suggests that deviations from additivity may be due to reductions in SO_2 and aerosols (in SR6) affecting CH_4.

2.3.3 Tropospheric sulfate changes

There is considerable variability and disagreement in the sign of SO_4^{2-} responses among the four CTMs evaluated (Figure 2.5). The greatest variability in global SO_4^{2-} burden across the CTMs occurs for the CH_4 reduction and for NO_x reductions from all four regions. There is less variability across CTMs for NMVOC and CO reductions, but still differences in the sign of change.

The four CTMs analyzed here account for SO_4^{2-} formation through two main oxidation pathways: 1) gas-phase oxidation of sulfur dioxide (SO_2) by OH, and 2) aqueous-phase oxidation of SO_2 by H_2O_2 or O_3 (Houweling et al., 1998; Jeuken et al., 1999, 2001; Barth et al., 2000; Rasch et al., 2000; Horowitz et al., 2003; Rotman et al., 2004; Tie et al., 2005). Since CH_4, NMVOC, and CO reductions increase OH concentrations, SO_2 oxidation via pathway (1) is expected to increase tropospheric SO_4^{2-} formation. At the same time, increases in H_2O_2 (occurring with increases in OH) are expected to increase SO_2 oxidation via pathway (2), but decreases in O_3 may decrease oxidation (also pathway (2)). NO_x reductions not only decrease O_3, but can also decrease OH and H_2O_2, which leads to decreases in SO_4^{2-} formation by pathways (1) and (2).

Figure 2.5 shows that the sign of SO_4^{2-} response is not consistent across all four CTMs, suggesting uncertainty in the modeled effects of O_3 precursors on oxidants, the relative importance of these oxidation pathways, and the lifetime and removal of SO_2 and SO_4^{2-}.

The global distributions of tropospheric total column SO_4^{2-} changes (Figure 2.6) show the greatest changes in SO_4^{2-} over the region of emission change, with only slight changes globally. The individual CTMs and HTAP ensemble mean results show that NO_x reductions from EA, EU, and NA cause both increases and decreases in SO_4^{2-} over the reduction region, which correspond to changes in oxidants (OH, H_2O_2, O_3); localized decreases in SO_4^{2-} are due in part, to localized decreases in OH (Figure A5) and decreases in O_3. The distributions of H_2O_2 are not analyzed, as they were not reported in the CTM simulations. NMVOC reductions from EU increase SO_4^{2-} over northeastern Africa and decrease SO_4^{2-} over western Europe in three of the CTMs and the ensemble mean. All four CTMs consistently show that the EA NMVOC reduction decreases SO_4^{2-} and the SA NMVOC reduction increases SO_4^{2-} regionally, while two CTMs show SO_4^{2-} decreases over the eastern U.S. from the NA NMVOC reduction. For CO reductions from all four regions, the ensemble mean shows localized increases, while the individual CTMs differ in the sign of regional SO_4^{2-} change for all CO reductions except SA. Regional increases in SO_4^{2-} from the NMVOC and CO reductions can be explained partly by localized increases in OH (Figure A5); however, decreases in SO_4^{2-} may be related to the differing effects on oxidants (including H_2O_2) and on the SO_2 oxidation pathways in each CTM, as discussed in the previous paragraph.

2.4 Radiative forcing due to precursor emission changes

Figure 2.7 (and Table A1) show the global annual net RF due to O_3, CH_4, and SO_4^{2-}, estimated from RTM simulations, first for multimodel mean O_3 and CH_4, and second for multimodel mean O_3, CH_4, and SO_4^{2-}, for each SR scenario relative to the base case. We calculated the net RF distributions for each perturbation scenario (SR2 through SR6) by subtracting (in each grid cell and month) the simulated radiative fluxes for the base case (SR1) from those for each perturbation. To estimate the contribution of the multimodel mean SO_4^{2-} to the global annual net RF, we subtracted the net RF results due to O_3 and CH_4 from the net RF due to O_3, CH_4, and SO_4^{2-} for each SR scenario, assuming the effects of O_3, CH_4, and SO_4^{2-} are additive. To distinguish the contributions of O_3 and CH_4 to the global annual net RF, we estimated the net RF due to the multimodel mean CH_4 for each SR scenario, using the formula of Ramaswamy et al. (2001), attributing the difference to O_3 RF.

Computational limitations prevented us from simulating the RFs individually for each CTM's 18 SR scenarios. Instead, we simulate RFs for multimodel means, and for the multimodel mean ±1 standard deviation O_3 and CH_4 and the multimodel mean +1 standard deviation SO_4^{2-} to account for uncertainty in the net RF due to differences in the CTMs. We show uncertainty (mean ±1 standard deviation) for the resulting net RF, which includes the uncertainty in O_3 and CH_4 RFs, as changes in O_3 and CH_4 are not strongly correlated among the 11 CTMs for most scenarios (Figure A4). For NO_x reductions, because the RF due to O_3 opposes that of CH_4, a broader uncertainty range would have resulted had we instead simulated together the multimodel mean +1 standard

deviation O_3 and the multimodel mean -1 standard deviation CH_4 (and the reverse) to estimate uncertainty.

Figure 2.7 shows that O_3 and CH_4 RFs have the same sign as the tropospheric composition changes in section 3; since SO_4^{2-} is cooling, SO_4^{2-} RF has the opposite sign. NO_x reductions from all four regions produce an overall positive net RF due to increases in CH_4, which outweigh the negative net RF due to decreases in O_3 (Figure 2.7a). Negative global net RFs are produced by CO and NMVOC reductions, due to O_3 and CH_4 decreases, and also by the combined precursor reductions, as increases in CH_4 from NO_x reductions roughly cancel CH_4 decreases from NMVOC and CO reductions (Fiore et al., 2009). The net RF due to the combined precursor reduction is 98% to 117% of the sum of the net RFs (of O_3 and CH_4) due to reductions of each individual precursor, across the four regions, showing approximate additivity for the different precursors.

Consistent with the SO_4^{2-} changes in Figure 2.5, NO_x reductions from EU and SA contribute a positive SO_4^{2-} RF, while EA and NA NO_x reductions produce negative SO_4^{2-} RF. The SO_4^{2-} RFs for NMVOC and CO reductions vary in magnitude and sign across the four regions, corresponding to the disagreement in SO_4^{2-} response across the CTMs (Figure 2.5). We do not estimate the contribution of SO_4^{2-} to net RF for the combined reductions, since many of these perturbations included 20% reductions in SO_2 and aerosols, making it difficult to isolate the effect of NO_x, NMVOC, and CO on SO_4^{2-} RF.

Figure 2.7 also shows an estimate of the RF due to the CO_2 equivalent emission resulting from the influence of surface O_3 on plants' ability to remove CO_2 from the atmosphere, from Collins et al. (2010), based on one HTAP CTM (STOCHEM) and not the HTAP ensemble. The CO_2 responses to pulse changes from Collins et al. (2010) were

converted to equilibrium responses by integrating over 100 years. The range of CO_2 RF represents high to low sensitivity of vegetation to O_3. With the additional consideration of CO_2 RF, the global annual net RF due to regional NO_x reductions changes sign to an overall net climate cooling (-0.83 to -4.28 mWm^{-2} for all four regions), while the negative net RFs for regional NMVOC and CO reductions are reinforced by the addition of CO_2 RF (Table A1).

We normalize the global annual net RF estimates (Figure 2.7a) by each region's reduction in emissions (Table 2.3). The net RF per unit change in NO_x and NMVOC emissions is greatest for SA reductions out of the four regions (Figure 2.7b), corresponding to the sensitivity findings in section 3.1. For CO reductions, all four regions are approximately as effective at reducing global net RF per unit CO emissions, consistent with CO's longer atmospheric lifetime.

We compare our ensemble mean global annual net RF estimates per unit NO_x emissions to those of Naik et al. (2005), who used a single CTM and analyzed 10% NO_x reductions. Our estimates are approximately 32% to 63% (EU, NA, SA) and 16% (EA) of those reported by Naik et al. (2005), but these differences in net RF (CH_4 and O_3 RF combined) are small in comparison to the magnitudes of CH_4 and O_3 forcing individually.

The net RF distributions (Figure 2.8) correspond to the distributions of total column O_3 (Figure 2.3) and SO_4^{2-} changes (Figure 2.6), where regional to hemispheric RF corresponds to O_3 changes and more localized RF is dominated by SO_4^{2-} changes, as illustrated by shortwave forcings (Figure A2). Changes in CH_4 influence net RF globally, since a uniform CH_4 mixing ratio was specified in each RTM simulation. For NO_x reductions, we find positive net RFs in the SH due to CH_4 and long-term O_3

increases globally, but in the NH these positive RFs are outweighed by the negative RF of O_3 decreases (Figure 2.8). For CH_4, NMVOC, CO, and combined reductions, negative net RFs from O_3 decreases in the NH overlay negative RFs globally due to CH_4. While Figure 2.7 presents globally averaged forcings, the regionally inhomogeneous forcings in Figure 2.8 are also relevant for regional climate change (Shindell and Faluvegi, 2009). However, regional RF patterns resulting from changes in tropospheric loadings do not directly translate to regional climate responses (Levy et al., 2008; Shindell et al., 2010).

In Figure 2.9, the relationship between tropospheric O_3 burden changes and global O_3 RF is strongly linear, giving a RF efficiency of approximately 3.27 mW m^{-2} per Tg O_3 or 35.6 mWm^{-2} DU^{-1} (1 DU ≈ 10.88 Tg O_3 [Park et al., 1999]). This efficiency compares well with those estimated in previous studies, 34 to 48 mWm^{-2} DU^{-1} (Hauglustaine and Brasseur, 2001; Wild et al., 2001; Fiore et al., 2002) and 23 mWm^{-2} DU^{-1} (for NO_x) and 43 mWm^{-2} DU^{-1} (for CH_4 and CO+VOCs) (Shindell et al., 2005). Here reductions from EU and NA (with exception of NA NO_x) fall at or above the average RF efficiency line, suggesting lower RF efficiency. EA and SA reductions (except for EA NMVOC) have RF efficiency greater than average, as these regions have greater influences on the UT where RF is the most efficient (Lacis et al., 1990; Wang et al., 1993; Forster and Shine, 1997; West et al., 2009a).

2.5 Global warming potentials

Beyond analyzing RF, the climate impacts of O_3 precursor emissions can be compared with each other, and with the emissions of other species using climate metrics such as the global warming potential (GWP). Forster et al. (2007) suggest that there are serious limitations to the use of GWPs for comparing short-lived species. While other

metrics have been proposed to compare climate effects, such as the global temperature potential (GTP) (Shine et al., 2005; 2007), none are as widely used as the GWP. We choose to analyze the GWP here for comparison with earlier studies.

The basis for the GWP calculation is the integrated RF following a pulse emission. In section 4, O_3 RF was calculated for equilibrium conditions for the sum of the short and long-term O_3 responses (Figure 2.7 and Table A1). Here long-term O_3 RF is calculated by scaling O_3 RF from SR2 by the ratio of steady-state O_3 burden change in a particular SR scenario (SR minus base) to those of SR2 (SR2 minus base). The short-term O_3 RF is then the difference between the steady-state RF (section 4) and long-term RF. Following Collins et al. (2010), RF as a function of time is calculated for a one-year emissions perturbation, for each SR scenario. The short-term RF components (SO_4^{2-} and short-term O_3) are assumed to be constant over the one-year pulse and then drop to zero instantaneously; whereas, the long-term components (CH_4 and long-term O_3) respond and decay with the multimodel mean CH_4 perturbation lifetime (11.65 years). For the 20% CH_4 reduction (SR2), an analytical expression is used to calculate the impact of a one-year emissions pulse and subsequent decay (Collins et al., 2010). This CH_4 perturbation is used to scale the SO_4^{2-} and O_3 RFs from SR2 in Figure 2.7. The formula by Ramaswamy et al. (2001) is used to calculate the CH_4 RF.

GWP_H is given by the RF integrated out to a time horizon H and normalized by the change in emissions, divided by the equivalent for CO_2. In Figure 2.10 and Table A2, we present GWPs for the 20- and 100-year time horizons (GWP_{20} and GWP_{100}). The uncertainties are dominated by the variation in CH_4 response across the CTMs. For NO_x emissions, this uncertainty is sufficiently large that it is not possible to identify the sign of

the GWPs. The patterns of GWP_{100} are very similar to the normalized forcings in Figure 2.7b (the patterns would be identical for GWP_{∞}), whereas the GWP_{20} patterns give more emphasis to short-lived O_3 and SO_4^{2-} than GWP_{100}. For NO_x emissions, this brings GWP_{20} proportionally closer to zero.

For NO_x reductions, the GWP_{100} estimates are similar to those of Forster et al. (2007) and Fuglestvedt et al. (2010), though substantially smaller than those found in Shindell et al. (2009). The O_3 contribution from Asian NO_x found by Berntsen et al. (2005) is within the range of the HTAP CTMs' results, but slightly higher than the HTAP multimodel mean. We neglect RFs of nitrate aerosols, but Bauer et al. (2007) suggest nitrate contributions to NO_x GWPs on the order of -80 for GWP_{20} and -20 for GWP_{100}. The NMVOC GWPs (Figure 2.10) are generally smaller than Collins et al. (2002); however, Collins et al. (2002) covered a range of individual NMVOCs. For CO, the GWPs are comparable to Derwent et al. (2001), but smaller than Berntsen et al. (2005), largely due to the lower O_3 response of the HTAP multimodel mean; the O_3 response to Asian CO emissions of Berntsen et al. (2005), however, is within the range of the HTAP CTMs. The CO GWP_{100} estimates are also smaller than the no-aerosol results of Shindell et al. (2009), due to a lower CH_4 response. The O_3 contribution to GWP_{100} for CH_4 is smaller in this multimodel study (21% of the direct CH_4 contribution) than the 25% assumed by Forster et al. (2007), mostly because changes in O_3 above the tropopause are neglected. Adding in the contribution of O_3 in the lower stratosphere (15% of O_3 RF) (Søvde et al., 2011), and that for stratospheric water vapor (15% of the CH_4 contribution) would give a total GWP_{100} for CH_4 of 24.2 ±4.2.

For NO_x and NMVOCs, SA emissions have a larger impact than emissions from the other regions. This suggests that some latitudinal dependence may be appropriate for GWPs of O_3 precursors. Note that equatorial or SH emission changes were not considered in this study, but Fuglestvedt et al. (2010) found a dependence on latitude. European NO_x emissions have a more negative GWP than other regions in the northern mid-latitudes, as O_3 production in this NO_x-saturated region is lower.

2.6 Conclusions

We quantify the magnitude and distribution of global net RF due to changes in O_3, CH_4, and SO_4^{2-} for 20% reductions in global CH_4 and regional NO_x, NMVOC, CO, and combined precursor emissions. We find that the 20% NO_x reductions produce global, annually averaged positive net RFs, as positive CH_4 RFs outweigh negative O_3 RFs, consistent with previous studies (Fuglestvedt et al., 1999; Wild et al., 2001; Naik et al., 2005; West et al., 2007). For CH_4, NMVOC, and CO reductions, O_3 and CH_4 RFs are synergistic, yielding overall negative net RFs, consistent with previous global-scale studies (Fiore et al., 2002; West et al., 2007; Shindell et al., 2009). Including the effects of O_3 on plant growth and the carbon cycle may change the sign of net RF for NO_x reductions to an overall net climate cooling, in contrast to previous results that neglect this effect, while reinforcing the negative net RFs due to NMVOC and CO reductions, but future research is needed to better quantify this effect.

By normalizing the net RF estimates by changes in emissions (for NO_x, NMVOC, and CO), we find that RF is more sensitive to NO_x and NMVOC emission reductions from regions closer to the equator (i.e. SA), consistent with our findings that changes in O_3 burden per change in emissions (full troposphere and UT O_3 for NO_x, and UT O_3 for

NMVOC) are greatest for SA reductions. RF is more uniformly sensitive to CO emission reductions from each of the four regions, which agrees with O_3 burden changes per unit CO being less variable across the four regions. The trends in GWP_{100} across the four regions, for each precursor, reflect the normalized net RF results. Compared to GWP_{100}, the GWP_{20} patterns are influenced more by short-term O_3 and SO_4^{2-}. The large uncertainties in the NO_x GWP estimates, mainly from the variation in calculated CH_4 responses across the CTMs, limit the determination of the sign of NO_x GWPs. The estimated GWPs for individual regions are from the largest model ensemble that has been analyzed to date, and are broadly comparable to previous studies.

We find that regional RFs correspond to localized increases and decreases in SO_4^{2-} burden. O_3 changes are most important for RF on the regional to hemispheric scales, and CH_4 influences RF globally, dominating the RF response in the SH. The estimated contribution of SO_4^{2-} (direct effect only) to net RF is small compared to the RF of O_3 and CH_4. Shindell et al. (2009) found with a single CTM that for global NO_x, CO, and VOC emissions, changes in SO_4^{2-} contributed a RF more comparable in magnitude to the RFs of O_3 and CH_4. Our findings contrast with those of Shindell et al. (2009) on the importance of SO_4^{2-} RF due to O_3 precursors. However, the robustness of these results is limited, since there was substantial variability in SO_4^{2-} among only four HTAP CTMs. The effects of O_3 precursors on SO_4^{2-} via oxidants merit further research, using newer models that include improved treatment of oxidant-aerosol interactions.

We account for variability in O_3, CH_4, and SO_4^{2-} across the ensemble of CTMs, but our estimates of uncertainty only include the variability in CTMs, using a single RTM for all RF estimates. We therefore understate the uncertainty in net RF. In addition,

while we capture the most important forcings, a more complete analysis of RF could include RFs due to changes in nitrate aerosols (likely important for NO_x reductions), the indirect effect of aerosols, internal mixing of aerosols, changes in stratospheric O_3 and water vapor, and changes to the carbon cycle via nitrogen deposition. Finally, we estimate RF due to changes in the radiative budget of the global atmosphere, but do not estimate the full climate response to regional forcings. Future research should link global and regional RF to climate responses.

Our analysis contributes to the understanding of the effects of O_3 precursors on global and regional RF, and provides motivation for evaluating the climate benefits of policies addressing tropospheric O_3 and its precursors. We show that among short-lived O_3 precursors, NMVOC and CO emission reductions most effectively reduce RF. Our GWP estimates could form the basis for regionally-specific GWPs (or comparable metrics), which may allow O_3 precursors to be included in future climate agreements and emissions trading schemes, as well as provide information that could be used to estimate the influence of national or regional policies. Variability in GWPs among regions for NO_x and NMVOCs suggests that regionally-specific estimates would be important. For CO, the consistency in RF per unit emissions and GWP_{100} across the four regions implies that the error in using a uniform GWP for CO may be small. However, the RF per unit CO emissions may differ in other regions not studied here. Future studies should analyze additional source regions, such as near the equator and in the SH, as other precursors show greater sensitivity in these regions (e.g., Naik et al., 2005).

2.7 Tables and Figures

Table 2.1. HTAP source-receptor sensitivity simulations, where the four regions of reduction are East Asia, Europe, North America, and South Asia for SR3 through SR6.

Scenario	Description
SR1	Base simulation
SR2	20% reduction in global CH_4 mixing ratio
SR3	20% reduction in regional NO_x emissions
SR4	20% reduction in regional NMVOC emissions
SR5	20% reduction in regional CO emissions
SR6	20% reduction in regional NO_x, NMVOC, CO, and aerosol emissions

Table 2.2. Global CTMs used for multimodel mean O_3, CH_4, and SO_4^{2-} estimates.

Model	Institution
CAMCHEM-3311m13[a]	NCAR, USA
FRSGCUCI-v01	Lancaster University, UK
GISS-PUCCINI-modelE	NASA GISS, USA
GMI-v02f	NASA GSFC, USA
INCA-vSSz	LSCE, France
LLNL-IMPACT-T5a[a]	LLNL, USA
MOZARTGFDL-v2[a]	GFDL, USA
MOZECH-v16	FZ Juelich, Germany
STOC-HadAM3-v01	University of Edinburgh, UK
TM5-JRC-cy2-ipcc-v1[a]	JRC, Italy
UM-CAM-v01	University of Cambridge, UK/NIWA, NZ

[a] The four global CTMs used for multimodel mean SO_4^{2-} estimates.

Table 2.3. Multimodel mean ± 1 standard deviation reductions in the anthropogenic emissions of NO_x, NMVOC, and CO (20% of total anthropogenic emissions) among the 11 HTAP CTMs used here[a].

Region	NO_x (Tg N a^{-1})	NMVOC (Tg C a^{-1})	CO (Tg a^{-1})
EA	1.17 ±0.24 (0.20)	3.13 ±1.24 (0.40)	25.58 ±7.25 (0.28)
EU	1.48 ±0.14 (0.09)	3.77 ±1.88 (0.50)	15.40 ±3.26 (0.21)
NA	1.48 ±0.10 (0.07)	3.11 ±1.34 (0.43)	19.69 ±3.66 (0.19)
SA	0.46 ±0.04 (0.09)	1.94 ±0.63 (0.33)	15.82 ±3.74 (0.24)

[a] Coefficient of variation (CV = standard deviation/mean) is in parentheses. Emissions for the individual CTMs are provided in Tables A2 and A3 of Fiore et al. (2009).

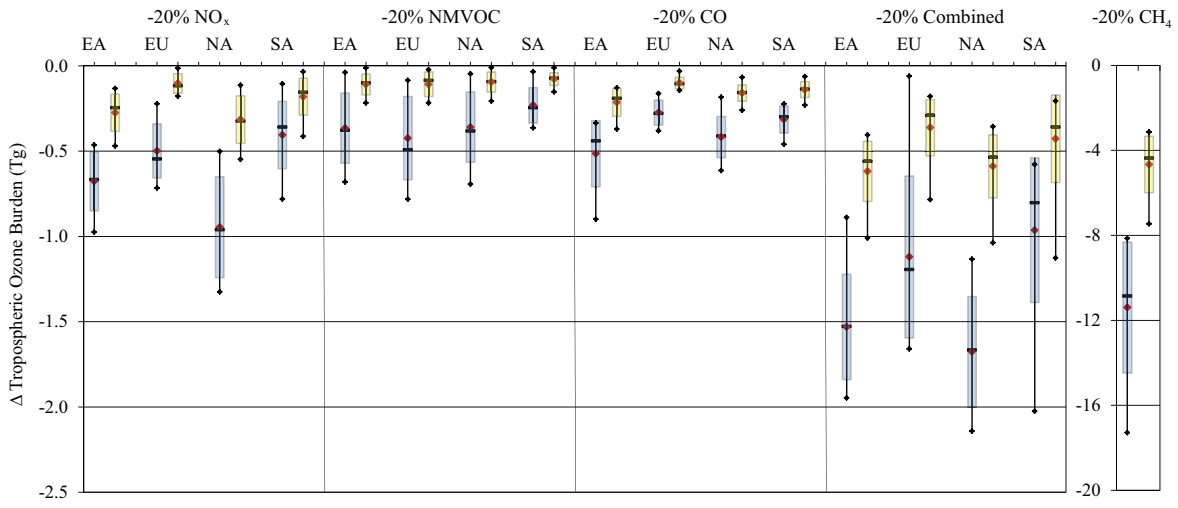

Figure 2.1. Global annual average changes in full (blue) and upper (yellow) tropospheric O_3 burden (Tg) at steady state (perturbation minus base), where the upper troposphere is from 500 hPa to the tropopause, for the HTAP ensemble of 11 models, showing the median (black bars), mean (red points), mean ±1 SD (boxes), and max and min (whiskers), for each precursor reduction scenario (-20% global CH_4 burden, and -20% regional emissions of NO_x, NMVOC, CO, and combined from East Asia [EA], Europe and Northern Africa [EU], North America [NA], and South Asia [SA]).

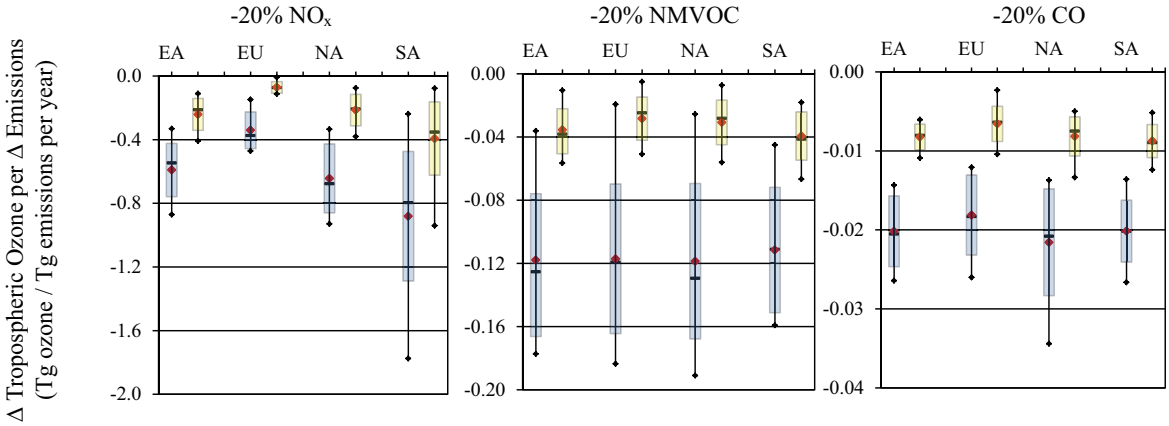

Figure 2.2. Global annual average changes in full (blue) and upper (yellow) tropospheric O_3 burden per change in emissions (Tg O_3 / Tg emissions per year) at steady state for the individual 11 models, where the units of emissions are Tg N (for NO_x), Tg C (for NMVOCs), and Tg CO (for CO), showing the median (black bars), mean (red points), mean ±1 SD (boxes), and max and min (whiskers) across the HTAP ensemble.

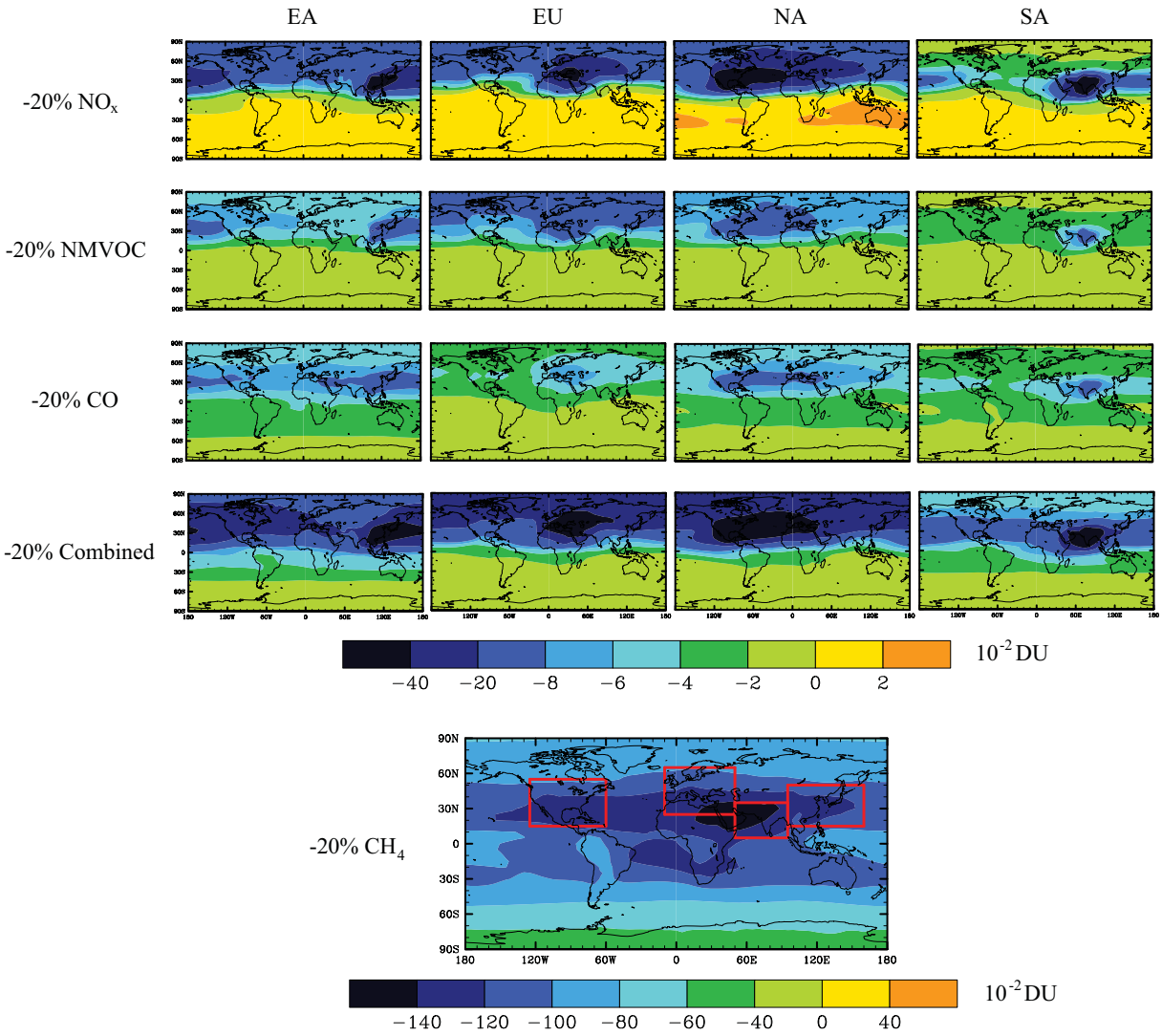

Figure 2.3. Annual average steady-state tropospheric total column O_3 burden changes (10^{-2} DU) for the multimodel mean of 11 HTAP models, for each of the precursor reduction scenarios (-20% CH_4 burden, and -20% regional emissions of NO_x, NMVOC, CO, and combined). The 4 regions of reduction (NA, EU, SA, EA) are outlined in red in the -20% CH_4 plot.

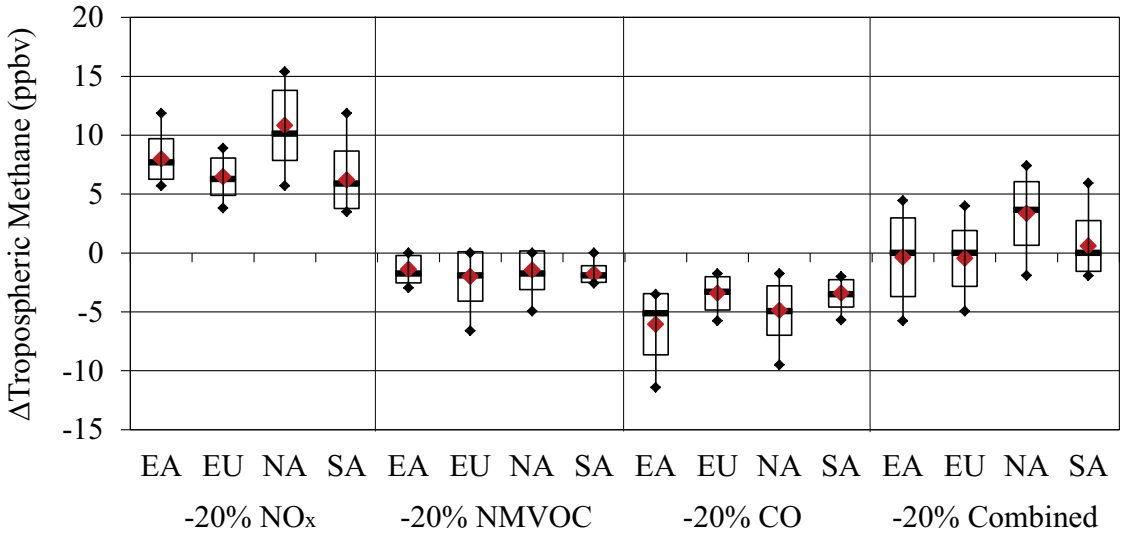

Figure 2.4. Global annual multimodel changes (perturbation minus 1760 ppbv) in tropospheric CH_4 (ppbv) for -20% regional emissions of NO_x, NMVOC, CO, and combined: median (black bars), mean (red points), mean ±1 SD (boxes), and max and min (whiskers) for the HTAP ensemble of 11 models, estimated directly from the CH_4 loss by tropospheric OH archived by each HTAP CTM (Fiore et al., 2009). Tropospheric CH_4 changes were not available from INCA-vSSz for SA 20% NMVOC reduction and from LLNL-IMPACT-T5a for 20% NO_x reductions (EA, EU, NA, SA); these models are excluded from the multimodel CH_4 changes for these perturbations.

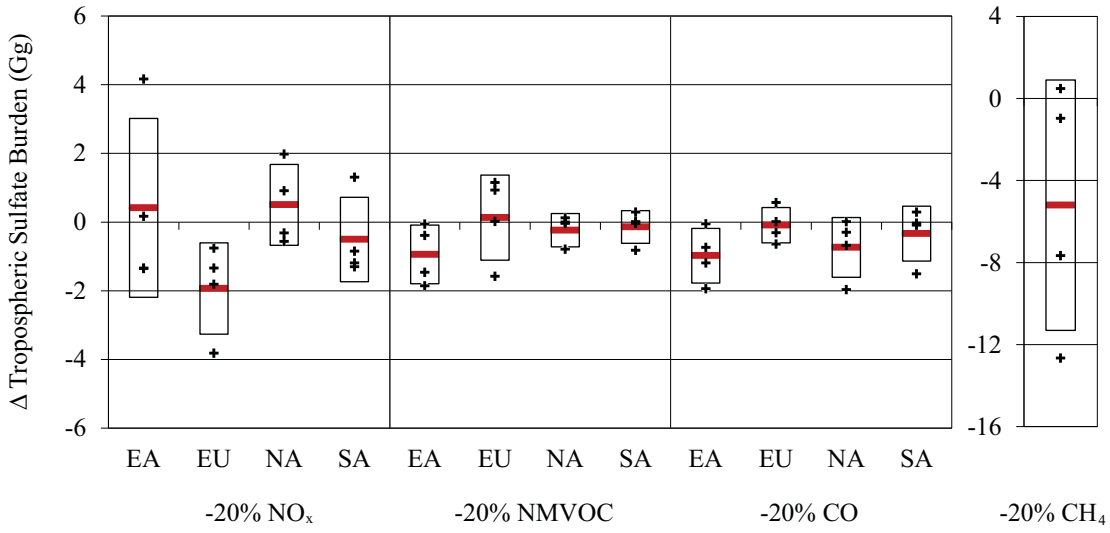

Figure 2.5. Global annual multimodel changes (perturbation minus base) in short-term tropospheric SO_4^{2-} (Gg) for -20% CH_4 burden and -20% regional emissions of NO_x, NMVOC, and CO: mean (red bars) and mean ±1 SD (boxes) across the HTAP ensemble of four models. The individual model results are shown in black (+).

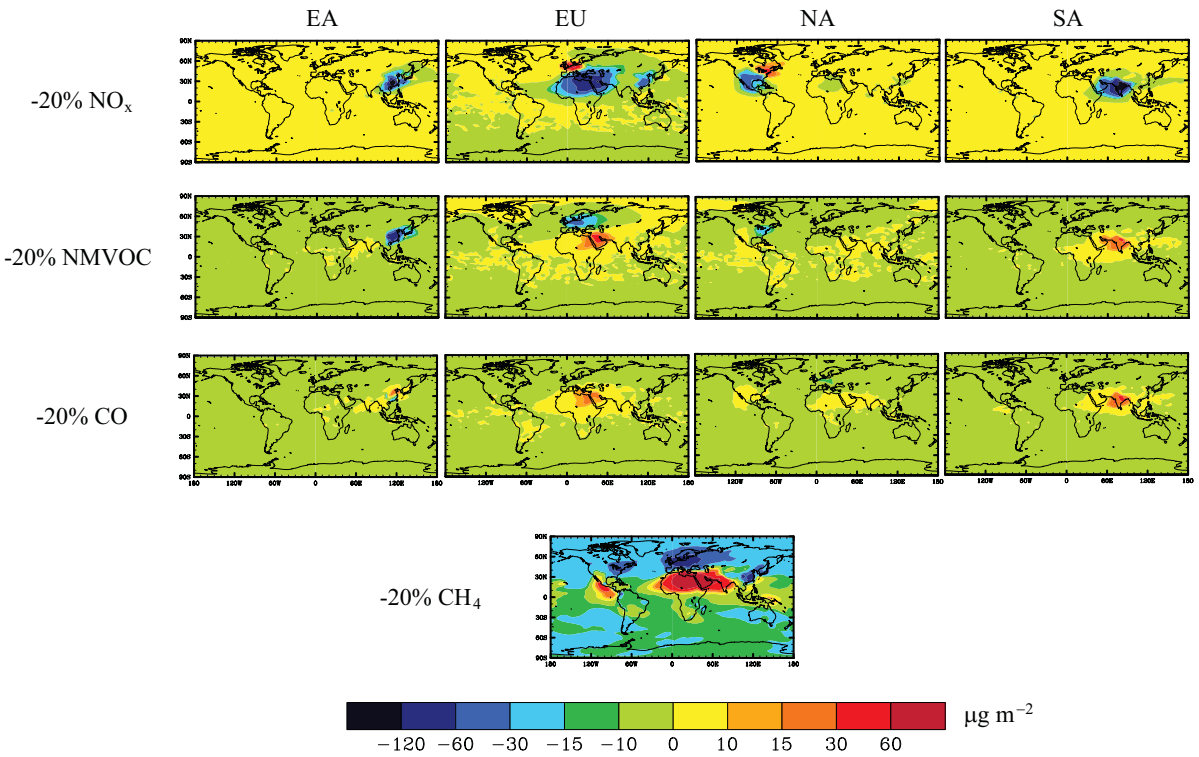

Figure 2.6. Annual average tropospheric total column SO_4^{2-} burden changes (µg m^{-2}) for the multimodel mean of four HTAP models for -20% CH_4 burden and -20% regional emissions of NO_x, NMVOC, and CO scenarios.

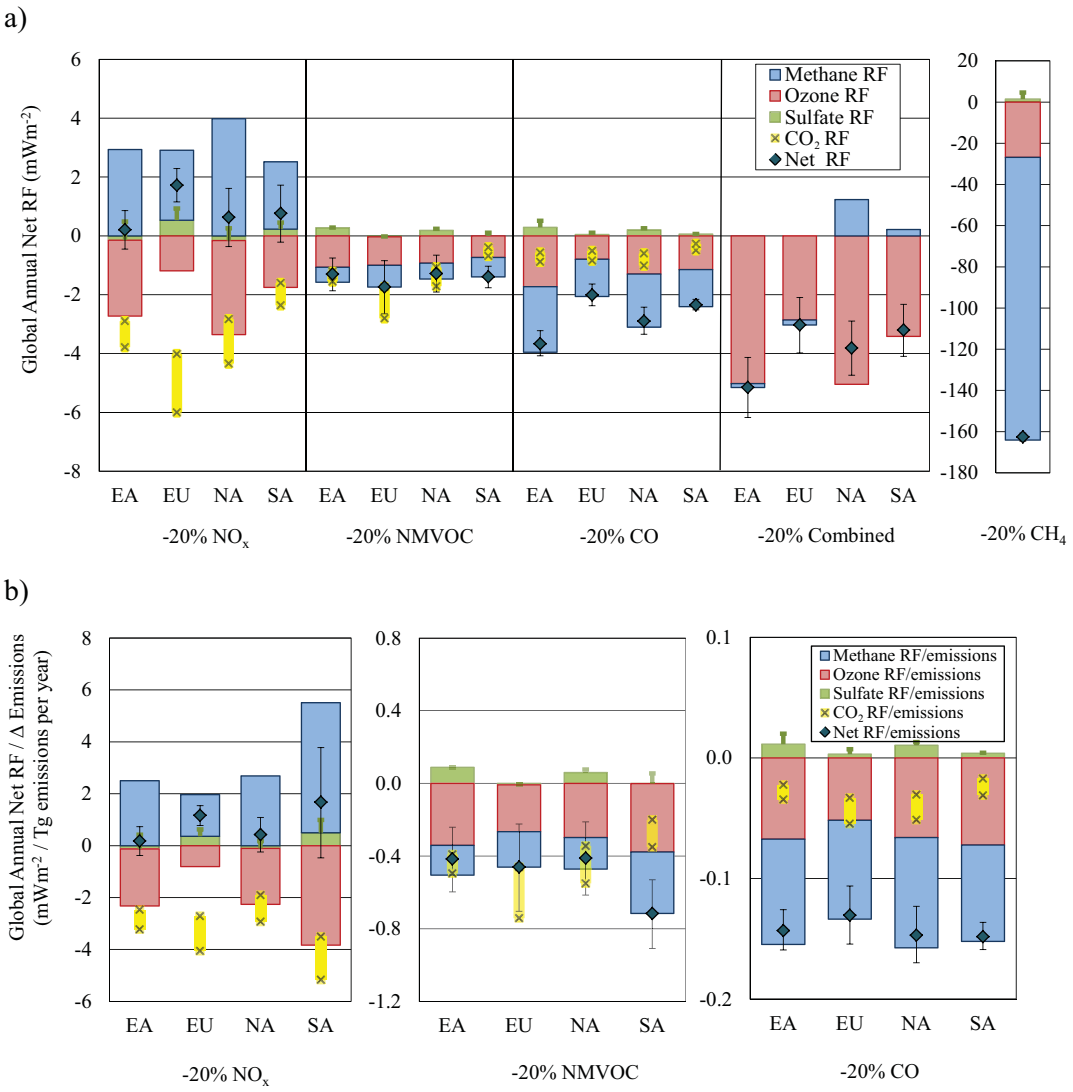

Figure 2.7. a) Global annual average RF (mW m^{-2}) for the HTAP ensembles of 11 models (for O_3 and CH_4 forcing) and four models (for SO_4^{2-} forcing) due to multimodel mean changes in steady-state O_3, CH_4, and SO_4^{2-}. Vertical black bars represent the uncertainty in net RF across models, calculated as the net RF of the multimodel mean ±1 standard deviation O_3 and CH_4, for each perturbation (-20% CH_4 burden, and -20% regional emissions of NO_x, NMVOC, CO, and combined), relative to the base simulation. The uncertainty estimates for -20% CH_4 account only for the variability in simulated O_3 changes across the CTMs, since all CTMs uniformly reduced CH_4 (1760 ppbv to 1408 ppbv). Vertical green bars represent the upper uncertainty bound of SO_4^{2-} RF across models, calculated as the net RF of the multimodel mean +1 standard deviation SO_4^{2-}. The RF of changes in CO_2 uptake by the biosphere (yellow), are shown as a range from high to low sensitivity of vegetation to O_3, estimated for a single CTM (STOCHEM) by Collins et al. (2010); these estimates are not included in the net RF (Supporting data

provided in Table A1). Note the difference in scale between the -20% regional (NO_x, NMVOC, CO, combined) and -20% CH_4 reduction scenarios.
b) Global, annual average RF per multimodel mean change in emissions (mW m^{-2} / Tg emissions per year) due to multimodel mean changes in steady-state O_3, CH_4, and SO_4^{2-}, and uncertainty (vertical black bars) as the net RF of the multimodel mean ±1 standard deviation changes in O_3 and CH_4 per unit change in emissions for each perturbation, relative to the base simulation. Vertical green bars represent the upper uncertainty bound of SO_4^{2-} RF per unit change in emissions across models.

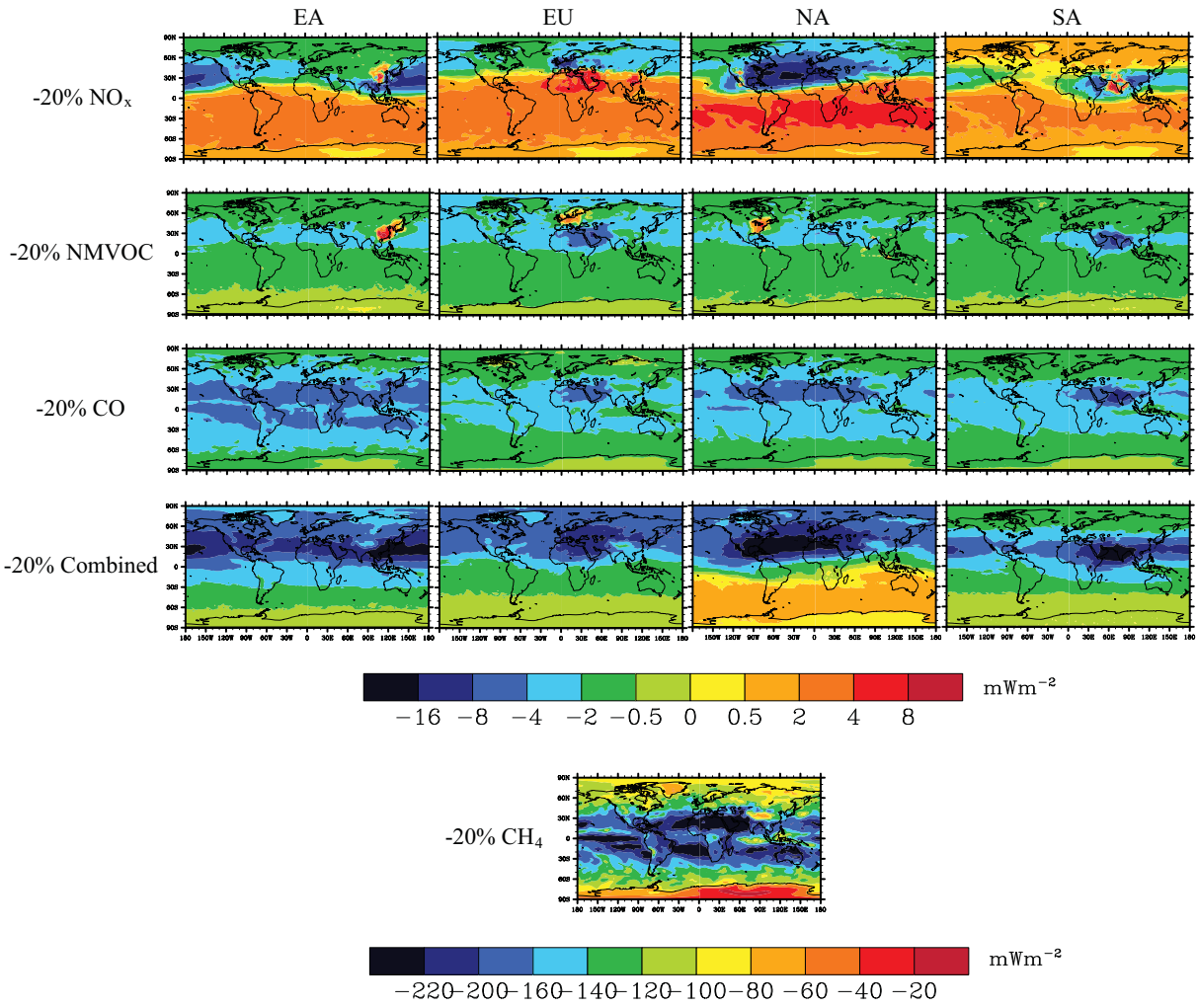

Figure 2.8. Annual average net RF distributions (mW m^{-2}), calculated as the annual shortwave radiation minus the annual longwave radiation, due to tropospheric O_3, CH_4, and SO_4^{2-} for the multimodel mean, for each of the precursor reduction simulations (-20% CH_4 burden and -20% regional emissions of NO_x, NMVOC, CO, and combined) minus the base simulation. Note the difference in scale between the -20% regional (NO_x, NMVOC, CO, combined) and -20% CH_4 reduction scenarios.

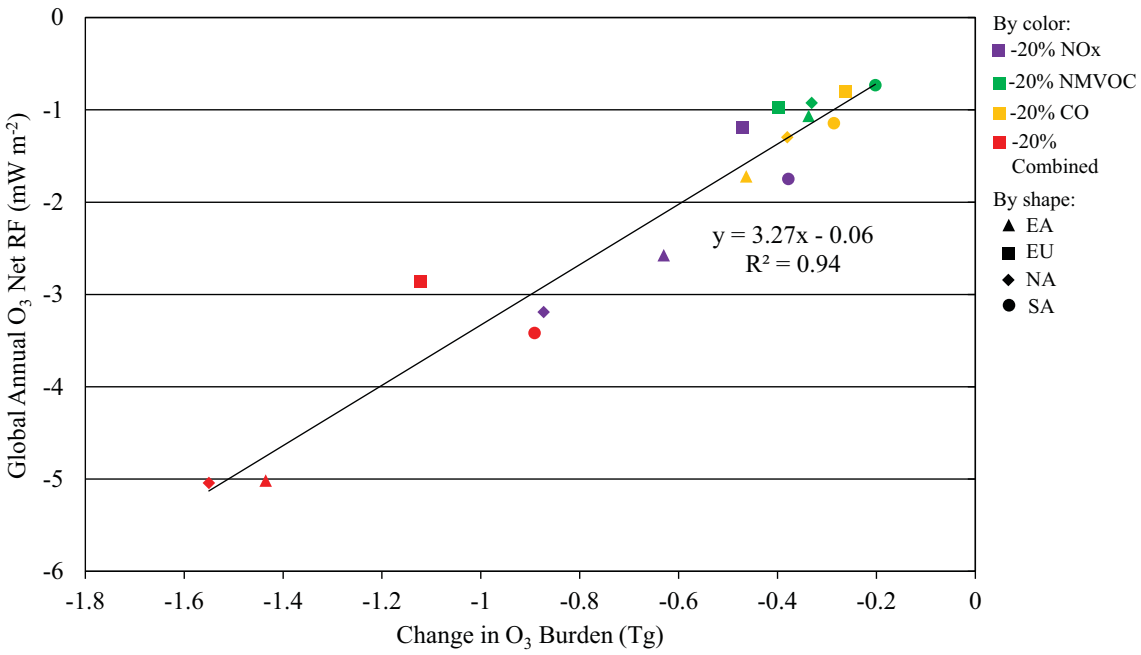

Figure 2.9. Radiative forcing efficiency of O_3 for the 16 SR simulations (SR3 through SR6) for the multimodel mean, showing the global, annual average O_3 net RF (mW m^{-2}), calculated as the difference between the simulated net RF due to O_3 and CH_4 and estimated net RF due to CH_4 (Ramaswamy et al., 2001), versus the global, annual average steady-state changes in tropospheric O_3 burden (Tg). The SR simulations are distinguished by precursor (color) and region (shape).

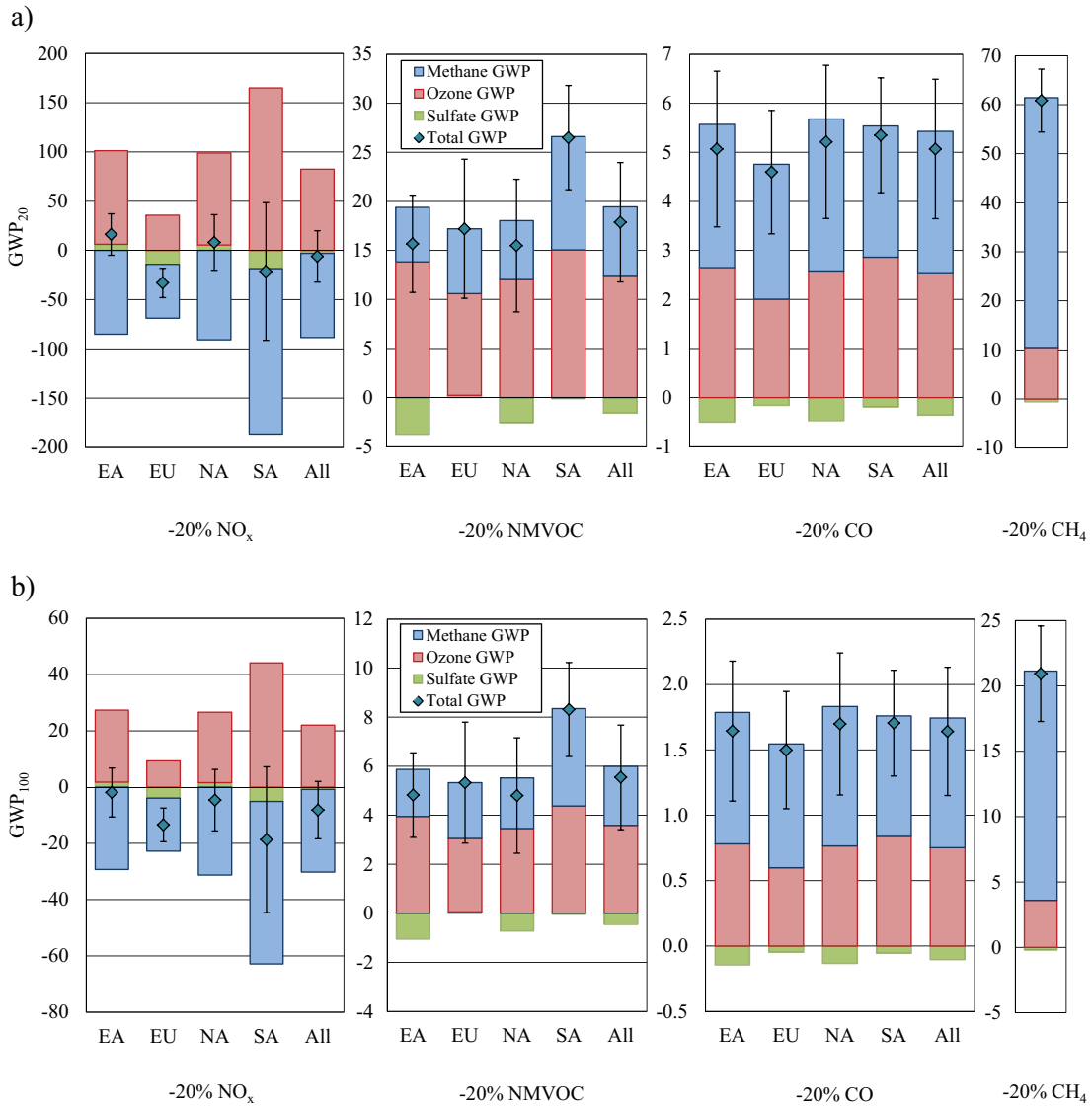

Figure 2.10. GWPs for time horizons of a) 20 years and b) 100 years for the -20% CH_4 burden and -20% regional emissions of NO_x, NMVOC, and CO scenarios. The four regions estimates (labeled "All") represent the GWP due to the sum of the four regions' responses (to O_3, CH_4, SO_4^{2-}, and all three species [Total GWP]). Uncertainty analysis is as in Figure 2.7, but also includes the uncertainty in the CH_4 lifetimes for the base simulation (SR1) (Supporting data available in Table A2).

Chapter 3. Net radiative forcing and air quality responses to regional CO emissions reductions[2]

3.1 Introduction

Carbon monoxide (CO) is emitted from the incomplete combustion of carbon fuels, and contributes indirectly to climate change through its influence on tropospheric ozone (O_3) and atmospheric oxidants (e.g. hydroxyl radical [OH], hydrogen peroxide [H_2O_2], O_3), which in turn affect the abundance of methane (CH_4) and aerosols (Pham et al., 1995; Unger et al., 2006; Shindell et al., 2009). CO emission reductions impact both climate and air quality by increasing tropospheric OH concentrations, which lead to decreases in global CH_4 and thus, long-term O_3 (Prather et al., 1996; Wild et al., 2001; Fiore et al., 2002; Naik et al., 2005), as CH_4 is a longer-lived precursor to tropospheric O_3 (West et al., 2007, 2009a; Fiore et al., 2009). Here, we assess the net climate impact of reducing anthropogenic CO emissions globally and from 10 world regions individually, to inform future policies that may address air quality and climate jointly. We omit reductions in co-emitted species (e.g. black carbon [BC], organic carbon [OC]) that would be affected by measures to reduce CO emissions, to examine the sensitivity of air quality and RF to CO emissions alone, and to derive CO climate metrics. Future studies may model emission control measures that address multiple species (e.g. Shindell et al.,

[2] Fry, M. M., M. D. Schwarzkopf, Z. Adelman, V. Naik, W. J. Collins, and J. J. West (2013), Atmospheric Chemistry and Physics, 13, 5381-5399, doi:10.5194/acp-13-5381-2013

2012), or combine these results with those for co-emitted pollutants to determine the net effect of emission control measures.

Tropospheric O_3 and CH_4, both greenhouse gases, have contributed abundance-based anthropogenic radiative forcings (RF) of 0.35 [-0.1, +0.3] W m^{-2} and 0.48 ±0.05 W m^{-2}, respectively, the largest greenhouse gas forcings behind CO_2 (Forster et al., 2007). CO and volatile organic compounds (VOC) emissions provide important contributions toward these forcings, estimated as 0.21 ±0.10 W m^{-2} due to tropospheric O_3 and CH_4 changes (Shindell et al., 2005; Forster et al., 2007), and 0.25 ±0.04 W m^{-2} (from 1750 to 2000) when the effects on sulfate and nitrate aerosols and CO_2 are included (Shindell et al., 2009).

In addition to being near-term climate forcers, products of CO reactions (O_3 and aerosols) are important air pollutants. CO emissions not only affect O_3 concentrations locally, but also intercontinentally (Akimoto, 2003; TF HTAP, 2010), given tropospheric ozone's mean lifetime of 22 days (Stevenson et al., 2006) and CO's lifetime of one to three months, both of which exceed typical intercontinental transport times (5 to 10 days) (Fiore et al., 2009; West et al., 2009a). Because of its lifetime, the transport of CO makes an important contribution to long-range O_3 (Heald et al., 2003). However, recent studies have identified large uncertainties in regional CO emissions inventories (Duncan et al., 2007), compared to satellite data (Heald et al., 2004; Pétron et al., 2004, Pfister et al., 2004, 2005; Kopacz et al., 2009), e.g., underestimating tropical biomass burning emissions and northern mid-latitude seasonal variation in bottom-up inventories (Kopacz et al., 2010). CO emissions also affect atmospheric aerosols including sulfate (SO_4^{2-}) by influencing the oxidation of sulfur dioxide (SO_2) by OH in the gas phase, or by H_2O_2 or

O_3 in the aqueous phase. OH increases from CO reductions lead to increased gas-phase SO_4^{2-} formation, and hence, climate cooling, while H_2O_2 and O_3 decreases lead to decreased aqueous-phase SO_4^{2-} formation (locally to intercontinentally) and climate warming (Unger et al., 2006; Leibensperger et al., 2011). In addition, CO influences the abundance of ammonium nitrate (NH_4NO_3) and secondary organic aerosols (SOA) via oxidant changes (Bauer et al., 2007; Hoyle et al., 2009).

For more than a decade, many have suggested that short-lived climate forcers and their precursors, like CO, be considered in international climate agreements, in addition to national air quality programs (Fuglestvedt et al., 1999; Rypdal et al., 2005, 2009; Naik et al., 2005; Fry et al., 2012), and it is among these short-lived climate forcers for which reducing emissions can slow the near-term rate of climate change (Jackson, 2009; Shindell et al., 2012). One reason why CO has not been included in a climate mitigation strategy is that its RF varies by region of emissions, given its relatively short lifetime in the troposphere (Berntsen et al., 2005). Global warming potentials (GWP) have been estimated for global CO emissions, with values ranging from 1.0 to 3.0 for a 100-year time horizon (GWP_{100}) (Fuglestvedt et al., 1996; Johnson and Derwent, 1996; Daniel and Solomon, 1998; Collins et al., 2002), based on O_3 production and feedbacks on CH_4. Few studies have estimated GWPs for CO emissions from particular world regions. Berntsen et al. (2005) estimated GWPs for CO emissions from Europe and Southeast Asia, finding that the GWP for Asian CO emissions was 25% higher than that for European emissions. Fry et al. (2012) also calculated CO GWP estimates for four world regions using an ensemble of global models, showing a small range (GWP_{20}: 4.6 ±1.3 to 5.3 ±1.2; GWP_{100}: 1.5 ±0.4 to 1.7 ±0.5) with coefficients of variation (CV = standard

deviation/mean) of 0.065 for GWP_{20} and 0.059 for GWP_{100}, where the European reduction produced a lower GWP than North America, East Asia, and South Asia reductions. Further research on the sensitivity of net RF and CO GWPs to the region of CO emissions, including regions within the tropics and southern hemisphere (SH), may inform future policies that address climate change over the next 30 years, in coordination with longer-term CO_2 mitigation (Daniel and Solomon, 1998; Shindell et al., 2012).

In this paper, we evaluate the effects of 50% anthropogenic CO emission reductions from 10 regions individually, and globally, on stratospheric-adjusted net RF, tropospheric burdens (O_3, CH_4, and aerosols), and surface O_3 air quality to inform future coordinated actions addressing air quality and climate. We simulate the influence of CO emission reductions on tropospheric chemical composition using a global chemical transport model (CTM) and then apply a standalone radiative transfer model (RTM) to estimate the RF from changes in O_3, CH_4, and the direct effect of aerosols. We present the variability in CO RF and GWPs from 10 regions, while previous studies only evaluated CO emissions perturbations from a few regions (Berntsen et al., 2005; Fiore et al., 2009; TF HTAP, 2010; Fry et al., 2012). The global annually averaged net RF estimates given here are indicators of global mean surface temperature changes, but do not account for regional climate changes from spatially nonuniform forcings (Shindell et al., 2009).

3.2 Methods

3.2.1 Chemical transport modeling

Using the Model for Ozone and Related chemical Tracers, version 4 (MOZART-4) (Emmons et al., 2010), we simulate anthropogenic CO emission reductions from 10

regions (North America [NA], South America [SA], Europe [EU], Former Soviet Union [FSU], Africa [AF], India [IN], East Asia [EA], Southeast Asia [SE], Australia and New Zealand [AU], and Middle East and Northern Africa [ME]) (Figure 3.1) and globally (sum of emissions from 10 regions only), relative to a base simulation. We use the Coupled Model Intercomparison Project Phase 5 (CMIP5) Representative Concentration Pathway 8.5 (RCP8.5) emissions inventory for the year 2005 (Riahi et al., 2007, 2011) and global meteorology from the Goddard Earth Observing System Model, version 5 (GEOS-5) for the years 2004 to 2006 (Rienecker et al., 2008) as inputs to MOZART-4.

The RCP8.5 volatile organic compound (VOC) species are re-speciated to MOZART-4 VOC categories by matching like species. Monthly temporal variation is added to all emissions species from anthropogenic sources, in each grid cell, by scaling to the monthly profile of emissions species in the REanalysis of the TROpospheric chemical composition over the past 40 years (RETRO) global emissions dataset (Schultz et al., 2007), while shipping, aircraft, and biomass burning emissions already have monthly temporal variation. Biogenic emissions of isoprene and monoterpenes are calculated online in MOZART-4 using the Model of Emissions of Gases and Aerosols from Nature (MEGAN) (Guenther et al., 2006), based on the methods of Pfister et al. (2008); global annual isoprene and monoterpene emissions are 738 Tg yr^{-1} and 107 Tg yr^{-1}. All other natural emissions are taken from the Precursors of Ozone and their Effects in the Troposphere (POET) emissions inventory for the year 2000 (Olivier et al., 2003; Granier et al., 2005; Emmons et al., 2010). The global annual mean lightning NO_x and soil NO_x emissions (for 2005) are estimated as 2.4 Tg N yr^{-1} and 8.0 Tg N yr^{-1}, respectively, which

are within the range of other modeling studies (Schumann and Huntrieser, 2007; Hudman et al., 2012).

The global and regional reduction simulations are run from July 1, 2004 through December 31, 2005 at 1.9˚ x 2.5˚ (latitude x longitude) horizontal resolution and 56 vertical levels. The base simulation is run through December 31, 2006 to allow further comparisons with observations. Although the perturbation simulations are 1.5 years in length, we account for the influence of CO emissions on CH_4 (via OH), and thus long-term changes in O_3 on the decadal timescale of CH_4 perturbation lifetime, using methods from previous studies (Prather et al., 2001; West et al., 2007; Fiore et al., 2009; Fry et al., 2012). We set global CH_4 to a uniform mixing ratio in the base and perturbation simulations of 1783 parts per billion by volume (ppbv) (WMO, 2006). We then simulate an additional CH_4 control simulation, which reduces global CH_4 by 20% to 1426.4 ppbv. Using the results from the base and CH_4 control simulations, we estimate CH_4 lifetime against loss by tropospheric OH (τ_{OH}, 11.24 years), total CH_4 lifetime based on τ_{OH} and CH_4 loss to soils and the stratosphere (τ_{total}, 9.66 years), and methane's feedback factor (F, 1.29) by the methods of Prather et al. (2001) and more recently, Stevenson et al. (2013), finding that our τ_{OH} agrees with a recent estimate of τ_{OH} based on observations (11.2 ±1.3 years) (Prather et al., 2012), and is within the range of other models: 8.2 to 11.7 years (Stevenson et al., 2006), 10.2 ±1.7 years (Fiore et al., 2009), and 9.8 ±1.6 years (Voulgarakis et al., 2013). Using the offline formulation of West et al. (2007) and our estimated parameters (τ_{OH}, τ_{total}, and F), we estimate the steady-state tropospheric CH_4 change for each perturbation. We then calculate long-term O_3 responses by scaling the change in O_3 from the CH_4 control simulation (CH_4 control simulation minus base) in

each grid cell by the ratio of global CH_4 burden change calculated for each perturbation to that of the CH_4 control simulation. Long-term O_3 responses are added to the short-term O_3 responses simulated directly for each CO emission reduction (described below) to yield O_3 concentrations at steady state (West et al., 2007; Fiore et al., 2009; Fry et al., 2012).

Because MOZART-4 does not have complete stratospheric chemistry (Emmons et al., 2010), three-dimensional monthly mean stratospheric O_3 concentrations from the AC&C/SPARC O_3 database prepared for CMIP5 (Available: http://pcmdi-cmip.llnl.gov/cmip5/forcing.html) (Cionni et al., 2011) are merged with the calculated steady-state (short-term + long-term) tropospheric O_3 concentrations for each simulation including the base case. Søvde et al. (2011) estimated that ~15% of the RF of O_3 precursors is due to lower stratosphere O_3 changes, using a single model with both standard and updated chemistry. Since we do not account for lower stratospheric O_3 changes, our RF estimates may underestimate the full effect of CO emissions.

MOZART-4 simulates the tropospheric aerosols SO_4^{2-}, BC, OC, primary and secondary organics, NH_4NO_3, and sea salt aerosols (Lamarque et al., 2005; Emmons et al., 2010). Here we quantify the changes in SO_4^{2-}, NH_4NO_3, and SOA, as these aerosols are most directly influenced by anthropogenic CO emissions via changes in oxidants. SO_4^{2-} aerosols in MOZART-4 are produced from SO_2 and dimethylsulfide (DMS) emissions through gas and aqueous-phase oxidation (Barth et al., 2000), while NH_4NO_3 aerosols are calculated from the oxidation of nitrogen oxides (NO_x) to nitric acid (HNO_3), and subsequent reaction with NH_3 emissions (Metzger et al., 2002). SOA is formed

through the gas-phase oxidation of monoterpenes by OH, O_3, and nitrate (NO_3), and the gas-phase oxidation of toluene by OH (Chung and Seinfeld, 2002).

Each perturbation simulation reduces anthropogenic CO emissions by 50% in one region (or globally), while leaving all other emissions unchanged. Figure 3.2 shows the total anthropogenic CO emissions by region and sector for the base simulation. Anthropogenic CO emissions include all source categories in Figure 3.2, but exclude biomass burning (except for the agriculture and waste burning categories), such as forest fires and grassland fires, which are also large sources of CO. We exclude biomass burning as actions to address biomass burning differ from the other sectors addressed here, and would reduce a suite of emissions simultaneously (Naik et al., 2007). Using the global, three-dimensional results from each perturbation, global and regional changes in air quality (O_3 and aerosols) at the surface (within the first vertical level) and across the troposphere (region with O_3 levels less than 150 ppbv) are quantified, relative to the base simulation, including the influence of each regional reduction on O_3 long-range transport.

3.2.2 MOZART-4 Evaluation

Previous MOZART-4 simulations, with comparable model formulations but different inputs, have reproduced O_3 and CO observations well (e.g., Pfister et al., 2005, 2006; Lapina et al., 2006; Horowitz et al., 2007; Pfister et al., 2008; Emmons et al., 2010). Table 3.1 summarizes the total anthropogenic CO emissions and annual average surface O_3, SO_4^{2-}, and CO concentrations regionally and globally for the base simulation. The base simulation produces an average bias of 4.5 ppbv O_3 across all sites compared to the Clean Air Status and Trends Network (CASTNET) (Figure B1), and 0.8 ppbv O_3 compared to the European Monitoring and Evaluation Programme (EMEP) network

(Figure B2). MOZART-4 performs the least well during the summer months (June to August) in the US, with biases of nearly 20 ppbv in the Great Lakes, North East US, and South East US regions. Simulated annual average surface SO_4^{2-} concentrations are mostly within a factor of two of observations from the Interagency Monitoring of Protected Visual Environments (IMPROVE) and EMEP monitoring networks for 2005 (Figure B3). The base simulated monthly mean surface CO concentrations also generally agree with the seasonal cycle of NOAA CMDL surface CO measurements, but overestimate CMDL measurements in the SH (Figure B4), as was also found by Emmons et al. (2010).

Simulated monthly 2005 and 2006 vertical O_3 profiles are comparable to 1995 to 2009 monthly mean and median ozonesonde climatology (Tilmes et al., 2012) (Figure B5), with the greatest agreement at 800 and 500 millibar (mb) altitudes (Figure B6). Larger differences exist between the base simulated O_3 and ozonesonde climatology at 200 mb, which may reflect the model's upper boundary conditions and constraints (Emmons et al., 2010).

Our base 2005 simulated OH burdens are lower than Spivakovsky et al. (2000), but fairly comparable to those of Lawrence (1996), Lawrence et al. (1999), von Kuhlmann (2001), and Emmons et al. (2010) (Table B1). Low modeled OH concentrations may contribute in part to the surface CO overestimates of CMDL measurements in the SH. The percentage loss of tropospheric CH_4 by reaction with OH in the base simulation is comparable to Fiore et al. (2008) (Table B2), yet slightly lower in the lower troposphere (surface to 750 hPa), and slightly higher in the mid and upper troposphere (750 to 250 hPa).

3.2.3 Radiative transfer modeling

The NOAA Geophysical Fluid Dynamics Laboratory (GFDL) RTM is used to estimate the stratospheric-adjusted net RF due to changes in tropospheric steady-state O_3, CH_4, and SO_4^{2-} aerosols (direct effect). The GFDL RTM is a module of the GFDL coupled atmosphere-ocean model (AM2) and simulates solar and infrared radiative transfer (GFDL GAMDT, 2004; Naik et al., 2005, 2007). This RTM has been applied in studies of long-lived greenhouse gases (Schwarzkopf and Ramaswamy, 1999) and short-lived forcing agents (Naik et al, 2005, 2007; West et al., 2007; Fiore et al., 2008; Saikawa et al., 2009; Fry et al., 2012). Here the RTM is employed as in Fry et al. (2012) at 144 x 90 x 24 levels, and with updated well-mixed greenhouse gas concentrations including CO_2 and nitrous oxide (N_2O) (Meinshausen et al., 2011) and CMIP5 solar forcing data (http://www.geo.fu-berlin.de/en/met/ag/strat/forschung/SOLARIS/Input_data/CMIP5_solar_irradiance.html). The RTM simulations do not include the indirect effects of aerosols on clouds or the internal mixing of aerosols. Aerosol indirect effects are highly uncertain, and may account for considerable RF contributions beyond the direct effect of aerosols (Forster et al., 2007). Changes in the RF contributions from nitrate aerosols, stratospheric O_3, water vapor, the carbon cycle via O_3 and nitrogen deposition, and CO_2 (from changes in CH_4 and CO oxidation) are also excluded. CO oxidizes to CO_2 in the atmosphere, with a minor influence on the net RF of CO (Shindell et al., 2009). Since this carbon is likely already accounted for in inventories of CO_2, we do not estimate CO_2 forcing here (Daniel and Solomon, 1998).

Tropospheric O_3, CH_4, SO_4^{2-}, BC, and OC concentrations from the MOZART-4 base and perturbed simulations are used as inputs to the RTM simulations, along with meteorological fields from GFDL's atmosphere model (AM2) and land model (LM2), sampled one day per month at midmonth for the year 2005, to represent monthly mean conditions (Naik et al., 2005). BC and OC concentrations are not evaluated further as changes in these species between the base and perturbed simulations are negligible, but we include them as inputs to the RTM simulations. The RTM currently does not calculate the RF of SOA and NH_4NO_3 aerosols. The net RF is calculated as the difference between the perturbed and base cases' simulated monthly mean net radiation fluxes (net shortwave minus net longwave), in each grid cell and month, at the tropopause after allowing stratospheric temperatures to readjust to radiative equilibrium (Naik et al., 2007; Saikawa et al., 2009; Fry et al., 2012).

3.3 Global and regional air quality responses

3.3.1 Surface CO concentrations

We first analyze the magnitude and distribution of annual average surface CO concentrations for each 50% reduction in anthropogenic CO emissions, relative to the base. Figure 3.3 shows that the largest decreases in surface CO occur within each reduction region, with lesser decreases intercontinentally. The foreign region that most influences the U.S. is EA, which contributes 39% of the change in U.S. surface CO that results from the NA reduction (Table 3.2). Responses normalized by emission change are listed in Table B3. Given that modeled OH concentrations are lower than a previous study (Spivakovsky et al., 2000), simulated surface CO concentrations may be slightly overestimated, such as in the SH when compared to CMDL measurements.

3.3.2 Responses of methane and ozone

Tropospheric methane

Changes in global tropospheric steady-state CH_4 abundance for each perturbation relative to the base are calculated using the tropospheric CH_4 loss flux diagnosed from the model (West et al., 2007; Fiore et al., 2009; Fry et al., 2012) (Table 3.3). The EA reduction produces the greatest change in global CH_4 (-19.4 ppbv), followed by IN (-11.5 ppbv) and AF (-10.9 ppbv) reductions. Upon normalizing by the change in CO emissions, global CH_4 varies little among regions (CV = 0.054), suggesting that the sensitivity of global CH_4 to CO emissions is nearly independent of emission region (Figure B7, Table B9). Fry et al. (2012) also found that CH_4 sensitivity to CO emission changes varies little (0.22 to 0.24 ppbv CH_4 (Tg CO)$^{-1}$), in contrast to the more regionally-variable effects of NO_x and NMVOC emissions on CH_4.

Surface and tropospheric ozone

Global CH_4 changes are used to calculate long-term tropospheric O_3 changes, which vary little among regions, that are then added to short-term changes to give steady-state O_3 responses (Table 3.4). Steady-state global O_3 changes are 40 to 83% greater than short-term changes, suggesting that the long-term influence of CO via CH_4 is relevant for air quality (West et al., 2007). Both short-term and steady-state global surface O_3 responses are approximately proportional to the level of CO emissions change (Figure 3.4). Values in Table 3.4 could be scaled to other emissions changes, allowing long-term effects to be included in future global or regional modeling exercises (e.g. West et al., 2009b for NO_x).

Surface O_3 responses are greatest within the hemisphere of reduction; since inter-hemispheric transport takes about 1 year, little mixing occurs across hemispheres (Jacob, 1999; West et al., 2009a). The long-term O_3 component (via CH_4), however, impacts air quality globally. The distributions of steady-state surface O_3 changes are shown in Figure 3.5, and are quantified as annual average changes within all 10 regions and the U.S. (Table 3.5). The greatest steady-state surface O_3 decreases occur within the reduction region, with smaller decreases hemispherically, except for the AU reduction, which has little effect (< 2.1 pptv) on foreign regions (Table 3.5). Similar trends are seen in regional steady-state surface O_3 responses normalized per unit change in CO emissions (Table B4).

The sum of global annual mean steady-state surface O_3 changes from the 10 regional reductions (-448 pptv) is nearly equivalent to that of the global CO reduction (-450 pptv). However, steady-state surface O_3 (normalized per unit change in CO emissions) is most sensitive to FSU and EU reductions (-2.1 and -2.0 pptv/Tg CO yr^{-1}, respectively) (Table 3.4). The largest CO emitters (EA, IN, AF, and NA) (Table 3.1) produce the greatest impacts within the reduction region or between regions. EA is the foreign region that most influences the U.S., with an influence on surface O_3 that is nearly as large (93%) as the influence from NA CO emissions. Fiore et al. (2009) also found that East Asia CO emissions can influence surface O_3 in North America by as much as 50% of the response from domestic emissions. Reducing NA CO emissions strongly impacts EU and ME surface O_3, with an influence that is 77% and 75%, respectively, of domestic impacts. In some cases, foreign CO emission reductions have a greater impact on O_3 than a region's own domestic reduction, such as EA which reduces

surface O_3 in EU by 22% more than the EU reduction (Table 3.5). As in Fiore et al. (2009), for NH sources and receptors, the greatest transport and intercontinental influences of each region on other regions are mainly from March to June (Figure B10).

The distributions of steady-state tropospheric total column O_3 changes (Figure 3.6) are similar to surface O_3 responses (Figure 3.5), yet more widespread hemispherically to globally. The troposphere is defined for O_3 less than 150 ppbv, and the upper troposphere (UT) from 500 hPa to the tropopause. We distinguish between full troposphere and UT O_3 burdens, since O_3 in the UT has a higher RF efficiency per molecule (Lacis et al., 1990; Wang et al., 1993; Forster and Shine, 1997). The EA reduction has the strongest impact on total column O_3 across the NH, while the AU CO reduction has the least impact on total column O_3 globally. Tropospheric total column O_3 changes are less than 2% in all locations, for each perturbation (Figure B11). Normalized global annual mean full and UT steady-state O_3 burden changes (Table B5) are greatest for SE, IN, and AF reductions, due to the stronger photochemistry and more active vertical convection in the tropics.

3.3.3 Response of aerosols

Tropospheric annual mean burden changes in SO_4^{2-}, NH_4NO_3, and SOA are presented in Table 3.3. The IN, ME, and AF reductions increase global SO_4^{2-} burden, while all other perturbations decrease global SO_4^{2-}. Global NH_4NO_3 burden also increases and decreases across the regional perturbations, but the global SOA burden decreases in all cases. The sums of global SO_4^{2-}, NH_4NO_3, and SOA burden changes for all 10 regional reductions are 0-8% less than those of the global CO reduction, suggesting some dependence on regional conditions and chemistry. Increases in OH are expected to

increase the global annual average SO_4^{2-}, NH_4NO_3, and SOA burdens, while decreases in O_3 (and H_2O_2 for SO_2 oxidation) are expected to decrease the global annual average SO_4^{2-} and SOA burdens.

Most regional perturbations show stronger increases in tropospheric OH within the source region, and smaller, widespread increases in the tropics (30˚S to 30˚N) (Figure B12). Tropospheric total column H_2O_2 changes are opposite in sign, with the greatest decreases within the reduction region and extending longitudinally (Figure B13).

In Figure 3.7, annual average tropospheric total column SO_4^{2-} changes result from several SO_2 oxidation pathways, where CO's lifetime is long enough that the resulting SO_4^{2-} patterns are fairly independent of reduction region. In the northern mid-latitudes, SO_4^{2-} decreases likely relate to the prevalence of clouds and decreased aqueous-phase SO_2 oxidation (in clouds) by O_3 and H_2O_2. Near the equator and in drier regions (i.e. near ME and AF), gas-phase SO_2 oxidation by OH dominates, leading to increases in SO_4^{2-}. The greatest total column SO_4^{2-} percentage decreases (i.e. for NA, EU, and EA reductions) and greatest SO_4^{2-} percentage increases (i.e. for AF, IN, EA, and ME reductions) over the reduction region are 2% or less. Intercontinental to hemispheric effects are generally 0.1% or less, for all regional reductions (Figure B14). Global annual average tropospheric NH_4NO_3 and SOA changes are likewise small: -21% and 61%, respectively, of tropospheric SO_4^{2-} changes, for the global CO reduction. Our regional annual average surface $PM_{2.5}$ changes (0.059 μg m^{-3} or less) are only slightly smaller than those estimated by Leibensperger et al. (2011) (~0.1 μg m^{-3} from Asian NO_x and CO on northern Europe and eastern China, and ~0.25 μg m^{-3} from U.S. NO_x and CO on northern Europe and eastern China) who zeroed-out anthropogenic emissions, while we halve

them here. CO generally does not have a strong influence on $PM_{2.5}$ air quality in our simulations.

3.4 Changes in production and export of CO and ozone

SA, EU, FSU, and AU reductions produce the greatest changes in global CO burden per unit change in CO emissions, and also result in the longest CO lifetimes (82 to 94 days) (Table 3.6, Table B9). More than 79% of CO burden changes occur outside of the reduction region for all perturbations, and between 41% and 50% of CO burden changes take place in the UT for SE, SA, AF, and IN reductions, consistent with the regions that have the greatest impact on O_3 production in the UT (Table 3.7). We find decreases in CO export from the reduction region in all cases, and increases in global CO production. These increases in CO production (~2% for the global CO reduction) result from tropospheric OH increases that cause faster oxidation of CH_4 and non-methane volatile organic compounds (NMVOCs) (Shindell et al., 2006). However, the global CO loss frequency (or inverse lifetime) (Prather et al., 2012) increases by ~3.4% for the global CO reduction, indicating that as CO is reduced, increases in OH lead to further CO loss. Therefore in this study, the CO perturbation lifetime ($\Delta B_{CO}/\Delta E_{CO}$) is slightly greater than the CO atmospheric lifetime ($B_{CO}/(E_{COanthro}+E_{COnatural}+P_{CO})$) (feedback factor of ~1.06), which suggests that perturbing CO emissions can have an overall amplifying effect. Although we do not account for the long-term effects on CH_4 directly in our 1.5-year simulations, these can be calculated offline from the changes in CH_4 lifetime as was done for O_3. Global CH_4 decreases also lead to decreases in CO production at steady state, and furthermore, increases in OH that cause increases in CO loss and production. These are summarized in Table B9. The long-term changes further amplify the CO signal

leading to a total increase in CO loss frequency of ~4.5%, and a total feedback factor $(\Delta B_{CO}/B_{CO})/(\Delta E_{CO}/(E_{CO}+P_{CO}))$ of 1.19.

O_3 production and export changes are also calculated for each regional reduction to determine whether the transport of O_3 or CO is more important for long-range O_3. Table 3.7 shows that the change in short-term tropospheric O_3 burden per unit change in CO emissions (Table B9 shows steady-state burden changes) is most sensitive to SE, IN, and AF reductions, which agrees with previous studies showing greater sensitivity of O_3 (especially in the mid- to upper troposphere) to emissions from the tropics, compared to more temperate regions (Fuglestvedt et al., 1999; Berntsen et al., 2005; Naik et al., 2005; West et al., 2009b). In the tropics, stronger photochemistry enhances O_3 and more active convection increases the transport of O_3 and CO to the UT, where O_3 lifetimes are longer (Naik et al., 2005; West et al., 2009b). Table 3.7 also shows that SE, SA, AF, and IN reductions produce the highest fractions of change in global O_3 production in the UT (above 500 hPa) (between 50% and 59%), suggesting that these regions also produce the greatest changes in the vertical convection of CO to the UT. As in West et al. (2009a), the higher water vapor concentrations and convective mixing in the tropics, which would lead to shorter O_3 lifetimes than at higher latitudes (Lawrence et al., 2003), appear to be less important, as CO reductions near the tropics have the greatest influence on global O_3 burden and production.

For all of the regional reductions, more than 70% of the changes in global O_3 burden and global O_3 production occur outside the reduction region, with changes in O_3 production (ΔP) outside the reduction region greatly exceeding changes in O_3 export (ΔX) (Table 3.7). This demonstrates that the downwind production of O_3 from CO is

more important for long-range O_3 transport than the direct formation and export of O_3 from CO within each source region. This differs from the case of NO_x for which changes in O_3 export exceed changes in O_3 production downwind (West et al., 2009a), reflecting the longer lifetime of CO compared to NO_x.

3.5 Radiative forcing and global warming potentials

The stratospheric-adjusted net RF impacts for the combined effect of tropospheric O_3, CH_4, and SO_4^{2-} concentration changes are shown in Figure 3.8 and Table 3.8. Annual average net RF distributions show widespread cooling (negative net RFs) across the NH and SH, for all of the regional (and global) CO reductions (Figure 3.8), due to global decreases in CH_4 (and long-term O_3) and regional to hemispheric decreases in short-term O_3. Localized to regional cooling and warming patterns, especially from the NA, EU, FSU, and EA reductions, correspond to localized increases and decreases in SO_4^{2-} aerosols (Figure 3.7, Figure 3.8). While changes in NH_4NO_3 and SOA are not accounted for by the RTM, regional SOA decreases (lesser in magnitude than SO_4^{2-} changes) likely provide slight regional warming, while regional NH_4NO_3 increases and decreases (also less than SO_4^{2-} changes) likely add small regional cooling and warming effects. On the global scale, tropospheric changes in NH_4NO_3 and SOA, like SO_4^{2-}, are expected to contribute little to the global net RF. The large-scale influences of CH_4 and O_3 are consistent with the longwave radiation distributions (Figure B17), while the local influences of SO_4^{2-} are reflected in the shortwave radiation distributions (Figure B18). The strongest annual average net RFs occur within the 28˚S to 28˚N latitudinal band in all cases (Table 3.8), despite the wide range of reduction regions. This finding is explained by the hotter surface temperatures in the tropics, which result in greater

outgoing longwave radiation absorption by greenhouse gases. However, longwave forcings are not as strong directly over the equator, since water vapor is abundant and competes with O_3 absorption in this region (Figure B17).

Across all 10 regional reductions, the global annual average net RF per unit emissions is -0.12 ±0.0055 mW m^{-2} (Tg CO yr^{-1})$^{-1}$ (mean ±1 standard deviation) (CV = 0.045), suggesting little variability. Global annual net RF (normalized per unit change in CO emissions), however, is more sensitive to regions close to the equator (ME, SE, and IN). This is consistent with the regions that produce the greatest changes in tropospheric O_3 burden per unit change in CO emissions, but the response for ME emissions is larger than expected given its O_3 burden change (Table 3.7, Table B9), due to the hotter and drier conditions of this region. Monthly global net RF estimates also vary from ~56% less to ~34% greater than the annual mean, with the greatest RFs from June to September (Figure B20). By doubling the global annual average net RF of the 50% global CO reduction (-0.0361 W m^{-2}) and scaling for biomass burning emissions (43.6% of global anthropogenic CO emissions), which were excluded in the 50% anthropogenic CO emissions reductions, the global net RF of CO is 0.128 W m^{-2}. This is only ~11% greater than the ACCMIP multimodel mean global net RF of CO emissions due to O_3 and CH_4 changes alone (0.115 W m^{-2}) (for 1850-2000) (Stevenson et al., 2013). It is smaller than the RF of CO + NMVOC emissions in previous studies: 0.21 ±0.10 W m^{-2} (Shindell et al., 2005; Forster et al., 2007) and 0.25 ±0.04 W m^{-2} (Shindell et al., 2009), and is approximately 8.2% of the global net RF of CO_2 (1.56 W m^{-2}). Among the positive forcing agents with short lifetimes (CO, CH_4, NMVOCs, and BC), our estimated CO RF is ~8.2% of their total RF (~1.57 W m^{-2}) (Forster et al., 2007).

Following the methods of Collins et al. (2012) and Fry et al. (2012), we estimate GWPs for each regional perturbation at 20 and 100-year time horizons (Table 3.8, Figure 3.9). GWP_H estimates are calculated as the RF integrated to a time horizon H due to an emission pulse, normalized by the change in emissions, and divided by the equivalent for CO_2. Since O_3 RF has both short and long-term components, we calculate long-term O_3 RF by scaling the O_3 RF from the CH_4 control simulation by the ratio of long-term O_3 burden changes in each regional perturbation to those of the CH_4 control simulation. We then calculate short-term O_3 RF as the difference between steady-state and long-term O_3 RF. We assume that short-term RF components (SO_4^{2-} and short-term O_3) are constant over one year and then drop to zero instantaneously. Long-term components (CH_4 and long-term O_3) respond and decay with the calculated CH_4 perturbation lifetime (12.48 years). Figure 3.9 shows the breakdown of total GWP into short and long-term components, and error bars representing the average uncertainty of CO GWPs (GWP_{20}: ±1.4 and GWP_{100}: ±0.5) from Fry et al. (2012) across multiple global CTMs (±1 standard deviation). However, the error bars do not account for the full uncertainty, as additional forcings, such as from CO_2, are excluded, which may alter total net RF and GWP estimates. We estimate GWP_{20} and GWP_{100} values of 4.07 and 1.34, respectively, for the global CO reduction, and ranges of 3.71 to 4.37 (CV = 0.059) and 1.26 to 1.44 (CV = 0.043) among regions, suggesting little regional variability.

Our GWP_{100} estimates are comparable to those of Derwent et al. (2001) (GWP_{100} of 1.0 due to O_3 changes, and 0.6 due to CH_4 changes) and Daniel and Solomon (1998) (GWP_{100} of 1.0), yet smaller than the GWP_{100} estimates of Fuglestvedt et al. (1996) (GWP_{100} of 3.0) and Johnson and Derwent (1996) (GWP_{100} of 2.1). Our GWP_{20} and

GWP_{100} estimates are also about 65 to 70% lower than those estimated by Berntsen et al. (2005) for Europe and East Asia, but those did not include SO_4^{2-} impacts as we do here, and 16 to 23% lower than those estimated by Fry et al. (2012), likely due to differences among the CTMs, such as a lower sensitivity of O_3 and CH_4 to CO emissions in MOZART-4, but regional definitions also differ (Table B10). Although the absolute GWP estimates of Fry et al. (2012) are more robust than those presented here, reflecting an ensemble of CTMs, the present study more fully addresses the variability of GWPs over a wide range of regions encompassing the tropics and northern and southern extra-tropics.

As mentioned earlier, our GWP estimates do not include the forcing from CO_2 once CO oxidizes. This reflects the accounting of carbon emissions in CO_2 inventories (Fuglestvedt et al., 1996; Daniel and Solomon, 1998; Collins et al., 2002). If the CO_2 forcing were accounted for, the GWP_{100} and GWP_{20} estimates would each increase by 1.57 (44 g CO_2 mol^{-1} (28 g CO $mol^{-1})^{-1}$).

3.6 Conclusions

Reducing CO emissions can slow near-term climate change while improving air quality from O_3 and CO itself. The present-day CO RF is estimated as 8.2% of that from CO_2, and also 8.2% of the short-lived forcing agents that provide an opportunity to slow climate change in the coming decades. We find here that the global net RF of CO reductions varies little among the regions where it is emitted, but CO may cause changes in regional climate that were not quantified. While emission control measures would likely affect co-emitted species (e.g. BC, OC), this study focuses on the sensitivity of air quality and RF to the location of CO emissions, which is also relevant for determining the

GWP of CO. For measures affecting multiple pollutants, the results reported here can be combined with those for co-emitted pollutants.

Halving anthropogenic CO emissions globally and from 10 regions has widespread effects on surface and tropospheric concentrations in addition to net RF. For the global CO emission reduction, global annual net RF, GWP_{20}, and GWP_{100} estimates are -0.124 mW m^{-2} (Tg CO)$^{-1}$, 4.07, and 1.34, respectively, with ranges of -0.115 to -0.131 mW m^{-2} (Tg CO)$^{-1}$, 3.71 to 4.37, and 1.26 to 1.44 among the 10 regions, with regions in the tropics (ME, SE, and IN) having the greatest sensitivities. We find little variability in the net RF and GWP estimates among source regions. Our GWP estimates agree well with previous studies (Daniel and Solomon, 1998; Derwent et al., 2001), but are less than the GWP_{20} and GWP_{100} estimates of Berntsen et al. (2005) and Fry et al. (2012), likely related to differences among CTMs. The GWP values should be increased by 1.57 for fossil fuel sources to account for the CO_2 generated as an oxidation product. However, care should be taken to avoid double counting, as CO_2 emissions are often calculated by assuming complete oxidation of the fuel rather than being measured in the exhaust. It is always preferable for climate to emit the carbon as CO_2 rather than CO.

Net RF distributions for the regional (and global) reductions show widespread cooling across the NH and SH corresponding to the patterns of regional short-term O_3 and global CH_4 (and long-term O_3) decreases, and localized positive and negative net RFs due to changes in SO_4^{2-} aerosols. The strongest annual net RFs occur within the tropics (28˚S to 28˚N), independent of the location of CO emissions change, due to higher temperatures and greater absorption of infrared radiation.

For all regional reductions, we show that the greatest changes in surface CO and O_3 concentrations are within the reduction region, with lesser decreases hemispherically. The regions with the highest anthropogenic CO emissions (EA, IN, AF, and NA) show the largest impacts on surface CO and O_3 concentrations within that region and between regions. The impact of EA's reduction on U.S. surface CO and O_3 concentrations is 39% and 93%, respectively, of that resulting from NA. The NA CO reduction also has a strong impact on EU and ME surface O_3 concentrations. Anthropogenic CO emissions overall contribute ~6.1% (1.6 ppbv) to global annual average steady-state surface O_3, by doubling the change from the 50% global CO reduction (-0.45 ppbv) and scaling for biomass burning emissions.

All of the reductions increase tropospheric OH leading to decreases in global CH_4 and hence, long-term O_3. At the same time, tropospheric H_2O_2 decreases in all cases. We generally find that increases in OH contribute to increases in SO_4^{2-} through gas-phase oxidation, which is dominant in drier regions and near the equator. Decreases in H_2O_2 and O_3 contribute to decreases in SO_4^{2-} via aqueous-phase oxidation, which prevails mostly in the northern mid-latitudes.

For all regional reductions, more than 70% of the global O_3 burden and production changes, and more than 79% of global CO burden changes, occur outside the reduction region. In addition, O_3 production changes outside the source region greatly exceed changes in O_3 export from each region, suggesting that long-range O_3 is influenced substantially by the transport of CO and subsequent production of O_3 downwind, and less by the transport of O_3 itself. Tropospheric O_3 burden changes (per unit change in CO emissions) are most sensitive to SE, IN, and AF reductions, due to

stronger photochemistry and more active vertical convection in the tropics compared to other regions (Naik et al., 2005; West et al., 2009a).

Limitations of this study include only accounting for O_3, CH_4, and SO_4^{2-} changes in net RF and GWP estimates. We exclude changes in nitrate aerosols, secondary organic aerosols, stratospheric O_3, water vapor, the carbon cycle via O_3 and nitrogen deposition, and CO_2, as these components are not part of the current RTM configuration. Our RTM simulations also do not include the indirect effects of aerosols on clouds or the internal mixing of aerosols, but these effects may be large. We estimate only small changes in NH_4NO_3 and SOA, consistent with previous studies that show these aerosols contributing much less to CO RF than SO_4^{2-} (Shindell et al., 2009). Stratospheric O_3 and water vapor RFs are believed to be relatively small (Forster et al., 2007). The contribution of CO emissions to CO_2 RF via changes in the CO_2 uptake by plants is estimated as 12 and 42% of the net RF (Fry et al., 2012), which would increase GWPs and perhaps the variability among regions, depending on regional vegetation distributions.

We do not assess climate responses as in Shindell and Faluvegi (2009), but show how CO emissions location affects the latitudinal distribution of net RF and CO GWPs. Regional CO emissions are also considered fairly uncertain (Duncan et al., 2007), according to a number of studies that have used inverse modeling or adjoint methods to constrain CO emissions by satellite data (Heald et al., 2004; Pétron et al., 2004, Pfister et al., 2004, 2005; Kopacz et al., 2009, 2010), but this uncertainty likely does not strongly influence normalized forcings and GWPs. Uncertainties in the emissions of other O_3 precursors and in MOZART-4's chemical and transport processes are likewise important (Berntsen et al., 2005). Future work could examine the influence of dynamic climate

feedbacks on chemistry, and future changes in emissions that may alter the air quality and RF sensitivities given here for present-day emissions.

Future international climate agreements or emissions trading mechanisms could include CO among a suite of long-lived greenhouse gases, using a single GWP globally, given that the uncertainty in the global GWP for CO is greater than the range among regions estimated here. Alternatively, different GWPs could be applied to different continents. In either case, this work provides an incentive to reduce CO emissions, as part of coordinated policies addressing climate and air quality.

3.7 Tables and Figures

Table 3.1. For the base simulation, total anthropogenic CO emissions by region, and regional (or global) annual average area-weighted surface O_3, SO_4^{2-}, and CO concentrations.

Reduction region	Total anthropogenic CO emissions (Tg yr^{-1})	Annual average surface O_3 (ppbv)	Annual average surface SO_4^{2-} ($\mu g\ m^{-3}$)	Annual average surface CO (ppbv)
NA	70.0	35.3	1.6	151.0
SA	24.5	24.8	0.7	147.4
EU	31.2	36.5	3.0	166.0
FSU	21.9	33.2	1.4	166.3
AF	86.9	30.0	0.9	172.9
IN	96.4	41.2	2.9	279.4
EA	152.9	42.4	4.3	235.0
SE	54.3	28.1	1.6	174.5
AU	2.9	22.8	0.5	101.9
ME	42.6	40.4	2.5	147.5
Global	584.7	26.2	1.0	122.7

Table 3.2. Source-receptor matrix of annual average surface CO concentration changes (ppbv), for the regional reduction simulations, with the United States (US) also defined as a receptor in addition to the 10 regions. The largest changes for each source reduction region are in bold.

	Receptor										
Source	NA	SA	EU	FSU	AF	IN	EA	SE	AU	ME	US
NA	-12.5	-0.69	-4.56	-4.07	-1.34	-1.75	-3.27	-1.17	-0.32	-3.36	**-19.3**
SA	-0.19	**-3.81**	-0.13	-0.13	-0.56	-0.32	-0.17	-0.45	-0.83	-0.18	-0.15
EU	-2.32	-0.31	**-18.3**	-4.96	-0.98	-0.85	-2.56	-0.63	-0.13	-3.90	-2.16
FSU	-2.05	-0.18	-3.66	**-9.70**	-0.47	-0.69	-2.96	-0.49	-0.08	-2.03	-1.88
AF	-1.05	-2.47	-0.87	-0.87	**-10.2**	-1.84	-1.11	-1.47	-1.58	-1.42	-0.95
IN	-1.93	-1.03	-1.82	-2.00	-2.21	**-75.5**	-4.23	-3.50	-0.57	-2.76	-1.97
EA	-7.08	-1.29	-6.53	-7.68	-2.36	-4.79	**-50.0**	-8.36	-0.73	-5.08	-7.52
SE	-0.82	-0.72	-0.74	-0.73	-0.90	-1.90	-1.48	**-8.96**	-0.73	-0.83	-0.83
AU	-0.01	-0.11	-0.01	-0.01	-0.07	-0.04	-0.01	-0.10	**-0.81**	-0.02	-0.01
ME	-1.65	-0.49	-2.33	-2.95	-1.69	-5.91	-2.51	-0.94	-0.22	**-13.7**	-1.66

Table 3.3. For the global and regional reduction simulations relative to the base, global annual mean burden changes in tropospheric and upper tropospheric (UT) steady-state O_3, tropospheric CH_4, SO_4^{2-}, NH_4NO_3, and SOA. The total global annual average tropospheric O_3 (at steady state), SO_4^{2-}, NH_4NO_3, and SOA burdens in the base simulation are 352 Tg O_3, 1788 Gg SO_4^{2-}, 457 Gg NH_4NO_3, and 237 Gg SOA.

Reduction region	ΔO_3 (Tg yr^{-1})	ΔUT O_3 (Tg yr^{-1})	ΔCH_4 (ppbv)	ΔSO_4^{2-} (Gg yr^{-1})	ΔNH_4NO_3 (Gg yr^{-1})	ΔSOA (Gg yr^{-1})
NA	-0.64	-0.37	-9.1	-0.54	0.24	-0.11
SA	-0.21	-0.14	-3.2	-0.05	-0.003	-0.02
EU	-0.27	-0.15	-4.1	-0.37	0.19	-0.07
FSU	-0.19	-0.11	-2.9	-0.22	0.12	-0.05
AF	-0.80	-0.51	-10.9	0.03	-0.09	-0.06
IN	-0.93	-0.61	-11.5	0.48	-0.29	-0.17
EA	-1.38	-0.84	-19.4	-1.25	0.22	-0.43
SE	-0.56	-0.38	-6.6	-0.11	-0.04	-0.12
AU	-0.02	-0.01	-0.4	-0.01	0.001	-0.001
ME	-0.38	-0.23	-5.6	0.37	0.003	-0.09
Global	-5.39	-3.35	-73.0	-1.82	0.39	-1.11
CH_4 control	-8.76	-2.30	-356.6	-3.05	0.78	0.26

Table 3.4. For the global and regional reduction simulations, global annual mean changes in short-term surface O_3, steady-state surface O_3, steady-state surface O_3 per unit change in CO emissions, and long-term surface O_3 per unit change in CO emissions.

Reduction region	Δ Short-term surface O_3 (pptv)	Δ Steady-state surface O_3 (pptv)	Δ Steady-state surface O_3 per Tg CO emissions (pptv (Tg CO yr^{-1})$^{-1}$)	Δ Long-term surface O_3 per Tg CO emissions (pptv (Tg CO yr^{-1})$^{-1}$)
NA	-42.8	-63.0	-1.8	-0.58
SA	-8.7	-15.9	-1.3	-0.59
EU	-22.1	-31.2	-2.0	-0.58
FSU	-16.0	-22.4	-2.1	-0.58
AF	-31.3	-55.4	-1.3	-0.55
IN	-40.8	-66.4	-1.4	-0.53
EA	-77.8	-120.8	-1.6	-0.56
SE	-19.9	-34.5	-1.3	-0.54
AU	-1.2	-2.2	-1.5	-0.68
ME	-24.1	-36.5	-1.7	-0.58
Global	-287.8	-450.1	-1.5	-0.56

Table 3.5. Source-receptor matrix of annual average steady-state changes in surface O_3 concentrations (pptv), for the regional reduction simulations, with the United States (US) also defined as a receptor in addition to the 10 regions. The largest changes for each source reduction region are in bold.

	Receptor										
Source	NA	SA	EU	FSU	AF	IN	EA	SE	AU	ME	US
NA	-178.2	-26.0	-131.1	-97.3	-46.8	-71.5	-102.4	-35.1	-20.7	-119.6	**-253.3**
SA	-14.4	**-25.3**	-14.2	-11.9	-16.4	-17.5	-15.6	-12.9	-15.2	-17.1	-15.4
EU	-48.4	-11.3	**-170.8**	-68.9	-24.7	-32.9	-57.9	-16.4	-9.1	-91.5	-56.0
FSU	-36.9	-7.6	-58.3	**-75.1**	-14.5	-25.8	-53.3	-12.1	-6.3	-50.9	-43.5
AF	-59.8	-52.1	-59.6	-49.9	**-97.2**	-77.2	-66.4	-46.0	-41.5	-77.7	-64.1
IN	-85.0	-37.6	-89.0	-76.8	-66.9	**-454.6**	-129.2	-67.2	-30.7	-114.5	-96.0
EA	-197.0	-53.4	-209.2	-178.2	-90.5	-158.6	**-437.7**	-118.9	-45.7	-202.0	-235.7
SE	-41.5	-24.3	-42.6	-35.6	-34.5	-57.0	-52.3	**-57.9**	-24.0	-50.0	-46.4
AU	-1.6	-1.9	-1.6	-1.4	-1.9	-2.1	-1.8	-2.0	**-4.8**	-2.0	-1.7
ME	-49.7	-17.1	-63.4	-59.0	-38.4	-105.9	-69.1	-25.0	-13.4	**-159.3**	-57.5

Table 3.6. For each regional reduction, changes in global annual average (short-term) tropospheric CO burden (B_{CO}), and B_{CO} per unit change in CO emissions (E_{CO}). Also shown are CO lifetime calculated as $\Delta B_{CO} / (\Delta E_{CO} + \Delta P_{CO})$, the fractions of B_{CO} change outside each reduction region and in the UT, and the changes in net CO export (X_{CO}) from the reduction region, global CO production (P_{CO}), and P_{CO} outside the reduction region. The total global annual average CO burden in the base simulation is 462.6 Tg CO.

Reduction region	ΔB_{CO} short-term (Tg CO)	$\Delta B_{CO} / \Delta E_{CO}$ (days)	CO lifetime (days)	Fraction of ΔB_{CO} outside region	Fraction of ΔB_{CO} in UT	ΔX_{CO} from region (Tg yr^{-1})	ΔP_{CO} global (Tg yr^{-1})	ΔP_{CO} outside region (Tg yr^{-1})
NA	-6.7	70.3	78.2	0.82	0.37	-27.4	3.5	2.7
SA	-2.5	74.0	82.2	0.88	0.41	-10.4	1.2	1.0
EU	-3.4	79.3	88.2	0.92	0.30	-13.7	1.6	1.4
FSU	-2.5	83.7	93.1	0.79	0.29	-9.1	1.1	0.95
AF	-7.9	66.2	73.4	0.83	0.44	-33.6	4.3	3.3
IN	-8.0	60.5	66.7	0.92	0.45	-40.2	4.5	3.8
EA	-14.7	70.1	77.7	0.90	0.39	-64.6	7.5	6.5
SE	-4.9	66.4	73.4	0.89	0.50	-23.4	2.6	2.2
AU	-0.3	84.2	94.1	0.92	0.35	-1.3	0.2	0.14
ME	-4.0	68.2	75.8	0.90	0.36	-17.8	2.1	1.8

Table 3.7. Changes in global annual average (short-term) tropospheric O_3 burden (B_{O3}), O_3 production (P_{O3}), and net O_3 export (X_{O3}) from each regional reduction, normalized per change in CO emissions (E_{CO}), and the fractions of these above each reduction region and in the upper troposphere (UT). Regional O_3 lifetimes are also shown. For the base simulation, the total global annual average O_3 burden is 352.2 Tg O_3, and the chemical production and loss rates are 4782.5 Tg yr^{-1} and 3975.0 Tg yr^{-1}.

Reduction region	ΔB_{O3} short-term (Tg O_3)	$\Delta B_{O3}/\Delta E_{CO}$ (days)	ΔP_{O3} (Tg yr^{-1})	$\Delta P_{O3}/\Delta E_{CO}$ (Tg O_3 (Tg CO $yr^{-1})^{-1}$)	Regional O_3 lifetime ($\Delta B_{O3}/\Delta P_{O3}$) (days)	Fraction of global ΔB_{O3} above region	Fraction of global ΔP_{O3} above region	Fraction of global ΔP_{O3} in UT	ΔX_{O3} from region (Tg yr^{-1})	ΔP_{O3} outside region (Tg yr^{-1})
NA	-0.413	4.31	-8.19	-0.234	18.4	0.14	0.30	0.37	-0.91	-5.75
SA	-0.135	4.02	-2.48	-0.202	19.9	0.07	0.17	0.50	-0.12	-2.06
EU	-0.168	3.93	-3.63	-0.233	16.9	0.05	0.18	0.30	-0.34	-2.98
FSU	-0.120	4.00	-2.53	-0.231	17.3	0.13	0.19	0.31	-0.13	-2.06
AF	-0.533	4.48	-9.59	-0.221	20.3	0.12	0.29	0.50	-1.02	-6.83
IN	-0.652	4.94	-11.0	-0.229	21.5	0.04	0.22	0.50	-1.26	-8.67
EA	-0.902	4.31	-16.8	-0.220	19.6	0.06	0.20	0.41	-1.58	-13.4
SE	-0.395	5.31	-6.19	-0.228	23.3	0.05	0.17	0.59	-0.40	-5.15
AU	-0.014	3.49	-0.27	-0.188	18.6	0.05	0.14	0.41	-0.01	-0.24
ME	-0.247	4.23	-4.98	-0.234	18.1	0.08	0.24	0.36	-0.47	-3.78

Table 3.8. Annual net RF globally and by latitude band (mW m^{-2}) and total GWP_{20} and GWP_{100} estimates for the regional and global reduction simulations relative to the base simulation, due to changes in tropospheric steady-state O_3, CH_4, and SO_4^{2-} concentrations. Global annual net shortwave radiation, net longwave radiation, and net RF per unit change in CO emissions (mW m^{-2} (Tg CO $yr^{-1})^{-1}$) are also shown. The 10 regions estimates represent the sum of the net RFs from all 10 regional reductions; these estimates are not directly estimated by the RTM.

Reduction region	Global annual net RF	Global annual net shortwave radiation	Global annual net longwave radiation	Global annual net RF per Tg CO	Annual net RF 90˚S – 28˚S	Annual net RF 28˚S – 28˚N	Annual net RF 28˚N – 60˚N	Annual net RF 60˚N – 90˚N	Total GWP_{20}	Total GWP_{100}
NA	-4.25	-0.31	-3.94	-0.122	-2.69	-6.20	-4.76	-3.32	3.98	1.33
SA	-1.51	-0.10	-1.40	-0.123	-1.04	-2.39	-1.45	-0.88	4.04	1.35
EU	-1.79	-0.07	-1.71	-0.114	-1.20	-2.70	-1.72	-1.36	3.71	1.26
FSU	-1.28	-0.07	-1.21	-0.117	-0.85	-1.89	-1.34	-1.00	3.78	1.28
AF	-5.46	-0.55	-4.92	-0.126	-3.61	-8.89	-5.25	-3.11	4.18	1.37
IN	-6.21	-0.85	-5.36	-0.129	-3.60	-10.0	-6.90	-3.70	4.34	1.41
EA	-9.12	-0.61	-8.50	-0.119	-5.80	-13.4	-10.3	-6.71	3.91	1.31
SE	-3.51	-0.34	-3.17	-0.129	-2.21	-5.79	-3.47	-1.99	4.34	1.41
AU	-0.18	-0.004	-0.17	-0.121	-0.12	-0.28	-0.18	-0.11	3.94	1.35
ME	-2.80	-0.40	-2.40	-0.131	-1.68	-4.36	-3.16	-1.81	4.37	1.44

Global	-36.1	-3.25	-32.9	-0.124	-22.8	-56.0	-38.6	-24.1	4.07	1.34
10 regions	-36.1	-3.31	-32.8	-	-22.8	-55.9	-38.6	-24.0	-	-

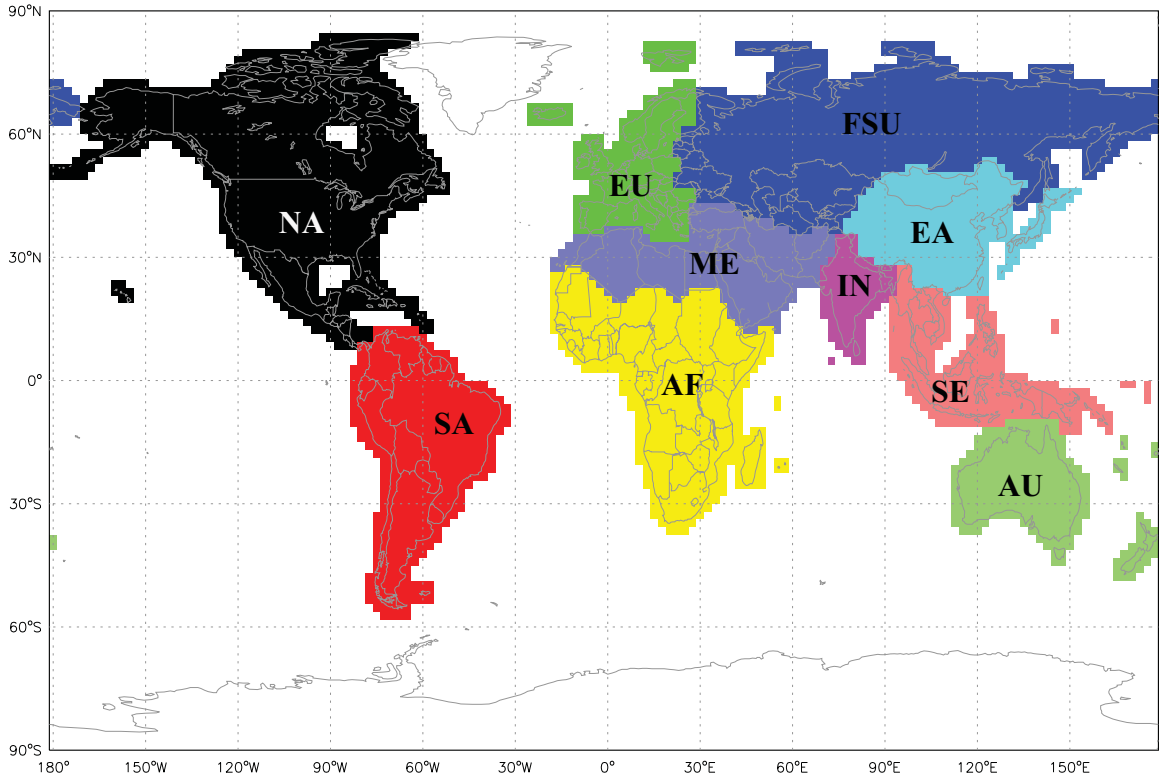

Figure 3.1. Definition of 10 reduction regions.

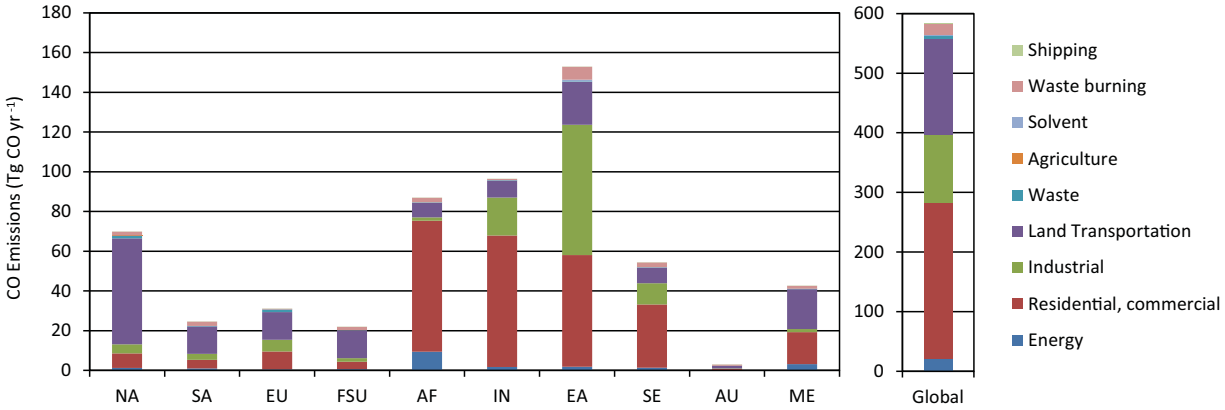

Figure 3.2. Annual average anthropogenic CO emissions (Tg CO yr^{-1}) by region and sector for the base simulation, from the RCP8.5 emissions inventory for the year 2005.

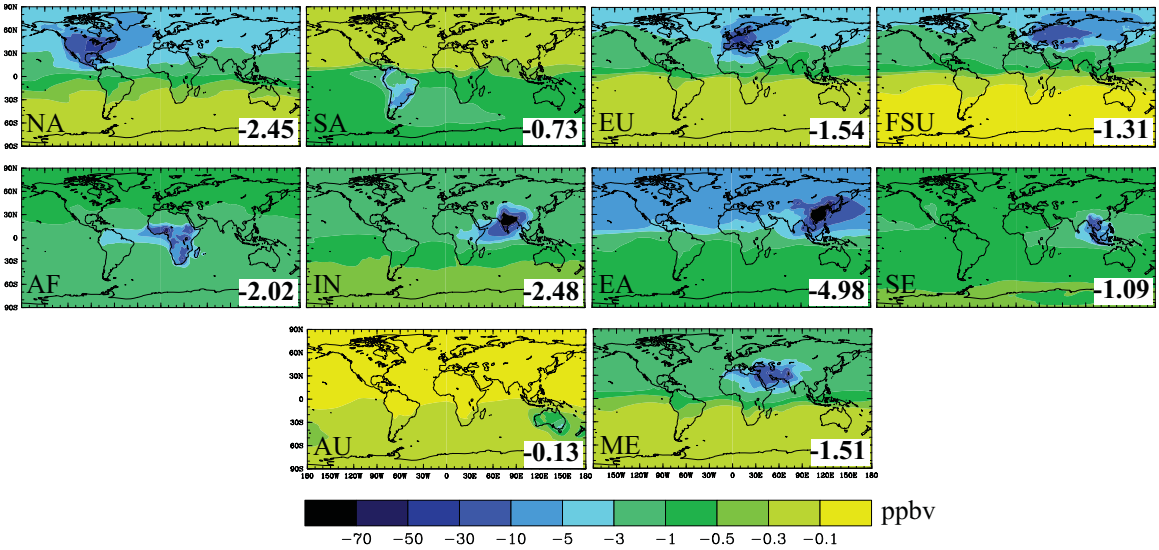

Figure 3.3. Global distribution of annual average surface CO concentration changes (ppbv) for each of the regional reduction simulations relative to the base. The global annual average surface CO concentration changes (ppbv) for each simulation are noted in the lower right of each panel.

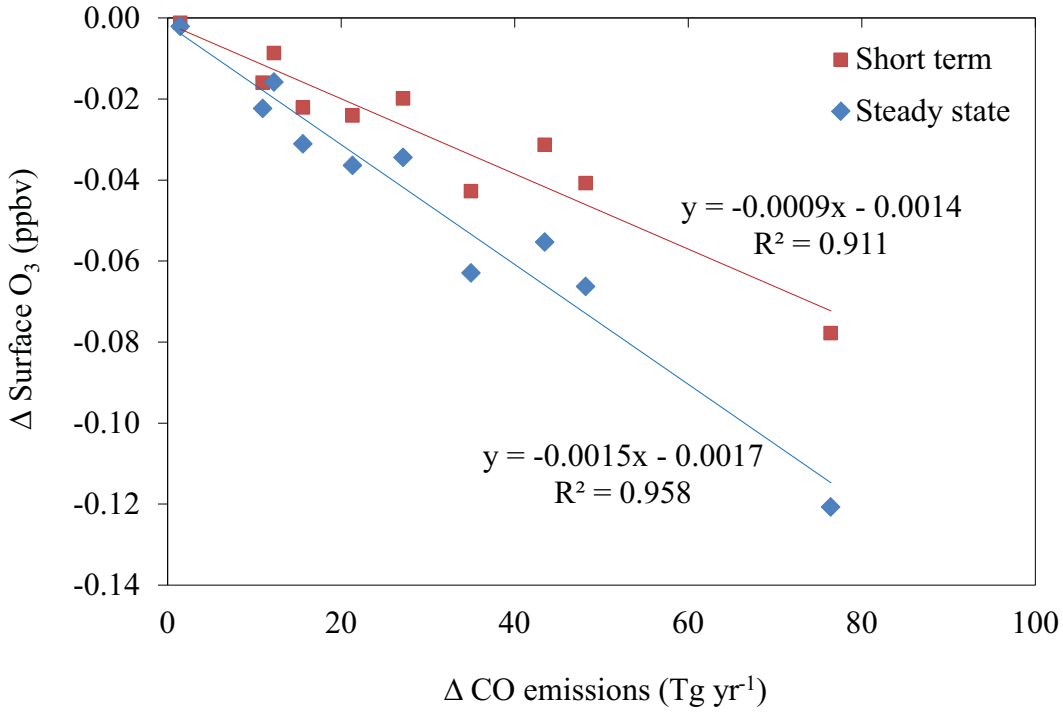

Figure 3.4. Short-term and steady-state surface ozone changes as a function of CO emissions change for each of the regional reductions relative to the base.

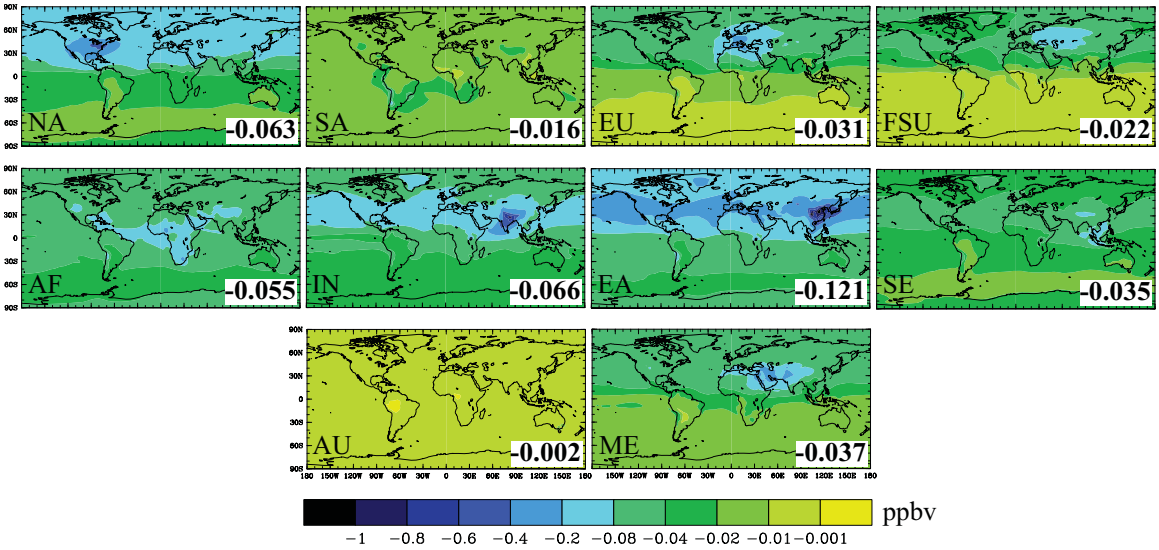

Figure 3.5. Global distribution of annual average steady-state surface O_3 concentration changes (ppbv) for each of the regional reduction simulations relative to the base. The global annual average steady-state surface O_3 concentration changes (ppbv) for each simulation are noted in the lower right of each panel.

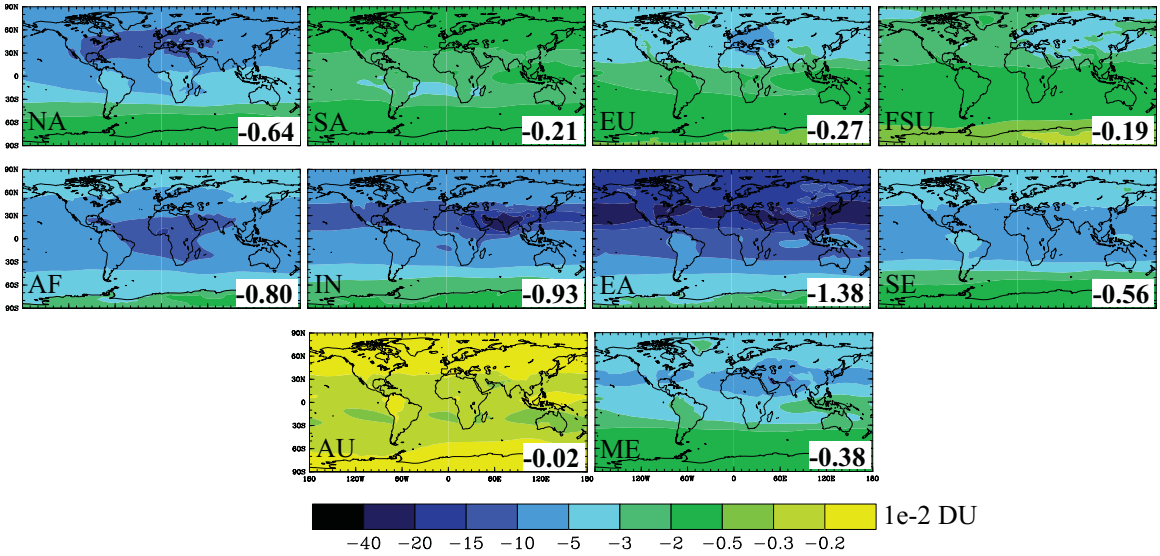

Figure 3.6. Global distribution of annual average changes in tropospheric total column O_3 at steady state (1e-2 DU) for each of the regional reduction simulations relative to the base. The global annual average steady-state tropospheric O_3 changes (Tg O_3) for each simulation are noted in the lower right of each panel.

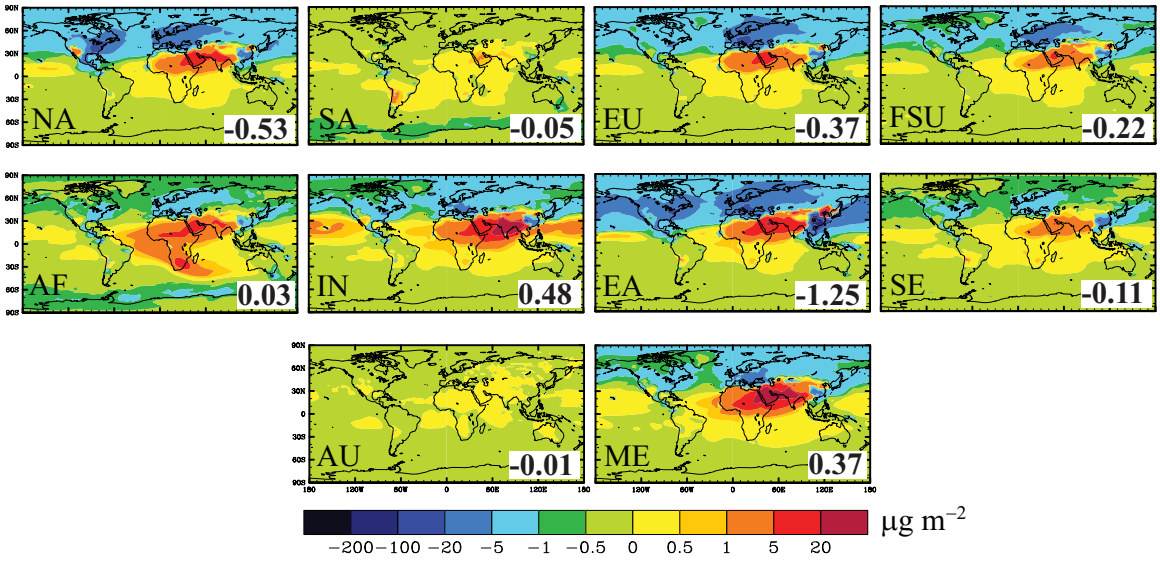

Figure 3.7. Global distribution of annual average changes in tropospheric total column SO_4^{2-} (μg m^{-2}) for each of the regional reduction simulations relative to the base. The global annual average tropospheric SO_4^{2-} changes (Gg) for each simulation are noted in the lower right of each panel.

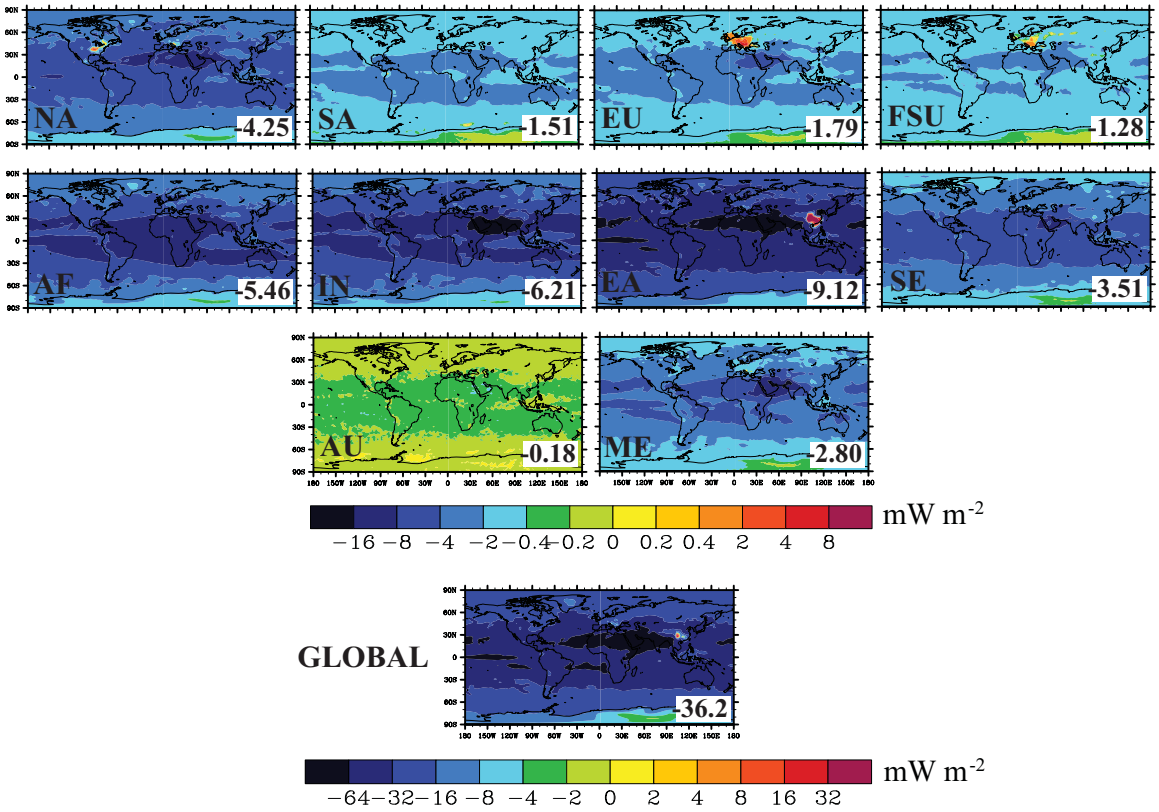

Figure 3.8. Annual average net RF distributions (mW m^{-2}) due to changes in tropospheric steady-state O_3, CH_4, and SO_4^{2-} for the regional and global CO reduction simulations minus the base simulation. Global annual average net RF (mW m^{-2}) for each simulation are noted in the lower right of each panel. Note the difference in scale between the regional and global reductions.

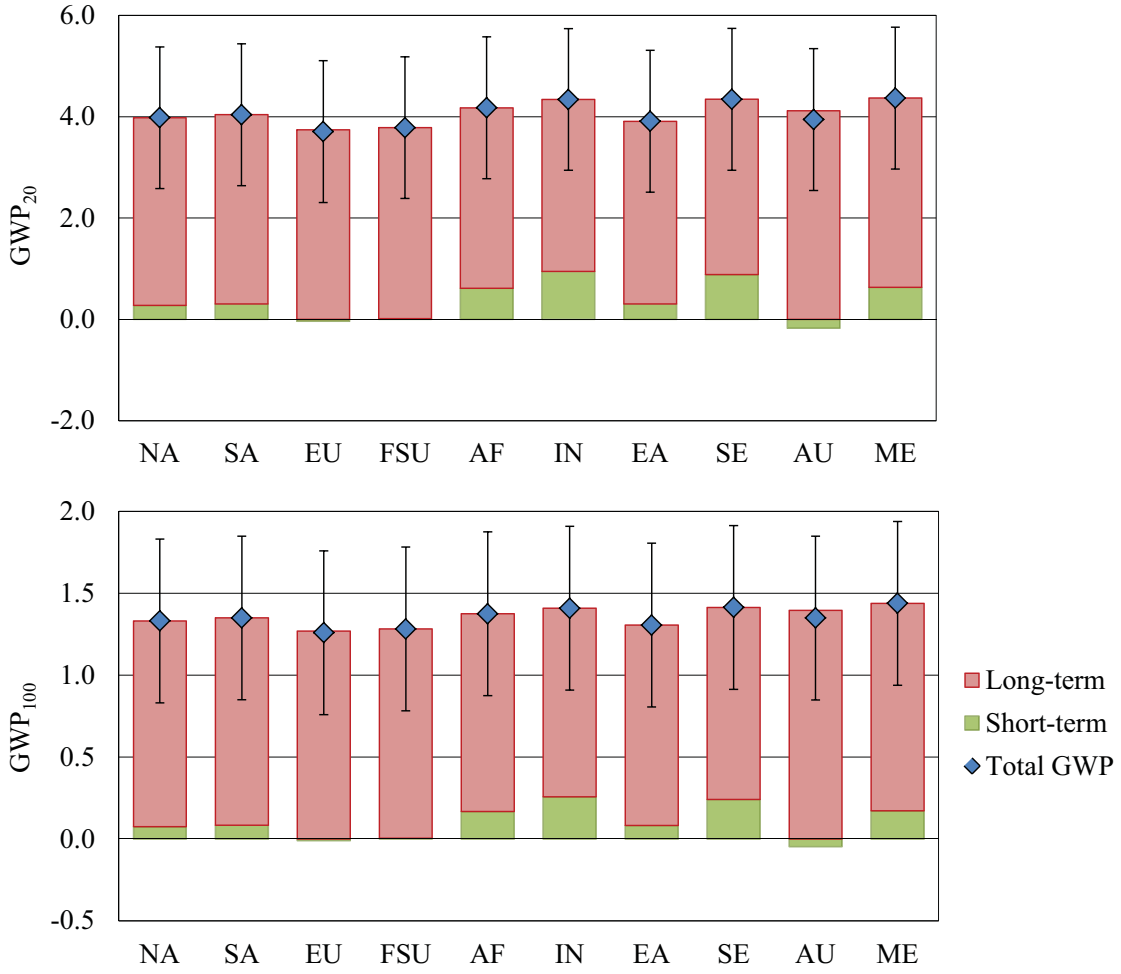

Figure 3.9. Global warming potentials for CO at time horizons of 20 and 100 years (GWP_{20}, GWP_{100}) for each regional reduction, and the contributions from short-term (O_3 and SO_4^{2-} changes) and long-term (long-term O_3 and CH_4) components. Uncertainty bars represent the average uncertainty found by Fry et al. (2012) based on the spread of atmospheric chemical models (1 standard deviation).

Chapter 4. Air quality and radiative forcing impacts of anthropogenic volatile organic compound emissions from ten world regions[3]

4.1 Introduction

Non-methane volatile organic compounds (NMVOCs) are chemically reactive gases emitted worldwide from natural and anthropogenic sources. NMVOCs impact air quality and climate by contributing to tropospheric photochemistry (e.g., ozone (O_3) production) and aerosol formation. Because of their influence on short-lived climate forcers (e.g., O_3, methane (CH_4), aerosols), NMVOC reductions could help slow the near-term rate of climate change (Shindell et al., 2012). Here we evaluate the net climate and air quality effects of anthropogenic NMVOC emission reductions, to inform future policies that may address air quality and climate change.

Tropospheric CH_4 and O_3 are the largest greenhouse gas contributors to global anthropogenic radiative climate forcing (RF) behind carbon dioxide (CO_2) with abundance-based RFs of 0.48 ±0.05 W m^{-2} and 0.35 (-0.1, +0.3) W m^{-2}, respectively (Forster et al., 2007). Tropospheric sulfate (SO_4^{2-}) has produced a global net RF of -0.40 ±0.2 W m^{-2} (direct effect only) (Forster et al., 2007). NMVOCs and carbon monoxide (CO) emissions together have contributed an estimated global mean RF of 0.21 ±0.10 W m^{-2} due to O_3 and CH_4 (1750 to 1998) (Shindell et al., 2005; Forster et al., 2007) and 0.25 ±0.04 W m^{-2} (1750 to 2000) when SO_4^{2-}, nitrate (NO_3^-), and CO_2 impacts are included

[3] Fry, M. M., M. D. Schwarzkopf, Z. Adelman, and J. J. West, Submitted to Atmospheric Chemistry and Physics, May 2013

(Shindell et al., 2009). More recently, the anthropogenic RF of NMVOC emissions (for 1850-2000) was estimated as 0.090 W m^{-2} (due to changes in O_3, CH_4, and CO_2) as part of the Atmospheric Chemistry and Climate Model Intercomparison Project (ACCMIP) (Stevenson et al., 2013).

NMVOCs are mainly oxidized by the hydroxyl radical (OH) in the troposphere, producing peroxyl radicals (RO_2) and hydroperoxy radicals (HO_2) that then oxidize nitric oxide (NO) to yield O_3. Because thousands of NMVOC species with varying lifetimes (from fractions of a day to months) and chemical reactivities have been documented, global chemical transport models (CTMs) use simplified representations of NMVOCs and reaction pathways (Ehhalt et al., 2001; Prather et al., 2001; Ito et al., 2007). Under high nitrogen oxide (NO_x = NO + NO_2) concentrations, NMVOCs contribute to the efficient cycling between OH and HO_2 and hence, O_3 production, while under low-NO_x conditions OH depletes, resulting in NMVOC and methane (CH_4) accumulation (Collins et al., 2002). CH_4 is a longer-lived O_3 precursor (perturbation lifetime of ~12 years) (Forster et al., 2007) that decreases as tropospheric OH increases (from NMVOC reductions), resulting in long-term O_3 decreases, in addition to direct, short-term O_3 decreases (Prather et al., 1996; Wild et al., 2001; Fiore et al., 2002; Naik et al., 2005). NMVOC emissions also affect O_3 at local to intercontinental scales, given that the lifetimes of tropospheric O_3 (~22 days) (Stevenson et al., 2006) and some NMVOCs (e.g., ethane, benzene) can exceed typical intercontinental transport times (5 to 10 days) (Fiore et al., 2009; West et al., 2009a). NMVOC reductions indirectly influence sulfate aerosol (SO_4^{2-}) formation via gas-phase oxidation of sulfur dioxide (SO_2) by OH, and aqueous-phase oxidation of SO_2 by H_2O_2 or O_3 (Unger et al., 2006; Leibensperger et al.,

2011). NMVOCs are also precursors to secondary organic aerosols (SOA), and influence NO_3^- aerosol abundance via oxidant changes (Ehhalt et al., 2001; Bauer et al., 2007; Hoyle et al., 2009).

Previous studies have shown that the RF and global warming potential (GWP) of NMVOCs, like other short-lived O_3 precursors, depend on emissions location given their short lifetime in the troposphere (Naik et al., 2005; Berntsen et al., 2006; Forster et al., 2007; Fry et al., 2012), but few studies quantify the range among different source regions. Fry et al. (2012) calculated 100-year and 20-year GWPs (GWP_{100}, GWP_{20}) of 4.8 ±2.4 to 8.3 ±1.9 and 15.5 ±6.8 to 26.5 ±5.3, respectively, for anthropogenic NMVOCs from four regions (due to O_3, CH_4, and SO_4^{2-}) using an ensemble of models. Collins et al. (2002) also presented GWP_{100} estimates of 1.8 to 5.5 (-50 to +100% uncertainty) due to CH_4 and O_3, but for individual anthropogenic NMVOCs globally.

Using global models of chemical transport and radiative transfer, we simulate the air quality and net RF impacts, via changes in O_3, CH_4, and SO_4^{2-}, of halving all anthropogenic NMVOC emissions together, globally and from 10 regions, as was done for CO emissions by Fry et al. (2013). We evaluate the sensitivity of air quality and RF to NMVOC emission location, and the corresponding NMVOC GWPs, which may support the inclusion of NMVOCs in multi-gas emission trading schemes for climate. We do not consider reductions in co-emitted species that would be affected by measures to reduce NMVOCs. Future studies could evaluate the impacts of measures on multiple species, or combine the results presented here with those for co-emitted species to determine the net effect of emission control measures (Shindell et al., 2012).

4.2 Methods

4.2.1 Global chemical transport model

We evaluate the impacts on surface air quality and tropospheric composition of halving anthropogenic NMVOC emissions globally and from 10 regions (North America [NA], South America [SA], Europe [EU], Former Soviet Union [FSU], Southern Africa [AF], India [IN], East Asia [EA], Southeast Asia [SE], Australia and New Zealand [AU], and Middle East and Northern Africa [ME]) (Figure C1) (Fry et al., 2013). We use the global chemical transport model (CTM), Model for OZone And Related chemical Tracers version 4 (MOZART-4) (Emmons et al., 2010).

The base and CH_4 control (where global CH_4 was reduced by 20%) simulations are documented in a previous study in which the base simulation was shown to generally agree with surface and tropospheric observations (Fry et al., 2013). Here we simulate new perturbation experiments that reduce regional and global anthropogenic NMVOC emissions by 50% for July 1, 2004 through December 31, 2005 using MOZART-4 at a horizontal resolution of 1.9˚ latitude x 2.5˚ longitude with 56 vertical levels. We use the Coupled Model Intercomparison Project phase 5 (CMIP5) Representative Concentration Pathway 8.5 (RCP8.5) emissions inventory for the year 2005 (Riahi et al., 2007, 2011) and global meteorology from the Goddard Earth Observing System Model, version 5 (GEOS-5) (2004 to 2006) (Rienecker et al., 2008). Anthropogenic emissions include all anthropogenic sectors except biomass burning emissions (Figure C2), which are excluded since actions to address biomass burning differ from the other anthropogenic sectors, and would likely reduce a suite of emissions simultaneously (Naik et al., 2007).

RCP8.5 NMVOC species are re-speciated to MOZART-4 NMVOC categories, and monthly temporal variation is added to all anthropogenic species and source categories, except for shipping, aircraft, and biomass burning, which already have monthly temporal variation (Figure C2, Table C1). The Model of Emissions of Gases and Aerosols from Nature (MEGAN) (Guenther et al., 2006) within MOZART-4 calculates the biogenic emissions of isoprene and monoterpenes ($C_{10}H_{16}$) (global annual totals of 738 Tg C yr^{-1} and 107 Tg C yr^{-1}, respectively), while all other natural emissions are from Emmons et al. (2010) (Table C2). The global annual lightning NO_x and soil NO_x emissions are also calculated by MOZART-4 as 2.4 Tg N yr^{-1} and 8.0 Tg N yr^{-1} (Fry et al., 2013).

Because the perturbation simulations are only 1.5 years in length, we account for the influence of NMVOC emissions on CH_4 (via OH), and thus long-term changes in O_3 on the decadal timescale of the CH_4 perturbation lifetime, using methods from previous studies (Prather et al., 2001; West et al., 2007; Fiore et al., 2009; Fry et al., 2012). Global CH_4 is set to a uniform mixing ratio of 1783 parts per billion by volume (ppbv) (WMO, 2006) in the base and perturbation simulations. The CH_4 control simulation reduced global CH_4 to 1426.4 ppbv. The results from the base and CH_4 control simulations were used by Fry et al. (2013) to estimate CH_4 lifetime against loss by tropospheric OH (τ_{OH}, 11.24 years), total CH_4 lifetime based on τ_{OH} and CH_4 loss to soils and the stratosphere (τ_{total}, 9.66 years), and methane's feedback factor (F, 1.29) by the methods of Prather et al. (2001) and Stevenson et al. (2013). We use these parameters to estimate the steady-state tropospheric CH_4 change for each of the NMVOC perturbations. Long-term O_3 responses are then calculated offline by scaling O_3 changes from the CH_4 control

simulation by the ratio of the global CH_4 change from each perturbation to that of the CH_4 control. We add long-term O_3 changes to direct short-term O_3 changes to estimate the net change at steady state (West et al., 2007, 2009b; Fiore et al., 2009; Fry et al., 2012).

Since MOZART-4 does not have complete stratospheric chemistry (Emmons et al., 2010), we merge each simulation's steady-state (short-term + long-term) tropospheric O_3 distributions (in three dimensions) with the monthly mean stratospheric O_3 concentrations from the AC&C/SPARC (Stratospheric Processes And their Role in Climate) O_3 database prepared for CMIP5 (Available: http://pcmdi-cmip.llnl.gov/cmip5/forcing.html) (Cionni et al., 2011). By omitting lower stratospheric O_3 changes between each perturbation and the base simulation, our RF estimates likely underestimate the full effect of NMVOC emissions (Søvde et al., 2011).

MOZART-4 accounts for the tropospheric aerosols SO_4^{2-}, black carbon (BC), primary and secondary organics, NO_3^-, dust, and sea salt aerosols (Lamarque et al., 2005). Here we focus on changes in SO_4^{2-}, NO_3^-, and SOA, as these species are most directly influenced by anthropogenic NMVOCs, where NMVOCs are precursors to SOA, and changes in oxidants affect all three aerosol species (Barth et al., 2000; Metzger et al., 2002; Chung and Seinfeld, 2002).

4.2.2 Radiative transfer model

We use the NOAA Geophysical Fluid Dynamics Laboratory (GFDL) standalone radiative transfer model (RTM) to perform stratospheric-adjusted net RF calculations (Schwarzkopf and Ramaswamy, 1999; GFDL GAMDT, 2004; Naik et al., 2005, 2007) as in Fry et al. (2012), with the same updates to long-lived greenhouse gases (Meinshausen

et al., 2011) and solar forcing (http://www.geo.fu-berlin.de/en/met/ag/strat/forschung/SOLARIS/Input_data/CMIP5_solar_irradiance.html) from Fry et al. (2013). Net RF is calculated as the difference between the perturbed and base cases' simulated monthly mean net radiation fluxes (net shortwave minus net longwave), in each grid cell and month, at the tropopause after stratospheric temperatures have readjusted to radiative equilibrium (Naik et al., 2007; Saikawa et al., 2009; Fry et al., 2012). We quantify the net RF from changes in tropospheric steady-state O_3, CH_4, and SO_4^{2-} (direct effect only), as modeled by the MOZART-4 simulations. Meteorological fields from GFDL's atmosphere model (AM2) and land model (LM2), sampled one day per month at midmonth for the year 2005, are also used as input to the RTM simulations, representing monthly mean conditions (Naik et al., 2005).

The RTM currently does not calculate the RF of SOA and NO_3^- aerosols. We also do not account for the RF of changes in stratospheric O_3, water vapor, the carbon cycle (via O_3 and nitrogen deposition, affecting plants), and CO_2 (via NMVOC oxidation, which has a minor influence on the net RF of NMVOCs) (Shindell et al., 2009). We do not estimate CO_2 forcing here, because this carbon is likely accounted for in CO_2 inventories (Daniel and Solomon, 1998). Our RTM simulations also exclude the indirect effects of aerosols on clouds and the internal mixing of aerosols, where aerosol indirect effects are highly uncertain and may account for considerable RF beyond aerosol direct effects (Forster et al., 2007; Shindell et al., 2013).

4.3 Tropospheric composition and surface air quality

4.3.1 Methane and ozone

Global annual average changes in steady-state tropospheric CH_4 abundance, calculated from the tropospheric CH_4 loss flux diagnosed from the model (West et al., 2007; Fiore et al., 2009; Fry et al., 2013), are largest for ME (-7.37 ppbv) and SA (-5.41 ppbv) reductions among the 10 regions (Table 4.1). Normalized global CH_4 changes range from 0.40 to 1.61 ppbv CH_4 (Tg C $yr^{-1})^{-1}$ among the 10 regions, and are most sensitive to reductions from AU, SA, SE, and AF. These are regions of low NO_x, as discussed below, where reducing NMVOCs lessens OH depletion creating greater global CH_4 changes per unit emission. CH_4 decreases are least sensitive to NMVOC reductions from high-NO_x regions (EA, EU, FSU). Naik et al. (2005) also found greater global CH_4 sensitivities for NO_x emissions from low-NO_x regions (SE, SA, and AU), and lower sensitivities for high-NO_x regions (EU, FSU).

Global short-term and steady-state surface O_3 changes for the 10 regional reductions are nearly proportional to NMVOC emissions changes (R^2 = 0.69 and 0.81) (Figure C3), but not as strongly correlated as for regional CO reductions (Fry et al., 2013). NMVOC emissions produce long-term O_3 decreases that augment short-term decreases by 13% for the global reduction, and by 5-18% for the regional reductions (Figure 4.1, Table 4.2), similar to Fiore et al. (2009) and West et al. (2007). SA, AF, and SE reductions provide more substantial long-term global surface O_3 changes, which account for ~34 to 89% of steady-state O_3 decreases.

Several of the regional reductions (SA, AF, SE, and AU) in the tropics and southern hemisphere (SH) produce regional to intercontinental tropospheric O_3 column

increases (Figure 4.2), as the sensitivity of O_3 to NMVOC emissions varies by world region. All of the regional reductions slow the formation of peroxyacetyl nitrate (PAN), causing PAN to decrease regionally to hemispherically and NO_x to increase regionally (Figures C5, C6, and C7). For SA, AF, SE, and AU, these NO_x increases cause O_3 column increases near or downwind of the region. For the other regions, decreases in NMVOCs decrease O_3, outweighing the influence of NO_x increases via slowing PAN production. Whether NMVOC reductions cause O_3 to increase or decrease depends on the regional chemical state. Here O_3-NO_x-VOC sensitivity is analyzed using the photochemical indicator ratios: $P(H_2O_2)/P(HNO_3)$, where P() refers to production rate, $(H_2O_2)/(HNO_3)$, and $(H_2O_2)/(NO_2)$ (Sillman et al., 1997; Liu et al., 2010). The modeled indicator ratios show that NO_x-sensitive conditions prevail in the tropics and southern midlatitudes, supporting the finding of tropospheric O_3 increases from SA, AF, SE, and AU reductions (Figures C8, C9, and C10). The northern mid- to high latitudes more frequently exhibit VOC-sensitivity (weaker NO_x-sensitivity), particularly from November to March, resulting in O_3 decreases.

The global distributions of steady-state surface and tropospheric O_3 show the greatest decreases within each reduction region, and smaller decreases intercontinentally (Figure 4.2, Figure C4, and Table C3). Although the largest changes in surface O_3 occur within the hemisphere of reduction, given that inter-hemispheric transport takes ~1 year (Jacob, 1999), more widespread decreases reflect global long-term O_3 decreases (via CH_4 decreases). NMVOC reductions in one region can also influence surface O_3 concentrations in other regions importantly (Tables C3 and C4). In fact, the EA, ME, and EU NMVOC reductions have an impact on US surface O_3 that is 43%, 34%, and 34%,

respectively, of that from the NA reduction. Two of the low-NO_x regions (SA and SE) experience greater decreases in surface O_3 from foreign regions' NMVOCs than domestic NMVOCs.

The global annual average steady-state tropospheric O_3 burden decreases by 0.073 Tg O_3 (Tg C yr^{-1})$^{-1}$ for the global reduction and by -0.008 to 0.101 Tg O_3 (Tg C yr^{-1})$^{-1}$ for the 10 regions (Table 4.1). Changes in O_3 production (ΔP) and export (ΔX) are also calculated to determine the importance of long-range transport of O_3 and its precursors. For most regions, changes in O_3 production outside of each reduction region exceed changes in O_3 export from each region, suggesting that the influence of NMVOC emissions on the downwind production of O_3 has a greater impact on long-range O_3 than the formation and export of O_3 from each region (Table 4.1). In contrast, for the SA, AF, and SE reductions, ΔX is positive due to regional O_3 increases. O_3 production outside the reduction region decreases for AF and SE, yet increases for SA, as SA causes widespread increases in tropospheric O_3 (Figure 4.2). For AU, regional tropospheric O_3 export decreases, while tropospheric O_3 production increases outside AU (Table 4.1, Figure 4.2).

4.3.2 Aerosols

NMVOC reductions affect the oxidation of SO_2, NO_x, monoterpenes, and toluene, influencing tropospheric SO_4^{2-}, NO_3^-, and SOA concentrations. Reductions from regions near the equator and in drier areas (SA, AF, IN, SE, and ME) produce widespread SO_4^{2-} increases (Figure 4.3), related to increased gas-phase SO_2 oxidation by OH. In fact, most of the regional reductions, except EA and AU, produce localized increases in SO_4^{2-} over drier areas (e.g., Middle East and India). Tropospheric O_3 increases from the SA, AF, and SE reductions also contribute to SO_4^{2-} increases via enhanced aqueous-phase SO_2

oxidation by O_3, where aqueous-phase SO_2 oxidation is more efficient than gas-phase oxidation (Unger et al., 2006). Regional reductions in the northern midlatitudes (NA, EU, FSU, and EA) result in widespread decreases in SO_4^{2-}, due to the prevalence of clouds and decreased aqueous-phase oxidation (in clouds) of SO_2 by O_3 and H_2O_2 (Figures 4.3, C11, and C12). NO_3^- changes include both regional increases and decreases. As with SO_4^{2-}, NO_3^- increases are expected due to OH increases that are global in scale, yet largest over the source region (Figures C13 and C14). SOA decreases globally, influenced not only by oxidant changes, but also by NMVOCs directly, as NMVOCs are precursors to SOA. The largest SOA decreases occur over the reduction region (Figure C15). While MOZART-4 accounts for SOA formation through the oxidation of monoterpenes and toluene, more research is needed to more fully model SOA. Current models greatly simplify the physical and chemical processes contributing to SOA burden, and underpredict SOA formation compared to observations (Carlton et al., 2009).

Global annual average SO_4^{2-} burden decreases for most regional reductions, yet increases for SA, AF, and ME (Table 4.3). For all 10 regional reductions, global NO_3^- burden increases and global SOA burden decreases. The sums of global burden changes for all 10 regional reductions, for SO_4^{2-}, NO_3^-, and SOA, are 95 to 99% of the burden changes for the global NMVOC reduction, suggesting some dependence on regional conditions and chemistry.

4.4 Radiative forcing and global warming potential

The global annual average net RF is estimated as -9.73 mW m^{-2} for the global 50% NMVOC reduction or 0.21 mW m^{-2} (Tg C yr^{-1})$^{-1}$ (Table 4.4). To compare with

other estimates of anthropogenic forcing, we double this net RF and scale for biomass burning emissions (29.9% of global anthropogenic NMVOC emissions), which were excluded in the 50% reductions, yielding a global net RF of -0.0277 W m^{-2}. This approach assumes that biomass burning emissions have the same locations and mixture of NMVOCs as anthropogenic emissions. This RF is ~49% of the ACCMIP multimodel mean global net RF of NMVOC emissions for 1850-2000 due to O_3 and CH_4 changes alone (0.057 W m^{-2}) (Stevenson et al., 2013). It is also 11 to 13% of previous CO + NMVOC RF estimates: 0.25 ±0.04 W m^{-2} (Shindell et al., 2009) and 0.21 ±0.1 W m^{-2} (Shindell et al., 2005; Forster et al., 2007). The RF of anthropogenic NMVOCs is ~1.8% of global net RF of CO_2 (1.56 W m^{-2}), and among the positive short-lived forcing agents (CO, CH_4, NMVOCs, and BC), ~1.8% of their total RF (1.57 W m^{-2}) (Forster et al., 2007). Potential reasons for our smaller RF (and GWP) estimates are discussed below.

Across the 10 regions, the global annual average net RF, normalized per unit change in NMVOC emissions, is 0.30 ±0.15 mW m^{-2} (Tg C yr^{-1})$^{-1}$ (mean ±1 standard deviation), suggesting variability in the forcings due to different regions' emissions. The normalized RF is most sensitive to NMVOC emissions from regions in the tropics and SH (ME, AU, AF, and IN). Monthly global net RF estimates vary from 0.03 to 3.5 times the annual mean (excluding EA, which has even greater variability), with the greatest negative RFs from June to August (Figure C17).

Regional changes in NMVOC emissions cause widespread negative net RFs (cooling) across both hemispheres from decreases in global CH_4 and long-term O_3 (Figure 4.4). Negative RFs over several source regions (e.g., IN, ME) result from short-term O_3 decreases and regional SO_4^{2-} increases (Figure 4.3). Regional positive RFs

(warming) arise from regional SO_4^{2-} decreases (e.g., NA, EU, FSU, EA, and SE reductions) (Figure 4.3), which can oppose the negative RFs of O_3 decreases, and tropospheric O_3 increases (e.g., SA, AF, SE, and AU reductions) (Figure 4.2). These influences are supported by the distributions of changes in longwave radiation (Figure C18), dominated by O_3 and CH_4 changes, and shortwave radiation (Figure C19), dominated by SO_4^{2-}. If changes in SOA and NO_3^- were accounted for by the RTM, tropospheric SOA decreases (greater than SO_4^{2-} changes in some regions) would likely add small regional warming, while tropospheric NO_3^- increases and decreases (mostly lesser than SO_4^{2-} changes) would add slight regional cooling and warming effects. Globally, NO_3^- and SOA would contribute small negative and positive RFs, respectively, to global net RF.

Using the methods of Collins et al. (2013) and Fry et al. (2012, 2013), we calculate GWPs for each reduction as the RF integrated to 20 and 100 years, normalized by the emissions change, and divided by the equivalent for CO_2 (Table 4.4). These GWPs represent short-term contributions from SO_4^{2-} and O_3 (assumed constant over one year and zero thereafter), and long-term contributions of CH_4 and O_3 (responding and decaying with the CH_4 perturbation lifetime of 12.48 years) (Fry et al., 2013). The long-term O_3 RF component is calculated by scaling the O_3 RF from the CH_4 control simulation by the ratio of the long-term O_3 burden change from each perturbation to that of the CH_4 control. Short-term O_3 RF is the difference between steady-state O_3 RF (simulated by the RTM) and long-term O_3 RF.

GWP_{20} and GWP_{100} are estimated as 5.83 and 2.36, respectively, for the global reduction, and -1.13 to 18.9 and 0.079 to 6.05 among the 10 regions, suggesting strong

dependence on emission location, consistent with the normalized net RFs (Figure 4.5). GWP_{20} and GWP_{100} are greatest for ME, which also had the largest net RF sensitivity, and smallest for EA, because of the nearly equivalent (opposing) short- and long-term effects. SA, SE, and AU reductions yield the largest (negative) short-term components for GWP_{20} and GWP_{100} due to the combined effect of SO_4^{2-} and tropospheric O_3 increases, which act in the opposite direction to the long-term component. Uncertainty in NMVOC GWPs is based on the spread across an ensemble of global CTMs from Fry et al. (2012) (±1 standard deviation, GWP_{20}: ±6.0 and GWP_{100}: ±2.1), but do not account for the full uncertainty, as additional forcings could change net RF and GWP estimates.

Our GWPs (and RFs) do not include the forcing from CO_2 as NMVOCs oxidize, since carbon emissions are often accounted for in CO_2 inventories (Fuglestvedt et al., 1996; Daniel and Solomon, 1998; Collins et al., 2002). Including CO_2 forcing, however, may provide a more complete accounting of the effects of NMVOCs, increasing each GWP_{20} and GWP_{100} estimate by 3.67 (44 g CO_2 mol^{-1} (56.6 g C mol^{-1})$^{-1}$ * 4.7 C per NMVOC molecule), based on the global annual average molecular weight and number of carbons per molecule for anthropogenic NMVOC emissions. This increases the global GWP_{20} and GWP_{100} by 63% and 155%, respectively, and makes all regional GWP_{20} and GWP_{100} estimates positive.

The GWP_{20} and GWP_{100} estimates for NA, EU, and IN (South Asia) reductions are approximately 32 to 41%, 61 to 69%, and 50 to 52% lower than the multimodel mean estimates of Fry et al. (2012) (Table C10). EA GWP_{20} and GWP_{100} estimates, being near zero, also greatly contrast with Fry et al. (2012). Here total NMVOC/NO_x emissions ratios are 57% greater globally and in NA than the multimodel mean ratios, partly due to

greater biogenic NMVOC emission sources (calculated online in MOZART-4). In EU, EA, and IN, the total NMVOC/NO_x emissions are closer to the multimodel mean ratios: 4% and 9% (EU and EA, respectively) less and 8% (IN) greater than those of the multimodel mean (Table C11). Global O_3 burden responses (in Tg O_3 (Tg C $yr^{-1})^{-1}$) are 27% to 51% less than those in Fry et al. (2012), likely due to the greater NMVOC/NO_x emission ratios in this study, which would suggest less sensitivity to NMVOC emissions, but differences in the representations of NMVOCs and oxidation chemistry among models may also contribute to these differences. Global SO_4^{2-} responses (in Gg SO_4^{2-} (Tg C $yr^{-1})^{-1}$) also highly vary, more commonly causing increases in SO_4^{2-} compared to the decreases in Fry et al. (2012) (Table C12). Collins et al. (2002) calculated GWP_{100} estimates for individual NMVOC species (due to CH_4 and O_3 only) ranging from 1.9 to 5.5 (-50% to 100% uncertainty), which are more similar to the GWP_{100} magnitudes estimated here. While our NMVOC GWP estimates consider all anthropogenic NMVOCs together and are derived from only one CTM and RTM, they represent emissions from a greater number of regions, including the tropics and extra-tropics.

4.5 Summary

Reducing NMVOC emissions provides regional to global benefits to air quality and climate. Halving anthropogenic NMVOCs from each region creates widespread small negative net RFs across both hemispheres from global CH_4 and long-term O_3 decreases. RF is also negative near several source regions (e.g., IN, ME) due to regional SO_4^{2-} increases and short-term O_3 decreases. Regional small positive RFs correspond to regional SO_4^{2-} decreases (e.g., NA, EU, FSU, EA, and SE) and tropospheric O_3 increases (e.g., SA, AF, SE, and AU).

The present-day NMVOC RF is estimated as 0.0277 W m^{-2}, or ~1.8% of CO_2 RF since the preindustrial. Our RF, GWP_{20}, and GWP_{100} estimates for the NA, EA, EU, and IN reductions are also lower than the multimodel mean estimates of Fry et al. (2012), due to differences in O_3-NO_x-VOC sensitivities and SO_4^{2-} responses, and in particular, because of regional O_3 increases and SO_4^{2-} decreases for some regions that oppose the long-term cooling. Considerable variability in the global net RF, GWP_{20}, and GWP_{100} estimates among regions suggests a strong dependence on emission location: 0.21 mW m^{-2} (Tg C $yr^{-1})^{-1}$, 5.83, and 2.36 for the global reduction, and 0.30 ±0.15 mW m^{-2} (Tg C $yr^{-1})^{-1}$, -1.13 to 18.9, and 0.079 to 6.05 for the 10 regions. GWP_{20} and GWP_{100} are greatest for regions in the tropics and SH (i.e., ME, IN, and AF) and less for regions in the northern midlatitudes (i.e., EU and FSU). The lowest GWP_{20} and GWP_{100} estimates are for EA, given the nearly equivalent (opposing) short- and long-term effects. Including additional forcings beyond CH_4, O_3, and SO_4^{2-} would likely change RF and GWP estimates.

Variability in global annual average tropospheric CH_4, O_3, and SO_4^{2-} responses contribute to the RF and GWP differences seen among regions: 0.81 ppbv CH_4 (Tg C $yr^{-1})^{-1}$, 0.073 Tg O_3 (Tg C $yr^{-1})^{-1}$, and 0.33 Gg SO_4^{2-} (Tg C $yr^{-1})^{-1}$ for the global reduction, and 0.40 to 1.61 ppbv CH_4 (Tg C $yr^{-1})^{-1}$, -0.008 to 0.101 Tg O_3 (Tg C $yr^{-1})^{-1}$, and -0.21 to 1.01 Gg SO_4^{2-} (Tg C $yr^{-1})^{-1}$ among the 10 regions. Several regions with high GWPs are low-NO_x regions (AF and AU), which have stronger CH_4 sensitivities to NMVOC reductions, and weak increases or decreases in SO_4^{2-}.

Anthropogenic NMVOC emissions overall contribute ~5.1% (1.9 ppbv) to global annual average steady-state surface O_3, by doubling the change from the 50% global

NMVOC reduction (-0.67 ppbv) and scaling for biomass burning emissions. Some regional reductions contribute importantly to surface O_3 in other regions, such as EA, ME, and EU, which impact US surface O_3 by 43%, 34%, and 34%, respectively, of that from NA emissions. NMVOC emission reductions mostly have a greater impact on downwind O_3 production than the formation and export of O_3 from each source region. Long-term surface O_3 changes (via CH_4) impact air quality globally, and for most regions add 5-18% to short-term changes.

In this study, the air quality and RF impacts are derived from one CTM and RTM, which limits our ability to capture a more complete range of CH_4, O_3, aerosols, and RF responses, as a model ensemble would. Previous studies have shown a large model spread in CH_4, O_3, and SO_4^{2-} responses to regional NMVOC emissions (Collins et al., 2002; Fiore et al., 2009; Fry et al., 2012). Future work could examine the emissions inventories of NMVOCs and other species, as they are fairly uncertain among models (Berntsen et al., 2005).

Other limitations include only accounting for CH_4, O_3, and SO_4^{2-} (direct effect only) in our net RF and GWP estimates, which may affect the magnitude of our estimates and variability among regions. Forcing mechanisms not accounted for include NO_3^-, SOA, stratospheric O_3, water vapor, the carbon cycle (via O_3 and nitrogen deposition), the indirect effects of aerosols, and the internal mixing of aerosols. Future research could include these additional forcings and their uncertainty. The contribution of anthropogenic NMVOCs to SOA, in particular, is fairly uncertain, and often underpredicted by models (Volkamer et al., 2006). The influence of climate feedbacks on chemistry and future changes in emissions also may alter the air quality and RF

sensitivities estimated here for present-day emissions. In addition, while we focus on the sensitivity of air quality and RF to NMVOC emissions, which is useful in determining the GWP of NMVOCs, emission control measures would likely affect co-emitted species. Our results can be combined with those for co-emitted pollutants to evaluate the net effect of measures affecting multiple pollutants. Full climate responses also could be evaluated, as in Shindell and Faluvegi (2009).

These findings of high variability in GWPs among regions for NMVOCs contrast with our earlier findings for CO, with little variability in GWPs among source regions (Fry et al., 2013). While it would be possible to include CO in multi-gas emissions trading schemes using a single GWP, with little error, using a single GWP for NMVOCs would cause significant error. Instead, international climate agreements could consider including NMVOCs in multi-gas emissions trading schemes using GWPs that are specific to each region. Although NMVOCs are a small climate forcing agent, this study motivates reductions in NMVOC emissions as part of future coordinated policies addressing air quality and climate change (Rypdal et al., 2005, 2009; Jackson et al., 2009; Shindell et al., 2012; Fry et al., 2013).

4.6 Tables and Figures

Table 4.1. Changes in global annual average short-term and steady-state tropospheric O_3 burden (B_{O3}) and tropospheric CH_4 for the global and regional reductions. Changes in O_3 production (P_{O3}), P_{O3} normalized per unit change in NMVOC emissions (E), and P_{O3} outside each reduction region are shown for each regional reduction. Changes in net O_3 export (X_{O3}) from each reduction region, and the fractions of B_{O3} and P_{O3} changes above each reduction region are also estimated.

Reduction region	ΔB_{O3} (Tg O_3) short-term	ΔB_{O3} (Tg O_3) steady-state	$\Delta B_{O3}/\Delta E$ (Tg O_3 (Tg C $yr^{-1})^{-1}$) steady-state	ΔCH_4 (ppbv)	$\Delta CH_4/\Delta E$ (ppbv (Tg C $yr^{-1})^{-1}$)	ΔP_{O3} (Tg yr^{-1})	$\Delta P_{O3}/\Delta E$ (Tg O_3 (Tg C $yr^{-1})^{-1}$)	ΔP_{O3} outside region (Tg yr^{-1})	ΔX_{O3} from region (Tg yr^{-1})	Fraction of global ΔB_{O3} above region	Fraction of global ΔP_{O3} above region
NA	-0.30	-0.41	0.082	-4.05	0.80	-6.13	1.21	-3.92	-0.84	0.19	0.36
SA	0.16	0.028	-0.008	-5.41	1.60	1.95	-0.58	0.67	0.72	0.13	0.66
EU	-0.31	-0.38	0.101	-2.30	0.61	-6.15	1.64	-4.17	-1.19	0.087	0.32
FSU	-0.21	-0.25	0.101	-1.61	0.64	-3.80	1.52	-2.83	-0.48	0.21	0.25
AF	-0.081	-0.20	0.049	-4.20	1.03	-2.22	0.54	-2.34	0.41	-0.041	-0.052
IN	-0.23	-0.30	0.081	-2.40	0.65	-5.09	1.38	-3.14	-0.67	0.071	0.38
EA	-0.90	-1.02	0.099	-4.10	0.40	-18.6	1.82	-11.2	-3.79	0.10	0.40
SE	0.075	-0.066	0.016	-5.16	1.22	-0.18	0.04	-1.40	0.80	0.21	-6.75
AU	0.013	0.00	0.000	-0.54	1.61	0.19	-0.58	0.20	-0.014	0.040	-0.032
ME	-0.50	-0.69	0.091	-7.37	0.97	-9.48	1.24	-6.31	-1.79	0.10	0.33
Global	-2.44	-3.33	0.073	-36.6	0.81	-52.1	1.15	-	-	-	-

Table 4.2. For the global and regional reduction simulations relative to the base, global annual average changes in short-term and steady-state surface O_3.

Reduction region	Δ Surface O_3 short term (pptv)	Δ Surface O_3 steady state (pptv)
NA	-81.0	-89.9
SA	-1.40	-13.3
EU	-87.5	-92.6
FSU	-71.0	-74.5
AF	-18.2	-27.5
IN	-28.9	-34.2
EA	-167.1	-176.2
SE	-9.40	-20.8
AU	0.60	-0.60
ME	-100.6	-116.8
Global	-592.9	-673.5

Table 4.3. For the global and regional reduction simulations relative to the base, global annual average tropospheric burden changes in SO_4^{2-}, NO_3^- (expressed as NH_4NO_3), and SOA. The global annual average tropospheric SO_4^{2-}, NH_4NO_3, and SOA burdens in the base simulation are 1785 Gg SO_4^{2-}, 416 Gg NH_4NO_3, and 227 Gg SOA.

Reduction region	ΔSO_4^{2-} (Gg yr^{-1})	ΔNH_4NO_3 (Gg yr^{-1})	ΔSOA (Gg yr^{-1})
NA	-1.63	0.61	-2.91
SA	0.05	0.17	-4.57
EU	-2.26	1.47	-1.30
FSU	-1.45	0.88	-0.74
AF	0.06	0.21	-2.84
IN	-0.03	0.05	-1.66
EA	-10.3	3.21	-3.69
SE	-0.06	0.38	-5.00
AU	-0.01	0.01	-0.25
ME	1.63	0.09	-1.89
Global	-14.8	7.27	-24.9

Table 4.4. Annual net RF globally and by latitude band (mW m^{-2}) and GWP_{20} and GWP_{100} estimates for the global and regional reduction simulations relative to the base, due to changes in tropospheric steady-state O_3, CH_4, and SO_4^{2-} concentrations. Global annual net RF per unit change in NMVOC emissions (mW m^{-2} (Tg C $yr^{-1})^{-1}$) is also shown. The 10 regions estimate represents the sum of the net RFs from all 10 regional reductions; this estimate is not directly estimated by the RTM.

Reduction region	Global annual net RF	Global annual net RF per Tg NMVOC	Annual net RF 90˚S – 28˚S	Annual net RF 28˚S – 28˚N	Annual net RF 28˚N – 60˚N	Annual net RF 60˚N – 90˚N	GWP_{20}	GWP_{100}
NA	-1.50	0.30	-1.19	-2.13	-0.46	-2.09	9.20	3.27
SA	-1.17	0.35	-0.63	-1.20	-1.98	-1.38	8.56	3.86
EU	-0.70	0.19	-0.69	-1.46	1.05	-1.16	5.36	2.05
FSU	-0.51	0.20	-0.48	-1.05	0.58	-0.71	5.96	2.24
AF	-1.56	0.38	-1.24	-1.99	-1.79	-1.17	11.8	4.19
IN	-1.38	0.37	-0.83	-2.12	-1.54	-0.96	12.7	4.08
EA	-0.05	0.0045	-1.41	-0.24	5.98	-3.30	-1.13	0.079
SE	-1.23	0.29	-1.24	-0.79	-1.85	-1.39	7.58	3.23
AU	-0.13	0.40	0.016	-0.25	-0.21	-0.14	10.5	4.41
ME	-4.22	0.55	-2.29	-6.80	-4.56	-3.06	18.9	6.05

Global	-9.73	0.21	-8.36	-13.8	-1.21	-14.0	5.83	2.36
10 regions	-12.5	0.28	-9.98	-18.0	-4.77	-15.3	-	-

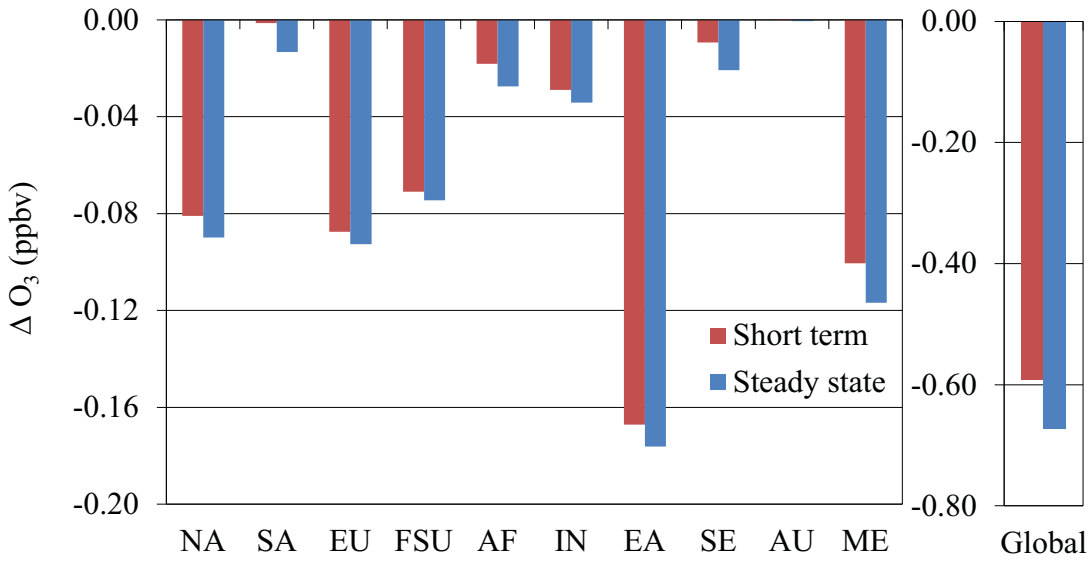

Figure 4.1. Global annual average surface O_3 concentration changes (ppbv) for the regional and global reduction simulations, in the short term and at steady state.

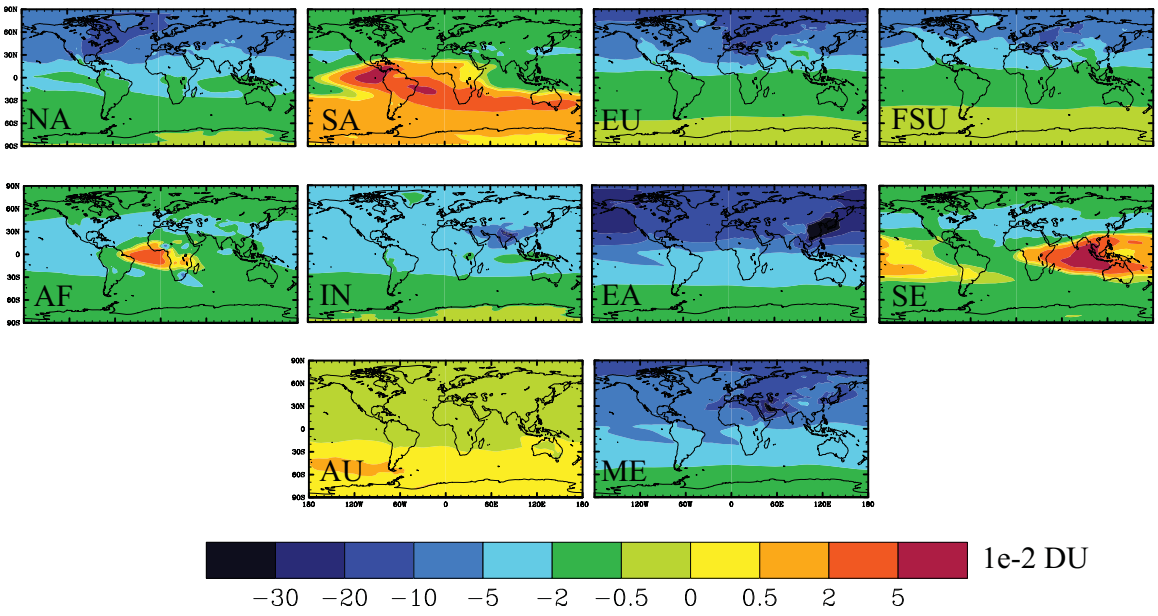

Figure 4.2. Global distribution of annual average changes in tropospheric total column O_3 at steady state (1e-2 DU) for each of the regional reduction simulations relative to the base.

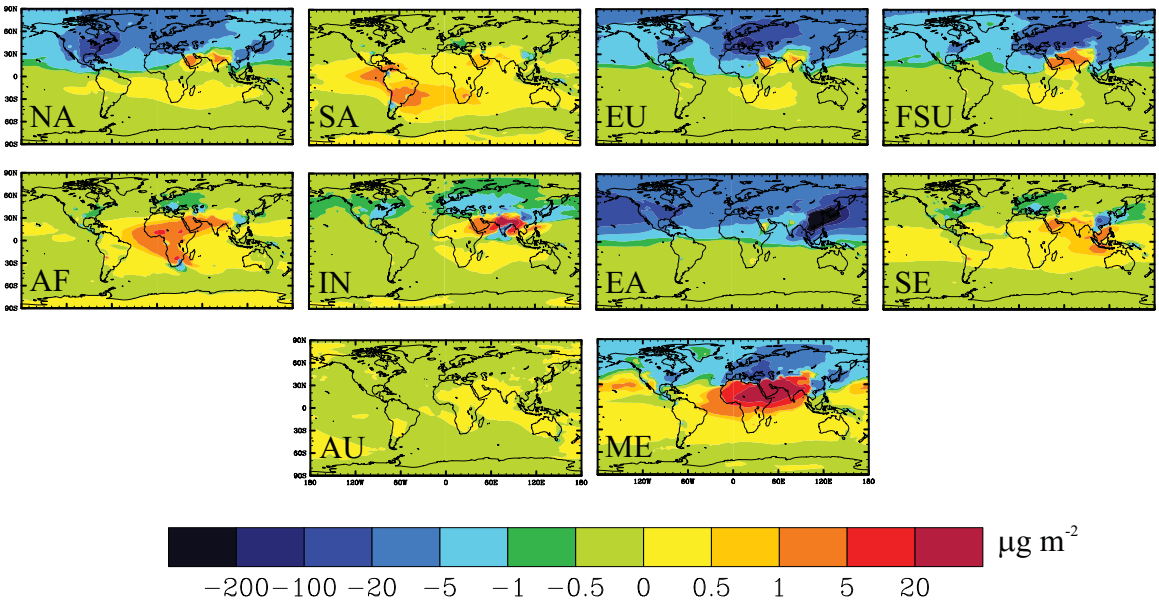

Figure 4.3. Global distribution of annual average changes in tropospheric total column SO_4^{2-} (μg m^{-2}) for each of the regional reduction simulations relative to the base.

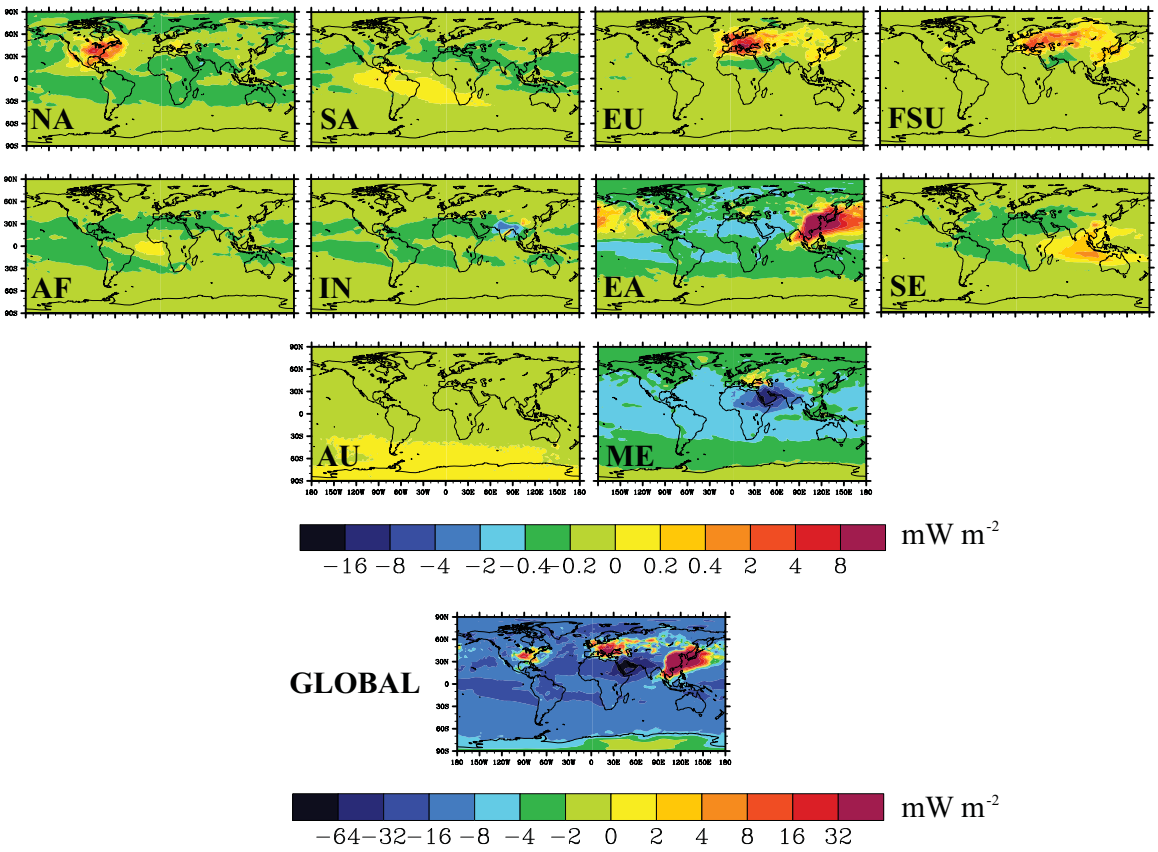

Figure 4.4. Annual average net RF distributions (mW m^{-2}) due to changes in tropospheric steady-state O_3, CH_4, and SO_4^{2-} for the regional and global NMVOC reduction simulations minus the base simulation.

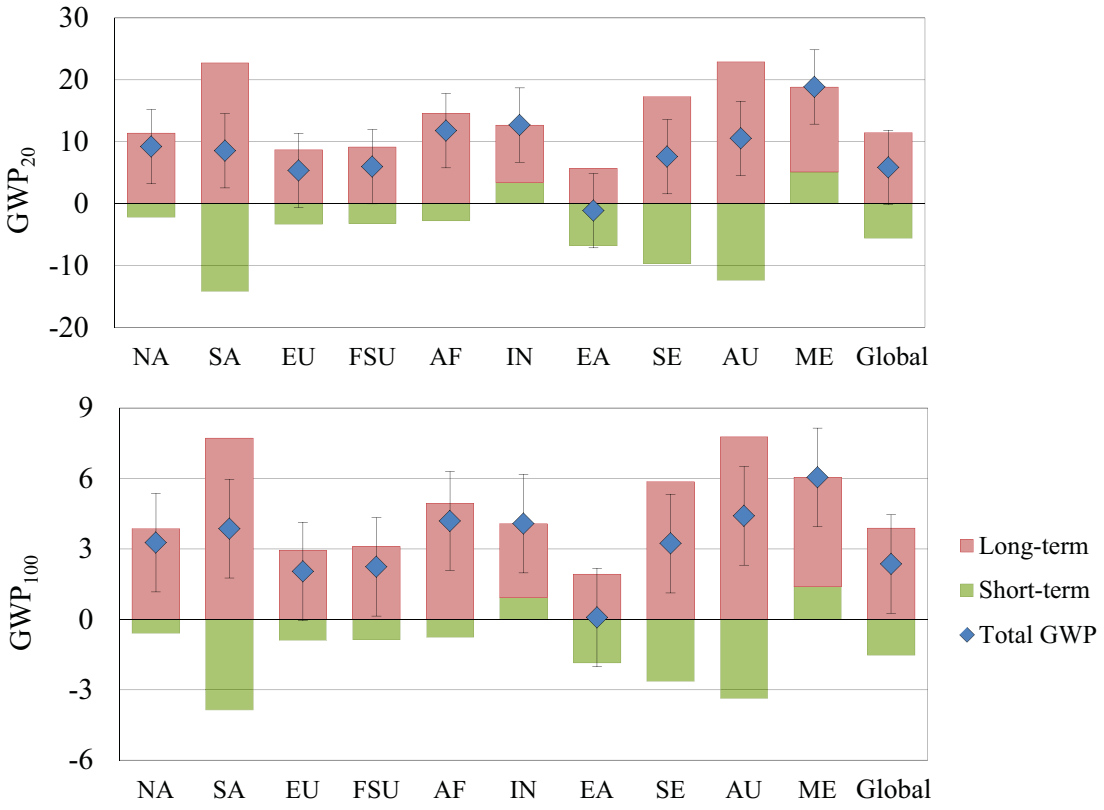

Figure 4.5. Global warming potentials for NMVOCs at time horizons of 20 and 100 years (GWP_{20}, GWP_{100}) for the regional and global reductions, with contributions from short-term (O_3 and SO_4^{2-}) and long-term (O_3 and CH_4) components, where total GWP is short-term + long-term. Uncertainty bars represent the average uncertainty found by Fry et al. (2012) based on the spread of atmospheric chemical models (±1 standard deviation).

Chapter 5. Conclusions

O_3 precursors influence climate and degrade air quality at regional to global scales. This dissertation builds upon previous studies by evaluating the impacts of O_3 precursors from various world regions, and across an ensemble of models. All three studies demonstrate that reducing anthropogenic O_3 precursor emissions can provide benefits by mitigating air pollution and global climate change in both the short and long term. Chapter 2 evaluates the impacts to tropospheric composition and RF from regional O_3 precursor reductions across an ensemble of models, and Chapters 3 and 4 analyze the air quality, tropospheric burden, and RF impacts of regional and global reductions in CO and NMVOC emissions. This chapter focuses on the key scientific findings, uncertainties, and future research needs from Chapters 2 to 4, as well as the implications for policy.

5.1 Scientific findings

Reducing O_3 precursor emissions can benefit air quality and climate by influencing secondary species: O_3, CH_4, and SO_4^{2-}, and atmospheric oxidants: OH and H_2O_2. Among the short-lived O_3 precursors, CO and NMVOC emission reductions most effectively mitigate climate warming (decreasing the tropospheric burdens of both CH_4 and O_3), while improving air quality. Regional CO and NMVOC emission reductions produce widespread cooling across the NH and SH due to large-scale O_3 and CH_4 decreases, and localized warming and cooling from SO_4^{2-} and regional O_3 changes. Reducing CH_4 also provides important benefits to global climate and air quality over a

longer timescale. Regional NO_x emission reductions alone can be detrimental to climate, producing warming in the opposite hemisphere of reduction, due to global CH_4 increases and thus, long-term O_3 (Chapter 2). Including the impact of O_3 on plant growth and the carbon cycle, however, may change the overall effect of NO_x reductions to a net climate cooling (Chapter 2).

The present day RF of CO and NMVOC emissions (anthropogenic and biomass burning) are estimated as 0.128 W m^{-2} and 0.0277 W m^{-2}, which are ~8.2% and ~1.8%, respectively, of the global RF of CO_2, and ~8.2% and ~1.8% of the RF due to short-lived forcing agents with the potential to slow climate change over the next few decades (CO, CH_4, NMVOCs, and BC). Based on the normalized net RF estimates, NO_x and NMVOC emission reductions from South Asia, the region closest to the tropics, provide the greatest global net RF per unit emission (Chapter 2). CO and NMVOC emission reductions from a greater number of regions (Chapters 3 and 4) also demonstrate that global net RF and tropospheric O_3 changes are more sensitive to emissions from the tropics and southern hemisphere, due to more active photochemistry and vertical convection in the tropics and greater CH_4 sensitivity. However, the RF and tropospheric O_3 impacts of CO vary much less among regions due to the longer lifetime of CO compared to NO_x and NMVOCs, allowing for more widespread influences. Some regional reductions (i.e. AU CO reduction, low-NO_x regions for NMVOC reductions) more effectively reduce global CH_4 than others, but there is substantial variability in tropospheric CH_4 changes for each precursor reduction, as estimated by the ensemble of 11 CTMs (Chapter 2). In addition, each of the O_3 precursors likely cause changes in regional climate that are not quantified as part of these studies.

Spatially, the impacts on O_3 at the surface and across the troposphere are greatest within the reduction region, and smaller intercontinentally to globally. Reducing global CH_4 by 20% produces the largest decrease in tropospheric O_3 globally. NO_x emission reductions result in overall decreases in tropospheric O_3 burden in the NH, yet slight increases in the SH due to long-term O_3 increases (via CH_4) (Chapter 2). CO and NMVOC emission reductions provide hemispheric to global decreases in tropospheric O_3, yet several NMVOC reductions (SA, AF, SE, and AU) increase tropospheric O_3 regionally to intercontinentally (Chapter 4). All of the regional NMVOC reductions slow the production of PAN, causing regional to hemispheric PAN decreases and regional NO_x increases. For the SA, AF, SE, and AU NMVOC reductions, a greater sensitivity to NO_x increases causes tropospheric O_3 to increase near or downwind of the region, outweighing the effect of NMVOC decreases.

At the surface, short-term and steady-state surface O_3 concentration changes are nearly proportional to the magnitude of CO and NMVOC emissions changes from each of the 10 regions (Chapters 3 and 4). Some regions can considerably influence the air quality in other regions such as EA CO and NMVOC emissions, which impact U.S. surface O_3 concentrations by 93% and 43%, respectively, of that from NA (CO and NMVOC) emissions. CO and NMVOC emission reductions can also impact air quality over large spatial scales. For all 10 regional CO reductions, more than 70% of global O_3 burden and production changes and more than 79% of global CO burden changes occur outside the reduction region. O_3 production changes outside of each reduction region greatly exceed changes in O_3 export from each region, suggesting that large scale O_3 impacts are mainly due to the transport of CO and subsequent production of O_3

downwind, rather than the transport of O_3 itself (Chapter 3). NMVOC emission reductions (excluding SA, AF, SE, and AU reductions) likewise have a greater impact on long-range O_3 through downwind O_3 production than the formation and export of O_3 from each reduction region (Chapter 4).

Aerosol changes at the surface are generally small, but tropospheric SO_4^{2-} changes show substantial variability and disagreement in the sign of change among the four CTMs evaluated in Chapter 2. This suggests that future research is needed to better model and understand aerosol-oxidant interactions. Across all three studies, tropospheric SO_4^{2-} changes are largest over the region of emissions change, with smaller changes intercontinentally. In general, OH increases contribute to increased SO_4^{2-} formation, particularly in drier regions and near the equator. H_2O_2 and O_3 decreases, on the other hand, contribute to decreased SO_4^{2-} formation, prevalent in the northern mid-latitudes. Reducing CH_4, CO, and NMVOCs increases and decreases tropospheric SO_4^{2-} by increasing OH (and H_2O_2), and decreasing O_3, respectively, while NO_x reductions decrease SO_4^{2-} by decreasing O_3, OH, and H_2O_2. The influence of O_3 precursors (via oxidant changes) on formation of other secondary aerosols (e.g. NO_3^- and SOA) is equally complex, and requires further research and improved model representation.

5.2 Uncertainties and future research

The design and development of future policies and emissions control strategies will require more information than can be presented in this dissertation. While these three studies were conducted mainly to evaluate the sensitivity of air quality and RF to different regions' individual O_3 precursor emissions, individual precursor reductions are likely infeasible to implement on regional to global scales. Future studies should

simulate more realistic emission control policies that address multiple pollutants together from common sources and sectors, or that combine our results with those of co-emitted pollutants to determine the net climate impact of specific emission control measures. These studies will likely require global three-dimensional chemistry-climate modeling to account for the complex interactions and nonlinear chemistry of co-emitted species (Fiore et al., 2012). More comprehensive studies could evaluate the climate impacts of long-lived greenhouse gases and short-lived climate forcers together, in both the near and long term. The net climate effects of specific emission control measures, however, are expected to change over time, with improvements and different applications.

The results presented here for individual species are consistent with the approach of the IPCC assessment reports, where the RF and GWP of individual emission species are provided as the basis for comparing and evaluating overall climate effects. Using methods similar to Shindell et al. (2012), priority emission control measures could be identified, ranking measures by their potential climate impact using the GWPs of each individual pollutant affected.

Emissions inventories are another large source of uncertainty in current modeling applications, as seen by the variability in emissions used by the CTMs (Chapter 2). Future work should consider improving the accuracy of modeled results with observations by further developing bottom-up emissions inventories, which rely on the accounting of emissions at their sources. Top-down (or inverse) methods, which utilize atmospheric measurements, could be used to further test and improve upon emissions estimates.

Global CTMs also greatly simplify atmospheric chemical mechanisms, such as by categorizing NMVOC species and streamlining various reaction pathways. The role of organic nitrates in recycling NO_x, affecting O_3 responses to biogenic VOC emissions, is not fully understood and is very uncertain in models (Fiore et al., 2012). There is also substantial variability in the simulated influence of O_3 precursor emissions on oxidants, O_3, and CH_4 across the CTM ensemble (Chapter 2), which may be due in part to the different models' meteorological inputs affecting the chemical production and lifetimes of short-lived species (Unger et al., 2012). Results from the CTM ensemble (Chapter 2) also suggest large uncertainties in aerosol-oxidant interactions, the role of the different oxidation pathways, and the lifetime and removal of SO_2 and SO_4^2 among models. MOZART-4, used in Chapters 3 and 4, is an updated model including an expanded chemical mechanism with detailed hydrocarbon chemistry and bulk aerosols, and improved online calculation of dry deposition, isoprene and monoterpene emissions, and photolysis frequencies (Emmons et al., 2010).

RF estimates derived here from the current version of the RTM are also uncertain, as they only account for tropospheric O_3, CH_4, and SO_4^{2-} changes. Future applications of the standalone RTM should consider updates to include additional forcing components such as changes in NO_3^-, SOA, stratospheric O_3, water vapor, and the carbon cycle via O_3 and nitrogen deposition. The RTM also does not presently account for the internal mixing of aerosols or the indirect effect of aerosols on clouds. With these additional forcing components, the RF and GWP of O_3 precursors from different regional sources will likely change, both in magnitude and relative to other regions. The variability in the RF and GWP among regions may increase, given that the importance of these forcings

can vary across regions, such as NO_3^- and SOA-derived forcings, which are influenced by regional chemical states and oxidation chemistry.

A fully coupled chemistry-climate model, such as the NOAA GFDL CM3, which includes an improved atmospheric component, AM3 (Donner et al., 2011), could be used in place of running a global CTM and RTM together. AM3 includes new treatments of cloud-aerosol interactions, interactive tropospheric and stratospheric chemistry, and emissions driving atmospheric chemistry and aerosols through advective, convective, and turbulent transport (Donner et al., 2011). Using CM3 would allow for an evaluation of the air quality and full climate responses due to emissions changes, including changes in surface temperature and precipitation. A fully coupled model may also account for the effects of physical climate changes (i.e. temperature, humidity, and precipitation) on biogenic emissions (e.g. isoprene), shifts in vegetation distributions over time (due to climate change and/or anthropogenic activities), and stratosphere-troposphere exchanges (Unger et al., 2006). Emissions changes over time or in a future year could be examined, as O_3 precursor emissions are expected to change with increased industrialization, new emissions controls, and population growth. Simulations could also be run for longer than 1.5 years and without fixing global CH_4 concentrations and meteorology. This would allow for the role of changing meteorology on climate and air quality to be studied, given that climate variables – temperature, humidity, precipitation, clouds, and convection all impact tropospheric O_3, CH_4, and SO_4^{2-} lifetimes and distributions (Unger et al., 2006). However, coupled chemistry-climate model simulations can be more computationally intensive than using a single offline global CTM and RTM.

Using the results of Shindell et al. (2012), future work could also focus on identifying the technical and regulatory emissions control measures that are most practical to implement in each region of the world, determining their effectiveness based on climate, air quality, human health, and agriculture benefits. An integrated assessment model (e.g. ObjECTS GCAM or IIASA MESSAGE) also could be applied in future studies to estimate the potential benefits of domestic and international climate policies and technology implementation strategies.

5.3 Policy implications

While several studies have investigated the impacts of regional short-lived O_3 precursor emissions on air quality and RF (Fuglestvedt et al., 1999; Wild et al, 2001; Berntsen et al., 2005; Naik et al., 2005), this dissertation offers results from a greater number of regions and across an ensemble of models. Because emissions from Asia, Africa, and South America are expected to rise over the next few decades (Akimoto, 2003), interest in assessing these countries' contributions, in particular, is growing and must be better understood before short-lived species can be considered in a comprehensive treaty. Actions to reduce O_3 and its precursors would also benefit human health and ecosystems, which may further motivate countries to undertake air quality and climate change mitigation programs and participate in joint climate agreements (Naik et al., 2005).

Examining the air quality and climate impacts of regional O_3 precursor emissions may support the inclusion of O_3 precursors in a comprehensive climate treaty, similar to the Kyoto Protocol, which uses GWPs to compare the climate change contribution of various greenhouse gas emissions over time. The 20 and 100-year GWPs calculated in

these three studies allow for the climate impacts of O_3 precursors to be compared to other species. A single global GWP for CO, for example, could be applied in a future international climate agreement or emissions trading mechanism among a suite of long-lived greenhouse gases, while NO_x and NMVOCs likely require different GWPs for each continent. For CO, the uncertainty in the global GWP is greater than the range in GWPs among regions, while the reverse is true for NMVOCs (Chapters 3 and 4).

The GWPs of regional O_3 precursor emissions also could be used, along with those of co-emitted species, to assess and identify the most effective emission control measures to implement in different regions of the world for maximum climate benefits (Shindell et al., 2012). Using satellite observations and adjoint modeling methods, grid-cell based RF sensitivities of O_3 precursor emissions also could provide insight into the design and implementation of effective policies and control measures (Bowman and Henze, 2012). We acknowledge that GWPs are imperfect and are only one indicator of climate impacts; they do not account for the rate of climate change or the sensitivity of climate responses (i.e. surface temperature, precipitation, and circulation) to RF distributions or RF location (Shindell et al., 2009).

We expect that short-lived species will continue to be regulated by local to regional scale policies aimed at improving air quality, but their effects should also be considered in future climate agreements (Shindell et al., 2009). Unlike long-lived greenhouse gases, short-lived climate forcers provide an opportunity to address near-term climate change with simultaneous benefits to human and ecosystem health. However, reductions in short-lived cooling agents (e.g. SO_4^{2-}) will need to be coordinated with long-lived greenhouse gas reductions to avoid potential warming surges from long-lived

greenhouse gases that have yet to be realized (Unger et al., 2012). Ultimately, policymakers will need to base their decisions on both long and short-lived species, when considering climate change impacts, costs, and feasibility (Unger et al., 2008; 2010).

Less attention has been given to the specific actions needed to maximize the climate and air quality benefits from reducing O_3 precursor emissions. The United Nations Environment Programme (UNEP) recently analyzed the climate, health, and air quality benefits from implementing control measures targeting BC and CH_4 emissions (UNEP, 2011). Building upon this analysis, Shindell et al. (2012) estimated that the global implementation of 14 of these measures (both technical and regulatory) to the maximum extent possible by 2030 would reduce global mean warming by ~0.5˚C (by 2050), decrease annual premature deaths by 0.7 to 4.7 million, increase annual crop yield by 30 to 135 million metric tons, and achieve nearly 90% of the maximum reduction in net GWP. Seven (of the 14) measures from Shindell et al. (2012) target emissions from the incomplete combustion of carbon fuels, including the O_3 precursors evaluated here (CH_4, NO_x, CO, and NMVOCs) in addition to BC, OC, SO_2, ammonia (NH_3), and $PM_{2.5}$.

While Shindell et al. (2012) estimated the benefits to near-term climate, human health, and agriculture from global implementation, this dissertation and the methods developed herein could provide a way to evaluate the benefits to RF and air quality from the regional implementation of a given set of control measures. As we have demonstrated, the climate and air quality impacts of O_3 precursors vary by location, and therefore, each region may require different mixes of control measures to achieve the maximum benefit.

Beyond this dissertation, further integrated analyses of the costs and benefits of reducing O_3 precursor emissions as part of climate and air pollution control policies are warranted (Dentener et al., 2006). By including O_3 precursors in a joint climate agreement or coordinated climate and air quality policies, we may find a greater incentive to reduce them in the future, and could lower the costs of meeting climate goals.

Appendix A. The influence of ozone precursor emissions from four world regions on tropospheric composition and radiative climate forcing: Supporting material

Table A1. Global annual net RF (mW m^{-2}) for the multimodel mean, corresponding to Figure 2.7a in the text. CO_2 RF is shown for high and low sensitivity of vegetation to O_3, and the global annual net RF including CO_2 RFs is shown in the last two columns. The 4 regions estimates represent the sum of the net RFs from all 4 regions; these estimates are not directly estimated using the RTM and are not presented in Figure 2.7a.

Simulation	Net RF (O_3, CH_4, SO_4^{2-})	Net RF (O_3)	Net RF (CH_4)	Net RF (SO_4^{2-})	Net RF (CO_2 high sens.)	Net RF (CO_2 low sens.)	Net RF (O_3, CH_4, SO_4^{2}, CO_2 high sens.)	Net RF (O_3, CH_4, SO_4^{2}, CO_2 low sens.)
-20% CH_4 burden	-162.6	-26.8	-137.2	1.48	-	-	-	-
-20% NO_x EA	0.21	-2.58	2.94	-0.15	-3.78	-2.90	-3.57	-2.69
-20% NO_x EU	1.72	-1.19	2.38	0.53	-6.00	-4.02	-4.28	-2.30
-20% NO_x NA	0.63	-3.19	3.98	-0.16	-4.34	-2.83	-3.71	-2.20
-20% NO_x SA	0.77	-1.75	2.29	0.23	-2.36	-1.60	-1.59	-0.83
-20% NO_x 4 regions	3.33	-8.71	11.6	0.45	-	-	-	-
-20% NMVOC EA	-1.30	-1.07	-0.51	0.28	-1.55	-1.22	-2.85	-2.52
-20% NMVOC EU	-1.74	-0.97	-0.74	-0.03	-2.80	-1.74	-4.54	-3.48
-20% NMVOC NA	-1.28	-0.93	-0.54	0.19	-1.71	-1.07	-2.99	-2.35
-20% NMVOC SA	-1.39	-0.73	-0.66	0.00	-0.68	-0.39	-2.07	-1.78
-20% NMVOC 4 regions	-5.71	-3.70	-2.45	0.44	-	-	-	-
-20% CO EA	-3.67	-1.72	-2.23	0.29	-0.88	-0.57	-4.55	-4.24
-20% CO EU	-2.01	-0.80	-1.26	0.05	-0.84	-0.51	-2.85	-2.52
-20% CO NA	-2.90	-1.30	-1.80	0.21	-1.01	-0.60	-3.91	-3.50
-20% CO SA	-2.35	-1.14	-1.26	0.06	-0.49	-0.27	-2.84	-2.62
-20% CO 4 regions	-10.9	-4.96	-6.55	0.61	-	-	-	-
-20% combined EA	-	-5.02	-0.13	-	-	-	-	-
-20% combined EU	-	-2.86	-0.17	-	-	-	-	-
-20% combined NA	-	-5.05	1.23	-	-	-	-	-
-20% combined SA	-	-3.42	0.22	-	-	-	-	-
-20% combined 4 regions	-	-16.4	1.15	-	-	-	-	-

Table A2. GWPs for 20- and 100-year time horizons for O_3 precursor emissions, corresponding to Figure 2.10 in the text. The O_3 and SO_4^{2-} contributions include both short- and long-term effects. The 4 regions estimates represent the GWP due to the sum of the four regions' responses (to O_3, CH_4, SO_4^{2-}, and all three species [Total]). Uncertainty analysis is as in Figure 2.7, but also includes the uncertainty in the CH_4 lifetimes for the base simulation (SR1).

	GWP_{20}				
	O_3	CH_4	SO_4^{2-}	Total	Uncertainty
-20% CH_4 burden	10.5	50.9	-0.6	60.8	6.4
-20% NO_x EA	95.1	-85.1	6.2	16.1	21.0
-20% NO_x EU	35.8	-54.7	-14.2	-33.1	14.9
-20% NO_x NA	93.4	-90.9	5.5	8.0	28.2
-20% NO_x SA	165.0	-167.8	-18.6	-21.4	69.9
-20% NO_x 4 regions	82.4	-85.5	-3.1	-6.1	26.1
-20% NMVOC EA	13.8	5.6	-3.7	15.7	5.0
-20% NMVOC EU	10.4	6.6	0.2	17.2	7.1
-20% NMVOC NA	12.0	6.0	-2.6	15.5	6.8
-20% NMVOC SA	15.1	11.6	-0.1	26.5	5.3
-20% NMVOC 4 regions	12.5	7.0	-1.6	17.9	6.1
-20% CO EA	2.6	2.9	-0.5	5.1	1.6
-20% CO EU	2.0	2.7	-0.2	4.6	1.3
-20% CO NA	2.6	3.1	-0.5	5.2	1.6
-20% CO SA	2.9	2.7	-0.2	5.3	1.2
-20% CO 4 regions	2.5	2.9	-0.4	5.1	1.4

	GWP_{100}				
	O_3	CH_4	SO_4^{2-}	Total	Uncertainty
-20% CH_4 burden	3.6	17.5	-0.2	20.9	3.7
-20% NO_x EA	25.6	-29.3	1.8	-1.9	8.7
-20% NO_x EU	9.3	-18.8	-3.9	-13.4	6.0
-20% NO_x NA	25.1	-31.3	1.6	-4.6	10.9
-20% NO_x SA	44.2	-57.8	-5.1	-18.7	25.9
-20% NO_x 4 regions	22.0	-29.4	-0.8	-8.2	10.2
-20% NMVOC EA	4.0	1.9	-1.0	4.8	1.7
-20% NMVOC EU	3.0	2.3	0.1	5.3	2.5
-20% NMVOC NA	3.5	2.1	-0.7	4.8	2.4
-20% NMVOC SA	4.4	4.0	0.0	8.3	1.9
-20% NMVOC 4 regions	3.6	2.4	-0.4	5.5	2.1
-20% CO EA	0.8	1.0	-0.1	1.6	0.5
-20% CO EU	0.6	0.9	0.0	1.5	0.4
-20% CO NA	0.8	1.1	-0.1	1.7	0.5
-20% CO SA	0.8	0.9	-0.1	1.7	0.4
-20% CO 4 regions	0.8	1.0	-0.1	1.6	0.5

Table A3. Global annual net RF (mW m^{-2}) estimates from additional RTM simulations: 1) multimodel mean +1SD O_3 and multimodel mean +1SD CH_4; 2) multimodel mean -1SD O_3 and multimodel mean -1SD CH_4; 3) multimodel mean O_3, multimodel mean CH_4, and multimodel mean +1SD SO_4^{2-}.

Simulation: Mean +1SD O_3, Mean +1SD CH_4	Net RF (O_3, CH_4)	Net RF (O_3)	Net RF (CH_4)
-20% CH_4 burden	-165.9	-28.7	-137.2
-20% NO_x EA	1.01	-2.56	3.57
-20% NO_x EU	1.76	-1.21	2.97
-20% NO_x NA	1.78	-3.30	5.08
-20% NO_x SA	1.50	-1.69	3.19
-20% NMVOC EA	-1.03	-0.95	-0.08
-20% NMVOC EU	-0.81	-0.85	0.04
-20% NMVOC NA	-0.85	-0.91	0.07
-20% NMVOC SA	-1.03	-0.63	-0.39
-20% CO EA	-3.51	-2.24	-1.27
-20% CO EU	-1.69	-0.94	-0.74
-20% CO NA	-2.63	-1.60	-1.03
-20% CO SA	-2.22	-1.38	-0.84
-20% combined EA	-4.13	-5.23	1.10
-20% combined EU	-2.09	-2.80	0.71
-20% combined NA	-2.90	-5.13	2.23
-20% combined SA	-2.33	-3.34	1.01

Simulation: Mean -1SD O_3, Mean -1SD CH_4	Net RF (O_3, CH_4)	Net RF (O_3)	Net RF (CH_4)
-20% CH_4 burden	-162.0	-24.8	-137.2
-20% NO_x EA	-0.30	-2.61	2.31
-20% NO_x EU	0.63	-1.18	1.80
-20% NO_x NA	-0.20	-3.09	2.89
-20% NO_x SA	-0.44	-1.83	1.39
-20% NMVOC EA	-2.14	-1.20	-0.94
-20% NMVOC EU	-2.63	-1.12	-1.51
-20% NMVOC NA	-2.10	-0.95	-1.14
-20% NMVOC SA	-1.77	-0.84	-0.92
-20% CO EA	-4.36	-1.17	-3.19
-20% CO EU	-2.43	-0.64	-1.79
-20% CO NA	-3.55	-0.97	-2.58
-20% CO SA	-2.58	-0.89	-1.69
-20% combined EA	-6.17	-4.81	-1.36
-20% combined EU	-3.98	-2.93	-1.04
-20% combined NA	-4.73	-4.97	0.24
-20% combined SA	-4.10	-3.52	-0.58

Simulation: Mean O_3, Mean CH_4, Mean +1SD SO_4^{2-}	Net RF (O_3, CH_4, SO_4^{2-})	Net RF (O_3)	Net RF (CH_4)	Net RF (SO_4^{2-})
-20% CH_4 burden	-159.4	-26.9	-137.2	4.65
-20% NO_x EA	-0.43	-2.58	2.94	-0.79
-20% NO_x EU	2.13	-1.19	2.38	0.93
-20% NO_x NA	0.22	-3.19	3.98	-0.57
-20% NO_x SA	0.54	-1.75	2.29	0.00
-20% NMVOC EA	-1.30	-1.07	-0.51	0.28
-20% NMVOC EU	-1.75	-0.97	-0.74	-0.04
-20% NMVOC NA	-1.33	-0.93	-0.54	0.14
-20% NMVOC SA	-1.50	-0.73	-0.66	-0.11
-20% CO EA	-3.44	-1.72	-2.23	0.51
-20% CO EU	-1.95	-0.80	-1.26	0.11
-20% CO NA	-2.84	-1.30	-1.80	0.26
-20% CO SA	-2.35	-1.14	-1.26	0.06
-20% combined EA	-	-	-	-
-20% combined EU	-	-	-	-
-20% combined NA	-	-	-	-
-20% combined SA	-	-	-	-

Table A4. Regional annual average net RF (mW m^{-2}) for the multimodel mean for each of the precursor reduction simulations. The greatest net RF for each precursor-source region pair is in bold, with the caveat that RFs over source regions (vs. over receptor regions) may be lower due to combining the effects of positive and negative RFs from local changes in O_3 and SO_4^{2-}. Regional net RFs do not translate to regional climate responses.

		Receptor region			
	Source region	EA	EU	NA	SA
-20% NO_x	EA	**-5.36**	-1.57	-2.38	-1.99
	EU	0.71	0.60	0.56	**3.41**
	NA	0.05	-7.72	**-9.07**	1.60
	SA	**-2.57**	-0.32	-0.07	-0.22
-20% NMVOC	EA	-0.14	-2.13	-2.02	**-2.27**
	EU	-2.27	-2.83	-2.16	**-3.55**
	NA	-1.01	**-2.73**	-2.10	-1.84
	SA	-1.88	-1.73	-1.39	**-5.80**
-20% CO	EA	-5.26	-4.27	-4.01	**-5.86**
	EU	-2.08	**-3.41**	-2.08	-3.33
	NA	-2.87	-3.87	**-4.36**	-4.14
	SA	-3.01	-2.73	-2.42	**-7.08**
-20% Combined	EA	**-15.66**	-8.00	-8.38	-9.50
	EU	-5.07	**-10.58**	-4.18	-4.65
	NA	-4.49	-13.76	**-16.96**	-3.96
	SA	-7.28	-4.56	-3.85	**-18.72**

Table A5. Global annual average changes in full tropospheric O_3 burden (Tg) at steady state for the 11 CTMs, for each precursor reduction scenario (-20% CH_4 burden, and -20% regional emissions of NO_x, NMVOC, CO, and combined).

	Source region	CAMCHEM-3311m13	FRSGCUCI-v01	GISS-PUCCINI-modelE	GMI-v02f	INCA-vSSz	LLNL-IMPACT-T5a
20% CH_4 burden		-8.60	-12.60	-10.86	-11.59	-8.14	-17.29
20% NO_x	EA	-0.91	-0.55	-0.62	-0.71	-0.75	-0.67
	EU	-0.67	-0.44	-0.22	-0.55	-0.54	-0.56
	NA	-1.32	-0.62	-0.50	-1.14	-0.96	-1.13
	SA	-0.41	-0.30	-0.24	-0.44	-0.36	-0.72
20% NMVOC	EA	-0.21	-0.68	-0.14	-0.38	-0.30	-0.04
	EU	-0.59	-0.78	-0.08	-0.15	-0.35	-0.10
	NA	-0.29	-0.60	-0.08	-0.31	-0.40	-0.05
	SA	-0.16	-0.36	-0.11	-0.24	--	-0.03
20% CO	EA	-0.58	-0.49	-0.90	-0.87	-0.33	-0.40
	EU	-0.22	-0.28	-0.36	-0.38	-0.17	-0.24
	NA	-0.36	-0.47	-0.61	-0.52	-0.18	-0.31
	SA	-0.33	-0.30	-0.36	-0.42	-0.23	-0.46
20% Combined	EA	-1.51	-1.69	-1.58	-1.85	-1.37	-1.86
	EU	-1.32	-1.47	-0.66	-1.05	-1.04	-1.66
	NA	-1.79	-1.67	-1.13	-1.87	-1.57	-2.07
	SA	-0.80	-0.96	-0.58	-1.08	-0.76	-2.02

	Source region	MOZARTGFDL-v2	MOZECH-v16	STOC-HadAM3-v01	TM5-JRC-cy2-ipcc-v1	UM-CAM-v01
20% CH_4 burden		-16.35	-9.10	-10.10	-12.15	-8.61
20% NO_x	EA	-0.50	-0.81	-0.50	-0.46	-0.98
	EU	-0.36	-0.57	-0.58	-0.27	-0.72
	NA	-0.82	-1.18	-0.81	-0.59	-1.32
	SA	-0.31	-0.44	-0.35	-0.11	-0.78
20% NMVOC	EA	-0.20	-0.45	-0.45	-0.58	-0.58
	EU	-0.28	-0.55	-0.64	-0.49	-0.64
	NA	-0.19	-0.69	-0.40	-0.56	-0.38
	SA	-0.17	-0.25	-0.27	-0.28	-0.31
20% CO	EA	-0.36	-0.48	-0.40	-0.42	-0.44
	EU	-0.35	-0.31	-0.25	-0.16	-0.28
	NA	-0.34	-0.46	-0.39	-0.54	-0.41
	SA	-0.24	-0.36	-0.25	-0.22	-0.29
20% Combined	EA	-0.89	-1.53	-1.32	-1.29	-1.95
	EU	-0.80	-1.19	-1.44	-1.06	-1.62
	NA	-1.17	-1.88	-1.58	-1.58	-2.14
	SA	-0.65	-0.91	-0.80	-0.63	-1.41

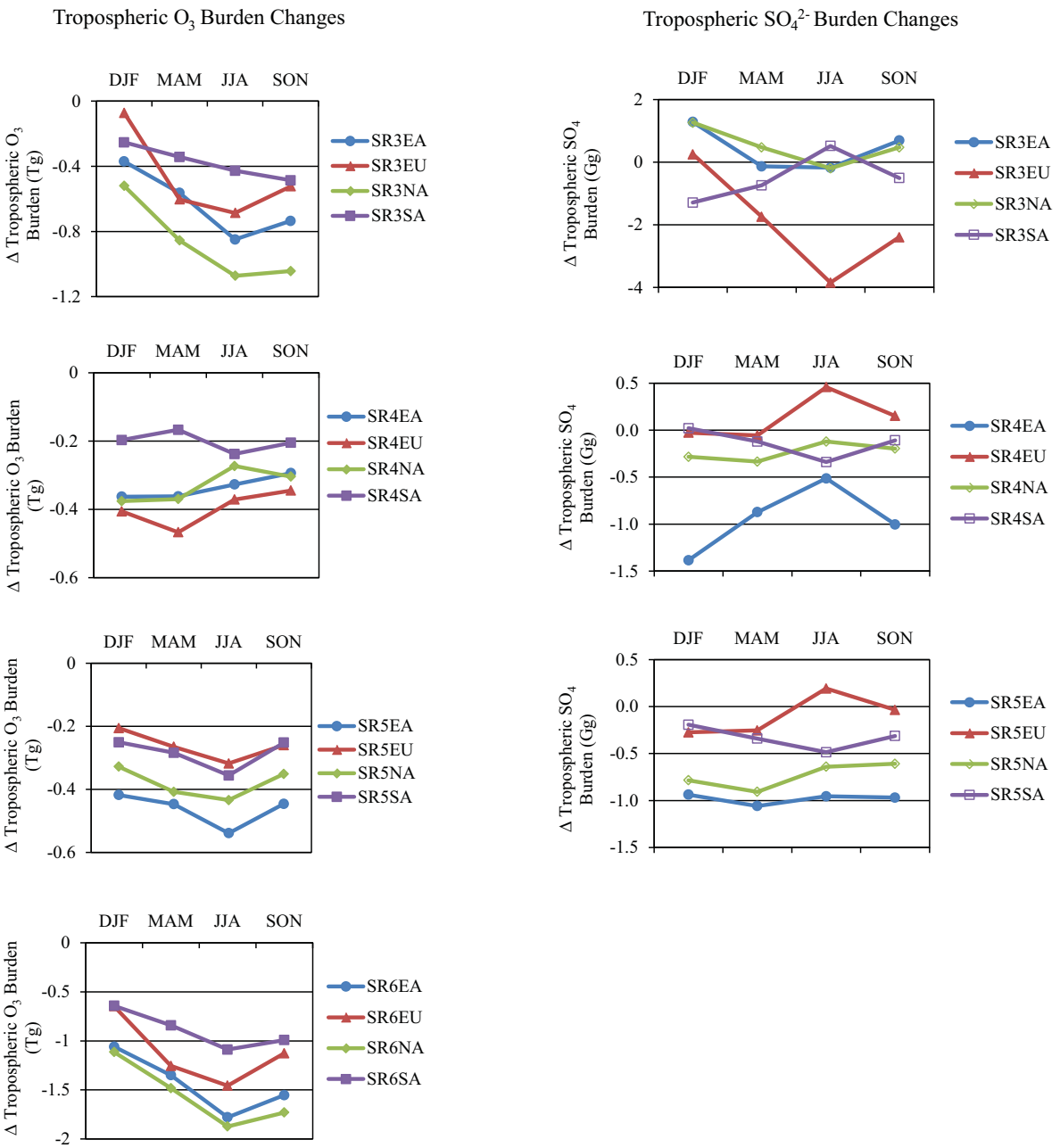

Figure A1. Seasonality of global annual average, ensemble mean tropospheric O_3 (at steady state) and SO_4^{2-} burden changes (perturbation minus base), for 11 and 4 HTAP models, respectively.

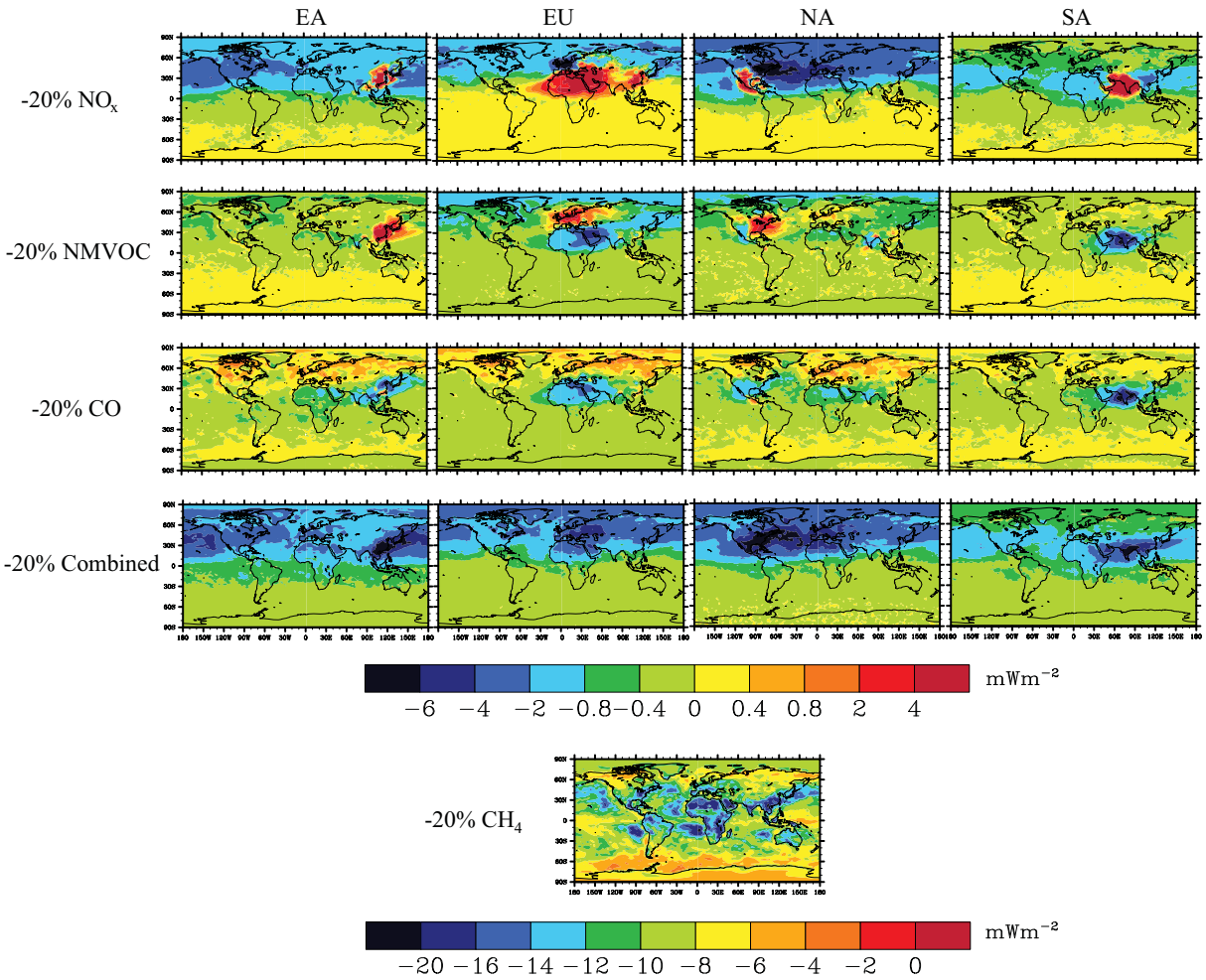

Figure A2. Annual average shortwave (solar) radiation distributions (mW m^{-2}) due to tropospheric O_3 (at steady state), CH_4, and SO_4^{2-} for the multimodel mean, for each of the precursor reduction simulations (-20% CH_4 burden and -20% regional emissions of NO_x, NMVOC, CO, and combined) minus the base simulation.

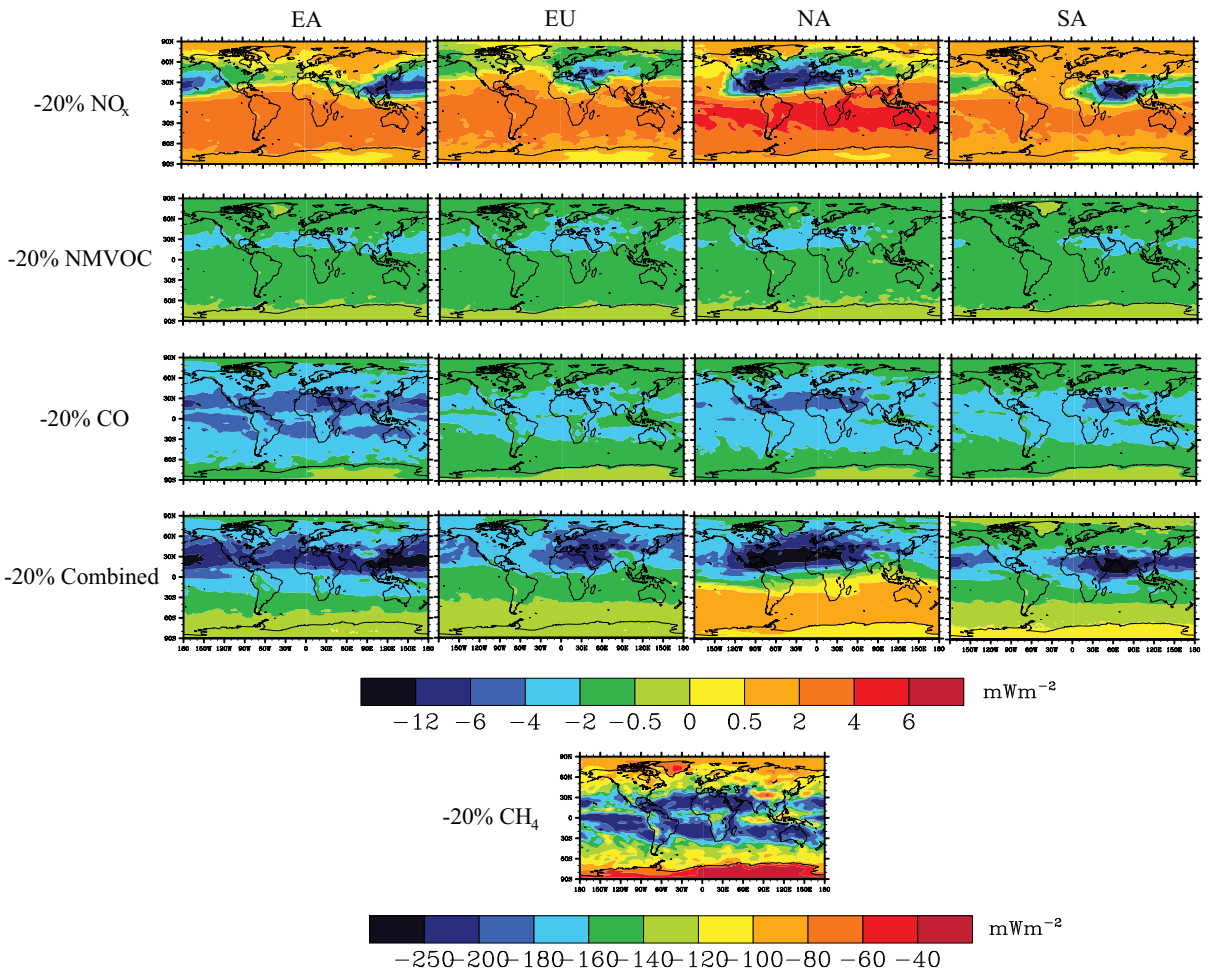

Figure A3. Annual average longwave (infrared) radiation distributions (mW m^{-2}) due to tropospheric O_3 (at steady state), CH_4, and SO_4^{2-} for the multimodel mean, for each of the precursor reduction simulations (-20% CH_4 burden and -20% regional emissions of NO_x, NMVOC, CO, and combined), where positive values correspond to a positive RF.

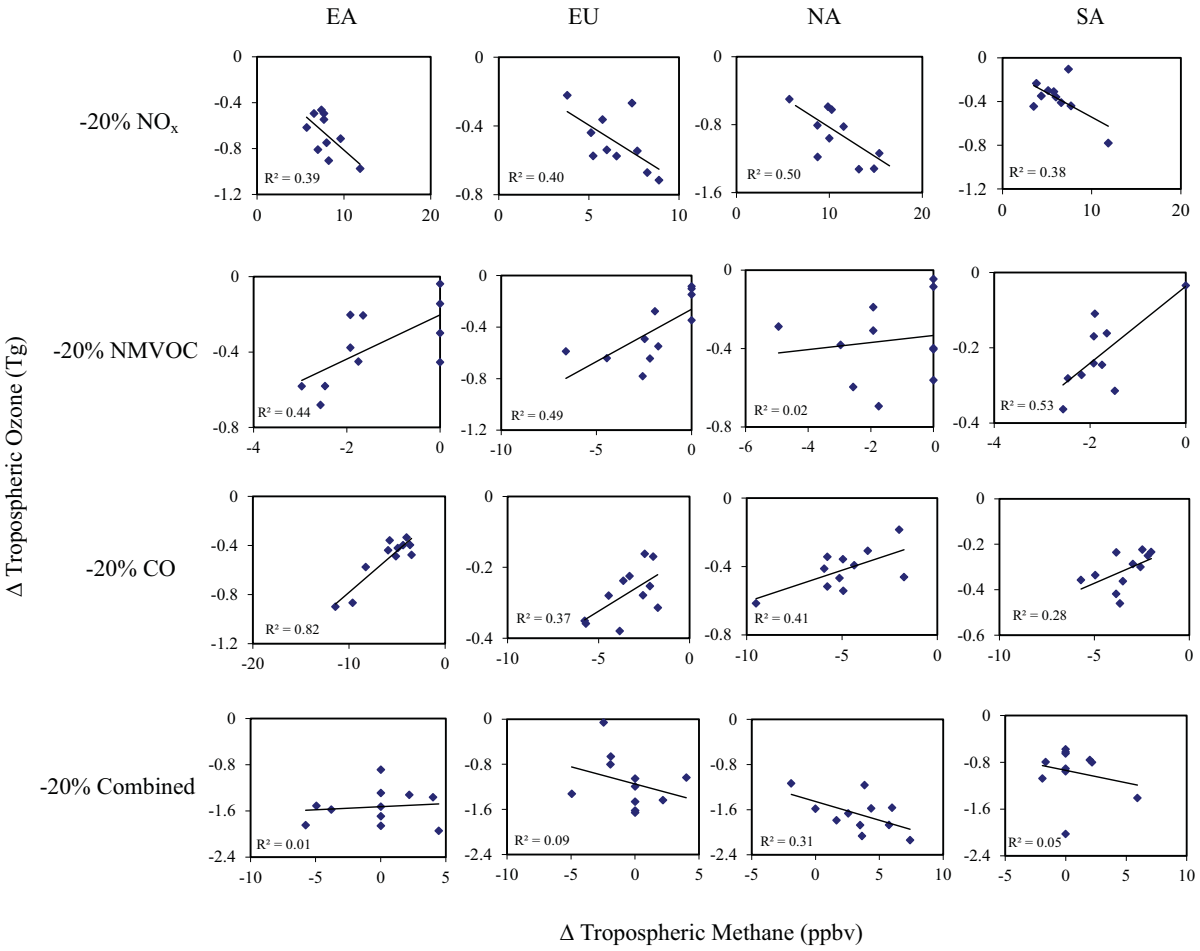

Figure A4. Global annual average changes in steady-state tropospheric O_3 burden (Tg) versus global annual average changes in tropospheric CH_4 concentration (ppbv) for the 11 HTAP models, showing the 16 SR simulations (-20% regional emissions of NO_x, NMVOC, CO, and combined, SR3 to SR6) relative to the base (SR1).

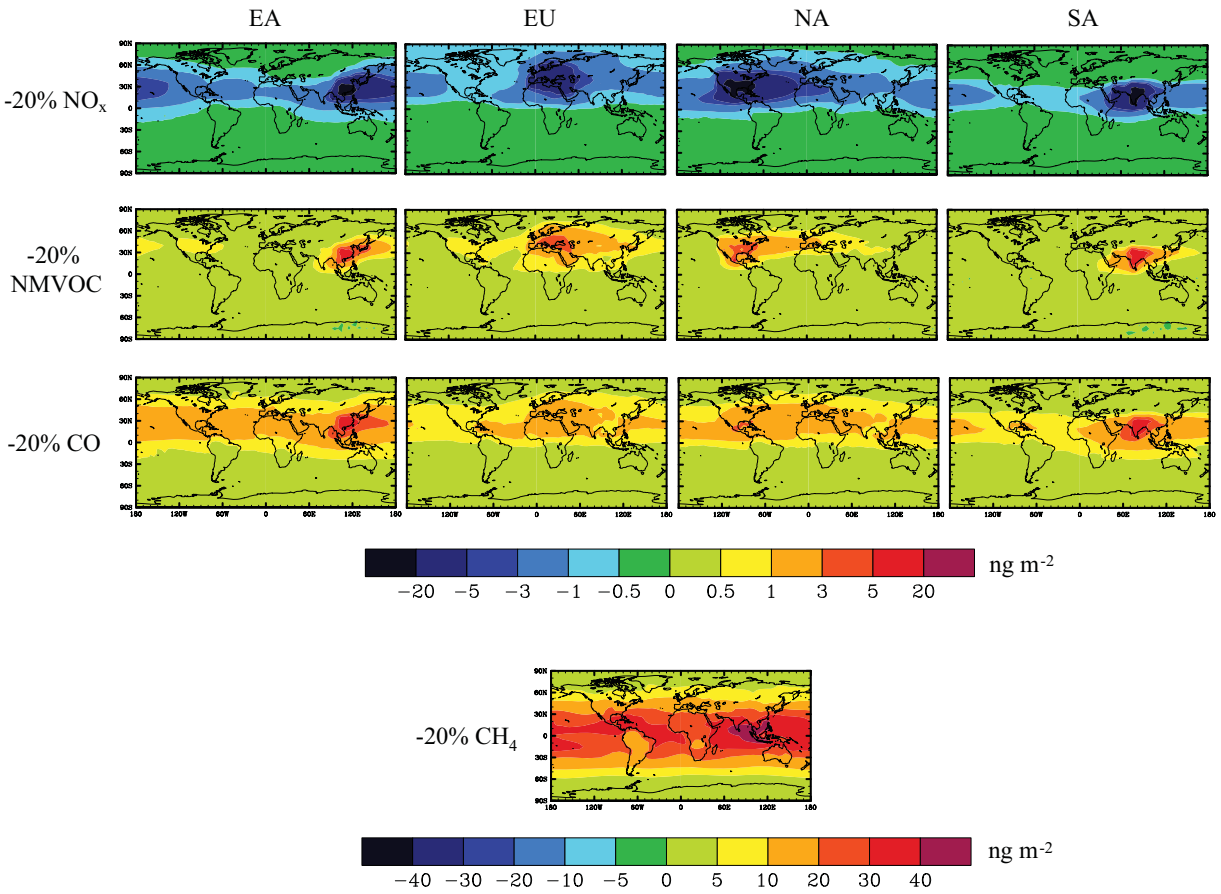

Figure A5. Annual average tropospheric total column OH burden changes (ng m^{-2}) for the multimodel mean of 4 HTAP models for -20% CH_4 burden and -20% regional emissions of NO_x, NMVOC, and CO scenarios.

Appendix B. Net radiative forcing and air quality responses to regional CO emission reductions: Supporting material

Table B1. Base simulated tropospheric OH burdens (labeled OH) compared to tropospheric OH burdens of Spivakovsky et al. (2000) (labeled OH-S), Lawrence et al. (1996) (labeled OH-L1), Lawrence et al. (1999) (labeled OH-L2), von Kuhlmann (2001) (labeled OH-V), and Emmons et al. (2010) (labeled OH-E) in 1e6 OH molecules cm^{-3}.

Region	OH	OH-S	OH-L1	OH-L2	OH-V	OH-E
Surface-750 hPa						
90°S - 30°S	0.43	0.47	0.44	0.35	0.51	0.42
30°S - 0°	1.11	1.44	1.56	1.30	1.51	1.25
0° - 30°N	1.35	1.52	1.86	1.52	1.76	1.37
30°N - 90°N	0.81	0.76	0.86	0.79	0.86	0.77
750 - 500 hPa						
90°S - 30°S	0.46	0.72	0.56	0.36	0.46	0.53
30°S - 0°	1.15	2.00	1.65	1.20	1.48	1.39
0° - 30°N	1.41	1.99	1.94	1.37	1.61	1.59
30°N - 90°N	0.67	0.88	0.91	0.65	0.72	0.72
500 - 250 hPa						
90°S - 30°S	0.40	0.64	0.65	0.37	0.36	0.54
30°S - 0°	0.80	1.43	1.55	1.04	0.82	1.05
0° - 30°N	1.05	1.36	1.76	1.15	0.96	1.26
30°N - 90°N	0.59	0.64	0.95	0.59	0.52	0.72

Table B2. Base simulated tropospheric CH_4 loss by reaction with OH (%) compared to Fiore et al. (2008).

Region	Base CH_4 loss by OH (%)	CH_4 loss by OH (%) (Fiore et al., 2008)
Surface-750 hPa		
90°S - 30°S	4.7%	4.4%
30°S - 0°	15.5%	18.9%
0° - 30°N	19.6%	23.6%
30°N - 90°N	9.7%	9.8%
Total	49.4%	56.7%
750 - 500 hPa		
90°S - 30°S	3.7%	3.2%
30°S - 0°	12.0%	11.3%
0° - 30°N	14.6%	13.1%
30°N - 90°N	5.8%	5.3%
Total	36.1%	32.9%
500 - 250 hPa		
90°S - 30°S	1.5%	1.2%
30°S - 0°	4.5%	3.4%
0° - 30°N	6.0%	4.0%
30°N - 90°N	2.5%	1.8%
Total	14.5%	10.4%

Table B3. Source-receptor matrix of annual average surface CO concentration changes per unit change in CO emissions (pptv CO (Tg CO $yr^{-1})^{-1}$), for the regional reduction simulations, with the US also defined as a receptor in addition to the 10 regions. The largest changes for each source reduction region are in bold.

	Receptor										
Source	NA	SA	EU	FSU	AF	IN	EA	SE	AU	ME	US
NA	-358	-19.8	-130	-116	-38.3	-50.0	-93.6	-33.4	-9.1	-96.0	**-552**
SA	-15.7	**-310**	-10.4	-10.4	-45.4	-25.7	-14.1	-37.0	-67.9	-14.6	-12.6
EU	-149	-20.0	**-1174**	-318	-63.0	-54.8	-164	-40.1	-8.3	-250	-139
FSU	-187	-16.8	-335	**-886**	-43.1	-62.8	-270	-45.1	-7.7	-185	-172
AF	-24.3	-56.9	-20.0	-20.0	**-235**	-42.4	-25.5	-33.9	-36.2	-32.6	-21.8
IN	-40.0	-21.3	-37.8	-41.4	-45.9	**-1567**	-87.8	-72.7	-11.9	-57.3	-40.9
EA	-92.6	-16.8	-85.4	-100	-30.8	-62.6	**-654**	-109	-9.5	-66.4	-98.3
SE	-30.1	-26.4	-27.3	-26.9	-33.2	-69.9	-54.4	**-330**	-27.0	-30.5	-30.6
AU	-8.3	-74.2	-6.3	-6.3	-47.4	-24.6	-10.2	-70.1	**-551**	-10.3	-7.4
ME	-77.6	-23.0	-109	-139	-79.3	-277	-118	-44.0	-10.3	**-642**	-77.9

Table B4. Source-receptor matrix of annual average steady-state changes in surface O_3 concentrations per unit change in CO emissions (pptv O_3 (Tg CO $yr^{-1})^{-1}$), for the regional reduction simulations, with the United States (US) also defined as a receptor in addition to the 10 regions. The largest changes for each source reduction region are in bold.

	Receptor										
Source	NA	SA	EU	FSU	AF	IN	EA	SE	AU	ME	US
NA	-5.09	-0.74	-3.75	-2.78	-1.34	-2.04	-2.93	-1.00	-0.59	-3.42	**-7.24**
SA	-1.17	**-2.06**	-1.16	-0.97	-1.34	-1.43	-1.27	-1.05	-1.24	-1.39	-1.26
EU	-3.10	-0.72	**-11.0**	-4.42	-1.58	-2.11	-3.71	-1.05	-0.58	-5.87	-3.59
FSU	-3.37	-0.69	-5.32	**-6.86**	-1.32	-2.36	-4.87	-1.10	-0.58	-4.65	-3.97
AF	-1.38	-1.20	-1.37	-1.15	**-2.24**	-1.78	-1.53	-1.06	-0.95	-1.79	-1.47
IN	-1.76	-0.78	-1.85	-1.59	-1.39	**-9.43**	-2.68	-1.39	-0.64	-2.38	-1.99
EA	-2.58	-0.70	-2.74	-2.33	-1.18	-2.07	**-5.73**	-1.56	-0.60	-2.64	-3.08
SE	-1.53	-0.89	-1.57	-1.31	-1.27	-2.10	-1.93	**-2.13**	-0.88	-1.84	-1.71
AU	-1.09	-1.30	-1.09	-0.96	-1.30	-1.43	-1.23	-1.36	**-3.28**	-1.36	-1.16
ME	-2.33	-0.80	-2.98	-2.77	-1.80	-4.97	-3.24	-1.17	-0.63	**-7.48**	-2.70

Table B5. For each regional reduction, changes in global annual average, steady-state full and upper tropospheric (UT) O_3 burden (B_{O3}) per unit change in CO emissions (E_{CO}) (Tg O_3/Tg CO).

	Δ Full B_{O3} / Δ E_{CO}	Δ UT B_{O3} / Δ E_{CO}
NA	0.0182	1.05E-02
SA	0.0174	1.10E-02
EU	0.0172	9.43E-03
FSU	0.0174	9.68E-03
AF	0.0184	1.18E-02
IN	0.0194	1.27E-02
EA	0.0180	1.10E-02
SE	0.0205	1.38E-02
AU	0.0171	9.55E-03
ME	0.0180	1.07E-02

Table B6. Source-receptor matrix of annual average surface SO_4^{2-} concentration changes (ng m^{-3}), for the regional reduction simulations, with the United States (US) also defined as a receptor in addition to the 10 regions.

	Receptor										
Source	NA	SA	EU	FSU	AF	IN	EA	SE	AU	ME	US
NA	-8.82	-0.11	-9.10	-2.83	0.16	1.01	-3.10	-0.37	-0.04	-0.18	-15.59
SA	-0.16	-0.06	-0.25	-0.09	0.01	-0.05	-0.19	-0.11	-0.14	0.06	-0.20
EU	-1.61	-0.04	-19.21	-4.26	0.17	0.53	-2.22	-0.22	-0.02	-0.43	-2.58
FSU	-1.29	-0.02	-4.70	-4.67	0.10	0.45	-2.07	-0.18	-0.01	-0.28	-2.08
AF	-0.96	-0.15	-2.15	-0.77	0.71	0.36	-1.18	-0.32	-0.24	0.32	-1.47
IN	-1.92	-0.11	-4.34	-1.88	0.39	21.75	-3.90	0.55	-0.07	0.82	-3.30
EA	-6.65	-0.10	-13.42	-4.96	0.28	1.17	-41.29	-3.70	-0.08	-0.15	-11.23
SE	-0.85	-0.05	-1.60	-0.56	0.08	0.01	-2.98	-0.81	-0.07	0.11	-1.44
AU	-0.01	-0.01	-0.01	-0.01	0.00	-0.01	-0.02	-0.02	-0.02	0.01	-0.01
ME	-1.40	-0.05	-4.91	-3.05	1.10	6.73	-2.39	-0.18	-0.03	5.98	-2.36

Table B7. Source-receptor matrix of percentage changes in surface CO concentrations, for each of the regional reduction simulations relative to the base. The largest percentage changes for each source reduction region are in bold.

	Receptor									
Source	NA	SA	EU	FSU	AF	IN	EA	SE	AU	ME
NA	**-8.29%**	-0.47%	-2.75%	-2.45%	-0.77%	-0.63%	-1.39%	-0.67%	-0.31%	-2.28%
SA	-0.13%	**-2.58%**	-0.08%	-0.08%	-0.32%	-0.11%	-0.07%	-0.26%	-0.82%	-0.12%
EU	-1.53%	-0.21%	**11.03%**	-2.98%	-0.57%	-0.31%	-1.09%	-0.36%	-0.13%	-2.64%
FSU	-1.36%	-0.12%	-2.21%	**-5.83%**	-0.27%	-0.25%	-1.26%	-0.28%	-0.08%	-1.38%
AF	-0.70%	-1.68%	-0.52%	-0.52%	**-5.91%**	-0.66%	-0.47%	-0.84%	-1.55%	-0.96%
IN	-1.28%	-0.70%	-1.10%	-1.20%	-1.28%	**27.02%**	-1.80%	-2.01%	-0.56%	-1.87%
EA	-4.69%	-0.87%	-3.93%	-4.62%	-1.36%	-1.71%	**21.26%**	-4.79%	-0.72%	-3.44%
SE	-0.54%	-0.49%	-0.45%	-0.44%	-0.52%	-0.68%	-0.63%	**-5.14%**	-0.72%	-0.56%
AU	-0.01%	-0.07%	-0.01%	-0.01%	-0.04%	-0.01%	-0.01%	-0.06%	**-0.79%**	-0.01%
ME	-1.10%	-0.33%	-1.40%	-1.78%	-0.98%	-2.11%	-1.07%	-0.54%	-0.21%	**-9.28%**

Table B8. Source-receptor matrix of percentage changes in steady-state surface O_3 concentrations, for each of the regional reduction simulations relative to the base. The largest percentage changes for each source reduction region are in bold.

	Receptor									
Source	NA	SA	EU	FSU	AF	IN	EA	SE	AU	ME
NA	**-0.50%**	-0.10%	-0.36%	-0.29%	-0.16%	-0.17%	-0.24%	-0.12%	-0.09%	-0.30%
SA	-0.04%	**-0.10%**	-0.04%	-0.04%	-0.05%	-0.04%	-0.04%	-0.05%	-0.07%	-0.04%
EU	-0.14%	-0.05%	**-0.47%**	-0.21%	-0.08%	-0.08%	-0.14%	-0.06%	-0.04%	-0.23%
FSU	-0.10%	-0.03%	-0.16%	**-0.23%**	-0.05%	-0.06%	-0.13%	-0.04%	-0.03%	-0.13%
AF	-0.17%	-0.21%	-0.16%	-0.15%	**-0.32%**	-0.19%	-0.16%	-0.16%	-0.18%	-0.19%
IN	-0.24%	-0.15%	-0.24%	-0.23%	-0.22%	**-1.10%**	-0.30%	-0.24%	-0.13%	-0.28%
EA	-0.56%	-0.22%	-0.57%	-0.54%	-0.30%	-0.38%	**-1.03%**	-0.42%	-0.20%	-0.50%
SE	-0.12%	-0.10%	-0.12%	-0.11%	-0.11%	-0.14%	-0.12%	**-0.21%**	-0.11%	-0.12%
AU	0.00%	-0.01%	0.00%	0.00%	-0.01%	-0.01%	0.00%	-0.01%	**-0.02%**	0.00%
ME	-0.14%	-0.07%	-0.17%	-0.18%	-0.13%	-0.26%	-0.16%	-0.09%	-0.06%	**-0.39%**

Table B9. For each regional reduction, changes in global annual average steady-state tropospheric CO production (P_{CO}), loss (L_{CO}), burden (B_{CO}), and B_{CO} per unit change in CO emissions (E_{CO}). Global annual average changes in steady-state tropospheric O_3 burden (B_{O3}), B_{O3} per unit change in E_{CO}, and steady-state tropospheric CH_4 per unit change in E_{CO} are also shown. Steady-state CO and O_3 changes represent the sum of short and long-term changes, where long-term changes are calculated by scaling ΔP_{CO}, ΔL_{CO}, ΔB_{CO}, and ΔB_{O3} from the CH_4 control simulation to the ratio of global CH_4 burden changes from each scenario divided by that from the CH_4 control simulation.

Reduction region	ΔP_{CO} (Tg CO)	ΔL_{CO} (Tg CO)	ΔB_{CO} (Tg CO)	$\Delta B_{CO} / \Delta E_{CO}$ (days)	ΔB_{O3} (Tg O_3)	$\Delta B_{O3} / \Delta E_{CO}$ (days)	$\Delta CH_4 / \Delta E_{CO}$ (pptv (Tg CO yr^{-1})$^{-1}$)
NA	1.12	-27.1	-7.56	78.9	-0.637	6.64	260
SA	0.39	-9.13	-2.78	82.6	-0.214	6.37	262
EU	0.49	-12.0	-3.76	88.0	-0.269	6.29	263
FSU	0.34	-8.45	-2.77	92.4	-0.191	6.37	265
AF	1.42	-33.1	-8.86	74.4	-0.800	6.72	250
IN	1.48	-35.9	-9.02	68.3	-0.934	7.08	239
EA	2.41	-57.7	-16.4	78.4	-1.38	6.58	253
SE	0.85	-20.4	-5.53	74.4	-0.557	7.49	243
AU	0.04	-1.09	-0.38	93.7	-0.024	6.08	289
ME	0.67	-16.6	-4.48	76.8	-0.384	6.58	262

Table B10. Comparison of GWP_{20} and GWP_{100} estimates, due to regional changes in CO emissions, to those in Fry et al. (2012) and Berntsen et al. (2005), where the region definitions differ slightly in the three studies.

	Current study		Fry et al. (2012)		Berntsen et al. (2005)	
Source region	GWP_{20}	GWP_{100}	GWP_{20}	GWP_{100}	GWP_{20}	GWP_{100}
North America	3.94	1.30	5.21	1.70	--	--
Europe	3.67	1.23	4.60	1.50	10.5	3.8
East Asia	3.87	1.27	5.07	1.64	--	--
South Asia	4.31	1.38	5.35	1.70	13	4.4

Table B11. Annual total anthropogenic and biomass burning emissions by region and globally for the year 2005 (Tg CO yr^{-1}) in the base simulation.

Anthropogenic	NA	SA	EU	FSU	AF	IN	EA	SE	AU	ME	Global
Energy	1.25	1.03	0.53	0.68	9.45	1.73	1.87	1.36	0.04	3.17	21.10
Residential, commercial	7.26	4.34	9.05	3.69	65.88	66.21	56.14	31.76	0.65	16.05	261.17
Industrial	4.57	2.90	5.89	1.78	1.70	19.02	65.65	10.79	0.32	1.65	114.29
Land Transportation	53.40	13.91	13.83	13.91	7.32	8.57	21.64	7.82	1.36	20.06	161.90
Waste	1.51	0.19	1.38	0.13	0.18	0.25	0.12	0.13	0.00	0.19	4.06
Agriculture	0.01	0.00	0.00	0.00	0.00	0.00	0.00	0.00	0.00	0.00	0.01
Solvent	0.04	0.00	0.02	0.01	0.00	0.00	0.88	0.01	0.00	0.00	0.96
Waste burning	1.80	2.15	0.38	1.70	2.36	0.60	6.53	2.39	0.54	1.45	19.91
Shipping	0.11	0.02	0.13	0.01	0.03	0.01	0.05	0.05	0.03	0.06	1.27
Total Anthropogenic	69.95	24.53	31.19	21.91	86.92	96.38	152.87	54.31	2.93	42.62	584.69
Biomass burning											
Grassland fires	5.49	19.95	1.28	11.65	162.75	0.83	1.16	2.61	16.59	0.19	222.52
Forest fires	20.09	43.96	0.82	33.61	18.68	6.16	5.32	97.54	3.28	0.04	229.51

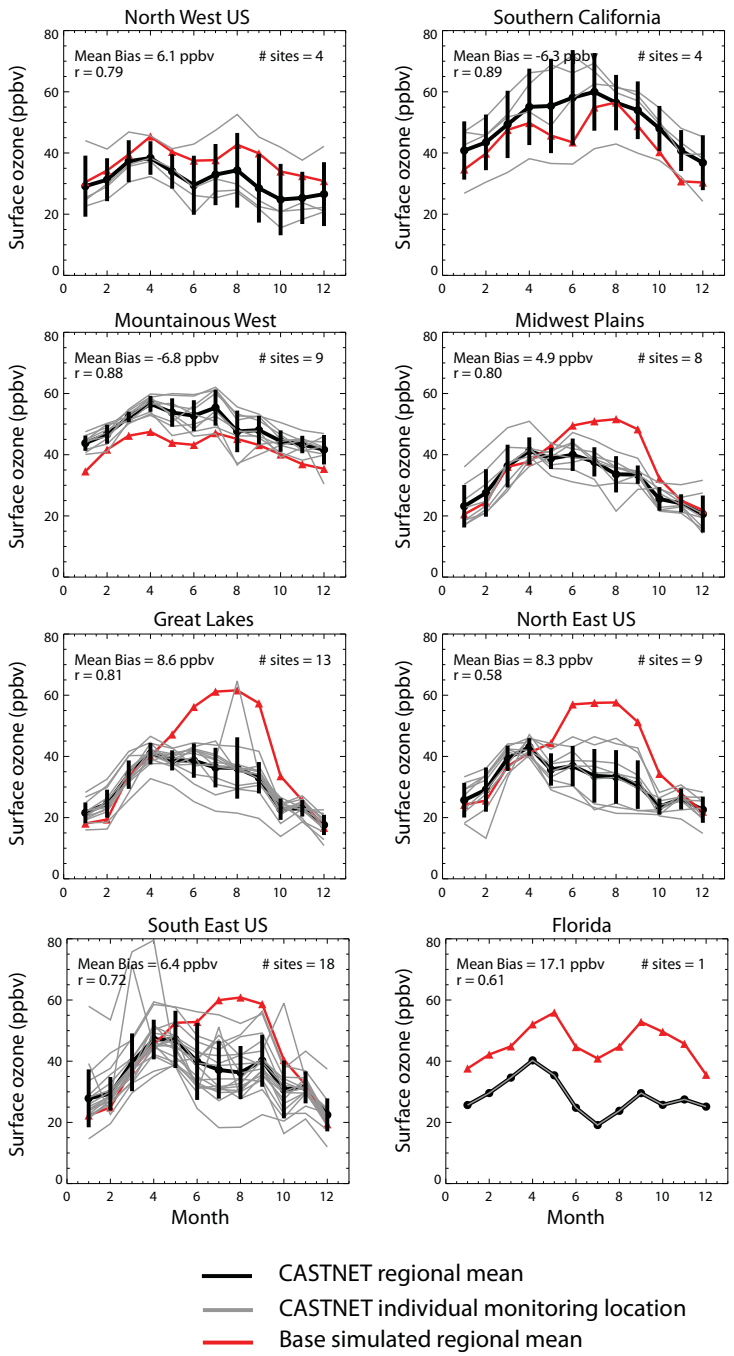

Figure B1. Comparison of the base simulated regional monthly mean short-term surface O_3 concentrations (red) for the year 2005 with 2005 observations from the CASTNET monitoring network in the U.S., showing CASTNET regional mean (black) and individual monitoring locations (grey). An overall model bias of 4.5 ppbv is calculated across all stations.

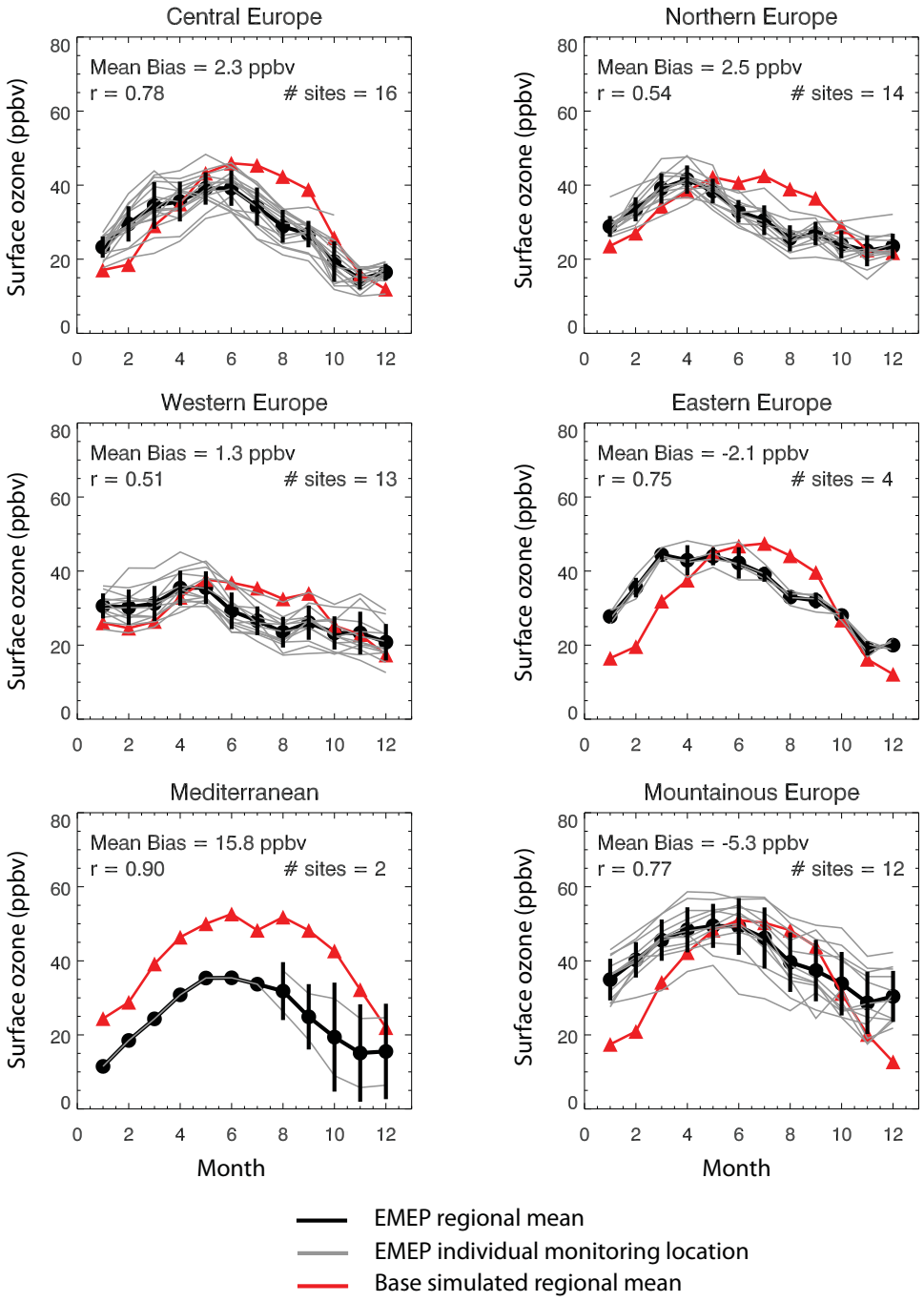

Figure B2. Comparison of the base simulated regional monthly mean short-term surface O_3 concentrations (red) for the year 2005 with 2005 observations from the EMEP monitoring network in Europe, showing EMEP regional mean (black) and individual monitoring locations (grey). An overall model bias of 0.8 ppbv is calculated across all stations.

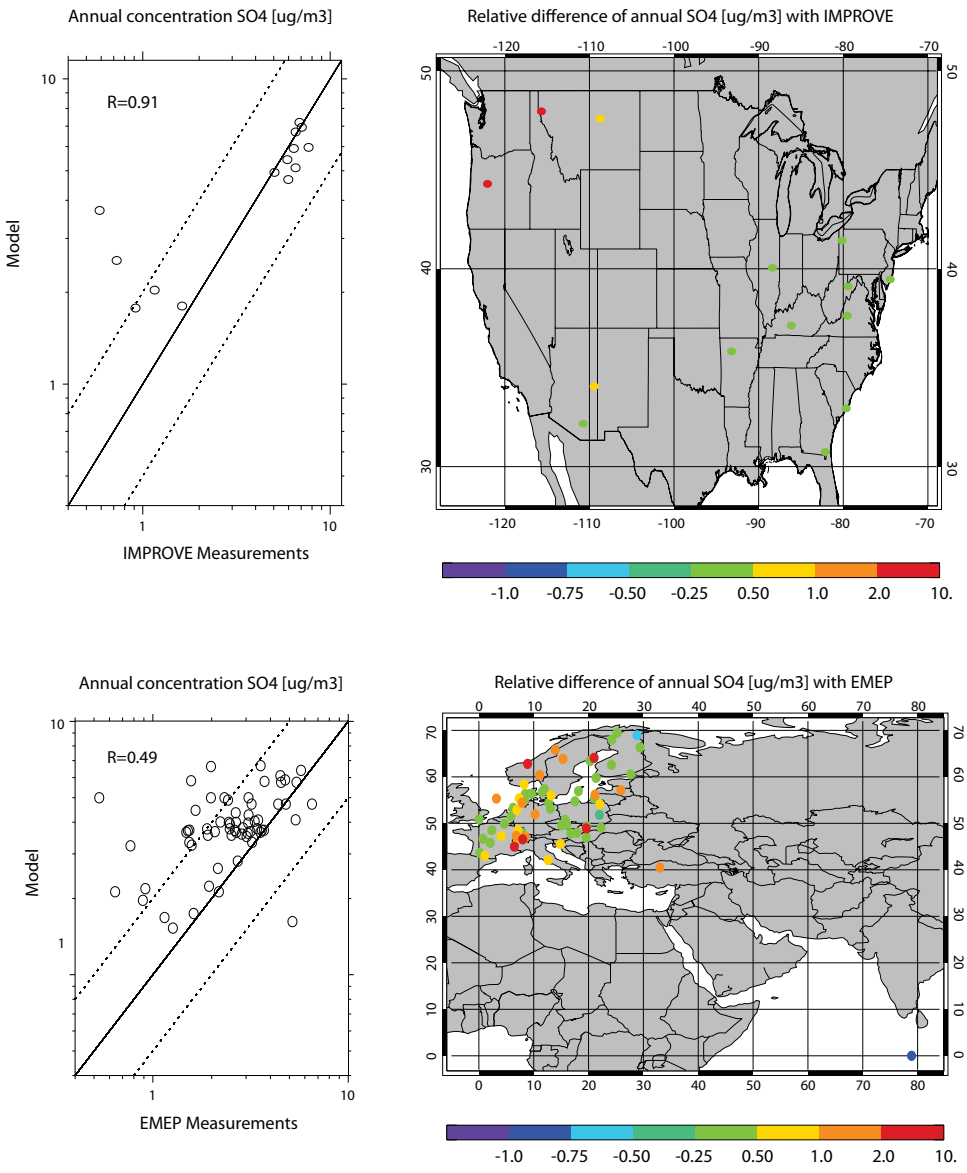

Figure B3. Comparison of the base simulated annual average (2005) surface SO_4^{2-} concentrations (μg m^{-3}) with annual average (2005) observations from (a) the IMPROVE surface monitoring network for remote locations in the U.S., and (b) the EMEP surface monitoring network for Europe. The left panels show modeled versus observed concentrations (μg m^{-3}) with the dashed 1:2 and 2:1 lines representing agreement within a factor of 2. The right panels show a map of [(modeled-observed)/observed] values.

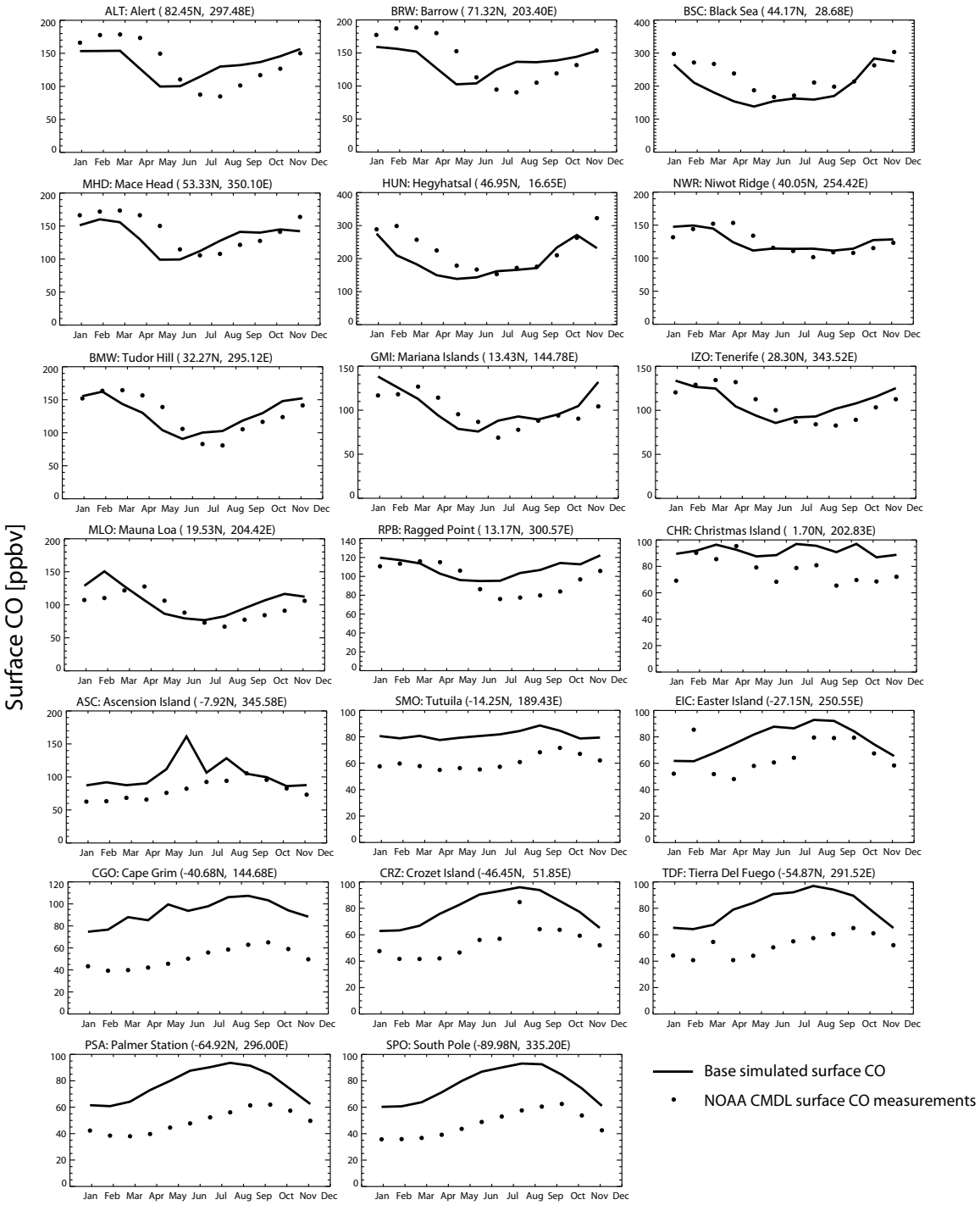

Figure B4. Comparison of the base simulated monthly mean (2005) surface CO concentrations with monthly mean NOAA CMDL surface CO measurements (in ppbv).

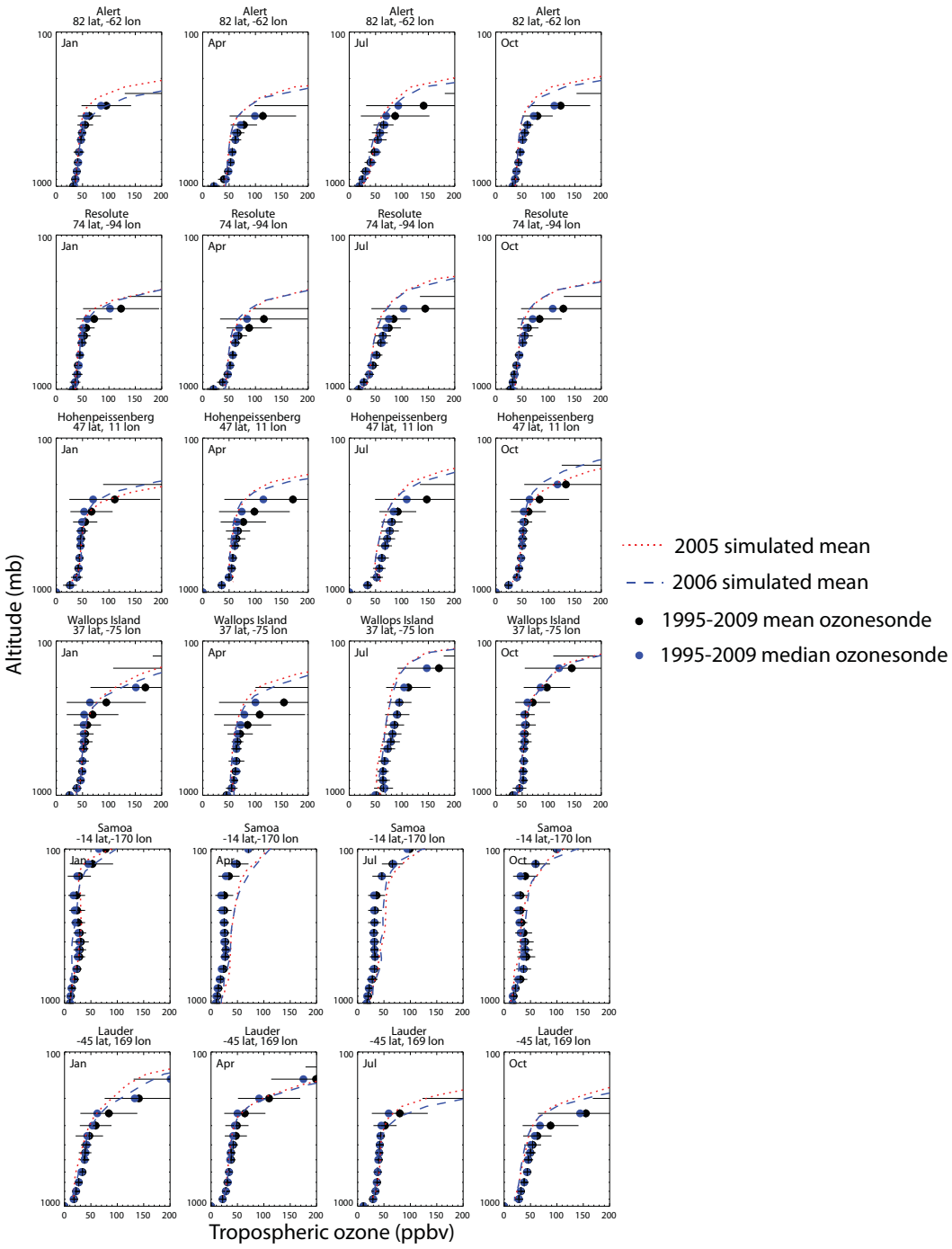

Figure B5. Vertical profile comparisons of the base simulated monthly mean tropospheric O_3 concentrations (ppbv) for the years 2005 (red line) and 2006 (blue line) with the monthly mean (black dot) and median (blue dot) ozonesonde climatology (average of 1995 through 2009) (Tilmes et al., 2012) for six selected ozonesonde stations that are latitudinally representative across the northern and southern hemispheres (Alert, Resolute, Hohenpeissenberg, Wallops Island, Samoa, and Lauder) in the months of January, April, July, and October.

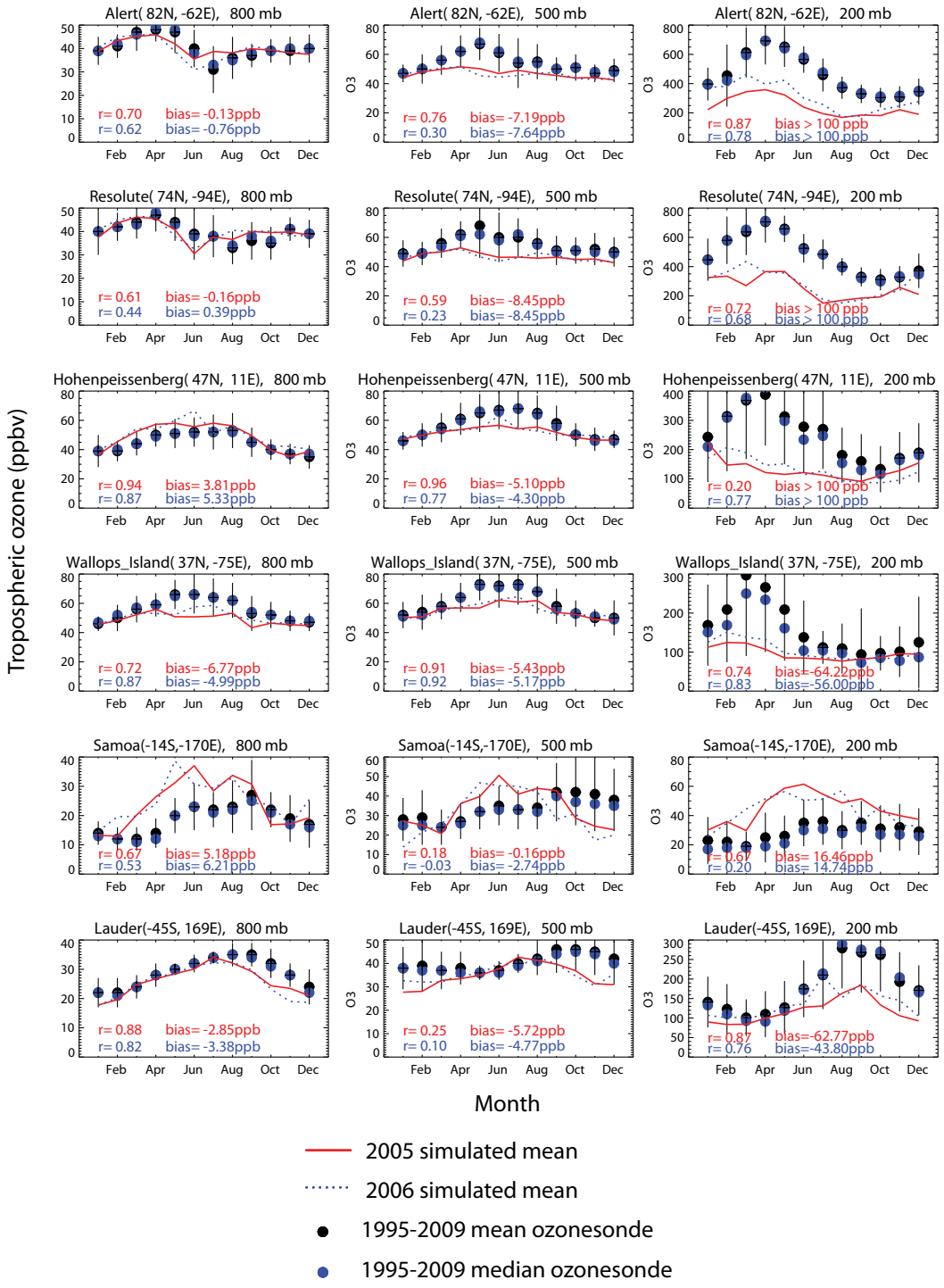

Figure B6. Time series comparisons of the base simulated monthly mean tropospheric O_3 concentrations (ppbv) for the years 2005 (red line) and 2006 (blue line) with the monthly mean (black dot) and median (blue dot) ozonesonde climatology (averaged over 1995 through 2009) (Tilmes et al., 2012) for six selected ozonesonde stations that are latitudinally representative across the northern and southern hemispheres (Alert, Resolute, Hohenpeissenberg, Wallops Island, Samoa, and Lauder) at altitudes of 800, 500, and 200 millibars (mb).

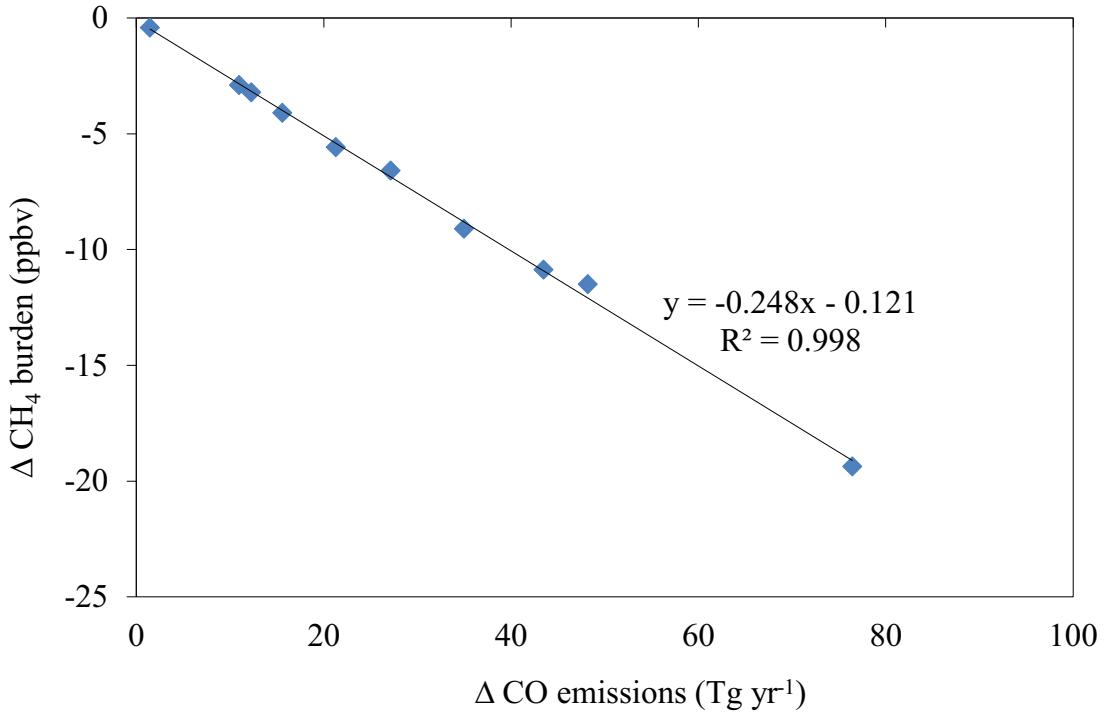

Figure B7. Changes in global steady-state tropospheric CH_4 burden as a function of CO emissions change for each of the regional reductions relative to the base.

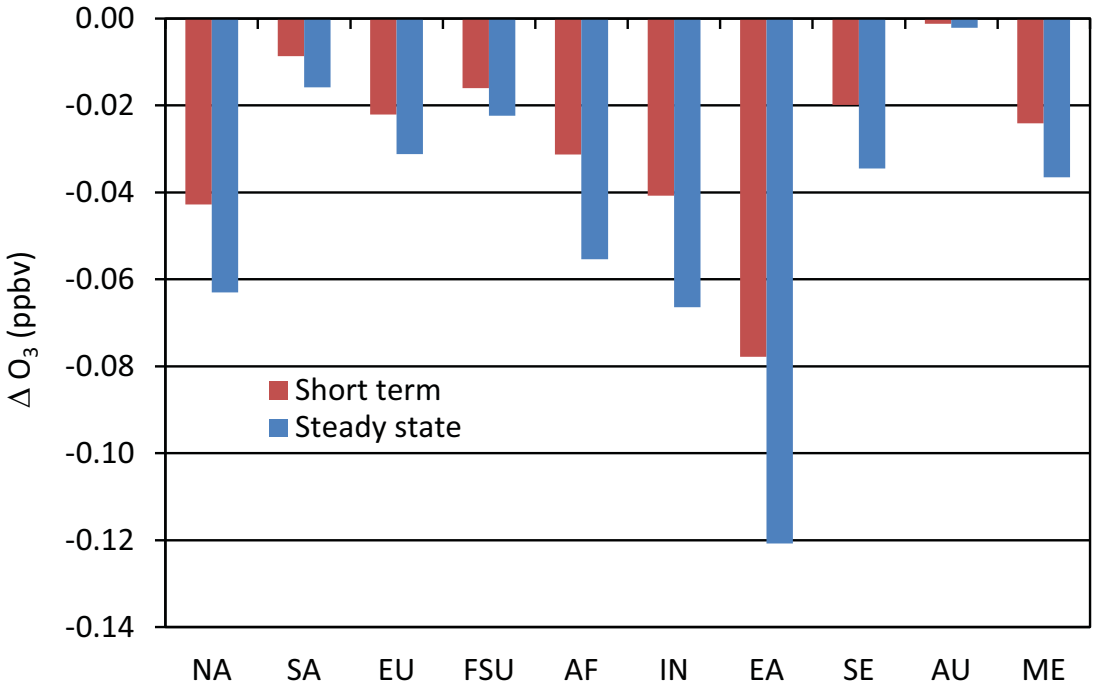

Figure B8. Global annual average surface O_3 concentration changes (ppbv) for each of the regional reduction simulations, in the short term and at steady state.

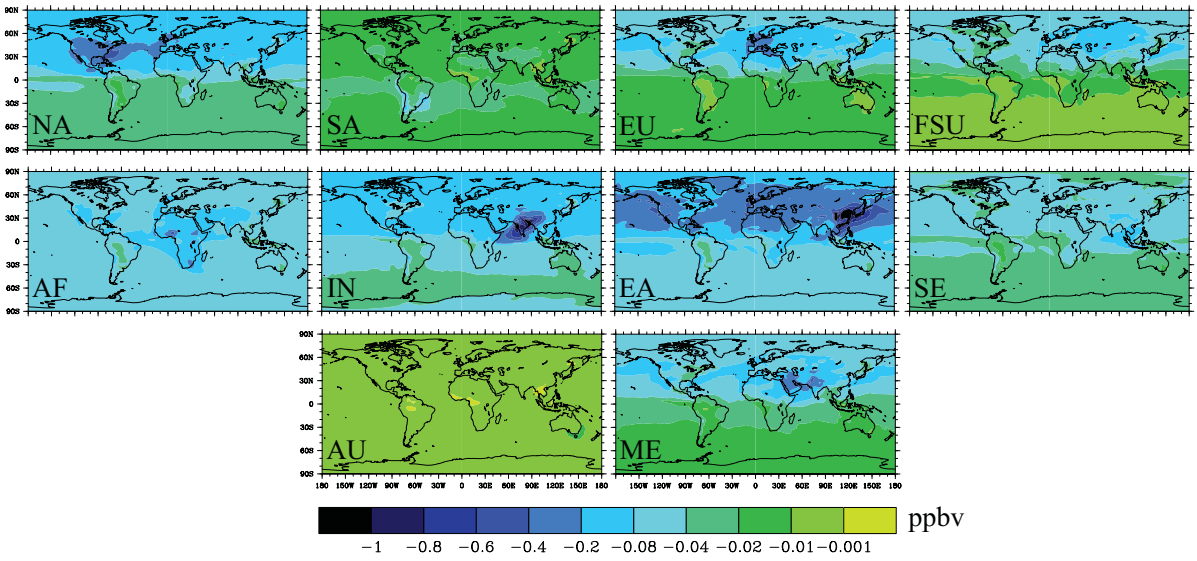

Figure B9. Changes in the three-month average of daily 8-hour maximum surface O_3 concentration changes (ppbv) relative to the base, for each of the regional reduction simulations, for the consecutive three-month period where daily 8-hour maximum surface O_3 changes are highest in each grid cell.

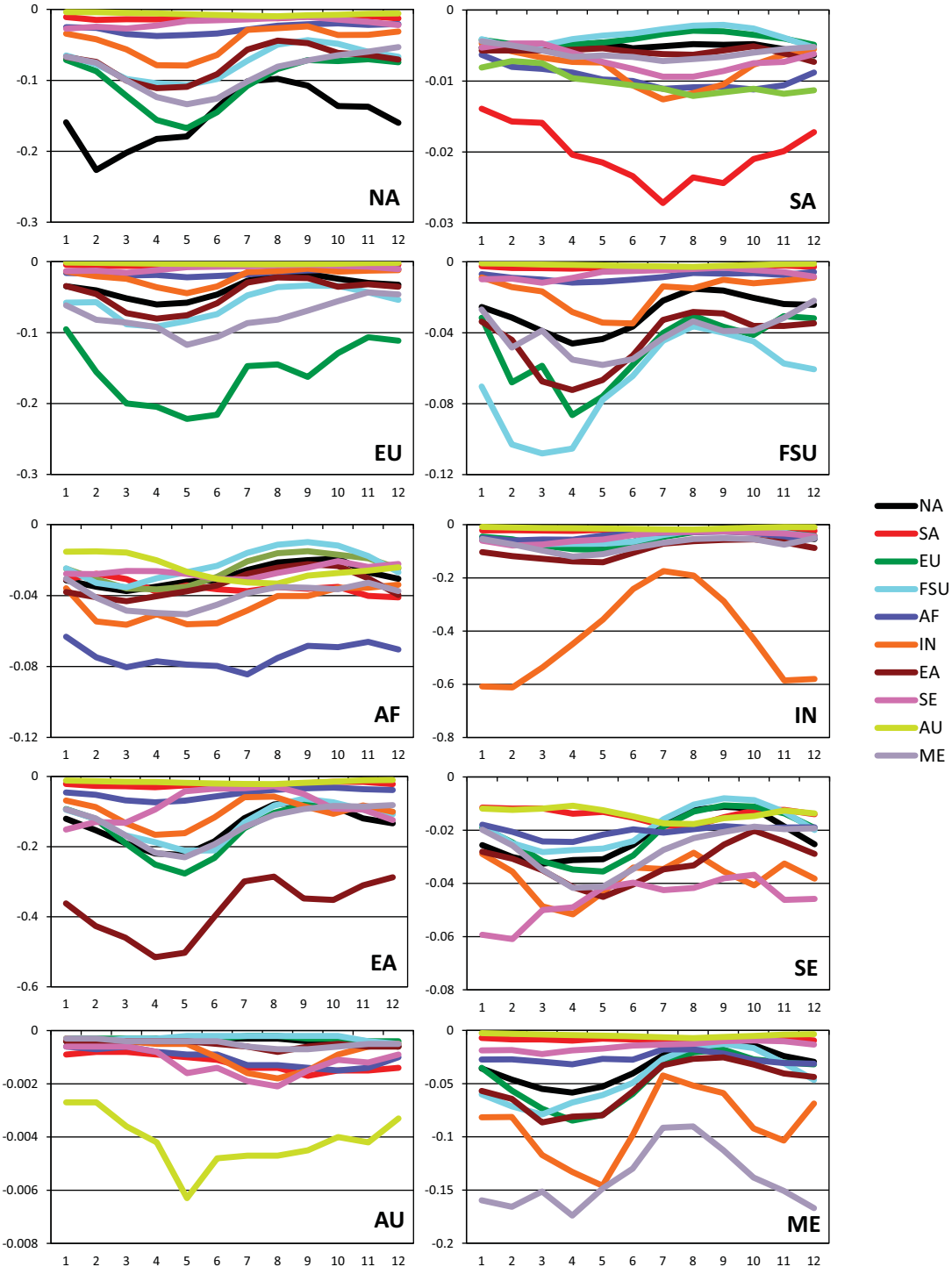

Figure B10. Changes in monthly average short-term surface O_3 (ppbv) for each of the regional reduction simulations, where the influence of each reduction region (noted in bottom right of each plot) on all 10 receptor regions (colored lines) is shown.

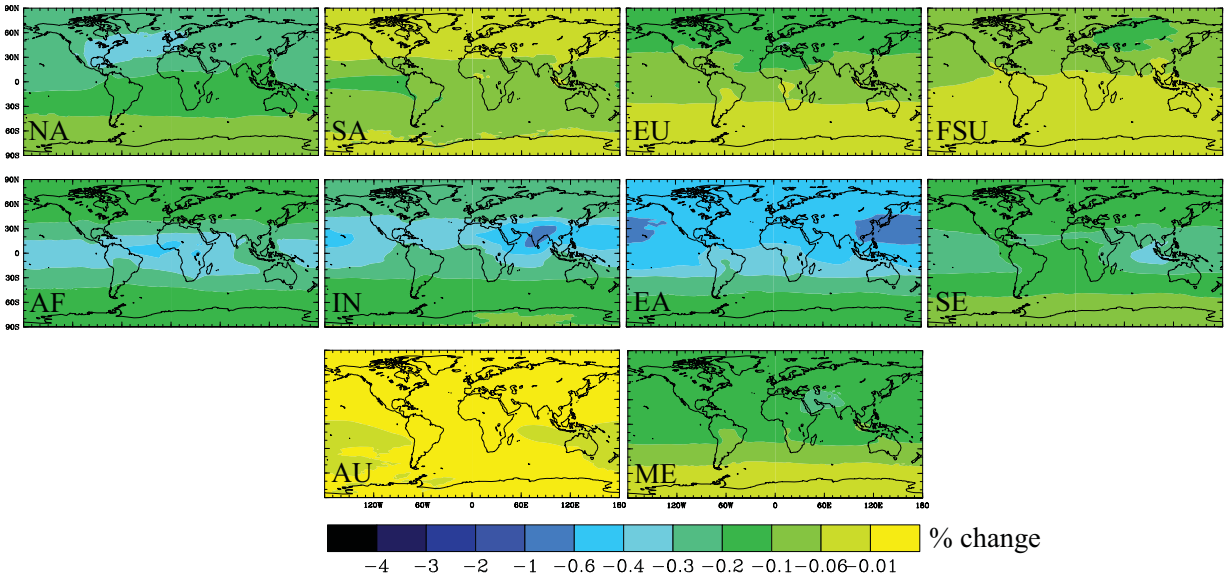

Figure B11. Global distribution of annual average percentage changes in tropospheric total column O_3 at steady state for each of the regional reduction simulations relative to the base.

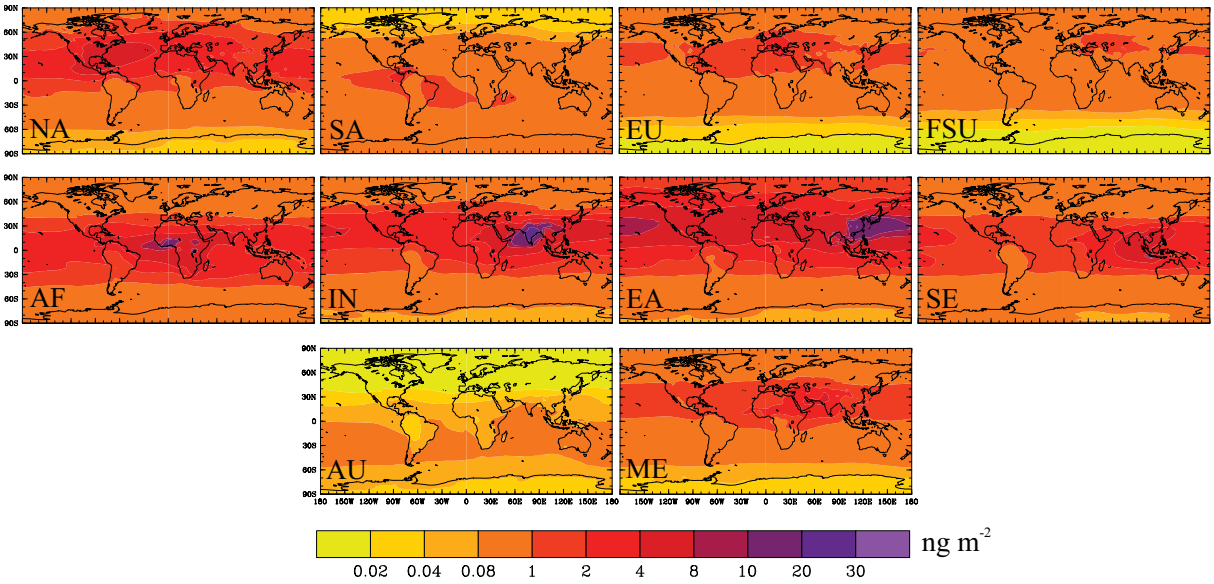

Figure B12. Global distribution of annual average changes in tropospheric total column OH burden (ng m^{-2}) for each of the regional reduction simulations relative to the base.

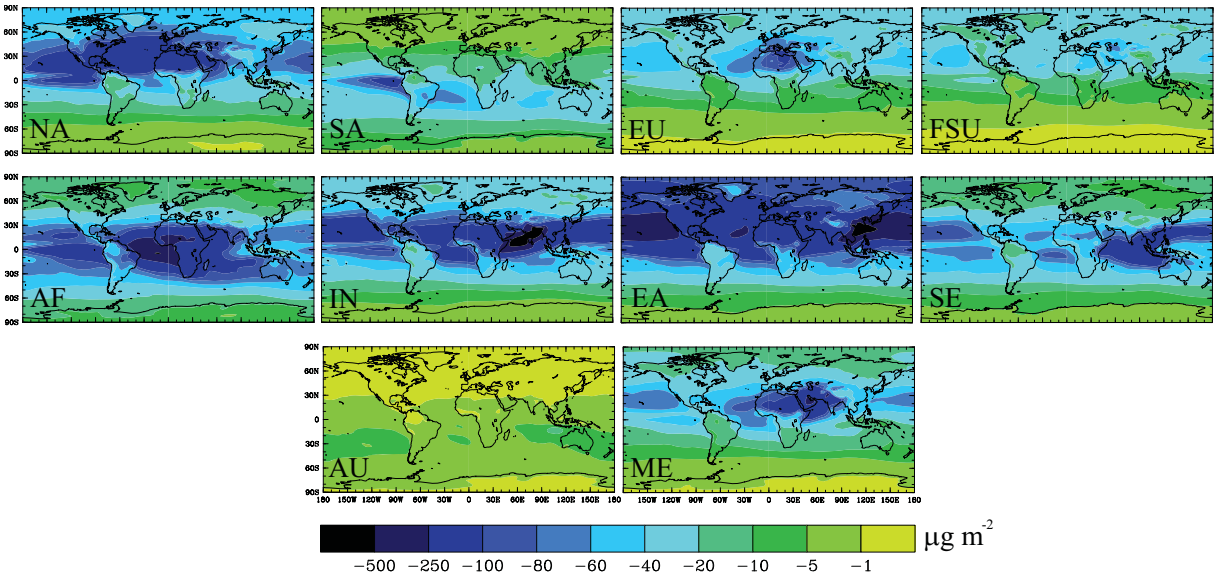

Figure B13. Global distribution of annual average changes in tropospheric total column H_2O_2 burden (µg m^{-2}) for each of the regional reduction simulations relative to the base.

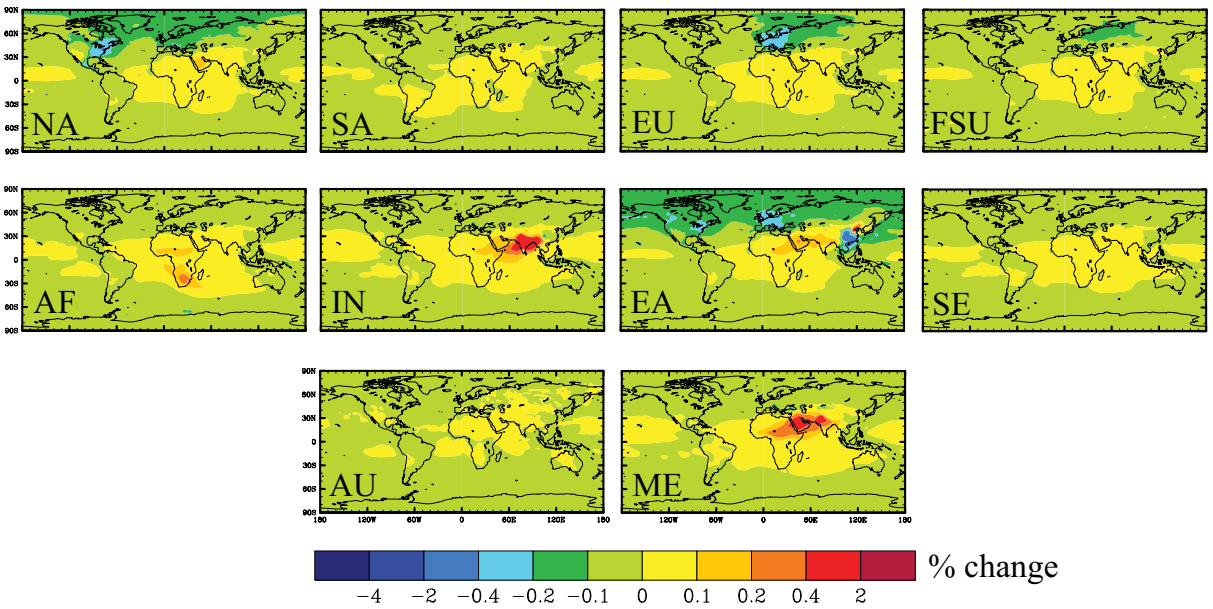

Figure B14. Global distribution of annual average percentage changes in tropospheric total column SO_4^{2-} for each of the regional reduction simulations relative to the base.

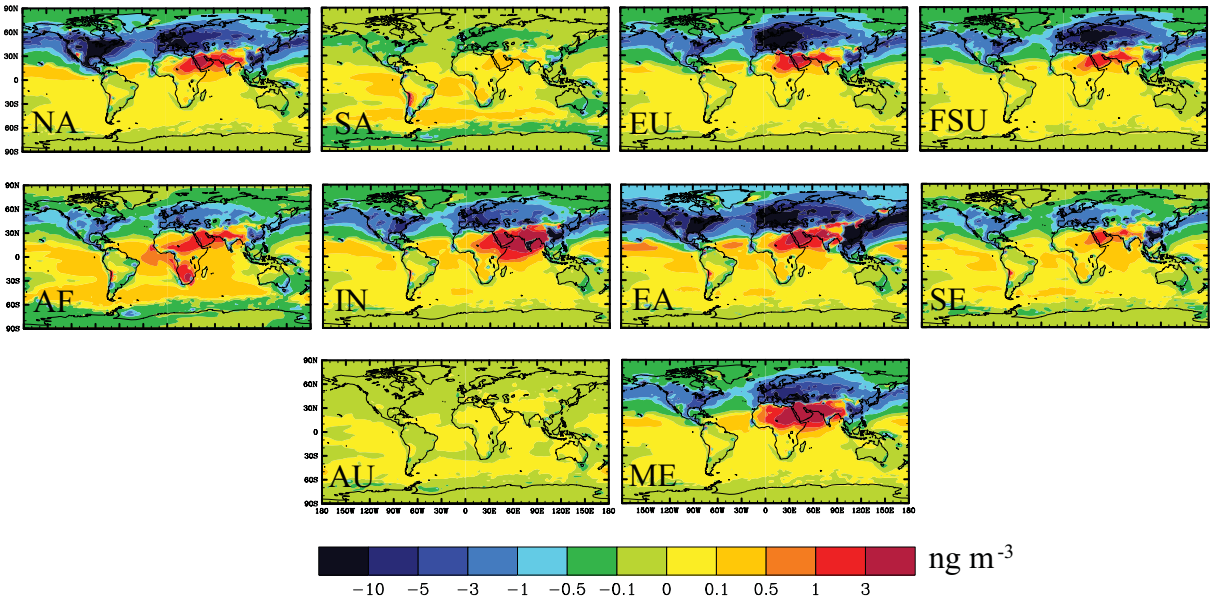

Figure B15. Global distribution of annual average surface SO_4^{2-} concentration changes (ng m^{-3}) for each of the regional reduction simulations relative to the base.

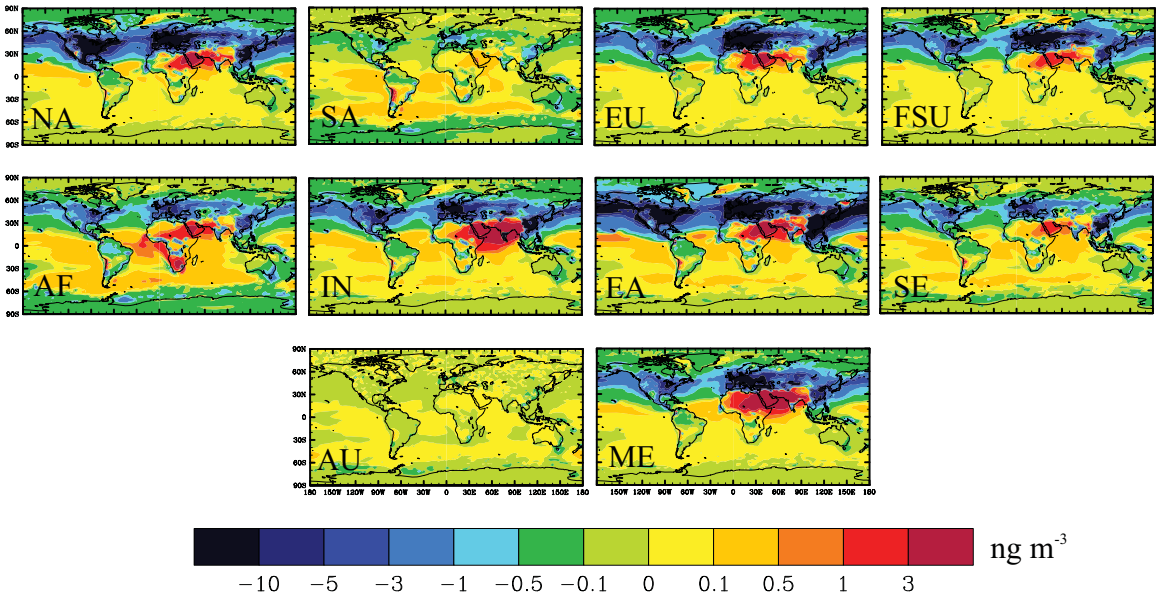

Figure B16. Global distribution of annual average changes in surface $PM_{2.5}$ (sum of BC, OC, $(NH_4)_2SO_4$, NH_4NO_3, SOA) (ng m^{-3}) for the global and regional reduction simulations relative to the base.

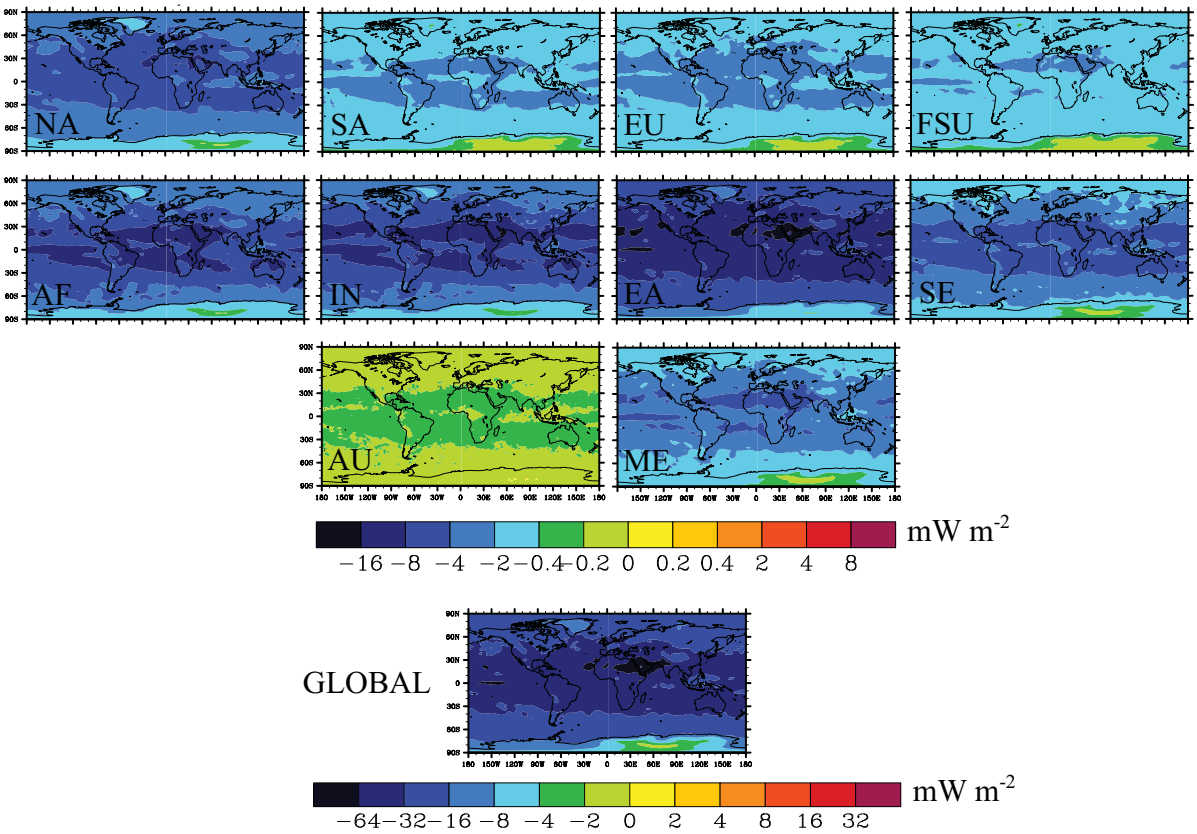

Figure B17. Annual average longwave (infrared) radiation distributions (mW m^{-2}) due to changes in tropospheric steady-state O_3, CH_4, and SO_4^{2-} for the regional and global CO reduction simulations minus the base simulation.

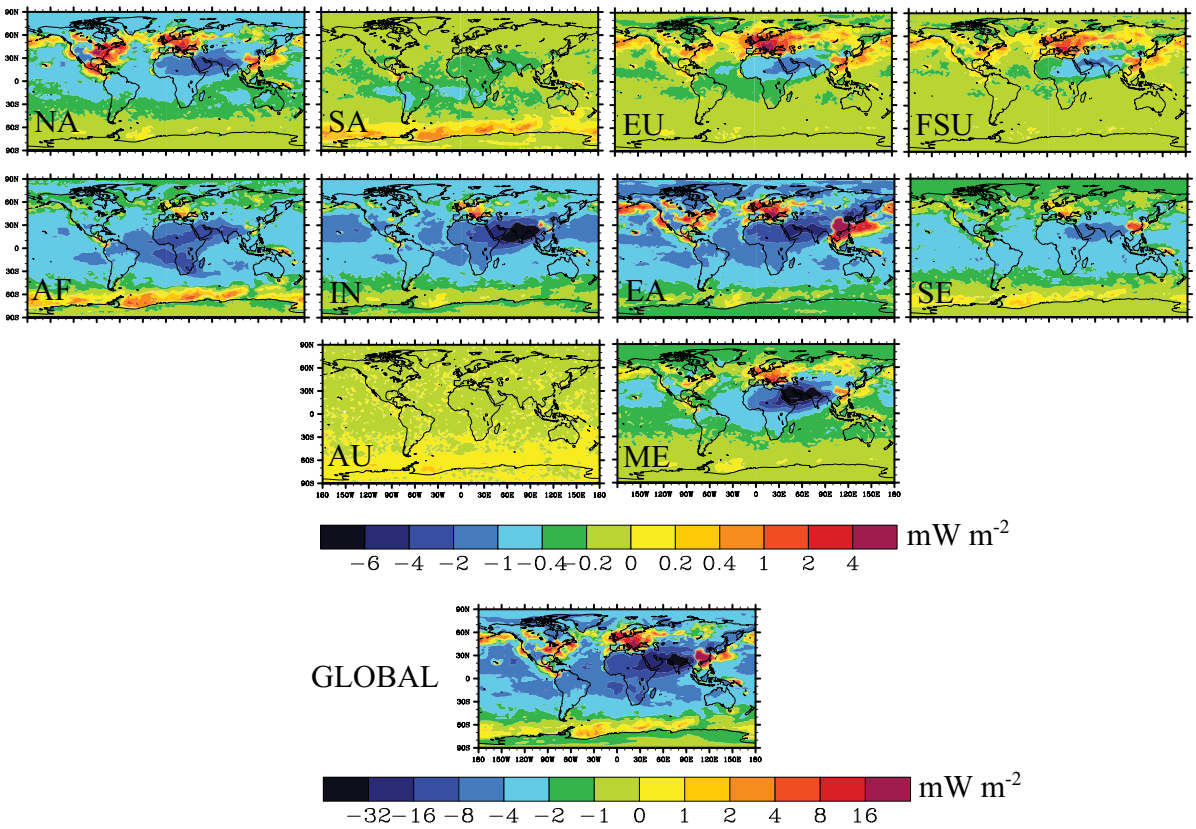

Figure B18. Annual average shortwave (solar) radiation distributions (mW m^{-2}) due to changes in tropospheric steady-state O_3, CH_4, and SO_4^{2-} for the regional and global CO reduction simulations minus the base simulation.

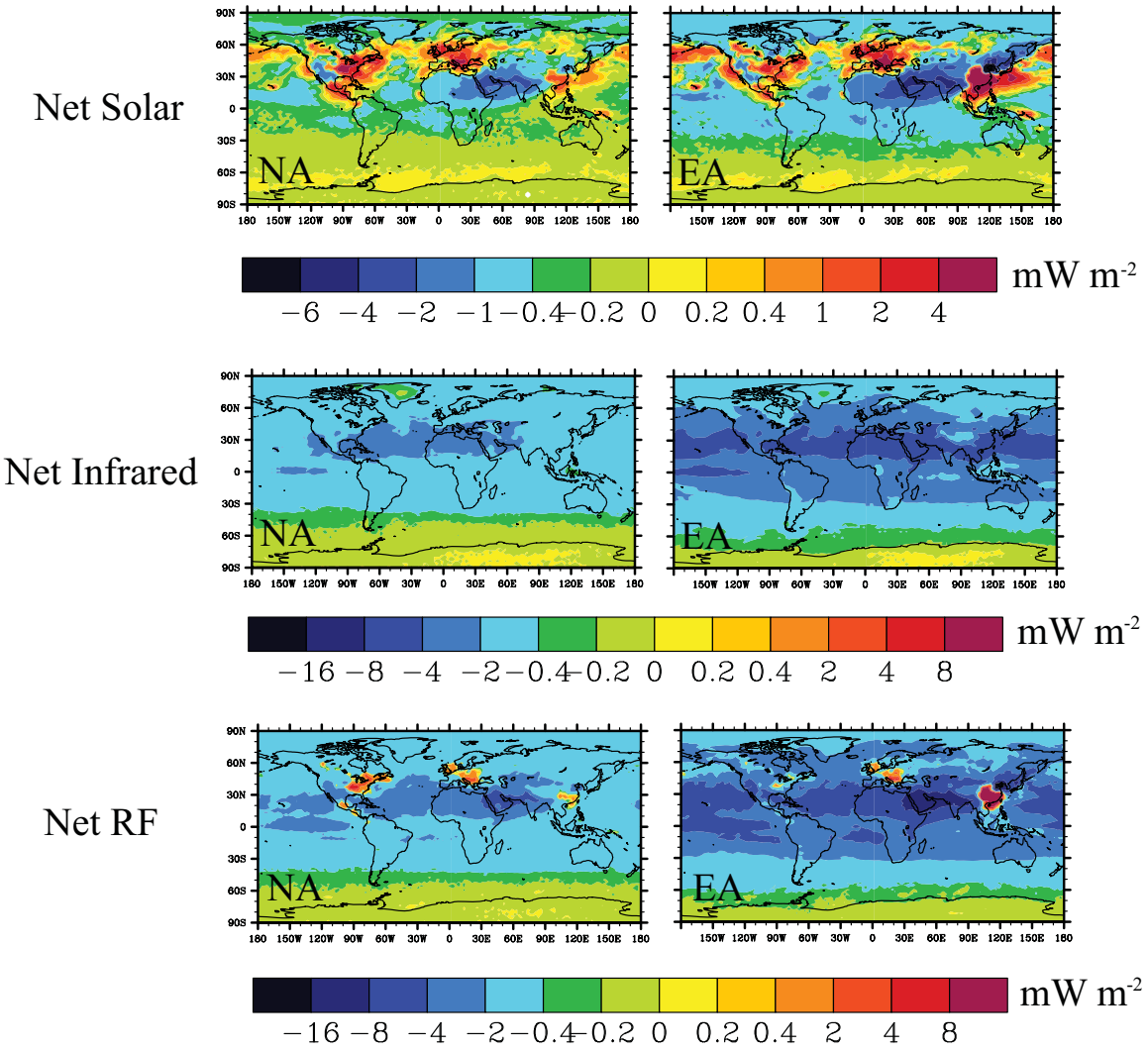

Figure B19. Short-term annual average shortwave (solar) radiation, longwave (infrared) radiation, and net RF distributions (mW m^{-2}) due to changes in tropospheric short-term O_3 and SO_4^{2-} for the NA and EA reduction simulations minus the base simulation.

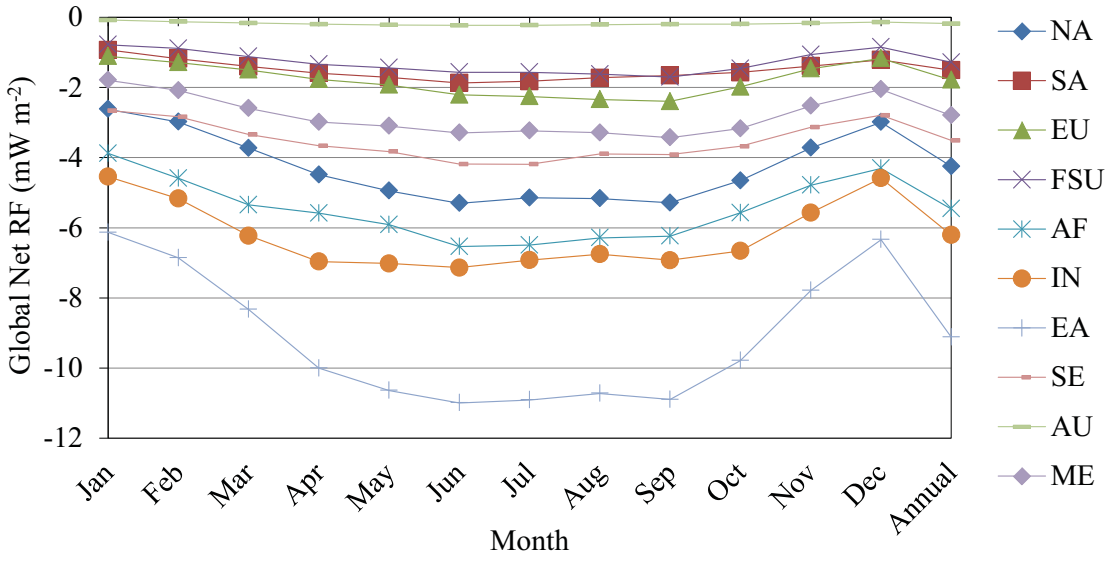

Figure B20. Global monthly and annual average net RF (mW m^{-2}) due to changes in tropospheric steady-state O_3, CH_4, and SO_4^{2-} for each regional CO reduction simulation minus the base simulation.

Appendix C. Air quality and radiative forcing impacts of anthropogenic volatile organic compound emissions from ten world regions: Supporting material

Table C1. Anthropogenic NMVOC emission species in MOZART-4 simulations (Emmons et al., 2010).

MOZART-4 species	Description
BIGALK	C_5H_{12}, lumped alkanes (C > 3)
BIGENE	C_4H_8, lumped alkenes (C > 3)
C2H4	ethene
C2H5OH	ethanol
C2H6	ethane
C3H6	propene
C3H8	propane
CH2O	formaldehyde
CH3CHO	acetaldehyde
CH3COCH3	acetone
CH3COOH	acetic acid
CH3OH	methanol
MEK	$CH_3C(O)CH_2CH_3$, methyl ethyl ketone
TOLUENE	$C_6H_5(CH_3)$, lumped aromatics

Table C2. Annual total anthropogenic, biomass burning, and natural NMVOC emissions by region and globally for the year 2005 (Tg C yr^{-1}) in the base simulation.

Anthropogenic	NA	SA	EU	FSU	AF	IN	EA	SE	AU	ME	Global
Shipping	0.13	0.16	0.18	0.02	0.26	0.03	0.07	0.10	0.03	0.76	2.64
Waste burning	0.09	0.13	0.02	0.10	0.14	0.03	0.58	0.14	0.02	0.06	1.31
Solvents	2.90	0.88	2.61	1.22	0.48	0.63	3.87	1.00	0.12	0.57	14.30
Agriculture	0.00	0.00	0.00	0.00	0.00	0.00	0.00	0.00	0.00	0.00	0.00
Waste	0.25	0.04	0.04	0.06	0.03	0.03	0.08	0.03	0.00	0.02	0.58
Land transportation	3.25	2.40	2.11	1.81	0.89	1.40	4.79	3.44	0.25	2.82	23.18
Industrial	1.67	0.29	0.93	0.51	0.11	0.22	1.74	0.13	0.08	0.41	6.08
Residential, commercial	0.81	0.32	0.74	0.26	3.96	4.56	8.21	2.29	0.05	1.25	22.46
Energy	0.99	2.54	0.89	1.02	2.31	0.48	1.11	1.33	0.13	9.33	20.13
Total Anthropogenic	10.10	6.76	7.52	4.99	8.17	7.38	20.47	8.47	0.67	15.23	90.67
Biomass burning											
Grassland fires	0.48	1.49	0.09	0.98	12.15	0.06	0.08	0.21	1.20	0.01	16.75
Forest fires	1.79	4.18	0.07	2.90	1.77	0.59	0.42	9.79	0.31	0.00	21.83
Natural											
$C_{10}H_{16}$	12.12	37.72	2.20	5.84	16.77	1.77	4.27	20.61	4.18	0.52	107.08
Isoprene	61.75	227.85	7.94	19.17	158.57	16.59	20.08	136.10	75.69	6.76	738.21

Table C3. Source-receptor matrix of annual average steady-state changes in surface O_3 concentrations (pptv), for the regional reduction simulations, with the United States (US) also defined as a receptor in addition to the 10 regions.

	Receptor										
Source	NA	SA	EU	FSU	AF	IN	EA	SE	AU	ME	US
NA	-426.8	-16.2	-174.7	-137.6	-45.1	-45.2	-100.4	-28.2	-9.8	-127.6	-657.2
SA	-18.0	-7.6	-20.6	-16.5	-12.6	-19.8	-18.9	-15.5	-7.9	-23.7	-22.0
EU	-143.6	-10.3	-915.4	-303.3	-56.8	-36.7	-144.2	-25.9	-5.6	-278.5	-138.4
FSU	-113.2	-6.5	-222.5	-525.0	-26.0	-30.4	-173.4	-22.2	-3.9	-134.7	-108.6
AF	-23.7	-23.3	-22.1	-18.6	-72.0	-27.0	-21.6	-20.0	-21.5	-29.5	-24.3
IN	-31.4	-12.7	-29.1	-31.7	-25.6	-843.3	-53.4	-36.5	-8.8	-50.7	-33.1
EA	-258.5	-25.5	-214.5	-263.5	-63.6	-111.3	-1594.4	-273.8	-15.9	-170.7	-280.3
SE	-25.1	-13.8	-25.4	-21.1	-19.9	-25.4	-26.4	-30.1	-13.6	-30.6	-27.9
AU	-1.7	-0.4	-1.9	-1.5	-1.4	-2.0	-1.9	-1.4	-5.1	-2.1	-1.9
ME	-143.6	-32.9	-216.9	-228.7	-114.9	-258.2	-164.7	-61.9	-20.1	-922.3	-147.7

Table C4. Source-receptor matrix of annual average steady-state changes in surface O_3 concentrations per unit change in NMVOC emissions (pptv (Tg C yr^{-1})$^{-1}$), for the regional reduction simulations, with the United States (US) also defined as a receptor in addition to the 10 regions.

	Receptor										
Source	NA	SA	EU	FSU	AF	IN	EA	SE	AU	ME	US
NA	84.53	3.21	34.60	27.25	8.93	8.95	19.88	5.59	1.94	25.27	130.16
SA	5.33	2.25	6.10	4.88	3.73	5.86	5.59	4.59	2.34	7.01	6.51
EU	38.21	2.74	243.6	80.71	15.12	9.77	38.37	6.89	1.49	74.11	36.83
FSU	45.33	2.60	89.10	210.23	10.41	12.17	69.44	8.89	1.56	53.94	43.49
AF	5.80	5.70	5.41	4.55	17.62	6.61	5.29	4.90	5.26	7.22	5.95
IN	8.51	3.44	7.89	8.60	6.94	228.67	14.48	9.90	2.39	13.75	8.98
EA	25.26	2.49	20.96	25.75	6.21	10.88	155.80	26.76	1.55	16.68	27.39
SE	5.93	3.26	6.00	4.98	4.70	6.00	6.24	7.11	3.21	7.23	6.59
AU	5.08	1.20	5.68	4.48	4.18	5.98	5.68	4.18	15.24	6.27	5.68
ME	18.85	4.32	28.48	30.03	15.08	33.90	21.62	8.13	2.64	121.09	19.39

Table C5. Changes in global annual average tropospheric PAN (ΔPAN) per unit change in NMVOC emissions (ΔE), PAN production (P_{PAN}), and PAN production (ΔP_{PAN}) per ΔE for the global and regional reductions.

Reduction region	ΔPAN / ΔE (Gg PAN (Tg C yr^{-1})$^{-1}$)	ΔP_{PAN} (Tg PAN yr^{-1})	$\Delta P_{PAN} / \Delta E$ (Tg PAN (Tg C yr^{-1})$^{-1}$)
NA	10.3	-18.4	3.65
SA	4.7	-4.0	1.18
EU	12.8	-16.1	4.30
FSU	14.0	-9.7	3.88
AF	4.4	-7.1	1.74
IN	5.7	-10.3	2.79
EA	9.9	-36.5	3.57
SE	5.4	-5.5	1.30
AU	6.0	-0.5	1.38
ME	8.0	-28.8	3.78
Global	8.5	-138.3	3.05

Table C6. Source-receptor matrix of annual average changes in surface SO_4^{2-} concentrations (ng m^{-3}) for the regional reduction simulations, with the United States (US) also defined as a receptor in addition to the 10 regions.

	Receptor										
Source	NA	SA	EU	FSU	AF	IN	EA	SE	AU	ME	US
NA	-27.30	-0.06	-7.16	-2.59	-0.26	-0.07	-3.11	-0.57	-0.01	-1.88	-50.76
SA	-0.16	-0.37	-0.34	-0.10	0.02	-0.08	-0.29	-0.11	-0.04	-0.01	-0.31
EU	-2.60	-0.03	-93.20	-16.51	-1.26	-0.02	-6.49	-0.77	-0.01	-12.13	-4.25
FSU	-2.02	-0.02	-15.97	-37.87	-0.38	0.21	-11.67	-0.78	0.00	-5.86	-3.35
AF	-0.29	-0.04	-0.60	-0.24	0.06	0.02	-0.50	-0.11	-0.07	0.04	-0.45
IN	-0.56	-0.03	-1.11	-1.26	0.01	-34.62	-2.46	0.46	-0.01	-0.63	-0.91
EA	-5.75	-0.11	-7.91	-9.26	-0.38	-1.94	-313.71	-33.48	-0.03	-2.24	-9.75
SE	-0.36	-0.02	-0.68	-0.21	-0.01	-0.17	-2.90	-1.32	-0.04	-0.04	-0.59
AU	0.00	0.00	-0.02	-0.01	0.00	0.00	-0.01	-0.01	-0.03	0.00	-0.01
ME	-2.23	-0.05	-13.57	-11.56	3.61	6.90	-5.73	-0.54	-0.02	10.55	-3.86

Table C7. Regional and global annual average changes in surface $PM_{2.5}$ concentrations (in ng m^{-3} and %) for the global NMVOC reduction simulation.

	Δ $PM_{2.5}$ (ng m^{-3})	% change
NA	-40.22	-0.99
SA	-3.00	-0.08
EU	-197.10	-1.79
FSU	-49.28	-0.83
AF	-3.57	-0.06
IN	-66.09	-0.41
EA	-383.86	-2.30
SE	-49.97	-0.76
AU	-1.76	-0.10
ME	-6.51	-0.12
US	-61.94	-1.05
Global	-28.02	-0.89

Table C8. Source-receptor matrix of annual average changes in surface $PM_{2.5}$ concentrations (ng m^{-3}) for the regional reduction simulations, with the United States (US) also defined as a receptor in addition to the 10 regions.

	Receptor										
Source	NA	SA	EU	FSU	AF	IN	EA	SE	AU	ME	US
NA	-20.79	-0.21	-14.38	-2.56	-0.84	-1.46	-6.33	-0.89	-0.03	-3.63	-32.27
SA	-0.28	-1.32	-0.47	-0.10	-0.34	-0.35	-0.45	-0.30	-0.36	-0.12	-0.35
EU	-3.10	-0.09	-108.62	-8.90	-2.28	-1.13	-10.73	-1.12	-0.01	-13.74	-4.45
FSU	-2.33	-0.05	-18.81	-19.98	-0.67	-0.40	-12.22	-1.09	-0.01	-5.85	-3.41
AF	0.36	-0.42	-0.89	-0.22	-1.42	-0.50	-0.82	-0.28	-0.26	-0.19	-0.50
IN	-0.69	-0.10	-1.99	-1.08	-0.17	-49.96	-2.15	-0.29	-0.03	-0.67	-1.02
EA	-7.05	-0.26	-16.65	-6.25	-0.95	-5.64	-325.08	-42.52	-0.05	-3.82	-11.07
SE	-0.45	-0.23	-1.00	-0.21	-0.23	-0.67	-3.48	-2.57	-0.25	-0.20	-0.66
AU	0.00	-0.04	-0.04	-0.01	-0.02	-0.02	-0.03	-0.07	-0.66	0.00	-0.01
ME	-2.56	-0.18	-17.59	-7.58	3.88	2.63	-8.83	-0.96	-0.04	24.77	-3.96

Table C9. Source-receptor matrix of annual average percentage changes (%) in surface $PM_{2.5}$ concentrations for the regional reduction simulations, with the United States (US) also defined as a receptor in addition to the 10 regions.

	Receptor										
Source	NA	SA	EU	FSU	AF	IN	EA	SE	AU	ME	US
NA	-0.511	-0.006	-0.131	-0.043	-0.014	-0.009	-0.038	-0.014	-0.002	-0.065	-0.546
SA	-0.007	-0.034	-0.004	-0.002	-0.006	-0.002	-0.003	-0.005	-0.021	-0.002	-0.006
EU	-0.076	-0.002	-0.988	-0.151	-0.037	-0.007	-0.064	-0.017	-0.001	-0.248	-0.075
FSU	-0.057	-0.001	-0.171	-0.338	-0.011	-0.003	-0.073	-0.017	0.000	-0.106	-0.058
AF	-0.009	-0.011	-0.008	-0.004	-0.023	-0.003	-0.005	-0.004	-0.015	-0.004	-0.009
IN	-0.017	-0.002	-0.018	-0.018	-0.003	-0.312	-0.013	-0.004	-0.002	-0.012	-0.017
EA	-0.174	-0.007	-0.152	-0.106	-0.015	-0.035	-1.947	-0.650	-0.003	-0.069	-0.187
SE	-0.011	-0.006	-0.009	-0.004	-0.004	-0.004	-0.021	-0.039	-0.014	-0.004	-0.011
AU	0.000	-0.001	0.000	0.000	0.000	0.000	0.000	-0.001	-0.038	0.000	0.000
ME	-0.063	-0.005	-0.160	-0.128	0.063	0.016	-0.053	-0.015	-0.002	0.447	-0.067

Table C10. Comparison of GWP_{20} and GWP_{100} estimates, due to regional changes in NMVOC emissions, to the multimodel mean ± 1 standard deviation of Fry et al. (2012), where the regional definitions differ slightly.

	Current study		Fry et al. (2012)	
Source region	GWP_{20}	GWP_{100}	GWP_{20}	GWP_{100}
North America	9.20	3.27	15.5 ± 6.8	4.80 ± 2.35
Europe	5.36	2.05	17.2 ± 7.1	5.33 ± 2.47
East Asia	-1.13	0.08	15.7 ± 5.0	4.82 ± 1.73
South Asia	12.7	4.08	26.5 ± 5.3	8.31 ± 1.92

Table C11. Comparison of global and regional anthropogenic (including biomass burning emissions) and total NO_x (Tg N yr^{-1}) and NMVOC (Tg C yr^{-1}) emissions from the base simulations to the multimodel mean ±1 standard deviation of Fiore et al. (2009), where the regional definitions differ slightly.

	Current study					Fiore et al. (2009)				
	Global	NA	EU	EA	IN	Global	NA	EU	EA	SA
Anthropogenic NO_x	37.8	6.6	3.7	6.8	2.0	32.5 ±6.0	7.4 ±0.4	7.3 ±0.6	6.0 ±1.4	2.4 ±0.4
Total NO_x	45.8	7.5	4.2	7.4	2.5	46.5 ±5.7	8.5 ±0.8	8.4 ±1.1	7.1 ±1.4	3.3 ±0.5
Anthropogenic NMVOC	129.3	12.4	7.7	21.0	8.0	96.8 ±41.8	16 ±7.0	19.0 ±11	16 ±6.5	10 ±3.9
Total NMVOC	974.5	86.2	17.8	45.3	26.4	630 ±221	62 ±24	37 ±13	48 ±14	33 ±8.8

Table C12. Comparison of global tropospheric CH_4, O_3, and SO_4^{2-} responses per unit emissions from 4 regional reductions to the multimodel mean ±1 standard deviation of Fry et al. (2012), where the regional definitions differ slightly.

	Current study				Fry et al. (2012)			
	NA	EU	EA	IN	NA	EU	EA	SA
Global CH_4 (ppbv (Tg C yr^{-1})$^{-1}$)	0.80	0.61	0.40	0.65	0.50 ±0.54	0.45 ±0.41	0.46 ±0.42	0.86 ±0.34
Global O_3 (Tg O_3 (Tg C yr^{-1})$^{-1}$)	0.059	0.082	0.088	0.061	0.12 ±0.05	0.12 ±0.05	0.12 ±0.04	0.11 ±0.04
Global SO_4^{2-} (Gg SO_4^{2-} (Tg C yr^{-1})$^{-1}$)	0.32	0.60	1.01	0.0092	-0.12 ± 0.43	0.11 ± 0.69	-0.40 ±0.38	-0.039 ±0.18

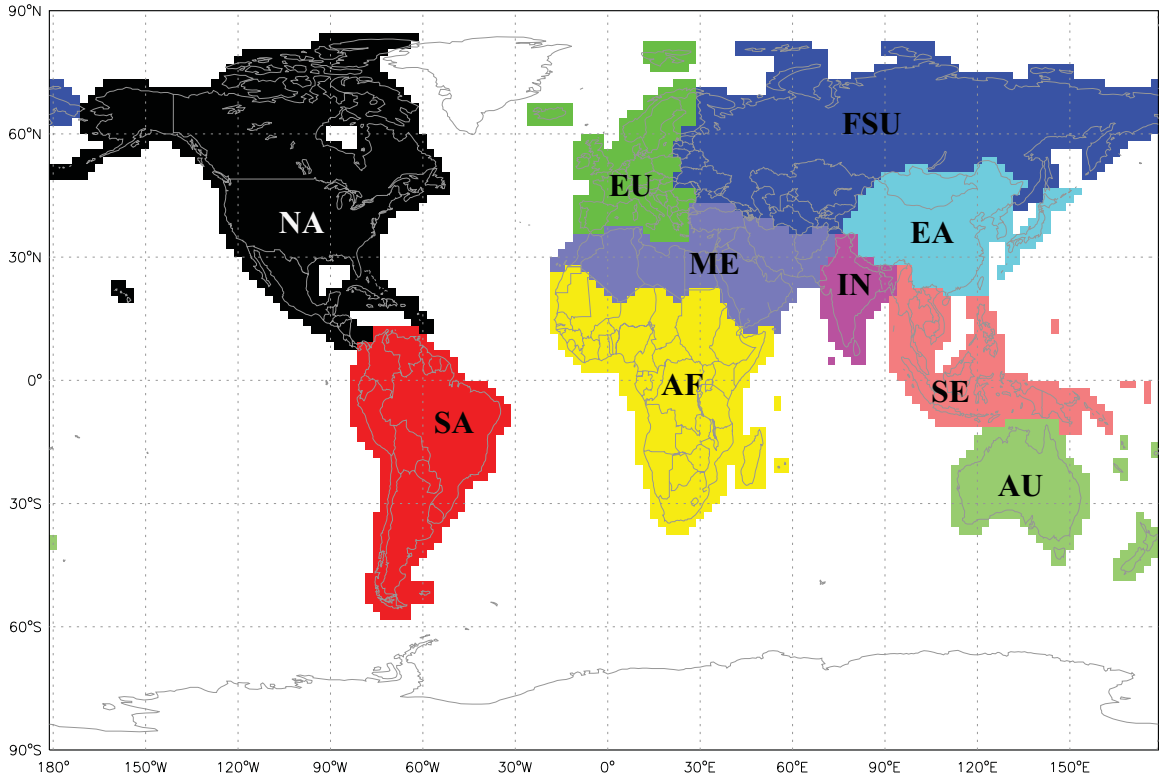

Figure C1. Definition of 10 regions.

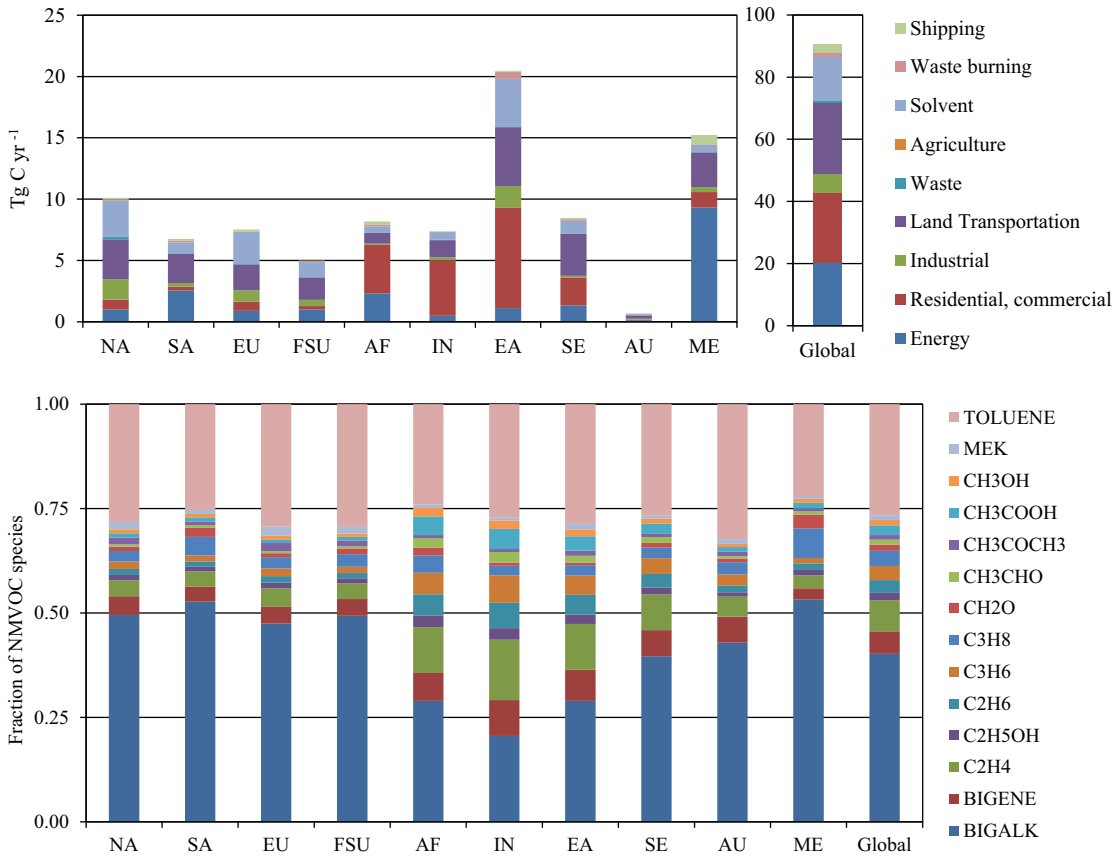

Figure C2. Annual average anthropogenic NMVOC emissions (Tg C yr^{-1}) by region and sector (top), and by region and fraction of individual MOZART-4 NMVOC species (bottom) for the base simulation, from the RCP8.5 emissions inventory for the year 2005.

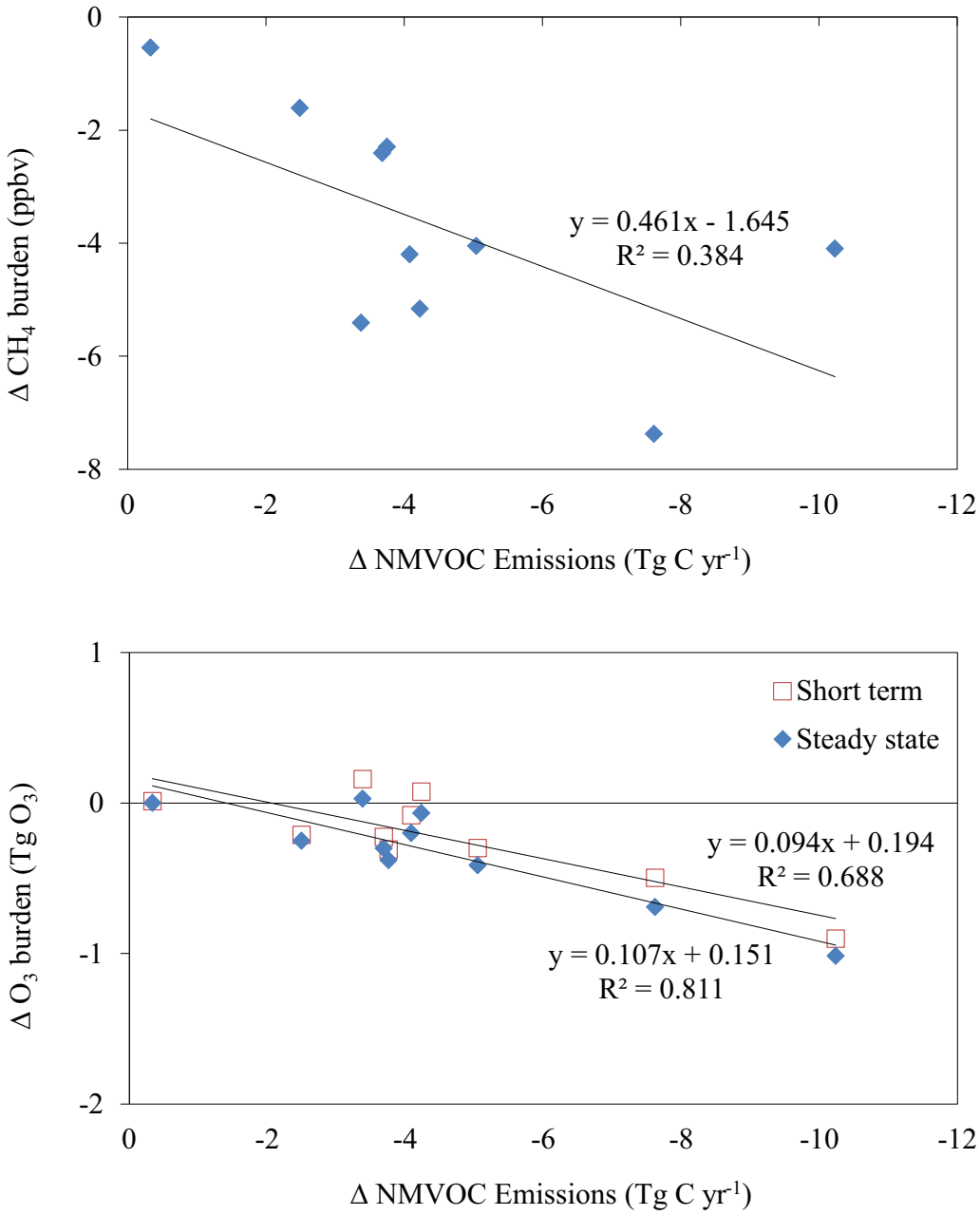

Figure C3. Changes in tropospheric CH_4 (top) and short-term and steady-state surface O_3 (bottom) as a function of NMVOC emissions change for each of the regional reductions relative to the base.

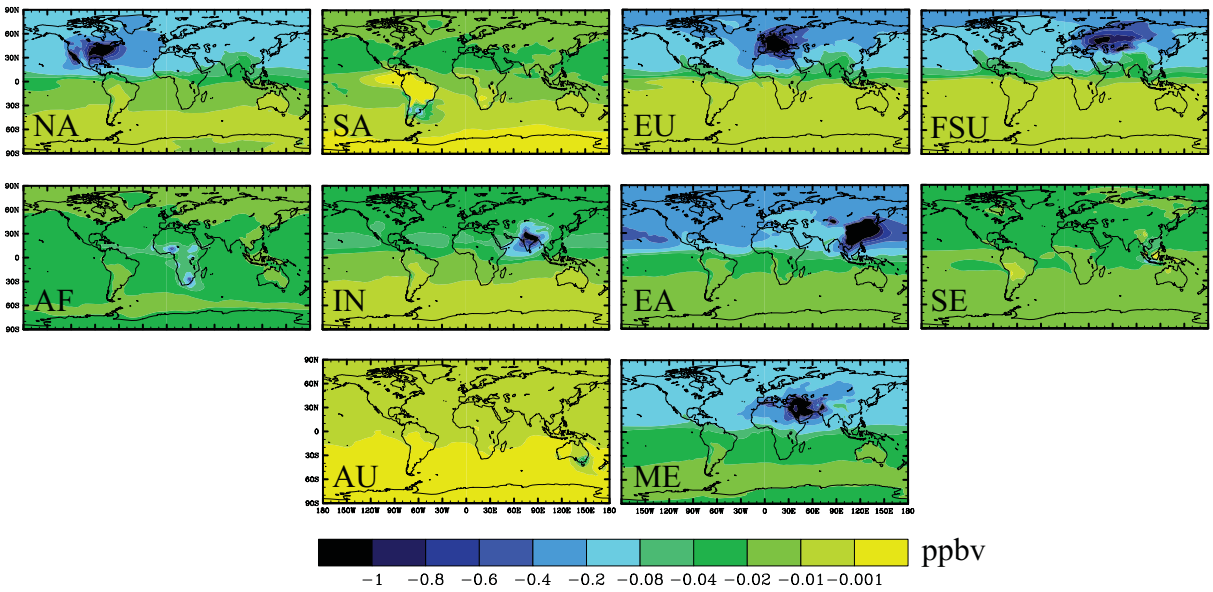

Figure C4. Global distribution of annual average changes in steady-state surface O_3 (ppbv) for each of the regional reduction simulations relative to the base.

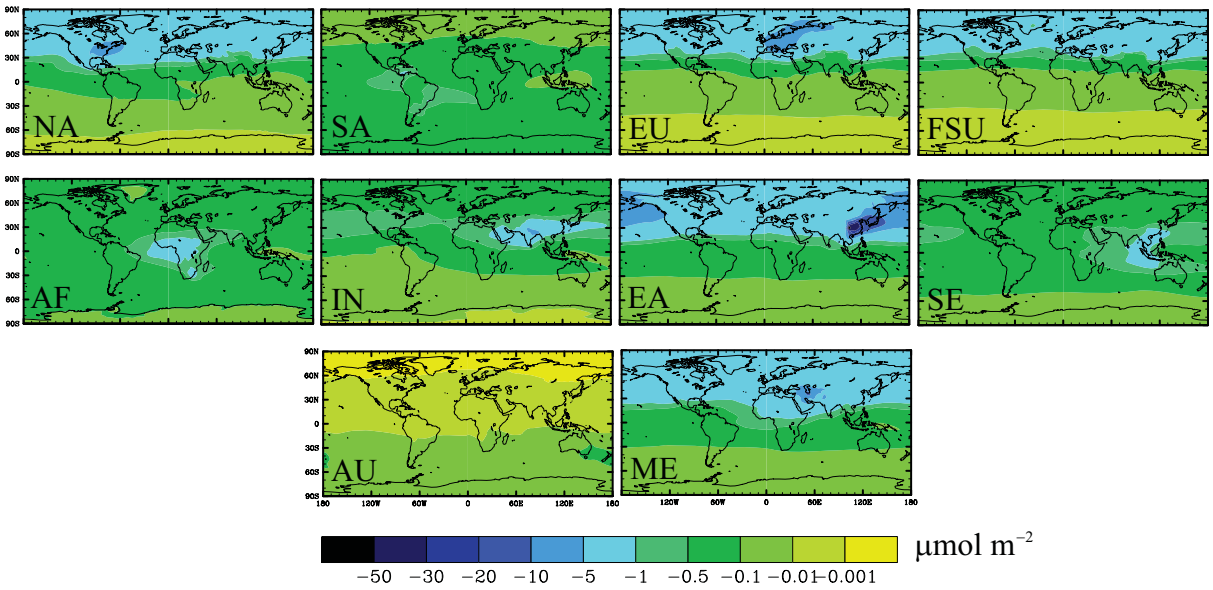

Figure C5. Global distribution of annual average changes in tropospheric PAN (μmol m^{-2}) for each of the regional reduction simulations relative to the base.

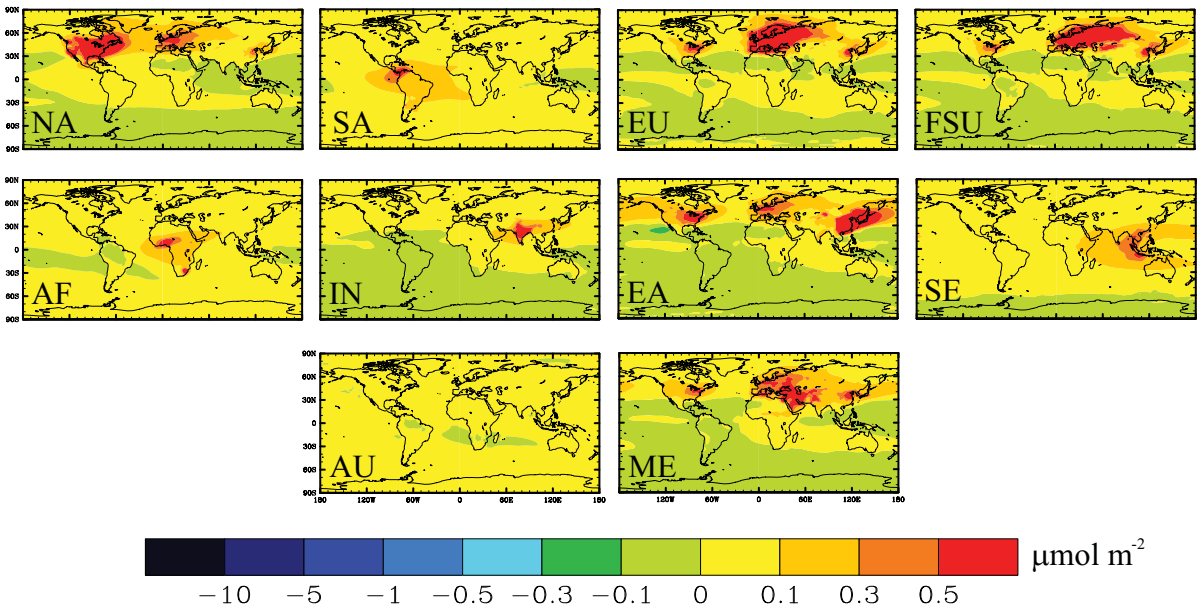

Figure C6. Global distribution of annual average changes in tropospheric NO_x (NO_x = NO + NO_2) (μmol m^{-2}) for each of the regional reduction simulations relative to the base.

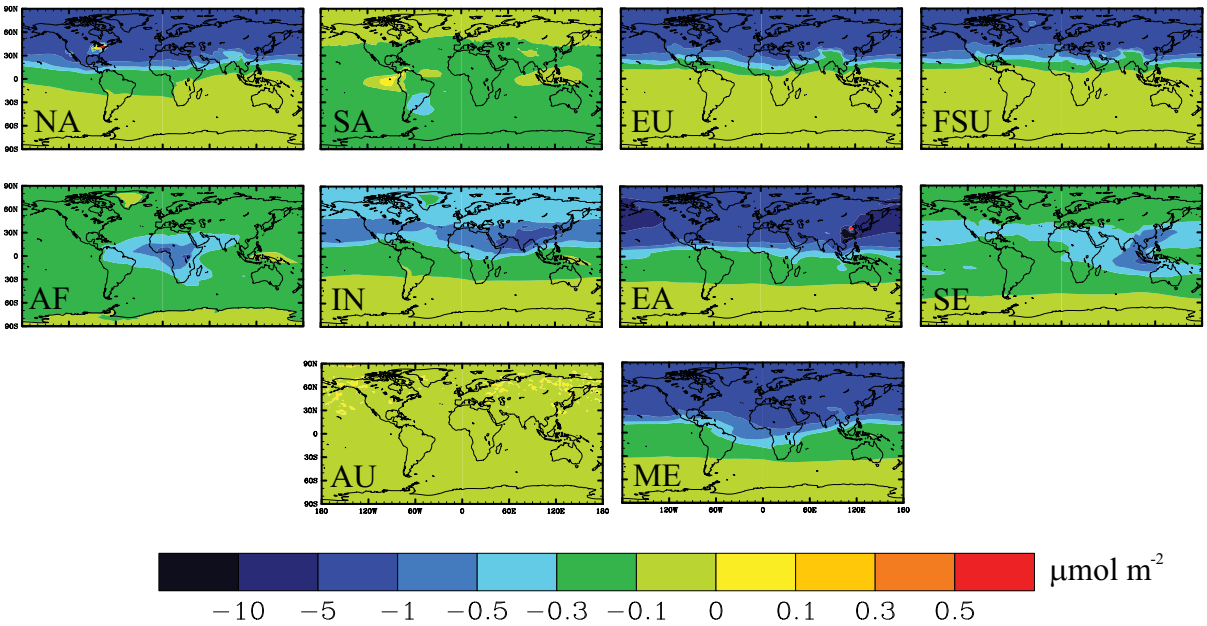

Figure C7. Global distribution of annual average changes in tropospheric NO_y (NO_y = NO + NO_2 + HNO_3 + PAN + HONO + NO_3 + N_2O_5 + organic nitrates + particulate nitrate + all other reservoir species) (μmol m^{-2}) for each of the regional reduction simulations relative to the base.

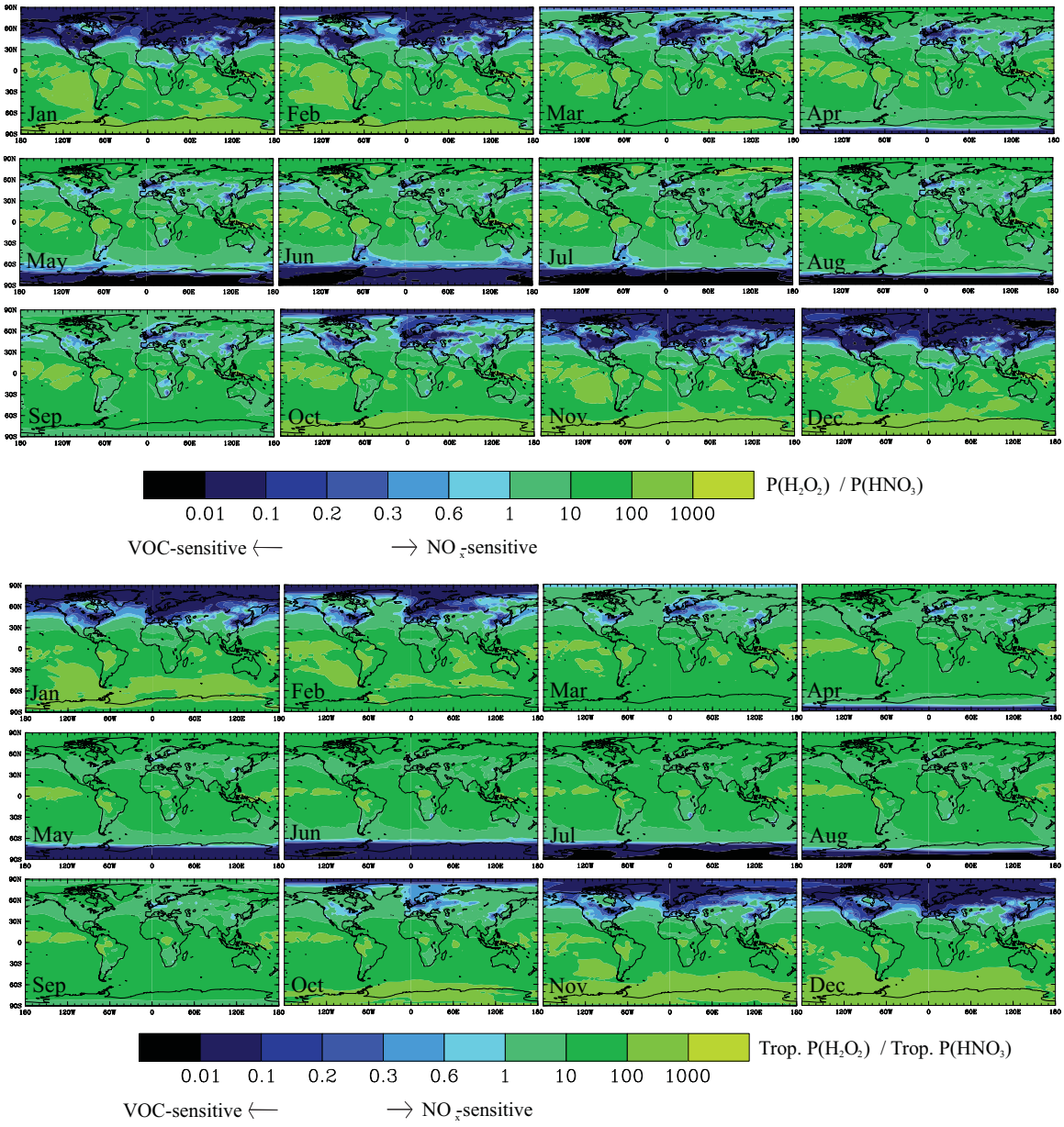

Figure C8. Global distribution of monthly average surface (top) and tropospheric column (bottom) H_2O_2 production / HNO_3 production ($P[H_2O_2]$ / $P[HNO_3]$) for the base simulation, where the transition between VOC-sensitive and NO_x-sensitive regimes is ~0.2 (Liu et al., 2010).

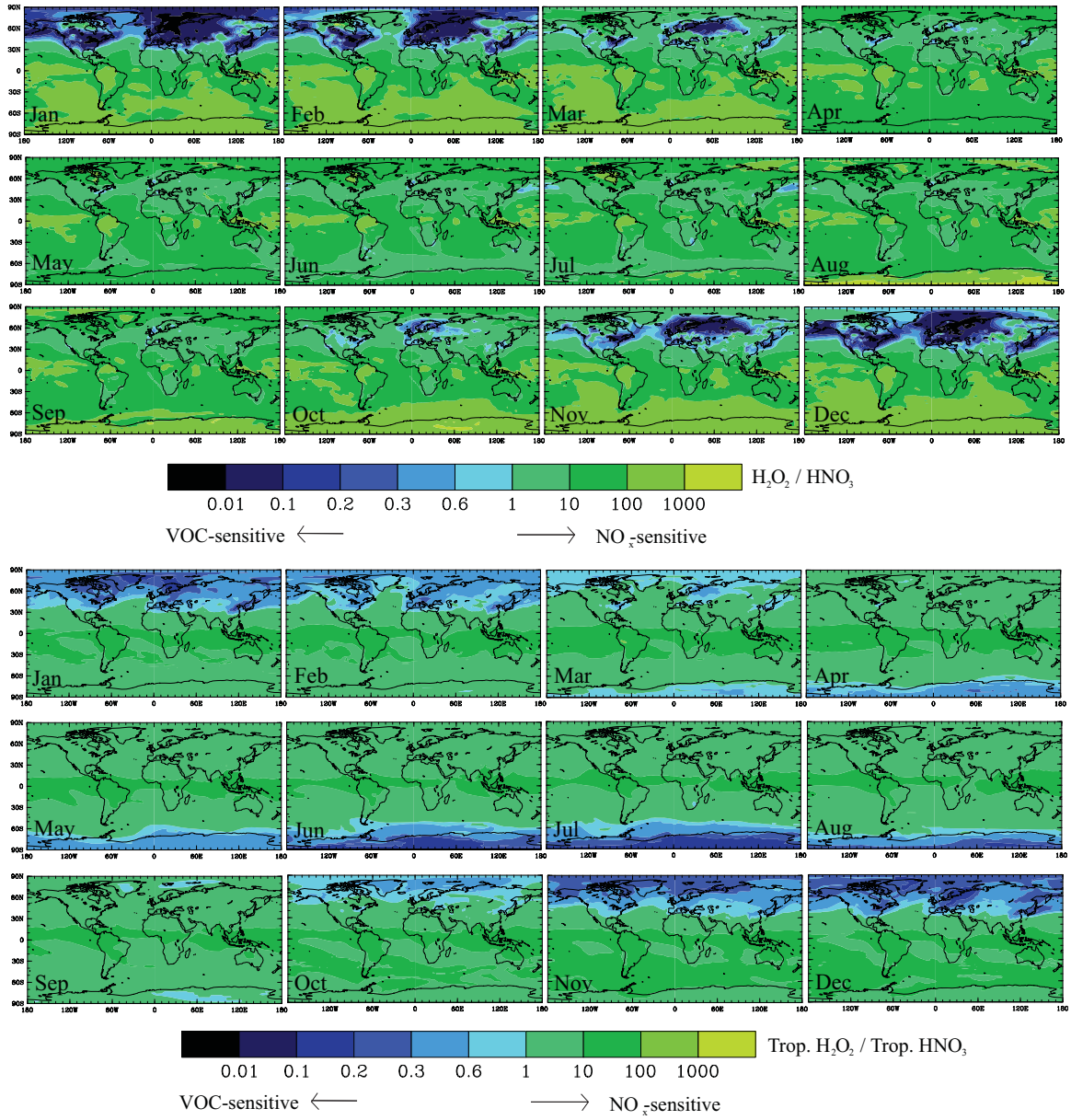

Figure C9. Global distribution of monthly average surface (top) and tropospheric column (bottom) H_2O_2 / HNO_3 for the base simulation, where the transition between VOC-sensitive and NO_x-sensitive regimes is ~0.3 to 0.6 (Sillman et al., 1997).

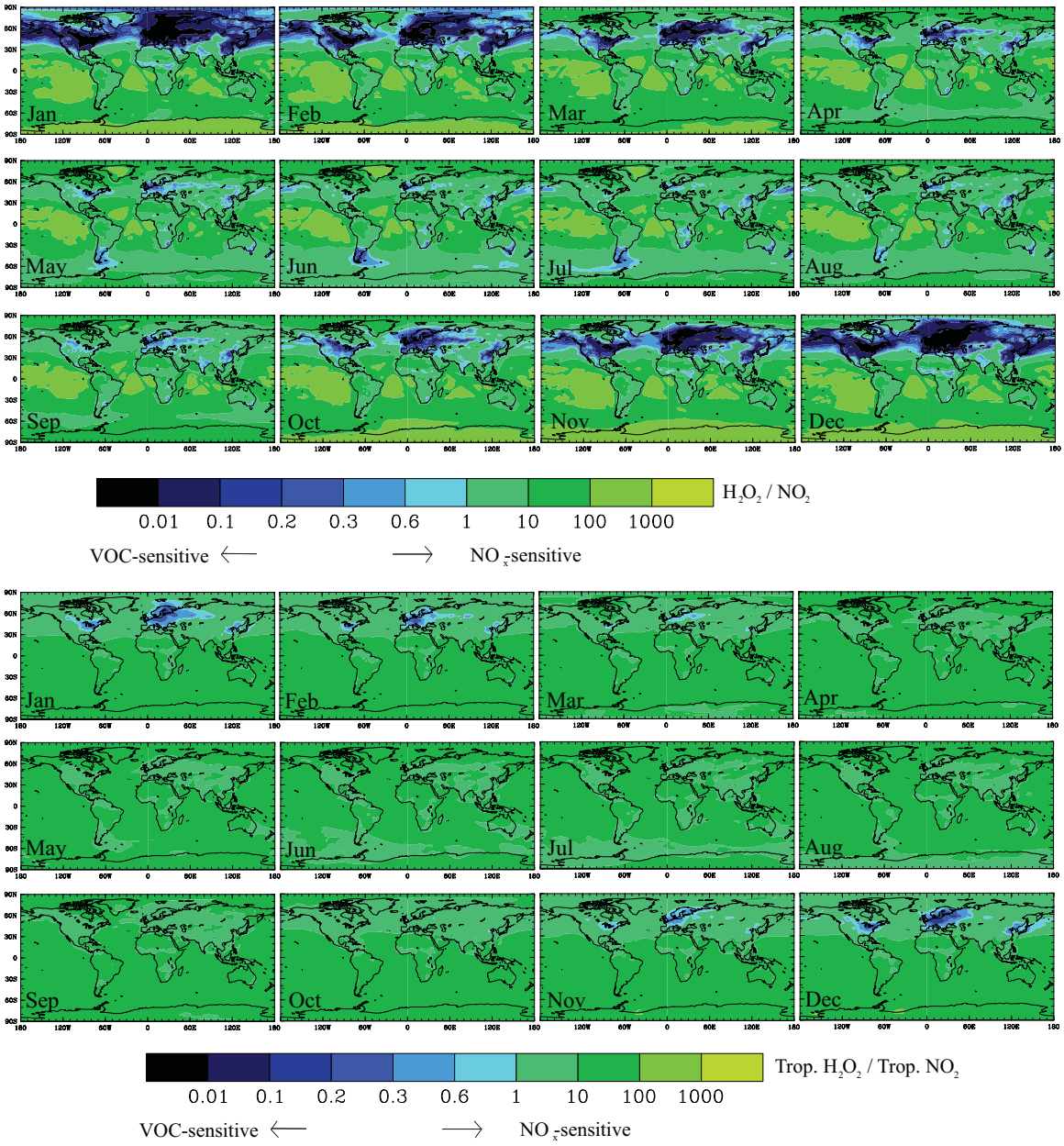

Figure C10. Global distribution of monthly average surface (top) and tropospheric column (bottom) H_2O_2 / NO_2 for the base simulation, where the transition between VOC-sensitive and NO_x-sensitive regimes is ~0.2 to 0.35 (Sillman et al., 1997).

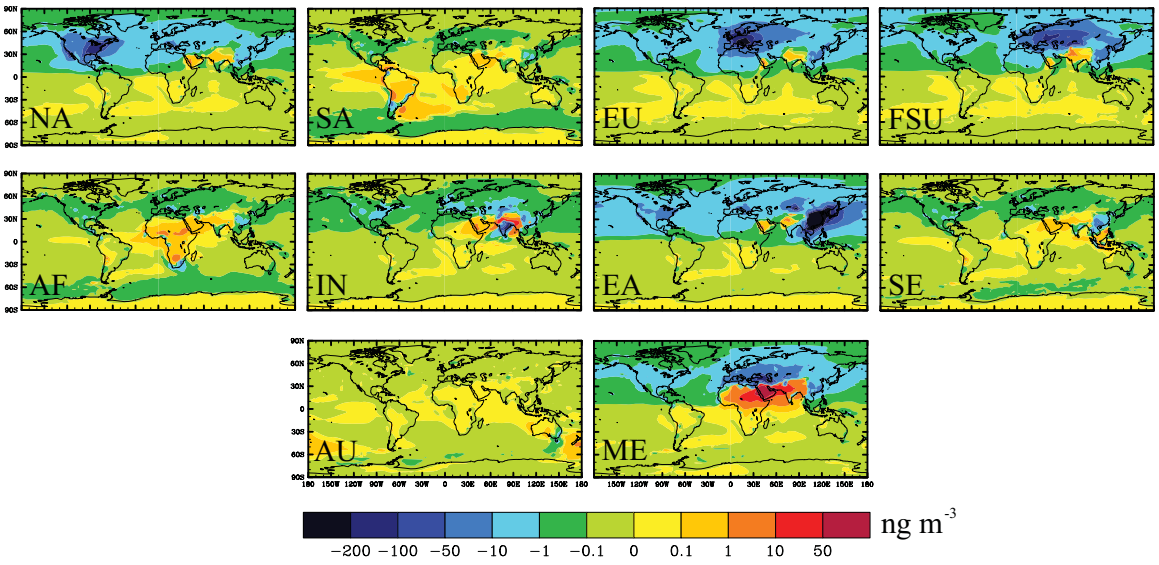

Figure C11. Global distribution of annual average changes in surface SO_4^{2-} (ng m^{-3}) for each of the regional reduction simulations relative to the base.

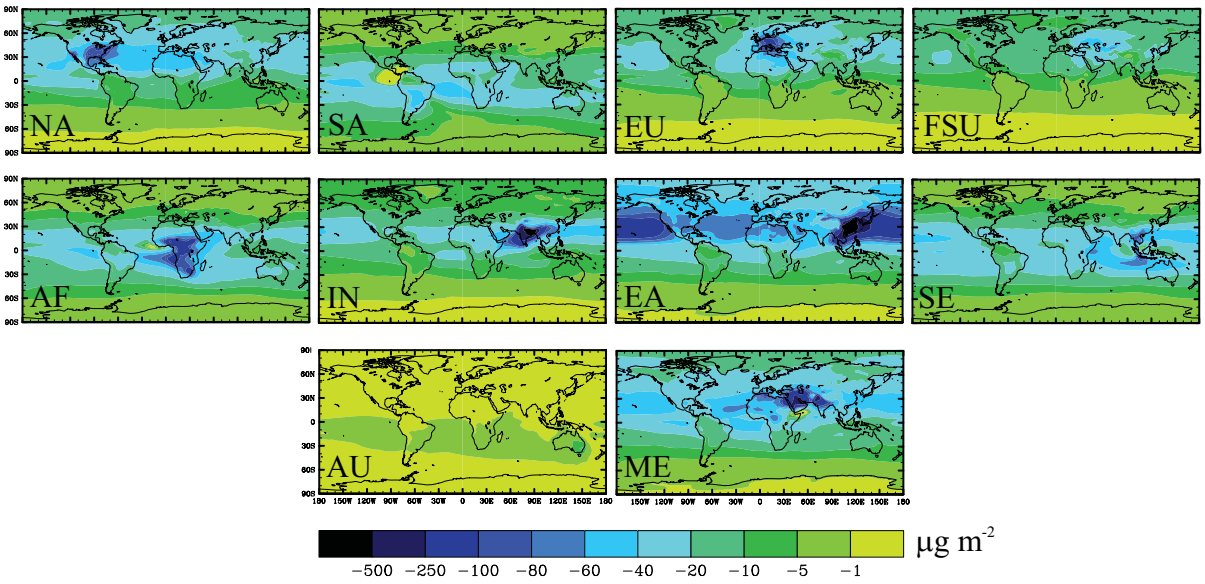

Figure C12. Global distribution of annual average changes in tropospheric H_2O_2 (µg m^{-2}) for each of the regional reduction simulations relative to the base.

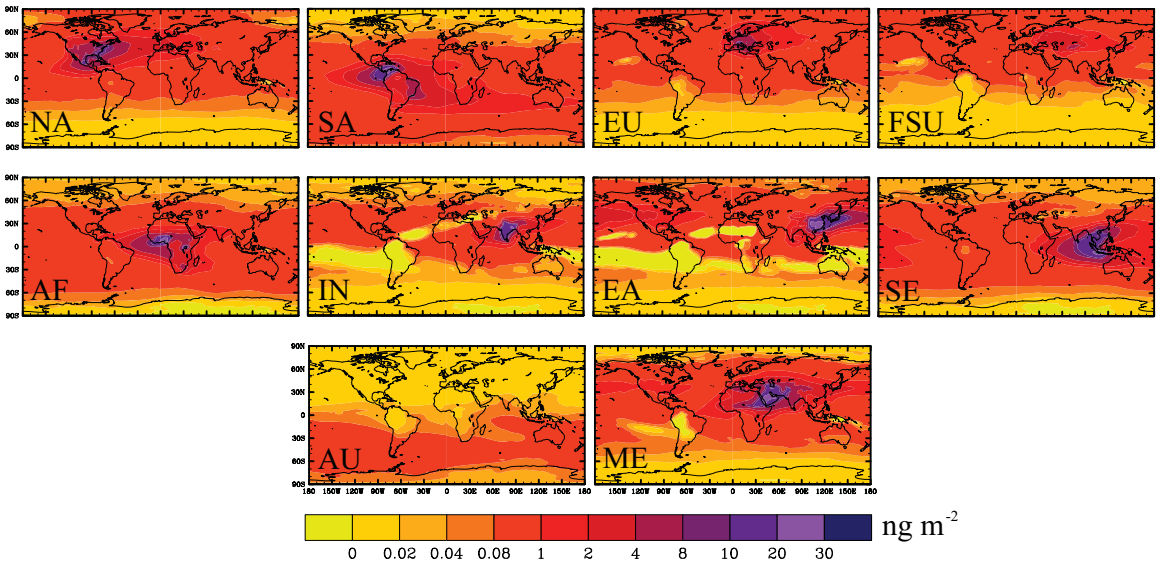

Figure C13. Global distribution of annual average changes in tropospheric OH (ng m^{-2}) for each of the regional reduction simulations relative to the base.

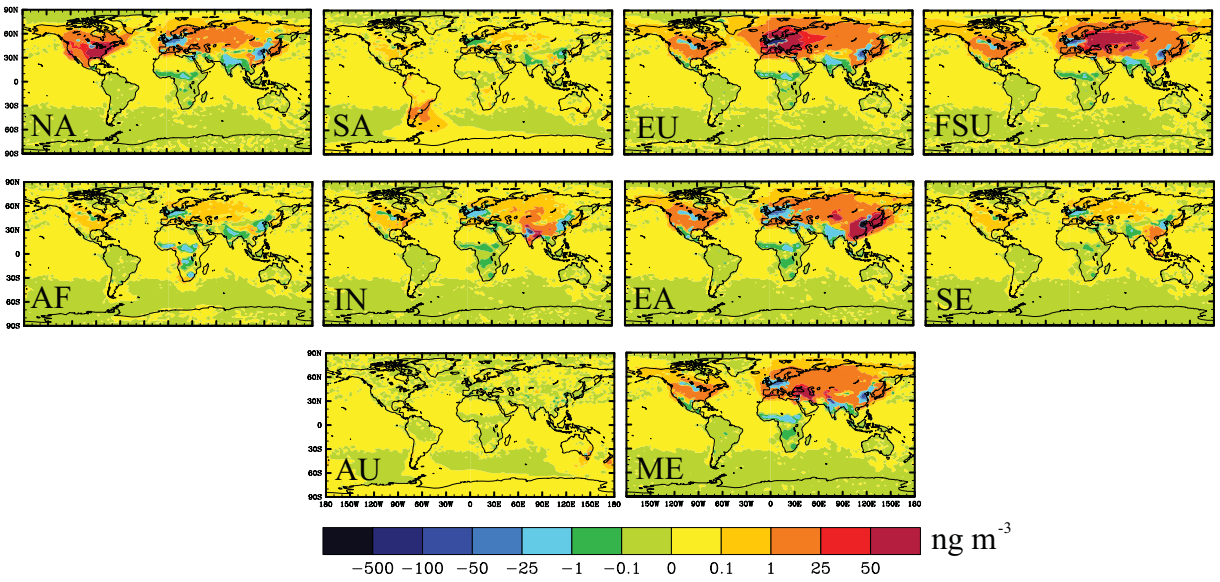

Figure C14. Global distribution of annual average changes in surface NO_3^- (expressed as NH_4NO_3 in ng m^{-3}) for each of the regional reduction simulations relative to the base.

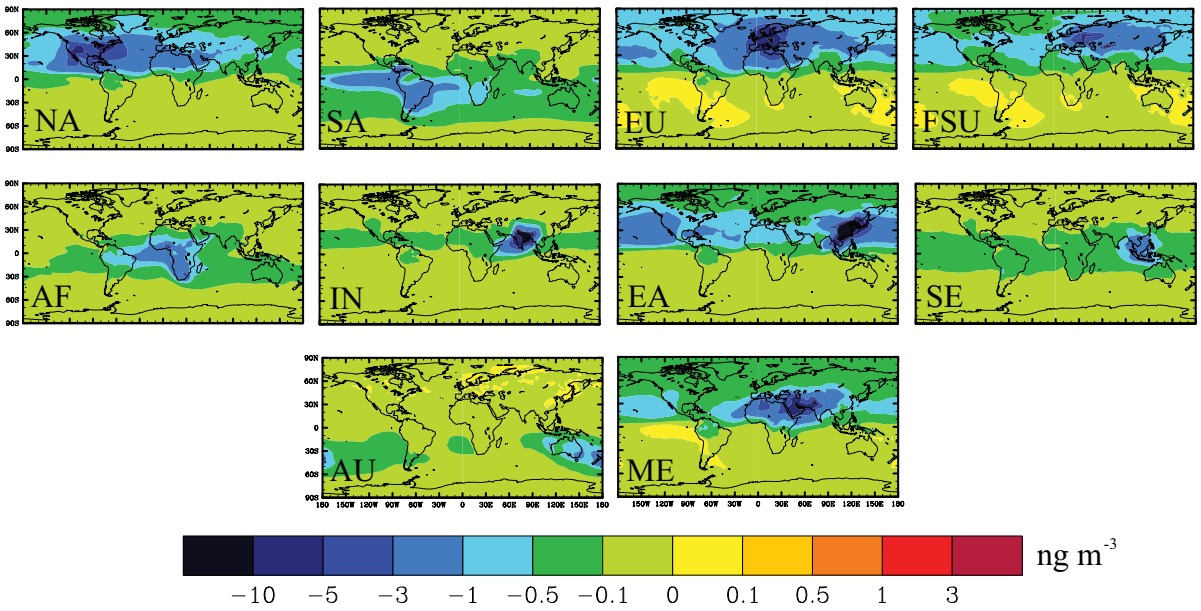

Figure C15. Global distribution of annual average changes in surface SOA (ng m^{-3}) for each of the regional reduction simulations relative to the base.

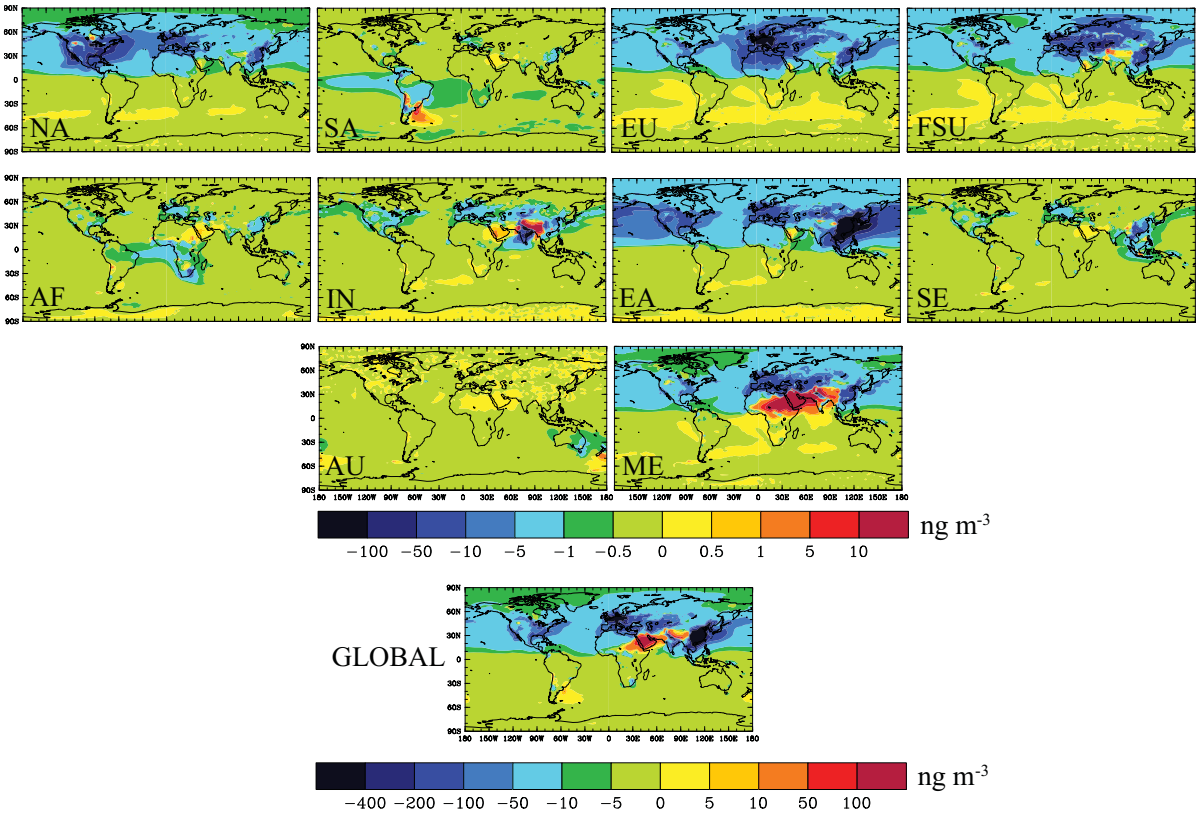

Figure C16. Global distribution of annual average changes in surface $PM_{2.5}$ (sum of BC, OC, $(NH_4)_2SO_4$, NH_4NO_3, SOA) (ng m^{-3}) for the global and regional reduction simulations relative to the base.

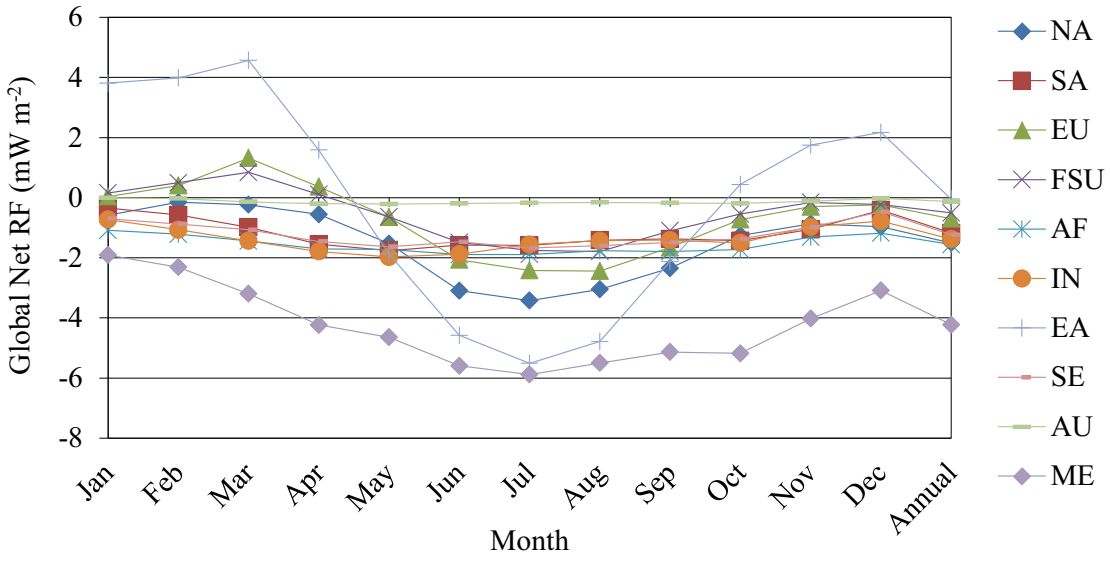

Figure C17. Global monthly and annual average net RF (mW m^{-2}) due to changes in tropospheric steady-state O_3, CH_4, and SO_4^{2-} for each regional CO reduction simulation minus the base simulation.

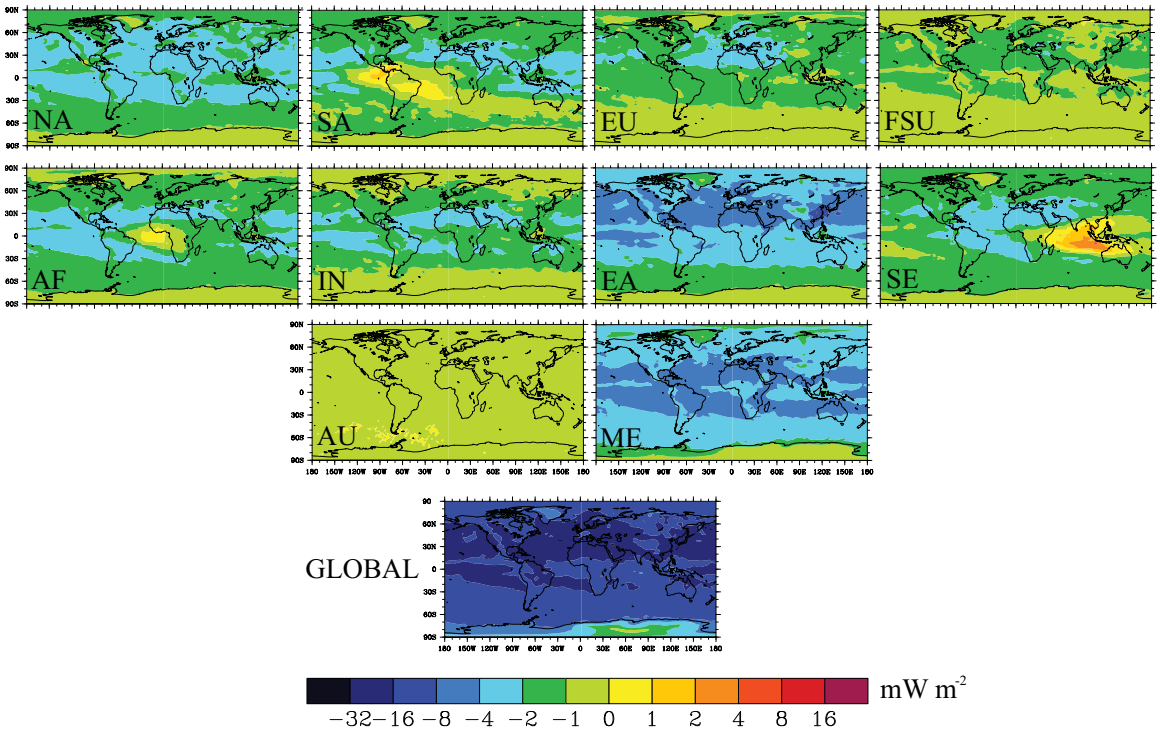

Figure C18. Annual average changes in longwave (infrared) radiation (mW m^{-2}) due to changes in tropospheric steady-state O_3, CH_4, and SO_4^{2-} for the regional reduction simulations minus the base simulation.

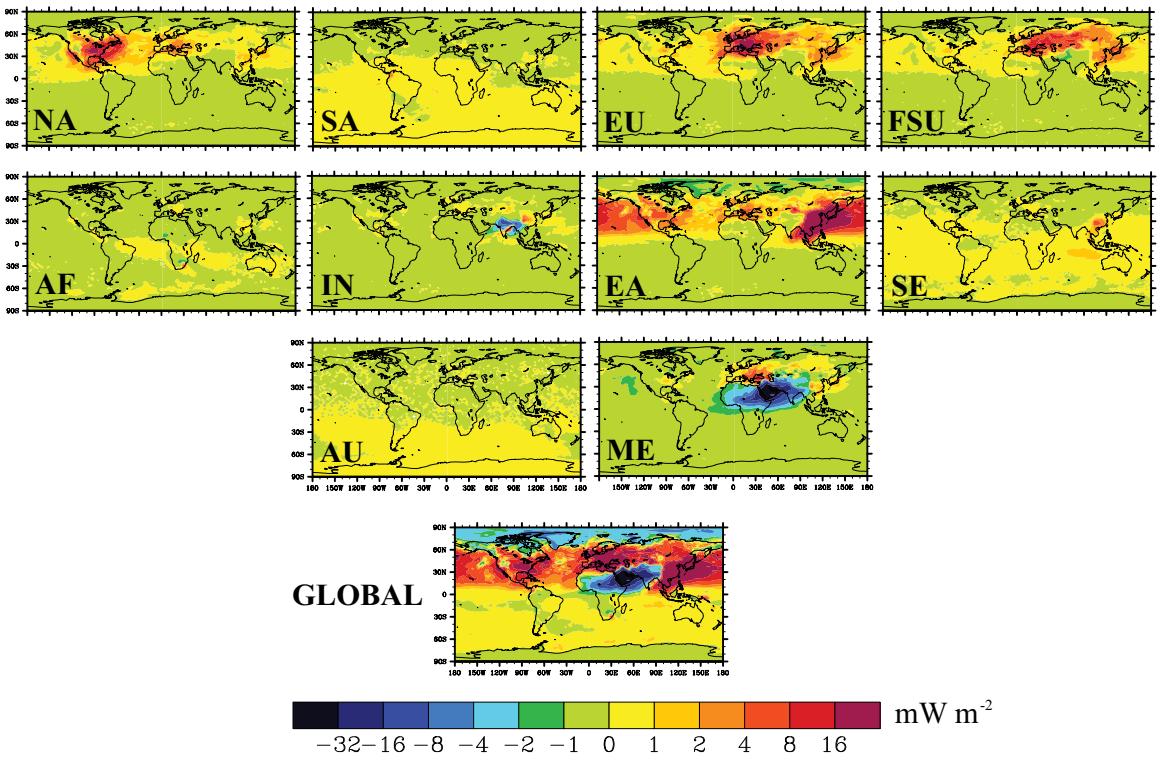

Figure C19. Annual average changes in shortwave (solar) radiation (mW m^{-2}) due to changes in tropospheric steady-state O_3, CH_4, and SO_4^{2-} for the regional reduction simulations minus the base simulation.

References

Akimoto, H. (2003), Global air quality and pollution, Science, 302, 1716-1719, doi:10.1126/science.1092666.

Barth, M. C., P. J. Rasch, J. T. Kiehl, C. M. Benkovitz, and S. E. Schwartz (2000), Sulfur chemistry in the National Center for Atmospheric Research Community Climate Model: Description, evaluation, features, and sensitivity to aqueous chemistry, J. Geophys. Res., 105, D1, 1387-1415, doi:10.1029/1999JD900773.

Bauer, S. E., D. Koch, N. Unger, S. M. Metzger, D. T. Shindell, and D. G. Streets (2007), Nitrate aerosols today and in 2030: a global simulation including aerosols and tropospheric ozone, Atmos. Chem. Phys., 7, 5043-5059.

Bauer, S. E., and S. Menon (2012), Aerosol direct, indirect, semidirect, and surface albedo effects from sector contributions based on the IPCC AR5 emissions for preindustrial and present-day conditions, J. Geophys. Res., 117, D01206, doi:10.1029/2011JD016816.

Berntsen, T. K., J. S. Fuglestvedt, M. M. Joshi, K. P. Shine, N. Stuber, M. Ponater, R. Sausen, D. A. Hauglustaine, and L. Li (2005), Response of climate to regional emissions of ozone precursors: sensitivities and warming potentials, Tellus, 57B, 283-304, doi:10.1111/j.1600-0889.2005.00152.x.

Berntsen, T. K., J. Fuglestvedt, G. Myhre, F. Stordal, and T. F. Berglen (2006), Abatement of greenhouse gases: Does location matter?, Climatic Change, 74, 377-411, doi:10.1007/s10584-006-0433-4.

Bowman, K. and D. K. Henze (2012), Attribution of direct ozone radiative forcing to spatially resolved emissions, Geophys. Res. Lett., 39, L22704, doi:10.1029/2012GL053274.

Carlton, A. G., C. Wiedinmyer, and J. H. Kroll (2009), A review of Secondary Organic Aerosol (SOA) formation from isoprene, Atmos. Chem. Phys., 9, 4987-5005.

Carlton, A. G., P. V. Bhave, S. L. Napelenok, E. O. Edney, G. Sarwar, R. W. Pinder, G. A. Pouliot, and M. Houyoux (2010), Model representation of secondary organic aerosol in CMAQv4.7, Environ. Sci. Technol., 44, 8553-8560, doi: 10.1021/es100636q.

Carlton, A. G., R. W. Pinder, P. V. Bhave, and G. A. Pouliot (2010), To what extent can biogenic SOA be controlled, Environ. Sci. Technol., 44, 3376-3380, doi:10.1021/es903506b.

Chung, S. and J. Seinfeld (2002), Global distribution and climate forcing of carbonaceous aerosols, J. Geophys. Res., 107, 4407, doi:10.1029/2001JD001397.

Cionni, I., V. Eyring, J.-F. Lamarque, W. J. Randel, D. S. Stevenson, F. Wu, G. E. Bodeker ,T. G. Shepherd, D. T. Shindell, and D. W. Waugh (2011), Ozone database in support of CMIP5 simulations: results and corresponding radiative forcing, Atmos. Chem. Phys., 11, 11267-11292, doi:10.5194/acp-11-11267-2011.

Collins, W. J., R. G. Derwent, C. E. Johnson, and D. S. Stevenson (2002), The oxidation of organic compounds in the troposphere and their global warming potentials, Clim. Change, 52, 453-479, doi:10.1023/A:1014221225434.

Collins, W. J., S. Sitch, and O. Boucher (2010), How vegetation impacts affect climate metrics for ozone precursors, J. Geophys. Res., 115, D23308, doi:10.1029/2010JD014187.

Collins, W.J., M. M. Fry, H. Yu, J. S. Fuglestvedt, D. T. Shindell, and J. J. West (2013), Global and regional temperature-change potentials for near-term climate forcers, Atmos. Chem. Phys., 13, 2471-2485, doi:10.5194/acp-13-2471-2013.

Daniel, J. S., and S. Solomon (1998), On the climate forcing of carbon monoxide, J. Geophys. Res., 103(D11), 13, 249-13, 260, doi:10.1029/98JD00822.

Dentener, F., D. Stevenson, J. Cofala, R. Mechler, M. Amann, P. Bergamaschi, F. Raes, and R. Derwent (2005), The impact of air pollutant and methane emission controls on tropospheric ozone and radiative forcing: CTM calculations for the period 1990-2030, Atmos. Chem. Phys., 5, 1731-1755.

Dentener, F., D. Stevenson, K. Ellingsen, T. V. Noije, M. Schultz, M. Amann, C. Atherton, N. Bell, D. Bergmann, I. Bey, L. Bouwman, T. Butler, J. Cofala, B. Collins, J. Drevet, R. Doherty, B. Eickhout, H. Eskes, A. Fiore, M. Gauss, D. Hauglustaine, L. Horowitz, I. S. A. Isaksen, B. Josse, M. Lawrence, M. Krol, J. F. Lamarque, V. Montanaro, J. F. Müller, V. H. Peuch, G. Pitari, J. Pyle, S. Rast, J. Rodriguez, M. Sanderson, N. H. Savage, D. Shindell, S. Strahan, S. Szopa, K. Sudo, R. V. Dingenen, O. Wild, and G. Zeng (2006), The global atmospheric environment for the next generation, Environ. Sci. Technol., 40, 11, 3586-3594, doi:10.1021/es0523845.

Derwent, R. G., W. J. Collins, C. E. Johnson, and D. S. Stevenson (2001), Transient behaviour of tropospheric ozone precursors in a global 3-D CTM and their indirect greenhouse effects, Climatic Change, 49, 463-487, doi:10.1023/A:1010648913655.

Derwent, R. G., D. S. Stevenson, R. M. Doherty, W. J. Collins, M. G. Sanderson, and C. E. Johnson (2008), Radiative forcing from surface NOx emissions: spatial and seasonal variations, Climatic Change, 88, 385-401, doi:10.1007/s10584-007-9383-8.

Donner, L. J., B. L. Wyman, R. S. Hemler, L. W. Horowitz, Y. Ming, M. Zhao, J.-C. Golaz, P. Ginoux, S.-J. Lin, M. D. Schwarzkopf, J. Austin, G. Alaka, W. F. Cooke, T. L. Delworth, S. M. Freidenreich, C. T. Gordon, S. M. Griffies, I. M. Held, W. J. Hurlin, S. A. Klein, T. R. Knutson, A. R. Langehorst, H.-C. Lee, Y. Lin, B. I. Magi, S. L. Malyshev, P. C. D. Milly, V. Naik, M. J. Nath, R. Pincus, J. J. Ploshay, V. Ramaswamy, C. J. Seman, E. Shevliakova, J. J. Sirutis, W. F. Stern, R. J. Stouffer, R. J. Wilson, M.

Winton, A. T. Wittenberg, and F. Zeng (2011), The dynamical core, physical parameterizations, and basic simulation characteristics of the atmospheric component AM3 of the GFDL global coupled model CM3, J. Climate, 24, 13, 3484-3519,

Duce, R. A, J. LaRoche, K. Altieri, K. R. Arrigo, A. R. Baker, D. G. Capone, S. Cornell, F. Dentener, J. Galloway, R. S. Ganeshram, R. J. Geider, T. Jickells, M. M. Kuypers, R. Langlois, P. S. Liss, S. M. Liu, J. J. Middelburg, C. M. Moore, S. Nickovic, A. Oschlies, T. Pedersen, J. Prospero, R. Schlitzer, S. Seitzinger, L. L. Sorensen, M. Uematsu, O. Ulloa, M. Voss, B. Ward, and L. Zamora (2008), Impacts of atmospheric anthropogenic nitrogen on open ocean, Science, 320, 893, doi:10.1126/science.1150369.

Duncan, B. N., J. A. Logan, I. Bey, I. A. Megretskaia, R. M. Yantosca, P. C. Novelli, N. B. Jones, and C. P. Rinsland (2007), The global budget of CO, 1988-1997: Source estimates and validation with a global model, J. Geophys. Res., 112, D22301, doi:10.1029/2007JD008459.

Ehhalt, D., Prather, M., Dentener, F., Derwent, R., Dlugokencky, E., Holland, E., Isaksen, I., Katima, J., Kirchhoff, V., Matson, P., Midgley, P., and Wang, M.: Atmospheric chemistry and greenhouse gases (2001), in: Climate Change 2001: The Scientific Basis, Contribution of Working Group I to the Third Assessment Report of the Intergovernmental Panel on Climate Change, edited by: Houghton, J. T., Ding, Y., Griggs, D. J., Noguer, M., van der Linden, P. J., Dai, X., Maskell, K., and Johnson, C. A., Cambridge University Press, Cambridge, UK.

Emmons, L. K., S. Walters, P. G. Hess, J.-F. Lamarque, G. G. Pfister, D. Fillmore, C. Granier, A. Guenther, D. Kinnison, T. Laepple, J. Orlando, X. Tie, G. Tyndall, C. Wiedinmyer, S. L. Baughcum, and S. Kloster (2010), Description and evaluation of the Model for Ozone and Related chemical Tracers, version 4 (MOZART-4), Geosci. Model Dev., 3, 43-67, doi:10.5194/gmd-3-43-2010.

Felzer, B. S., T. Cronin, J. M. Reilly, J. M. Melilloa, and X. D. Wang (2007), Impacts of ozone on trees and crops, C.R. Geoscience, 339, 784-798, doi:10.1016/j.crte.2007.08.008.

Fiore, A. M., D. J. Jacob, B. D. Field, D. G. Streets, S. D. Fernandes, and C. Jang (2002), Linking ozone pollution and climate change: The case for controlling methane, Geophys. Res. Lett., 29, 19, 1919, doi:10.1029/2002GL015601.

Fiore, A. M., J. J. West, L. W. Horowitz, V. Naik, and M. D. Schwarzkopf (2008), Characterizing the tropospheric ozone response to methane emission controls and the benefits to climate and air quality, J. Geophys. Res., 113, D08307, doi:10.1029/2007JD009162.

Fiore, A. M., F. J. Dentener, O. Wild, C. Cuvelier, M. G. Schultz, P. Hess, C. Textor, M. Schulz, R. M. Doherty, L. W. Horowitz, I. A. MacKenzie, M. G. Sanderson, D. T. Shindell, D. S. Stevenson, S. Szopa, R. Van Dingenen, G. Zeng, C. Atherton, D. Bergmann, I. Bey, G. Carmichael, W. J. Collins, B. N. Duncan, G. Faluvegi, G. Folberth, M. Gauss, S. Gong, D. Hauglustaine, T. Holloway, I. S. A. Isaksen, D. J. Jacob, J. E.

Jonson, J. W. Kaminski, T. J. Keating, A. Lupu, E. Marmer, V. Montanaro, R. J. Park, G. Pitari, K. J. Pringle, J. A. Pyle, S. Schroeder, M. G. Vivanco, P. Wind, G. Wojcik, S. Wu, and A. Zuber (2009), Multimodel estimates of intercontinental source-receptor relationships for ozone pollution, J. Geophys. Res., 114, D04301, doi:10.1029/2008JD010816.

Fiore, Arlene M., Vaishali Naik, Dominick V. Spracklen, Allison Steiner, Nadine Unger, Michael Prather, Dan Bergmann, Philip J. Cameron-Smith, Irene Cionni, William J. Collins, Stig Dalsøren, Veronika Eyring, Gerd A. Folberth, Paul Ginoux, Larry W. Horowitz, Béatrice Josse, Jean-François Lamarque, Ian A. MacKenzie, Tatsuya Nagashima, Fiona M. O'Connor, Mattia Righi, Steven T. Rumbold, Drew T. Shindell, Ragnhild B. Skeie, Kengo Sudo, Sophie Szopa, Toshihiko Takemura, and Guang Zeng (2012), Global air quality and climate, Chem. Soc. Rev., 41, 6663-6683, doi:10.1039/C2CS35095E.

Forster, P. M. D., and K. P. Shine (1997), Radiative forcing and temperature trends from stratospheric ozone changes, J. Geophys. Res., 102, 10, 481-10, 857, doi:10.1029/96JD03510.

Forster, P., V. Ramaswamy, P. Artaxo, T. Berntsen, R. Betts, D. W. Fahey, J. Haywood, J. Lean, D. C. Lowe, G. Myhre, J. Nganga, R. Prinn, G. Raga, M. Schulz and R. Van Dorland, (2007), Changes in Atmospheric Constituents and in Radiative Forcing. In: Climate Change 2007: The Physical Science Basis. Contribution of Working Group I to the Fourth Assessment Report of the Intergovernmental Panel on Climate Change [Solomon, S., D. Qin, M. Manning, Z. Chen, M. Marquis, K.B. Averyt, M. Tignor and H. L. Miller (eds.)], Cambridge University Press, Cambridge, UK, 129-234.

Fry, M. M., V. Naik, J. J. West, M. D. Schwarzkopf, A. M. Fiore, W. J. Collins, F. J. Dentener, D. T. Shindell, C. Atherton, D. Bergmann, B. N. Duncan, P. Hess, I. A. MacKenzie, E. Marmer, M. G. Schultz, S. Szopa, O. Wild, and G. Zeng (2012), The influence of ozone precursor emissions from four world regions on tropospheric composition and radiative climate forcing, J. Geophys. Res., 117, D07306, doi:10.1029/2011JD017134.

Fry, M. M., M. D. Schwarzkopf, Z. Adelman, V. Naik, W. J. Collins, and J. J. West (2013), Net radiative forcing and air quality responses to regional CO emission reductions, Atmos. Chem. Phys., 13, 5381-5399, doi:10.5194/acp-13-5381-2013.

Fry, M. M., M. D. Schwarzkopf, Z. Adelman, and J. J. West (submitted, 2013), Air quality and radiative forcing impacts of anthropogenic volatile organic compound emissions from ten world regions, Atmos. Chem. Phys., acp-2013-389.

Fuglestvedt, J. S., I. S. A. Isaksen, and W.-C. Wang (1996), Estimates of indirect global warming potentials for CH_4, CO, and NO_x. Clim. Change, 34, 405-437.

Fuglestvedt, J. S., T. K. Berntsen, I. S. A. Isaksen, H. T. Mao, X. Z. Liang, and W. C. Wang (1999), Climatic forcing of nitrogen oxides through changes in tropospheric ozone

and methane; global 3D model studies, Atmos. Environ., 33, 961-977, doi:10.1016/S1352-2310(98)00217-9.

Fuglestvedt, J. S., Shine, K. P., Berntsen, T., Cook, J., Lee, D. S., Stenke, A., Skeie, R. B., Velders, G. J. M., Waitz, I. A. (2010), Transport impacts on atmosphere and climate: metrics, Atmos. Environ., 44, 4648-4677, doi:10.1016/j.atmosenv.2009.04.044.

GFDL Global Atmospheric Model Development Team (GAMDT) (2004), The new GFDL global atmosphere and land model AM2-LM2: Evaluation with prescribed SST simulations, J. Clim., 17, 4641-4673.

Granier, C., A. Guenther, J. Lamarque, A. Mieville, J. Muller, J. Olivier, J. Orlando, J. Peters, G. Petron, G. Tyndall, and S. Wallens (2005), POET, a database of surface emissions of ozone precursors, available at: http://accent.aero.jussieu.fr/POET_metadata.php.

Granier, C., B. Bessagnet, T. Bond, A. D'Angiola, H. D. van der Gon, G. Frost, A. Heil, J. W. Kaiser, S. Kinne, Z. Klimont, S. Kloster, J.-F. Lamarque, C. Liousse, T. Masui, F. Meleux, A. Mieville, T. Ohara, J.-C. Raut, K. Riahi, M. G. Schultz, S. J. Smith, A. Thompson, J. van Aardenne, G. R. van der Werf, D. P. van Vuuren (2011), Evolution of anthropogenic and biomass burning emissions of air pollutants at global and regional scales during the 1980-2010 period, J. Climate, 109, 163-190, doi:10.1007/s10584-011-0154-1.

Guenther, A., T. Karl, P. Harley, C. Wiedinmeyer, P. L. Palmer, and C. Geron (2006), Estimates of global terrestrial isoprene emissions using MEGAN (Model of Emissions of Gases and Aerosols from Nature), Atmos. Chem. Phys., 6, 3181-3210.

Hauglustaine, D. A., and G. P. Brasseur (2001), Evolution of tropospheric ozone under anthropogenic activities and associated radiative forcing of climate, J. Geophys. Res., 106, 32, 337-32, 360, doi:10.1029/2001JD900175.

Heald, C. L., D. J. Jacob, A. M. Fiore, L. K. Emmons, J. C. Gille, M. N. Deeter, J. Warner, D. P. Edwards, J. H. Crawford, A. J. Hamlin, G. W. Sachse, E. V. Browell, M. A. Avery, S. A. Vay, D. J. Westberg, D. R. Blake, H. B. Singh, S. T. Sandholm, R. W. Talbot, and H. E. Fuelberg (2003), Asian outflow and trans-Pacific transport of carbon monoxide and ozone pollution: An integrated satellite, aircraft and model perspective, J. Geophys. Res., 108(D24), 4804, doi:10.1029/2003JD003507.

Heald, C. L., D. J. Jacob, D. B. A. Jones, P. I. Palmer, J. A. Logan, D. G. Streets, G. W. Sachse, J. C. Gille, R. N. Hoffman, and T. Nehrkorn (2004), Comparative inverse analysis of satellite (MOPITT) and aircraft (TRACE-P) observations to estimate Asian sources of carbon monoxide, J. Geophys. Res., 109, D15S04, doi:10.1029/2004JD005185.

Holland, E. A., and J.-F. Lamarque (1997), Modeling bio-atmospheric coupling of the nitrogen cycle through NO_x emissions and NO_y deposition, Nutrient Cycling in Agroecosystems, 48, 7-24, doi:10.1023/A:1009710122179.

Horowitz, L. W., S. Walters, D. L. Mauzerall, L. K. Emmons, P. J. Rasch, C. Granier, X. X. Tie, J.-F. Lamarque, M. G. Schultz, G. S. Tyndall, J. J. Orlando, and G. P. Brasseur (2003), A global simulation of tropospheric ozone and related tracers: Description and evaluation of MOZART, version 2, J. Geophys. Res., 108, D24, 4784, doi:10.1029/2002JD002853.

Horowitz, L. W., A. M. Fiore, G. P. Milly, R. C. Cohen, A. Perring, P. J. Wooldridge, P. G. Hess, L. K. Emmons, and J.-F. Lamarque, (2007), Observational constraints on the chemistry of isoprene nitrates over the eastern United States, J. Geophys. Res, 112, D12S08, doi:10.1029/2006JD007747.

Houweling, S., F. Dentener, and J. Lelieveld (1998), The impact of nonmethane hydrocarbon compounds on tropospheric photochemistry, J. Geophys. Res., 103 (D9), 10, 673-10, 696, doi:10.1029/97JD03582.

Hoyle, C. R., G. Myhre, T. K. Berntsen, I. S. A. Isaksen (2009), Anthropogenic influence on SOA and the resulting radiative forcing, Atmos. Chem. Phys., 9, 2715-2728, doi:10.5194/acp-9-2715-2009.

Hudman, R. C., N. E. Moore, A. K. Mebust, R. V. Martin, A. R. Russell, L. C. Valin, and R. C. Cohen (2012), Steps towards a mechanistic model of global soil nitric oxide emissions: implementation and space based-constraints, Atmos. Chem. Phys., 12, 7779-7795, doi:10.5194/acp-12-7779-2012.

Ito, A., S. Sillman, and J. E. Penner (2007), Effects of additional nonmethane volatile organic compounds, organic nitrates, and direct emissions of oxygenated organic species on global tropospheric chemistry, J. Geophys. Res., 112, D06309, doi:10.1029/2005JD006556.

Jackson, S. C. (2009), Parallel Pursuit of Near-term and Long-term Climate Mitigation, Science, 326, 5952, 526-527, doi: 10.1126/science.1177042.

Jacob, D.J. (1999), Introduction to Atmospheric Chemistry, Princeton University Press, Princeton, NJ, 52-53.

Jeuken, A., H. J. Eskes, P. F. J. van Velthoven, H. M. Kelder, and E. V. Holm (1999), Assimilation of total ozone satellite measurements in a three-dimensional tracer transport model, J. Geophys. Res., 104, D5, 5551-5563, doi:10.1029/1998JD100052.

Jeuken, A., J. P. Veefkind, F. Dentener, S. Metzger, and C. R. Gonzalez (2001), Simulation of the aerosol optical depth over Europe for August 1997 and a comparison with observations, J. Geophys. Res., 106, 28, 295-28, 311, doi:10.1029/2001JD900063.

Johnson, C.E. and R.G. Derwent (1996), Relative radiative forcing consequences of global emissions of hydrocarbons, carbon monoxide, and NO_x from human activities estimated with a zonally-averaged two-dimensional model. Clim. Change, 34, 439-462.

Jonson, J. E., A. Stohl, A. M. Fiore, P. Hess, S. Szopa, O. Wild, G. Zeng, F. J. Dentener, A. Lupu, M. G. Schultz, B. N. Duncan, K. Sudo, P. Wind, M. Schulz, E. Marmer, C. Cuvelier, T. Keating, A. Zuber, A. Valdebenito, V. Dorokhov, H. De Backer, J. Davies, G. H. Chen, B. Johnson, D. W. Tarasick, R. Stubi, M. J. Newchurch, P. von der Gathen, W. Steinbrecht, and H. Claude (2010), A multi-model analysis of vertical ozone profiles, Atmos. Chem. Phys., 9, 26095-26142, doi:10.5194/acp-10-5759-2010.

Kopacz, M., D. J. Jacob, D. K. Henze, C. L. Heald, D. G. Streets, and Q. Zhang (2009), Comparison of adjoint and analytical Bayesian inversion methods for constraining Asian sources of carbon monoxide using satellite (MOPITT) measurements of CO columns, J. Geophys. Res., 114, D04305, doi:10.1029/2007JD009264.

Kopacz, M., D. J. Jacob, J. A. Fisher, J. A. Logan, L. Zhang, I. A. Megretskaia, R. M. Yantosca, K. Singh, D. K. Henze, J. P. Burrows, M. Buchwitz, I. Khlystova, W. W. McMillan, J. C. Gille, D. P. Edwards, A. Eldering, V. Thouret, P. Nedelec (2010), Global estimates of CO sources with high resolution by adjoint inversion of multiple satellite datasets (MOPITT, AIRS, SCIAMACHY, TES), Atmos. Chem. Phys., 10, 855-876.

Kunhikrishnan, T., M. G. Lawrence, R. von Kuhlmann, A. Richter, A. Ladstatter-Weissenmayer, and J. P. Burrows (2004), Analysis of tropospheric NO_x over Asia using the model of atmospheric transport and chemistry (MATCH-MPIC) and GOME-satellite observations, Atmos. Environ., 38, 581-596, doi:10.1016/j.atmosenv.2003.09.074.

Lacis, A. A., D. J. Wuebbles, and J. A. Logan (1990), Radiative forcing of climate by changes in the vertical distribution of ozone, J. Geophys. Res., 95, 9971-9981, doi:10.1029/JD095iD07p09971.

Lamarque, J.-F., J. T. Kiehl, P. G. Hess, W. D. Collins, L. K. Emmons, P. Ginoux, C. Luo, and X. X. Tie (2005), Response of a coupled chemistry-climate model to changes in aerosol emissions: Global impact on the hydrological cycle and the tropospheric burdens of OH, ozone, and NOx, Geophys. Res. Lett., 32, L16809, doi:10.1029/2005GL023419.

Lapina, K., R. E. Honrath, R. C. Owen, M. V. Martin, and G. Pfister (2006), Evidence of significant large-scale impacts of boreal fires on ozone levels in the midlatitude Northern Hemisphere free troposphere, Geophys. Res. Lett., 33, L10815, doi:10.1029/2006GL025878.

Lawrence, M. G. (1996), Photochemistry in the tropical pacific troposphere: Studies with a global 3D chemistry-meteorology model, Ph.D. thesis, Georgia Institute of Technology.

Lawrence, M. G., Crutzen, P. J., Rasch, P. J., Eaton, B. E., and Mahowald, N. M. (1999), A model for studies of tropospheric photochemistry: Description, global distributions, and evaluation, J. Geophys. Res., 104, 26 245–26 277.

Lawrence, M., P. Jöckel, and R. von Kuhlmann (2001), What does the global mean OH concentration tell us?, Atmos. Chem. Phys., 1, 37-49.

Lawrence, M. G., R. von Kuhlmann, M. Salzmann, and P. J. Rasch (2003), The balance of effects of deep convective mixing on tropospheric ozone, Geophys. Res. Lett., 30, 1940, doi: 10.1029/2003GL017644.

Leibensperger, E. M., L. J. Mickley, D. J. Jacob, and S. R. H. Barrett (2011), Intercontinental influence of NO_x and CO emissions on particulate matter air quality, Atmos Env., 45, 3318-3324, doi:10.1016/j.atmosenv.2011.02.023.

Levy, H., M. D. Schwarzkopf, L. Horowitz, V. Ramaswamy, and K. L. Findell (2008), Strong sensitivity of late 21st century climate to projected changes in short-lived air pollutants, J. Geophys. Res., 113, D06102, doi:10.1029/2007JD009176.

Liao, H., and J. H. Seinfeld (2005), Global impacts of gas-phase chemistry-aerosol interactions on direct radiative forcing by anthropogenic aerosols and ozone, J. Geophys. Res., 110, D18208, doi:10.1029/2005JD005907.

Liu, X.-H., Y. Zhang, J. Xing, Q. Zhang, K. Wang, D. G. Streets, C. Jang, W.-X. Wang, and J.-M. Hao (2010), Understanding of regional air pollution over China using CMAQ, part II. Process analysis and sensitivity of ozone and particulate matter to precursor emissions, Atmos. Environ., 44, 3719-3727.

Meinshausen, M., S. J. Smith, K. V. Calvin, J. S. Daniel, M. L. T. Kainuma, J.-F. Lamarque, K. Matsumoto, S. A. Montzka, S. C. B. Raper, K. Riahi, A. M. Thomson, G. J. M. Velders and D. van Vuuren (2011), The RCP Greenhouse Gas Concentrations and their Extension from 1765 to 2300, Climatic Change (Special Issue), 109, 213-241, doi:10.1007/s10584-011-0156-z.

Metzger, S., F. Dentener, S. Pandis, and J. Lelieveld (2002), Gas/aerosol partitioning: 1. A computationally efficient model, J. Geophys. Res., 107(D16), 4312, doi:10.1029/2001JD001102.

Ming, Y., V. Ramaswamy, P. A. Ginoux, and L. H. Horowitz (2005), Direct radiative forcing of anthropogenic organic aerosol, J. Geophys. Res., 110, D20208, doi:10.1029/2004/JD005573.

Naik, V., D. Mauzerall, L. Horowitz, M. D. Schwarzkopf, V. Ramaswamy, and M. Oppenheimer (2005), Net radiative forcing due to changes in regional emissions of tropospheric ozone precursors, J. Geophys. Res., 110, D24306, doi:10.1029/2005JD005908.

Naik, V., D. L. Mauzerall, L. W. Horowitz, M. D. Schwarzkopf, V. Ramaswamy, and M. Oppenheimer (2007), On the sensitivity of radiative forcing from biomass burning aerosols and ozone to emission location, Geophys. Res. Lett., 34, L03818, doi:10.1029/2006GL028149.

Olivier, J., J. Peters, C. Granier, G. Petron, J. Muller, and S. Wallens (2003), Present and future surface emissions of atmospheric compounds, POET report #2, EU project EVK2-1999-00011, available at: http://accent.aero.jussieu.fr/POET_metadata.php.

Park, J. H., M. K. W. Ko, C. H. Jackman, R. A. Plumb, J. A. Kaye and K. H. Sage (eds.) (1999), M&M-2, NASA: Models and Measurements Intercomparison II.TM_1999_209554.

Pétron, G., C. Granier, B. Khattatov, V. Yudin, J. Lamarque, L. Emmons, J. Gille, and D. P. Edwards (2004), Monthly CO surface sources inventory based on the 2000-2001 MOPITT satellite data, Geophys. Res. Lett., 31, L21107, doi:10.1029/2004GL020560.

Pfister, G., G. Pétron, L. K. Emmons, J. C. Gille, D. P. Edwards, J.-F. Lamarque, J.-L. Attié, C. Granier, and P. C. Novelli (2004), Evaluation of CO simulations and the analysis of the CO budget for Europe, J. Geophys. Res., 109, D19304, doi:10.1029/2004JD004691.

Pfister, G., P. Hess, L. Emmons, J.-F. Lamarque, C. Wiedinmeyer, D. Edwards, G. Pétron, J. Gille, and G. Sachse (2005), Quantifying CO emissions from the 2004 Alaskan wildfires using MOPITT CO data, Geophys. Res. Lett., 32, 11, L11809, doi:10.29/2005GL022995.

Pfister, G. G., L. K. Emmons, P. G. Hess, R. Honrath, J.-F. Lamarque, M. Val Martin, R. C. Owen, M. A. Avery, E. V. Browell, J. S. Holloway, P. Nedelec, R. Purvis, T. B. Ryerson, G. W. Sachse, and H. Schlager (2006), Ozone production from the 2004 North American boreal fires, J. Geophys. Res., 111, D24S07, doi:10.1029/2006JD007695.

Pfister, G. G., L. K. Emmons, P. G. Hess, J.-F. Lamarque, J. J. Orlando, S. Walters, A. Guenther, P. I. Palmer, and P. J. Lawrence (2008), Contribution of isoprene to chemical budgets: A model tracer study with the NCAR CTM MOZART-4, J. Geophys. Res., 113, D05308, doi:10.1029/2007JD008948.

Pham, M., J. F. Muller, G. P. Brasseur, C. Granier, and G. Megie (1995), A three-dimensional study of the tropospheric sulfur cycle, J. Geophys. Res., 100, D12, 26061-26092, doi:10.1029/95JD02095.

Prather, M., R. Derwent, D. Ehhalt, P. Fraser, E Sanhueza, X. Zhou (1995), Chapter 2: Other tracer gases and atmospheric chemistry, in Climate Change 1994, Intergovernmental Panel on Climate Change, J.T. Houghton et al., eds., Cambridge U. Press, pp. 73-126.

Prather, M. J. (1996), Time scales in atmospheric chemistry: Theory, GWPs for CH_4 and CO, and runaway growth, Geophys. Res. Lett., 23, 2597-2600, doi:10.1029/96GL02371.

Prather, M., D. Ehhalt, F. Dentener, R. G. Derwent, E. Dlugokencky, E. Holland, I. S. A. Isaksen, J. Katima, V. Kirchhoff, P. Matson, P. M. Midgley, and M. Wang (2001), Climate Change 2001: The Scientific Basis, edited by J.T. Houghton, Y. Ding, D. J. Griggs, M. Noguer, P. J. Van der Linden, X. Dai, K. Maskell, and C. A. Johnson, Intergovernmental Panel on Climate Change, Cambridge University Press, Cambridge, 239-287.

Prather, M. J., C. D. Holmes, and J. J. Hsu (2012), Reactive greenhouse gas scenarios: systematic exploration of uncertainties and the role of atmospheric chemistry, Geophys. Res. Lett., 39, L09803, doi:10.1029/2012GL051440.

Ramaswamy, V., O. Boucher, J. Haigh, D. Hauglustaine, J. Haywood, G. Myhre, T. Nakajima, G. Y. Shi, S. Solomon, R. Betts, R. Charlson, C. Chuang, J. S. Daniel, A. Del Genio, R. van Dorland, J. Feichter, J. Fuglestvedt, P. M. de F. Forster, S. J. Ghan, A. Jones, J. T. Kiehl, D. Koch, C. Land, J. Lean, U. Lohmann, K. Minschwaner, J. E. Penner, D. L. Roberts, H. Rodhe, G. J. Roelofs, L. D. Rotstayn, T. L. Schneider, U. Schumann, S. E. Schwartz, M. D. Schwarzkopf, K. P. Shine, S. Smith, D. S. Stevenson, F. Stordal, I. Tegen, and Y. Zhang (2001), Radiative forcing of climate change, Climate Change 2001: The Scientific Basis. Contribution of Working Group I to the Third Assessment Report of the Intergovernmental Panel on Climate Change [Houghton, J.T., et al. (eds.)], Cambridge University Press, Cambridge, United Kingdom and New York, NY, USA, pp. 349–416.

Rasch, P. J., M. C. Barth, J. T. Kiehl, S. E. Schwartz, and C. M. Benkovitz (2000), A description of the global sulfur cycle and its controlling processes in the National Center for Atmospheric Research Community Climate Model, Version 3, J. Geophys. Res., 105, D1, 1367-1385, doi:10.1029/1999JD900777.

Reidmiller, D. R., A. M. Fiore, D. A. Jaffe, D. Bergmann, C. Cuvelier, F. J. Dentener, B. N. Duncan, G. Folberth, M. Gauss, S. Gong, P. Hess, J. E. Jonson, T. Keating, A. Lupu, E. Marmer, R. Park, M. G. Schultz, D. T. Shindell, S. Szopa, M. G. Vivanco, O. Wild, and A. Zuber (2009), The influence of foreign vs. North American emissions on surface ozone in the US, Atmos. Chem. Phys., 9, 5027-5042.

Riahi, K., A. Gruebler, and N. Nakicenovic (2007), Scenarios of long-term socio-economic and environmental development under climate stabilization, Technological Forecasting and Social Change, 74, 7, 887-935.

Riahi, K., S. Rao, V. Krey, C. Cho, V. Chirkov, G. Fischer, G. Kindermann, N. Nakicenovic, and P. Rafaj (2011), RCP 8.5 – A scenario of comparatively high greenhouse gas emissions, Climatic Change, 109, 33-57, doi:10.1007/s10584-011-0149-y.

Rienecker, M. M., M. J. Suarez, R. Todling, J. Bacmeister, L. Takacs, H.-C. Liu, W. Gu, M. Sienkiewicz, R. D. Koster, R. Gelaro, I. Stajner, and J. E. Nielsen (2008), The GEOS-5 Data Assimilation System—Documentation of versions 5.0.1, 5.1.0, and 5.2.0, NASA Tech. Memo., NASA/TM–2008–104606, vol. 27, 118 pp.

Rotman, D. A., C. S. Atherton, D. J. Bergmann, P. J. Cameron-Smith, C. C. Chuang, P. S. Connell, J. E. Dignon, A. Franz, K. E. Grant, D. E. Kinnison, C. R. Molenkamp, D. D. Proctor, and J. R. Tannahill (2004), IMPACT, the LLNL 3-D global atmospheric chemical transport model for the combined troposphere and stratosphere: Model description and analysis of ozone and other trace gases, J. Geophys. Res., 109, D04303, doi:10.1029/2002JD003155.

Rypdal, K., T. Berntsen, J. S. Fuglestvedt, K. Aunan, A. Torvanger, F. Stordal, J. M. Pacyna, and L. P. Nygaard (2005), Tropospheric ozone and aerosols in climate agreements: scientific and political challenges, Environ. Sci. Policy, 8, 29-43, doi:10.1016/j.envsci.2004.09.003.

Rypdal, K., N. Rive, T. Berntsen, H. Fagerli, Z. Klimont, T. K. Mideksa, and J. S. Fuglestvedt (2009), Climate and air quality-driven scenarios of ozone and aerosol precursor abatement, Environ. Sci. Policy, 12, 7, 855-869, doi: 10.1016/j.envsci.2009.08.002.

Saikawa, E., V. Naik, L. W. Horowitz, J. F. Liu, and D. L. Mauzerall (2009), Present and potential future contributions of sulfate, black and organic carbon aerosols from China to global air quality, premature mortality and radiative forcing, Atmos. Environ., 43, 2814-2822, doi:10.1016/j.atmosenv.2009.02.017.

Sanderson, M. G., F. J. Dentener, A. M. Fiore, C. Cuvelier, T. J. Keating, A. Zuber, C. S. Atherton, D. J. Bergmann, T. Diehl, R. M. Doherty, B. N. Duncan, P. Hess, L. W. Horowitz, D. J. Jacob, J. E. Jonson, J. W. Kaminski, A. Lupu, I. A. MacKenzie, E. Mancini, E. Marmer, R. Park, G. Pitari, M. J. Prather, K. J. Pringle, S. Schroeder, M. G. Schultz, D. T. Shindell, S. Szopa, O. Wild, and P. Wind (2008), A multi-model study of the hemispheric transport and deposition of oxidized nitrogen, Geophys. Res. Lett., 35, L17815, doi:10.1029/2008GL035389.

Schultz, M. G., L. Backman, Y. Balkanski, S. Bjoerndalsaeter, R. Brand, J. P. Burrows, S. Dalsoeren, M. de Vasconcelos, B. Grodtmann, D. A. Hauglustaine, A. Heil, J. J. Hoelzemann, I. S. A. Isaksen, J. Kaurola, W. Knorr, A. Ladstaetter-Weißenmayer, B. Mota, D. Oom, J. Pacyna, D. Panasiuk, J. M. C. Pereira, T. Pulles, J. Pyle, S. Rast, A. Richter, N. Savage, C. Schnadt, M. Schulz, A. Spessa, J. Staehelin, J. K. Sundet, S. Szopa, K. Thonicke, M. van het Bolscher, T. van Noije, P. van Velthoven, A. F. Vik, F. Wittrock (2007), REanalysis of the TROpospheric chemical composition over the past 40 years (RETRO) — A long-term global modeling study of tropospheric chemistry, Final Report, Jülich/Hamburg, Germany.

Schumann, U. and H. Huntrieser (2007), The global lightning-induced nitrogen oxides source, Atmos. Chem. Phys., 7, 3823-3907.

Schwarzkopf, M. D., and V. Ramaswamy (1999), Radiative effects of CH_4, N_2O, halocarbons and the foreign-broadened H_2O continuum: A GCM experiment, J. Geophys. Res., 104, 9467-9488, doi:10.1029/1999JD900003.

Seinfeld, J. H., G. B. Erdakos, W. E. Asher, and J. F. Pankow (2001), Modeling the formation of secondary organic aerosol (SOA), 2, The predicted effects of relative humidity on aerosol formation in the a-pinene-, b-pinene-, sabinene-, d3-carene-, and cyclohexene-ozone systems, Environ. Sci. Technol., 35, 1806-1817.

Seinfeld, J.H., and S. N. Pandis (2006), Atmospheric Chemistry and Physics - From Air Pollution to Climate Change (2nd Ed.). John Wiley and Sons, Inc., ISBN 0471828572.

Shindell, D. T., G. Faluvegi, N. Bell, and G. A. Schmidt (2005), An emissions-based view of climate forcing by methane and tropospheric ozone, Geophys. Res. Lett., 32, L04803, doi:10.1029/2004GL021900.

Shindell, D.T., G. Faluvegi, D. S. Stevenson, M. C. Krol, L. K. Emmons, J.-F. Lamarque, G. Pétron, F. J. Dentener, K. Ellingsen, M. G. Schultz, O. Wild, M. Amann, C. S. Atherton, D. J. Bergmann, I. Bey, T. Butler, J. Cofala, W. J. Collins, R. G. Derwent, R. M. Doherty, J. Drevet, H. J. Eskes, A. M. Fiore, M. Gauss, D. A. Hauglustaine, L. W. Horowitz, I. S. A. Isaksen, M. G. Lawrence, V. Montanaro, J.-F. Müller, G. Pitari, M. J. Prather, J. A. Pyle, S. Rast, J. M. Rodriguez, M. G. Sanderson, N. H. Savage, S. E. Strahan, K. Sudo, S. Szopa, N. Unger, T. P. C. van Noije, and G. Zeng (2006), Multimodel simulations of carbon monoxide: Comparison with observations and projected near-future changes, J. Geophys. Res., 111, D19306, doi:10.1029/2006JD007100.

Shindell, D. T., M. Chin, F. Dentener, R. M. Doherty, G. Faluvegi, A. M. Fiore, P. Hess, D. M. Koch, I. A. MacKenzie, M. G. Sanderson, M. G. Schultz, M. Schulz, D. S. Stevenson, H. Teich, C. Textor, O. Wild, D. J. Bergmann, I. Bey, H. Bian, C. Cuvelier, B. N. Duncan, G. Folberth, L. W. Horowitz, J. Jonson, J. W. Kaminski, E. Marmer, R. Park, K. J. Pringle, S. Schroeder, S. Szopa, T. Takemura, G. Zeng, T. J. Keating, and A. Zuber (2008), A multi-model assessment of pollution transport to the Arctic, Atmos. Chem. Phys., 8, 5353-5372, doi:10.5194/acp-8-5353-2008.

Shindell, D., and G. Faluvegi (2009), Climate response to regional radiative forcing during the twentieth century, Nature Geoscience, 2, 294-300, doi:10.1038/NGEO473.

Shindell, D. T., G. Faluvegi, D. M. Koch, G. A. Schmidt, N. Unger, and S. E. Bauer (2009), Improved attribution of climate forcing to emissions, Science, 326, 716-718, doi:10.1126/science.1174760.

Shindell, D. T., M. Schulz, Y. Ming, T. Takemura, G. Faluvegi, and V. Ramaswamy (2010), Spatial scales of climate response to inhomogeneous radiative forcing, J. Geophys. Res., 115, D19110, doi:10.1029/2010JD014108.

Shindell, D., J. C. I. Kuylenstierna, E. Vignati, R. van Dingenen, M. Amann, Z. Klimont, S.C. Anenberg, N. Muller, G. Janssens-Maenhout, F. Raes, J. Schwartz, G. Faluvegi, L. Pozzoli, K. Kupiainen, L. Höglund-Isaksson, L. Emberson, D. Streets, V. Ramanathan, K. Hicks, N.T.K. Oanh, G. Milly, M. Williams, V. Demkine, and D. Fowler (2012), Simultaneously mitigating near-term climate change and improving human health and food security. Science, 335, 183-189, doi:10.1126/science.1210026.

Shindell, D. T., J.-F. Lamarque, M. Schulz, M. Flanner, C. Jiao, M. Chin, P. J. Young, Y. H. Lee, L. Rotstayn, N. Mahowald, G. Milly, G. Faluvegi, Y. Balkanski, W. J. Collins, A. J. Conley, S. Dalsoren, R. Easter, S. Ghan, L. Horowitz, X. Liu, G. Myhre, T. Nagashima, V. Naik, S. T. Rumbold, R. Skeie, K. Sudo, S. Szopa, T. Takemura, A. Voulgarakis, J.-H. Yoon, and F. Lo (2013), Radiative forcing in the ACCMIP historical

and future climate simulations, Atmos. Chem. Phys., 13, 2939-2974, doi:10.5194/acp-13-2939-2013.

Shine, K. P., J. S. Fuglestvedt, K. Hailemariam, and N. Stuber (2005), Alternatives to the global warming potential for comparing climate impacts of emissions of greenhouse gases, Clim. Change, 68, 281-302, doi:10.1007/s10584-005-1146-9.

Shine, K. P., T. K. Berntsen, J. S. Fuglestvedt, R. B. Skeie, and N. Stuber (2007), Comparing the climate effect of emissions of short- and long-lived climate agents, Philos. Trans. R. Soc. A, 365, 1903-1914, doi:10.1098/rsta.2007.2050.

Sillman, S., D. He, C. Cardelino, and R. E. Imhoff (1997), The use of photochemical indicators to evaluate ozone-NOx-hydrocarbon sensitivity: Case studies from Atlanta, New York, and Los Angeles, Journal of Air & Waste Management Association, 47:10, 1030-1040.

Sitch, S., P. M. Cox, W. J. Collins, and C. Huntingford (2007), Indirect radiative forcing of climate change through ozone effects on the land-carbon sink, Nature, 448, 791-794, doi:10.1038/nature06059

Søvde, O. A., C. R. Hoyle, G. Myhre, and I. S. A. Isaksen (2011), The HNO_3 forming branch of the HO_2+NO reaction: pre-industrial-to-present trends in atmospheric species and radiative forcings, Atmos. Chem. Phys., 11, 8929-8943, doi:10.5194/acpd-11-8929-2011.

Spivakovsky, C. M., J. A. Logan, S. A. Montzka, Y. J. Balkanski, M. Foreman-Fowler, D. B. A. Jones, L. W. Horowitz, A. C. Fusco, C. A. M. Brenninkmeijer, M. J. Prather, S. C. Wofsy, and M. B. McElroy (2000), Three-dimensional climatological distribution of tropospheric OH: Update and evaluation, J. Geophys. Res., 105, 8931-8980.

Stevenson, D.S., F. J. Dentener, M. G. Schultz, K. Ellingsen, T. P. C. van Noije, O. Wild, G. Zeng, M. Amann, C. S. Atherton, N. Bell, D. J. Bergmann, I. Bey, T. Butler, J. Cofala, W. J. Collins, R. G. Derwent, R. M. Doherty, J. Drevet, H. J. Eskes, A. M. Fiore, M. Gauss, D. A. Hauglustaine, L. W. Horowitz, I. S. A. Isaksen, M. C. Krol, J.-F. Lamarque, M. G. Lawrence, V. Montanaro, J.-F. Muller, G. Pitari, M. J. Prather, J. A. Pyle, S. Rast, J. M. Rodriguez, M. G. Sanderson, N. H. Savage, D. T. Shindell, S. E. Strahan, K. Sudo, and S. Szopa (2006), Multimodel ensemble simulations of present-day and near-future tropospheric ozone, J. Geophys. Res., 111, D08301, doi:10.1029/2005JD006338.

Stevenson, D. S., P. J. Young, V. Naik, J.-F. Lamarque, D. T. Shindell, A. Voulgarakis, R. B. Skeie, S. B. Dalsoren, G. Myhre, T. K. Berntsen, G. A. Folberth, S. T. Rumbold, W. J. Collins, I. A. MacKenzie, R. M. Doherty, G. Zeng, T. P. C. van Noije, A. Strunk, D. Bergmann, P. Cameron-Smith, D. A. Plummer, S. A. Strode, L. Horowitz, Y. H. Lee, S. Szopa, K. Sudo, T. Nagashima, B. Josse, I. Cionni, M. Righi, V. Eyring, A. Conley, K. W. Bowman, O. Wild, and A. Archibald (2013), Tropospheric ozone changes, radiative forcing and attribution to emissions in the Atmospheric Chemistry and Climate Model Intercomparison Project (ACCMIP), Atmos. Chem. Phys., 13, 3063-3085, doi: 10.5194/acp-13-3063-2013.

Task Force on Hemispheric Transport of Air Pollution (2010), Hemispheric Transport of Air Pollution, United Nations Economic Commission for Europe, Geneva, Switzerland.

Tie, X. X., S. Madronich, S. Walters, D. P. Edwards, P. Ginoux, N. Mahowald, R. Y. Zhang, C. Lou, and G. Brasseur (2005), Assessment of the global impact of aerosols on tropospheric oxidants, J. Geophys. Res., 110, D03204, doi:10.1029/2004JD005359.

Tilmes, S., J.-F. Lamarque, L. K. Emmons, A. Conley, M. G. Schultz, M. Saunois, V. Thouret, A. M. Thompson, S. J. Oltmans, B. Johnson, and D. Tarasick (2012), Technical Note: Ozonesonde climatology between 1995 and 2011: description, evaluation and applications, Atmos. Chem. Phys., 12, 7475-7497, doi:10.5194/acp-12-7475-2012.

UNEP (2011), Near-term climate protection and clean air benefits: Actions for controlling short-lived climate forcers, United Nations Environment Programme (UNEP), Nairobi, Kenya, 78 pp.

Unger, N., D. T. Shindell, D. M. Koch, and D. G. Streets (2006), Cross influences of ozone and sulfate precursor emissions changes on air quality and climate, Proc. Natl. Acad. Sci., 103, 12, 4377-4380, doi:10.1073/pnas.0508769103.

Unger, N., D. T. Shindell, D. M. Koch, and D. G. Streets (2008), Air pollution radiative forcing from specific emissions sectors at 2030, J. Geophys. Res., 113, D02306, doi:10.1029/2007JD008683.

Unger, N., T. C. Bond, J. S. Wang, D. M. Koch, S. Menon, D. T. Shindell, S. Bauer, and A. R. Ravishankara (2010), Attribution of climate forcing to economic sectors, Proc. Natl. Acad. Sci., 107, 8, 3382-3387.

Unger, N. (2012), Global climate forcing by criteria air pollutants, Annu. Rev. Environ. Resour., 37, 1-24, doi:10.1146/annurev-environ-082310-100824.

Volkamer, R., J. L. Jimenez, F. San Martini, K. Dzepina, Q. Zhang, D. Salcedo, L. T. Molina, D. R. Worsnop, and M. J. Molina (2006), Secondary organic aerosol formation from anthropogenic air pollution: Rapid and higher than expected, Geophys. Res. Lett., 33, L17811, doi:10.1029/2006GL026899.

von Kuhlmann, R. (2001), Photochemistry of tropospheric ozone, its precursors and the hydroxyl radical: A 3D-modeling study considering non-methane hydrocarbons, Ph.D. thesis, Johannes Gutenberg-Universit¨at Mainz, Mainz, Germany.

Voulgarakis, A., V. Naik, J.-F. Lamarque, D. T. Shindell, P. J. Young, M. J. Prather, O. Wild, R. D. Field, D. Bergmann, P. Cameron-Smith, I. Cionni, W. J. Collins, S. B. Dalsøren, R. M. Doherty, V. Eyring, G. Faluvegi, G. A. Folberth, L. W. Horowitz, B. Josse, I. A. McKenzie, T. Nagashima, D. A. Plummer, M. Righi, S. T. Rumbold, D. S. Stevenson, S. A. Strode, K. Sudo, S. Szopa, and G. Zeng (2013), Analysis of present day and future OH and methane lifetime in the ACCMIP simulations. *Atmos. Chem. Phys.*, 13, 2563-2587, doi:10.5194/acp-13-2563-2013.

Wang, W. C., Y. C. Zhuang, and R. D. Bojkov (1993), Climatic implications of observed changes in ozone vertical distribution in the middle and high latitudes of the Northern Hemisphere, Geophys. Res. Lett., 20, 1567-1570, doi:10.1029/93GL01318.

West, J. J., A. M. Fiore, V. Naik, L. W. Horowitz, M. D. Schwarzkopf, and D. L. Mauzerall (2007), Ozone air quality and radiative forcing consequences of changes in ozone precursor emissions, Geophys. Res. Lett., 34, L06806, doi:10.1029/2006GL029173.

West, J. J., V. Naik, L. W. Horowitz, and A. M. Fiore (2009a), Effect of regional precursor emission controls on long-range ozone transport – Part 1: Short-term changes in ozone air quality, Atmos. Chem. Phys., 9, 6077-6093.

West, J. J., V. Naik, L. W. Horowitz, and A. M. Fiore (2009b), Effect of regional precursor emission controls on long-range ozone transport – Part 2: Steady-state changes in ozone air quality and impacts on human mortality, Atmos. Chem. Phys., 9, 6095-6107.

Wild, O., M. J. Prather, and H. Akimoto (2001), Indirect long-term global radiative cooling from NO_x emissions, Geophys. Res. Lett., 28, 9, 1719-1722, doi:10.1029/2000GL012573.

World Meteorological Organization (2006), WMO Greenhouse Gas Bulletin: The State of Greenhouse Gases in the Atmosphere using Global Observations through 2005, Bulletin No. 1: March 2006.